

Development of a Pre-Treatment Process for Magnesium & Magnox Wastes

Joseph Alexander Vickers

Submitted in accordance with the requirements for the degree of
Doctor of Philosophy

The University of Leeds
School of Chemical and Process Engineering

October 2022

The candidate confirms that the work submitted is his/her own and that appropriate credit has been given where reference has been made to the work of others.

This copy has been supplied on the understanding that it is copyright material and that no quotation from the thesis may be published without proper acknowledgement.

The right of Joseph Alexander Vickers to be identified as Author of this work has been asserted by him in accordance with the Copyright, Designs and Patents Act 1988.

© 2022 The University of Leeds and Joseph Alexander Vickers

Acknowledgements

The work that went into this thesis would not have been possible without the funding provided by EPSRC via iCASE award EP/P510555/1 associated with the Next Generation Nuclear (NGN) Centre for Doctoral Training funded by EP/L015390/1.

First and foremost, I would like to thank my supervisor Bruce for all the years of support and advice, both technical and otherwise, that helped me become a confident researcher. Thank you for giving me the opportunity to join your group, the years I spent as part of the research community at Leeds are ones that I will look back on with much fondness. To the Nuclear Engineering group, thank you for making every day a pleasure to be at work with your friendship and support. Likewise, to my colleagues in NGN Cohort 3, thank you for making me feel like part of a thriving scientific and engineering community, I look forward to running into you time and again for the rest of my career.

To Katie and Adiza, thank you for the enthusiasm and diligence with which you tackled your research projects. It was a privilege to be your mentor and your contributions to this work were invaluable; I can only hope that for my part I was able to be a positive influence during your time in the research group.

To Richard and Colin and the Nuclear Engineering group at Lancaster, thank you for helping me take my first steps in electrochemistry and for all the advice and support since then.

To the staff in SCAPE, particularly Chris the indomitable technician, thank you for enabling me to carry out my work and for finding easy solutions to difficult problems.

Finally, thanks to my family for all the love and unwavering encouragement, without which I would never have come so far. Last and utmost, thank you to my darling wife: the esteemed Dr. Sweeney and Mrs. Vickers for her unending love, support, advice, patience and proof-reading ability.

Abstract

A new process for stabilising contaminated Magnox swarf wastes was proposed, termed "Cementisation". The process utilises enhanced corrosion in concentrated magnesium chloride solutions, producing a hydrated magnesium oxychloride cement product. The chemical reactivity of the metal is eliminated and the hazards of chronic corrosion are effectively circumvented. A campaign of experimental work in three parts was performed to underpin Cementisation, focussing on the corrosion and dissolution of Mg and Magnox in concentrated salt solutions as the key step in the process.

To determine the corrosion rate of magnesium and Magnox in concentrated solutions of MgCl_2 and AlCl_3 , the findings of previous researchers, specifically the activation energy of Mg dissolution in 4M MgCl_2 , were validated using the recently developed method of gravimetric hydrogen collection. The activation energy in all systems was determined to lie in the range $42\text{-}51\text{kJmol}^{-1}$, implying the reaction is under mixed transport/reaction control. Furthermore, in 4M MgCl_2 solution at temperatures $>50^\circ\text{C}$, a passive layer of aluminium oxide/hydroxides was observed to form on the surface of Magnox alloy samples.

An in-depth investigation of the corrosion mechanism in concentrated salt solutions was then performed using impedance spectroscopy, with a view to understanding the corrosion mechanism and inform optimisation of Cementisation. It was shown that the transition from passive to active corrosion behaviour is enabled by the increasing solubility of the corrosion product, particularly as the stable product transitions from magnesium hydroxide to oxychlorides where $[\text{MgCl}_2]>2\text{M}$. These results were discussed within the context of the corrosion mechanism of magnesium and its alloys.

Finally, a proof-of-concept experiment on the laboratory scale was performed to demonstrate that magnesium oxychloride cements could be synthesised from metallic magnesium powders and raspings. This was confirmed by physical analysis techniques: XRD, STA and SEM. By quantitative XRD analysis it was determined that $>95\%$ conversion to MOC phases was achieved for all samples.

Ultimately, it was demonstrated that Cementisation represents a viable method for stabilising Magnox swarf wastes and warrants further development towards optimisation and industrial deployment.

Table of Contents

Acknowledgements	2
Abstract	3
Table of Contents	4
List of Tables	7
List of Figures	9
List of Abbreviations	13
List of Variables	15
1 Introduction	17
1.1 Magnox.....	17
1.2 Current Strategy.....	17
1.3 Enhanced Corrosion as a Stabilising Treatment.....	19
2 Aims & Objectives	24
3 Literature Review	25
3.1 Radioactive Waste Disposal in the UK.....	25
3.1.1 Current Strategy.....	25
3.1.2 Cementation.....	26
3.2 Magnesium Corrosion.....	27
3.2.1 General Behaviour.....	28
3.2.2 Experimental Methods.....	31
3.2.2.1 Voltammetry & Tafel Extrapolation.....	31
3.2.2.2 Electrochemical Impedance Spectroscopy.....	32
3.2.2.3 Immersion Testing.....	34
3.2.3 Corrosion Mechanism.....	35
3.3 Differences Between Magnesium and Magnox Corrosion.....	37
3.4 Magnesium Oxychloride Cements.....	39
3.5 Summary.....	41
4 Corrosion Kinetics of Magnesium and Magnox Alloy in Concentrated Salt Solutions	43
4.1 Introduction.....	43
4.2 Experimental.....	44
4.2.1 Gravimetric Hydrogen Collection.....	44
4.2.2 Sample Preparation.....	46
4.2.3 Experimental Method.....	48
4.2.4 Error Analysis.....	51

4.2.5	Thermochemical Calculations.....	54
4.3	Results & Discussion	54
4.3.1	Corrosion Rate	54
4.3.2	Thermochemical Calculations.....	60
4.3.3	Corrosion Kinetics	62
4.3.4	Rate-Controlling Steps in Heterogeneous Reactions	67
4.4	Conclusions	70
5	Impedance Investigation of Magnesium and Magnox in Concentrated Salt Solutions	72
5.1	Introduction.....	72
5.2	Theory.....	72
5.2.1	Reaction Framework.....	72
5.3	Impedance Models	75
5.4	Experimental.....	80
5.4.1	Sample Preparation	80
5.4.2	Methods.....	81
5.4.3	Data Fitting.....	83
5.5	Results & Discussion	84
5.5.1	Validation.....	84
5.5.2	Potentiodynamic Polarisation	88
5.5.3	Post-Immersion Observations.....	93
5.5.4	Effect of MgCl ₂ Concentration	94
5.5.4.1	Low Concentration	94
5.5.4.2	Intermediate/Threshold Concentration.....	95
5.5.4.3	High Concentration	97
5.5.5	Impedance Response under Imposed Potential	104
5.5.6	Impedance in AlCl ₃ Solutions	109
5.5.7	Mg Corrosion Mechanism in Concentrated Salt Solutions.....	113
5.5.8	Magnox Alloy Corrosion in Concentrated Salt Solutions.....	116
5.6	Conclusions	126
6	Synthesis of Magnesium Oxychloride Cement by the Oxidation of Metallic Magnesium.....	128
6.1	Introduction.....	128
6.2	Materials & Methods	129
6.3	Experimental.....	132
6.3.1	Sample Preparation	132

6.3.2 Analysis.....	137
6.4 Results & Discussion	138
6.4.1 X-ray Diffraction.....	139
6.4.2 Thermal Analysis	145
6.4.3 Microscopy	150
6.5 Conclusions	154
7 Conclusions	155
7.1 Kinetics of Pure Mg and Magnox Dissolution	155
7.2 Corrosion Mechanisms.....	156
7.3 Cement Synthesis.....	157
8 Future Work.....	160
8.1 Kinetics of Pure Mg and Magnox Dissolution	160
8.2 Corrosion Mechanisms.....	162
8.3 Cement Synthesis.....	163
8.4 Summary.....	167
Publications and Conference Presentations	169
Bibliography	170

List of Tables

Table 4.1 Vapour pressure values calculated from saturation pressure of water modified for osmotic coefficients: $\text{MgCl}_2 = 2.5$, $\text{AlCl}_3 = 2.8$.	52
Table 4.2 Table of average corrosion rates in millimetres per hour [mmh^{-1}] \pmstandard deviation of 4 replicate measurements.	56
Table 4.3 Parameters used to calculate density, pH and viscosity in solutions of 4M MgCl_2 and 2.67M AlCl_3 using SPECE8.	60
Table 4.4 Table of values describing the effect of temperature on 4M MgCl_2 solution calculated via SPECE8 and the consequential effect on aluminium speciation calculated using Act2.	61
Table 4.5 Table of values describing the average measured effective activation energy of Mg and Magnox in 4M MgCl_2 and 2.67M AlCl_3 along with the standard deviation of 4 replicate measurements.	65
Table 5.1 Area-normalised parameter values for the impedance response of pure Mg in 0.6M NaCl fitted to the circuit model.	87
Table 5.2 Table of parameters determined by fitting of the kinetic model to the impedance response of pure Mg in 0.6M NaCl. Where the size of the associated standard error exceeds the value of the parameter the error value is highlighted in orange.	87
Table 5.3 Area-normalised parameter values for pure Mg in MgCl_2 solutions determined by fitting to the circuit model with associated standard error.	99
Table 5.4 Table of parameter values for pure Mg in MgCl_2 solutions determined by fitting to the Kinetic Model with associated standard error. Where error estimates exceed the magnitude of the parameter value the cell is highlighted in orange.	101
Table 5.5 Area-normalised parameter values determined by fitting impedance data to the circuit model for pure Mg in 4M MgCl_2 at bias potentials from -0.25V to +0.5V relative to OCP. Errors are the standard error of the regression for each parameter.	106
Table 5.6 Area-normalised parameter values for solutions of the circuit model fitted to the impedance response of pure Mg in saturated and unsaturated (with respect to Mg^{2+} ions) 2.67M AlCl_3.	111
Table 5.7 Table of solution properties determined by thermochemical calculations for evaluating dependence of Mg corrosion behaviour on water availability and Mg^{2+} ion concentration.	112

Table 5.8 Area-normalised parameter values determined by fitting impedance data to the circuit model for Magnox alloy in 4M MgCl₂ at bias potentials from -0.1V to +0.5V relative to OCP. Errors are the standard error of the regression for each parameter. Where standard error estimates exceed the magnitude of the parameter value the cell is highlighted in orange.	120
Table 5.9 Area normalised parameter values determined by fitting impedance data to the circuit model for Magnox alloy in 2.67M AlCl₃.....	123
Table 6.1 Elemental distribution of Mg raspings as determined by X-ray fluorescence.	131
Table 6.2 Active surface area of feed materials used to synthesise cement samples. Values shown are the average and standard deviation of 4 independent samples.	132
Table 6.3 Matrix of cement samples categorised by MgCl₂ solution batch, analysis stream and fill material.	134
Table 6.4 Reference patterns used for quantitative analysis of diffraction patterns obtained from cement samples. Magnesium (Mg) was only included for samples generated from metallic feeds.....	139
Table 6.5 Relative phase composition of cement samples as determined by quantitative Rietveld analysis of diffraction spectra. Quantities are expressed as the average weight fraction (wt%) ± standard deviation.	142
Table 6.6 Table of data concerning subsamples analysed by STA.....	145

List of Figures

Figure 3.1 Simplified representation of the surface layers formed on magnesium metal surfaces during aqueous corrosion.	29
Figure 4.1 Schematic representation of the apparatus used for gravimetric hydrogen collection. As fluid is displaced the net weight of the collector changes, allowing the volume of gas to be determined as a function of time.....	46
Figure 4.2 Schematic representation of the electrode construction used for dissolution and electrochemical testing.....	47
Figure 4.3 Photographs of the dummy Magnox fuel rod (left) and sections of fin that were cut off (right) to produce samples for dissolution testing.	47
Figure 4.4 Plot showing balance output as a function of time during the collection of hydrogen from Mg corroding in 4M MgCl ₂ at ambient conditions (~20°C) with simultaneous OCP monitoring. The highlighted region shows the period from which rate data were extracted corresponding with stable OCP as an indicator of dynamic equilibrium.	48
Figure 4.5 Diagram showing the forces acting on the submerged collector at steady state. The mass of the collector is represented as $m_{collector}$	50
Figure 4.6 Series of plots showing evaporative losses over time measured with no sample present for each temperature in 4M MgCl ₂	53
Figure 4.7 Series of plots showing the reaction rate of Mg in 4M MgCl ₂ over the temperature range 20-60°C as measured by gravimetric hydrogen collection and expressed in terms of moles per metre squared (molm ⁻²).	55
Figure 4.8 Series of plots showing average corrosion rate over the temperature range 20-60°C for all combinations of alloy and salt solution. Error bars are the standard deviation of 4 replicate measurements.....	57
Figure 4.9 Plot showing the cumulative dissolution of a Magnox sample (replicate #4) in 4M MgCl ₂ at 60°C as well as the OCP of the system monitored simultaneously.....	58
Figure 4.10 Photographs showing Magnox samples post immersion in AlCl ₃ (left) and MgCl ₂ (right) at 60°C, showing the formation of a surface film.....	58
Figure 4.11 Plot showing the result of speciation calculations for aluminium (activity = 1x10 ⁻⁶) in 4M MgCl ₂ from 20-90°C. The star icon (★) denotes a special case at 25°C where the transition point is discontinuous and the predicted transition is Al ³⁺ to Gibbsite.....	62

Figure 4.12 Example plot of the natural logarithm of the reaction rate of Mg in 4M MgCl₂ as a function of the inverse of solution temperature (1/T).....	63
Figure 4.13 Box plot representing the distribution of activation energy measurements for all Alloy/Salt systems. The mean of each distribution (♦) is plotted alongside the results of individual experiments (×).....	64
Figure 4.14 Graphical representation of the concentration of reactants approaching the interface under different reaction control schemes. The arrow represents the effect of improving transport in the liquid phase.	66
Figure 4.15 Graphical representation of a simplified multi-step process where the rate is controlled by a physical transport process (1), which when removed results in a chemically controlled reaction (2) that proceeds at a faster rate.....	69
Figure 5.1 Diagrammatic representation of the dissolution of Mg by the action of the adsorbed intermediates Mg*OH (green), Mg*H (orange) in parallel with an electrical double layer (dark blue). The circuit diagram used to model impedance spectra is overlaid with the individual reactions corresponding to each charge transfer step. The surface coverages θ_{OH}, θ_H, θ_M are shown along with their relationship to the circuit parameters L, C_2 and C_1. The solution resistance is represented by the resistor R_e.	75
Figure 5.2 Circuit model used to model the impedance response of corroding magnesium alloys, describing a charge-transfer process involving one capacitive (C_2/R_2) and one inductive (R_3/L) intermediate.	76
Figure 5.3 Simulated Nyquist plot showing the impedance response of the circuit model used in this work. The impedance was calculated over the frequency range 300kHz-1mHz according to the following parameters: $R_e=10\Omega$, $R_1=100\Omega$, $C_1=10\mu F$, $R_2=25\Omega$, $C_2=1mF$, $R_3=10\Omega$, $L=100H$.	77
Figure 5.4 Photographs of freshly prepared working electrodes for pure Mg (left) and Magnox alloy (right).....	81
Figure 5.5 Diagram of the three-electrode cell used to perform EIS measurements.....	82
Figure 5.6 Plot of residuals from Kramers-Kronig fitting to impedance data for pure Mg corroding in 0.6M NaCl.....	84
Figure 5.7 Bode plot showing impedance response of corroding pure Mg in 0.6M NaCl solution. The circuit (blue, solid) and kinetic (orange, dashed) models were fitted to the modulus (squares) and phase (diamonds) of the impedance data.....	85

Figure 5.8 Plot showing potentiodynamic polarisation data for pure Mg in saturated MgCl₂ solution (scan rate = 1mVs⁻¹). Fit line corresponds to a Tafel fit where $\beta_a = 1116\text{mV/decade}$ and $\beta_c = 4261\text{mV/decade}$.	89
Figure 5.9 Plot of voltage against current close to the OCP ($\pm 10\text{mV}$) during potentiodynamic polarisation of Mg in saturated MgCl₂ solution.	91
Figure 5.10 Potentiodynamic polarisation plots for pure Mg in 4M MgCl₂ over different voltage ranges (-250/+250mV at 1mVs⁻¹, yellow; -500/+1500mV at 5mVs⁻¹, blue). Dotted lines show the open circuit potential recorded prior to each corresponding voltage sweep.	92
Figure 5.11 Photo/Micrographs of pure Mg samples post immersion in 4M MgCl₂.	93
Figure 5.12 Nyquist plot of the impedance response for pure Mg corroding in 0.5 (squares) and 1M (diamonds) MgCl₂ solutions. Fit lines are shown for solutions of the circuit (blue, solid) and kinetic (orange, dashed) models.	95
Figure 5.13 Nyquist plot of the impedance response for pure Mg corroding in 2M MgCl₂ solution. Fit lines are shown for solutions of the circuit (blue, solid) and kinetic (orange, solid) models.	96
Figure 5.14 Nyquist plot of the impedance response for pure Mg corroding in Saturated (triangles) and 4M (inverted triangles) MgCl₂ solutions. Fit lines are shown for solutions of the circuit (blue, solid) and kinetic (orange, solid) models.	97
Figure 5.15 Plot of the polarisation resistance as predicted by the circuit (dashes) and kinetic (crosses) models as a function of concentration. Error bars for the circuit model are calculated from the standard error of regression and are not shown for the kinetic model due to poor fitting performance.	103
Figure 5.16 Series of plots showing the impedance response of pure Mg in 4M MgCl₂ under different bias voltages with fitted solutions for the circuit model (blue).	105
Figure 5.17 Plot of impedance response of pure Mg corroding in 2.67M AlCl₃ both saturated (pentagons) and unsaturated (stars) with respect to Mg²⁺ ions. Fit lines (dashed, blue) correspond to solutions of the circuit model.	110
Figure 5.18 Schematic representation of the inferred corrosion behaviour of pure Mg under the various conditions tested in this work. The thickness of the salt film induced by anodic polarisation is represented by the symbol δ.	114
Figure 5.19 Plot of potentiodynamic polarisations for pure Mg (yellow, scan rate = 5mVs⁻¹) and Magnox alloy (green, scan rate = 1mVs⁻¹) in 4M MgCl₂.	116

Figure 5.20 Plot of impedance data for Magnox alloy in 0.5M (blue, diamonds) and 1M (yellow, squares) MgCl ₂ solution at OCP.....	117
Figure 5.21 Series of plots showing the impedance response of Magnox alloy in 4M MgCl ₂ under different bias voltages with fitted solutions for the circuit model (blue).	119
Figure 5.22 Nyquist plot for Magnox corroding in 2.67M AlCl ₃ saturated with respect to Mg ²⁺ ions (squares). Fit line (blue) corresponds to a fitted solution of the circuit model.	123
Figure 5.23 Schematic representation of the inferred corrosion behaviour of Magnox alloy under the various conditions tested in this work. The thickness of the salt film induced by anodic polarisation is represented by the symbol δ	125
Figure 6.1 Photograph showing a representative sample of Mg powder (left) and raspings (right) used to synthesise cement samples.	129
Figure 6.2 Photograph showing aggregated samples of raspings arranged on a flat surface for sizing by image analysis.	130
Figure 6.3 Histogram of rasping cross-sectional area determined by image analysis. Fit line corresponds to a two-parameter gamma distribution where $\alpha = 2.92$ and $\theta = 0.58$	131
Figure 6.4 Background subtracted scattering data for sample 34r (MgO control), matched to component phases by comparison to reference patterns.	140
Figure 6.5 Background subtracted scattering data for samples 13r (Mg powder, top, green) and 16r (Mg Raspings, bottom, red), matched to reference patterns.	141
Figure 6.6 Plot of aggregated DSC results obtained during STA. Data for each feed material are presented as a confidence interval representing the standard deviation of heat flow measurements. Reference lines are plotted for transitions corresponding to the F5 (dashed) and F3 (dotted) phases as determined by previous researchers (Xia et al., 1991).	147
Figure 6.7 Plot of aggregated TGA results obtained during STA. Data for each feed material are presented as a confidence interval representing the standard deviation of weight measurements. After averaging, the data were normalised to originate at 100%. ..	149
Figure 6.8 Representative micrograph of processed cement powder from sample 33r (MgO control). This image was acquired in Secondary Electron (SE1) mode.	151
Figure 6.9 Representative micrograph of processed cement powder from sample 21r (Mg powder). This image was acquired in Secondary Electron (SE1) mode.	152
Figure 6.10 Representative micrograph of processed cement powder from sample 24r (Mg raspings). This image was acquired in Secondary Electron (SE1) mode.	153

List of Abbreviations

AC	Alternating Current
AHE	Anomalous Hydrogen Evolution
BEP	Box Encapsulation Plant
BET	Brunauer–Emmett–Teller
DC	Direct Current
DFT	Density Functional Theory
DSC	Differential Scanning Calorimetry
DTA	Differential Thermal Analysis
EDX	Energy Dispersive X-ray
EIS	Electrochemical Impedance Spectroscopy
FED	Fuel Element Debris
GWB	Geochemists WorkBench
ICDD	International Centre for Diffraction Data
LEMAS	Leeds Electron Microscopy and Spectroscopy Centre
LSV	Linear Sweep Voltammetry
Magnox	Magnesium Non-Oxidising
MOC	Magnesium Oxy-Chloride
MRP	Magnox Reprocessing Plant
MSSS	Magnox Swarf Storage Silo
NDE	Negative Difference Effect
PMMA	Poly(Methyl MethAcrylate)
PUREX	Plutonium Uranium Reduction Extraction
RDE	Rotating Disk Electrode
SEM	Scanning Electron Microscopy
SEP	Silo Emptying Plant
STA	Simultaneous Thermal Analysis
TGA	Thermo-Gravimetric Analysis
XRD	X-Ray Diffraction

XRF	X-Ray Fluorescence
XRR	X-Ray Reflectometry

List of Variables

i	Current
i_0	Exchange/Equilibrium/Corrosion current
E	Potential
E^0	Baseline potential (arbitrary)
E_{corr}	Corrosion Potential
b_a	Anodic Tafel constant
b_c	Cathodic Tafel constant
$b_{1,2,22}$	Tafel constants (arbitrary)
α	Asymmetry factor
F	Faraday constant
η	Overpotential
R	Ideal Gas Constant
T	Temperature
σ	Surface Area
g	Acceleration due to gravity
ρ_e	Density (electrolyte)
h_1	Interface height separation
P_{atm}	Atmospheric pressure
P_{H_2}	Pressure (hydrogen gas)
P_{vapour}	Pressure (water vapour)
m_{net}	Net weight (collector)
M_{Mg}	Moles (Mg, oxidised)
$m_{\text{collector}}$	Weight (collector)
V_{H_2}	Volume (hydrogen gas)
k	Reaction rate constant (zeroth order)
A	Arrhenius constant/pre-factor
E_a	Activation energy
G	Gibbs free energy

H	Enthalpy
S	Entropy
$R_{1,2,3}$	Circuit resistance(s)
R_e	Electrolyte resistance
R_t	Charge transfer resistance
R_p	Polarisation resistance
Z	Impedance
$C_{1,2}$	Circuit capacitance(s)
L	Inductance
K	Rate constant
j	Imaginary unit
ω	Frequency
β	Molecular surface coverage
θ	Fractional surface coverage
$D_{Mg^{2+}}$	Diffusion constant (Mg^{2+} ion)
δ	Surface layer thickness

1 Introduction

1.1 Magnox

The Magnesium Non-Oxidising (Magnox) family of magnesium alloys was developed for use as a fuel cladding material in the first generation of nuclear power reactors deployed in the UK (Clark et al., 2021). Magnox, after which the reactor type was named, refers to a number of different high-magnesium alloys used in the construction of ancillary components such as splitters (Hallam et al., 2016). For fuel cladding, however, Magnox A180 (0.8% Al, 0.005% Be by weight) was used exclusively (Burrows, 2013). Magnesium as a base material was selected primarily for its low neutron absorption cross-section, enabling the use of naturally enriched metallic uranium as a fuel material. In addition, the use of magnesium cladding allowed for higher temperatures to be used in a gas-cooled reactor design, as an improvement on the earlier air-cooled reactors deployed at Windscale which utilised aluminium cladding (Burrows, 2013).

From 1956 to 2015, a fleet of 26 Magnox reactors generated electricity for the UK power grid, representing over one thousand reactor-years of operation (WNA, 2016). In addition to electricity production, the first two Magnox stations (Calder Hall and Chapelcross) were designed for dual-use and produced plutonium for the UK nuclear weapons programme (Jensen and Nonboel, 1999). As such, the Magnox fuel cycle included reprocessing of spent fuel to separate the fissile content via the PUREX process of solvent extraction (Hanson, 2014). Efficient extraction of the actinide species required the removal of the magnesium cladding, which was achieved by forcing spent fuel rods through a cutting die (NEA and OECD, 2018). This operation produced a substantial amount of Magnox swarf contaminated with spent fuel/fission products as a waste product, which was stored in the specially built Magnox Swarf Storage Silo (MSSS) on the Sellafield site (Le Clere, 2012). Alongside other non-Magnox wastes, the total volume of material stored in the MSSS compartments has been estimated at $\sim 12,000\text{m}^3$ (NDA, 2019a).

1.2 Current Strategy

The oxidation of magnesium metal produces a significant amount of heat as well as flammable hydrogen gas as its by-product (Esmaily et al., 2017; J. Rumble, 2020b). As a result, the storage in ponds and silos of large quantities of magnesium metal wastes has led to MSSS being labelled “Sellafield’s most hazardous building” (NDA, 2018a). As a result, a programme of emptying has

been given priority as part of the portfolio of radiological risk reduction activities underway across the UK (NDA, 2021b). This is to be achieved via the installation of three Silo Emptying Plant (SEP) machines which will be used to transfer the wastes into interim storage containers (Sellafield Ltd., 2021). The containers to be used are known as “3m³ Boxes”, named for their internal volume and consisting of multiple barriers designed to keep the wastes contained (RWM, 2015).

Originally, the decommissioning plan for MSSS included cementation of the swarf wastes followed by decanting into 3m³ boxes, to be carried out in a new facility called the Silo Direct-encapsulation Plant (SDP). To achieve acceptable mixing of the cement and swarf prior to hardening, this process required complex manipulation of the wastes, including tumble mixing (Jones, 2014). As a result of its technical complexity, the construction of SDP was considerably delayed; at the time of its cancellation in 2015, the plant was not expected to be operational until 2026 at the earliest (NAO, 2018). One of the most significant technical issues concerned the potential for metals, after storage in water for long periods of time, to form hydrides. Such compounds would react upon exposure to atmospheric oxygen, creating a potential for fires and/or explosions when combined with the existing hazard of ongoing hydrogen generation. Considering the degree to which the magnesium swarf wastes were known to be contaminated with radionuclides, the mere possibility of this effect was enough for the risk associated to be considered intolerable. However, following detailed characterisation of these wastes, it was concluded that the probability of such an event was much lower than assumed (Parry, 2017). At this point, the hazard presented by the aging of the MSSS structure became dominant and a programme of accelerated retrievals of swarf into 3m³ boxes was initiated (Sellafield Ltd., 2018).

The 3m³ boxes consist of a sealed concrete-lined steel bund into which a steel skip (with its own sealed lid) containing the contaminated wastes can be placed (Sellafield Ltd., 2017a). The reactive nature of magnesium alloys necessitates additional features to mitigate the effects of chronic corrosion, specifically a system of vents to allow the release of evolved hydrogen (while preventing the escape of volatile radionuclides) and voidage/headspace to accommodate volume expansion as the metallic species oxidise into oxide/hydroxides with lower bulk density (NDA and RWM Ltd., 2011). Due to the complexity of the package design, its high material specification and the volume of wastes to be packaged, the capital cost of the 3m³ box manufacture is expected to cost £975m for the needs of MSSS alone (Sellafield Ltd., 2017b). Therefore, any

means by which the twofold issue of chronic corrosion (i.e., volume expansion and hydrogen evolution) can be addressed would enable radical simplification of the box design, with the potential for a substantial cost saving for the UK taxpayer. Furthermore, the reduction or removal of the chemical reactivity of the magnesium component would eliminate key uncertainties that currently impact the long term stability of the interim storage containers (Serco Technical Consulting Services, 2010). Specifically, the development of a stabilising treatment for Magnox wastes, to be applied during or after filling of the 3m³ boxes, may be essential to allow the waste packages to be fully compatible with geological disposal and achieve final compliance (RWM, 2016a).

1.3 Enhanced Corrosion as a Stabilising Treatment

This thesis describes a body of work undertaken following the proposal that the problems caused by chronic corrosion of magnesium alloy wastes may be effectively circumvented by encouraging the corrosion reaction to completion prior to packaging and disposal. By fully oxidising the metallic component, the chemical reactivity of the wastes could be reduced to a level comparable to the ores it was originally refined from and substantially reduce the thermodynamic driving force for further corrosion. In addition, following successful treatment the volume of the waste would be clearly defined, posing no further risk to the integrity of the waste package. Finally, as an oxide/hydroxide species, the corrosion product itself could act as an in-situ encapsulating material for other contaminants such as fuel fragments and other co-stored materials.

To be successfully deployed to wastes as hazardous as MSSS swarf, such a treatment must be able to be applied with minimal intervention, as manipulation of contaminated materials is likely to be expensive and/or impractical. It must be sufficiently fast as to not impede retrievals operations, which are already expected to take up to 25 years (from 2022-2046) to complete (NDA, 2021a). It should require minimal addition of reagents, so as to minimise the final volume of radioactive waste and not require additional packaging. By extension, it should not add a prohibitive level of additional processing steps. It must be compatible with contaminants and co-stored materials, as well as the vessel/package within which it is applied. Finally, the treatment must represent a cost saving in comparison to the existing strategy or comparable alternatives. A review of previous work on enhanced corrosion was henceforth carried out to evaluate comparable work on chemical

treatments, identify candidate reactions and inform the direction of experimental work.

Contaminated Magnox wastes have previously been conditioned for disposal by dissolution at individual reactor sites. These plants were set up to stabilise and consolidate Fuel Element Debris (FED) removed from spent fuel elements to enable transport to Sellafield for reprocessing, of which the major component is splitter blades made of the ZR55 Magnox alloy (Clark et al., 2021). While the exact process varies from site to site (NDA, 2013), the essential flowsheet remains the same. Firstly, the solid wastes are retrieved from vaults and placed into a dissolver where they are digested by an acid solution. The aqueous phase is then treated, for example by ion exchange, until the waste satisfies effluent requirements and can be discharged to the environment. Insoluble fragments left behind by the dissolution step are then processed for disposal, e.g. by encapsulation in cementitious grout (Magnox Ltd. and NDA, 2013).

Programmes of FED dissolution have been successfully completed at two reactor sites (Dungeness A and Bradwell) and is the preferred strategy for a further three (Oldbury, Hinkley Point A and Sizewell A) (Magnox Ltd. and NDA, 2017). However, despite these successes, dissolution is not planned for use at all sites, most notably at Berkeley where the diversity of co-stored materials makes the process technically difficult.

It is for similar reasons that the FED dissolution process is unlikely to be practicable for application to wastes arising from MSSS. Firstly, as with the Berkeley FED, the variety of wastes stored in MSSS is such that its effectiveness cannot be guaranteed. Furthermore, the radiological hazard presented by MSSS wastes is substantially greater, making physical manipulation significantly more difficult. Finally, while FED dissolution campaigns have successfully treated thousands of tonnes of Magnox wastes arising from reactor sites, vaults in the Legacy Ponds and Silos (including MSSS) have degraded to such an extent that processes involving multiple manipulation steps are no longer practical (NDA, 2019b).

Separately, a number of chemical treatment options have previously been explored for application to the problem of Magnox spent fuel (CEGB and SSEB, 1986). These proposals cover the stabilisation and disposal of intact fuel elements, both where they were too corroded to be reprocessed (due to long term storage in water) or where reprocessing capacity is expected to be unavailable due to the closure of the Magnox Reprocessing Plant (MRP) (NDA, 2014). Various options, including calcination, voloxidation and vitrification, were considered technically feasible; although the common compromising

factor identified in all cases was the requirement for additional facilities comparable in scale and complexity to a new reprocessing plant. As a result, the current strategy for outstanding Magnox spent fuel wastes remains interim storage in self-shielded containers similar to the 3m³ box (NDA, 2019c).

Enhanced corrosion has previously been evaluated as a method for stabilising Magnox spent fuel wastes as part of a review of contingency options published in a conference paper by Morris (Morris, Wickham, et al., 2009). This paper was a summary of a longer unpublished report (Morris, Richardson, et al., 2009), for which the sole reference pertaining to enhanced corrosion was an internal Sellafield Ltd. report by Trow (also unpublished) related to the Box Encapsulation Plant (BEP) (Trow, 2007). The proposal in essence was to use heating to accelerate the corrosion reaction in existing storage conditions, i.e. in 5mM aqueous sodium hydroxide solution (Burrows, 2013). By this method the metallic wastes could be converted into magnesium hydroxide similar in nature to the existing waste stream known as Magnox Sludge (Morgan et al., 2019). At this point, the sludge could be treated as part of the existing sludge waste stream, i.e., by dewatering and immobilisation in a cement matrix.

While the process in this form was considered technically feasible, Morris noted that extensive research and development would be required prior to implementation (Morris, Wickham, et al., 2009). It is also noted that enhanced corrosion was proposed for deployment at BEP, which is itself intended to handle the packaging of retrievals of both Magnox spent fuel from legacy storage ponds as well as Magnox swarf from MSSS (NDA, 2015). For the purposes of this work, it is assumed that treatment by enhanced corrosion is equally viable for both waste streams. The decision to focus on Magnox swarf was made because, in theoretical terms, it represents a simpler and more homogeneous system, as well as one where the competing effects of spent fuel contamination can be neglected, at least for the purposes of demonstrating proof of concept. In combination, these works represented a natural starting point for the research effort presented in this thesis and therefore represents the first step on precisely the programme of research and development proposed by Morris (Morris, Richardson, et al., 2009).

With this in mind, the focus shifted to identifying aqueous salt systems that would maximise the corrosion rate of magnesium alloys, relying on the aggressive pseudo-catalytic effect of the chloride ion and its ability to disrupt the formation of passive surface films (Esmaily et al., 2017). However, the bulk of research effort in the field of magnesium corrosion is carried out with the aim of reducing the rate of corrosion with a view to enabling its use as a

structural material (Abbott, 2015). Nevertheless, a notable exception is the work of Casey and Bergeron, who discovered that the corrosion behaviour of magnesium in concentrated magnesium chloride ($>1\text{M MgCl}_2$) was fundamentally different to that observed for other salts (Casey and Bergeron, 1953). Specifically, the effect of MgCl_2 was compared to potassium chloride (KCl) but is equally applicable to other common salts such as sodium chloride (NaCl). In a two-part work, it was demonstrated that the typical passivation of the metal surface was suppressed in concentrated MgCl_2 , resulting in a substantial increase in the corrosion rate (Casey et al., 1962). In addition, the activation energy was found to have significantly increased, representing a reaction that was more sensitive to temperature and no longer limited purely by the transport of reactants (Roller, 1935). The use of MgCl_2 at increased temperatures may therefore represent a means by which enhanced corrosion of Magnox wastes could be achieved in line with the proposal made by Trow (Trow, 2007; Morris, Wickham, et al., 2009).

In discussion, Casey postulated that the corrosion product formed during corrosion in concentrated MgCl_2 was not the typical magnesium hydroxide, but rather some form of hydroxychloride species (Mg(OH)Cl). This is reminiscent of the magnesium oxychloride (Sorel) family of non-hydraulic cement materials, which have previously been examined for use in nuclear waste disposal (Walling and Provis, 2016). Indeed, work in the field of cement science has shown that the transition between hydroxide and oxychloride as the stable product occurs at a threshold Mg^{2+} (and, by extension, MgCl_2) concentration of 1.96M (Mažuranić et al., 1982). This is co-incident with the substantial increase in the corrosion rate observed by Casey and thus it is hypothesised that they represent two different manifestations of the same fundamental process. If true, this implies that not only is it possible to use MgCl_2 to substantially enhance the corrosion rate of magnesium alloys, but also that the molar ratios could be tuned in such a way as to produce a cement as the final product. This treatment, therefore, could use the Magnox waste itself as a feed material for a self-immobilizing waste form. In addition, for a given box of MSSS waste, the resulting cement could encapsulate other contaminants and co-stored materials, substantially improving the overall stability of the package and enhancing its resilience in geological disposal.

In the field of nuclear waste disposal, the practice of encapsulating solid nuclear wastes in cement is known as Cementation (Ojovan et al., 2019). Since the process described in this thesis uses the waste itself to enable its own immobilisation (and by extension the encapsulation of co-stored materials), it

has been termed “Cementisation”, both for convenience and to distinguish it from traditional grouting processes.

2 Aims & Objectives

The principal aim of the work presented in this thesis was to demonstrate the viability of Cementisation as a practicable method for eliminating chemical reactivity in Magnox wastes and simultaneously producing a cementitious product compatible with disposal. As a result, the scope of the work was defined to include proof of concept on the laboratory scale. This was accompanied by more fundamental work towards a complete understanding of the corrosion reaction in concentrated MgCl_2 solutions. By determining the kinetic parameters of the corrosion reaction in dimensionless terms, the viability of Cementisation could subsequently be evaluated prior to optimisation and scale up towards industrial deployment.

These objectives were defined as a set of three hypotheses as shown:

1. Magnesium oxychloride cement can be directly produced from the corrosion products generated during dissolution of metallic Mg in MgCl_2 solution.
2. MgCl_2 solutions with a concentration greater than 2M promote rapid, active and uniform corrosion of magnesium metal.
3. Hypotheses 1 and 2 remain true for the case of Magnox alloy (Al80)

In the following section, a review of the relevant literature is presented with focus on inter-disciplinary overlap between magnesium corrosion and magnesium oxychloride cement research. The subsequent three sections present the results of experimental work performed to determine whether the above hypotheses are valid. Finally, a review of the discussion is presented along with conclusions relating to the above hypotheses and an evaluation of progress towards the stated aim of the project.

3 Literature Review

For the development of Cementisation as a treatment for Magnox wastes, it is necessary to understand the individual reactions that take place and determine their characteristics in the concentrated salt system. As the oxidation, dissolution, complexation and crystallisation reactions all occur simultaneously, optimisation of the process will require detailed knowledge of their respective rates and sensitivities, thereby allowing each step to be manipulated in the pursuit of an optimal product. In this section, the corrosion behaviour of magnesium and Magnox alloy will be reviewed with reference to the observations of previous researchers. Experimental techniques will be outlined and evaluated based on their application to comparable systems, justifying their use in this work and providing context to the results presented. Finally, an appraisal of the current state of knowledge regarding the formation and properties of magnesium oxychloride cements will be presented to underpin the proof of concept for Cementisation.

3.1 Radioactive Waste Disposal in the UK

3.1.1 Current Strategy

Radioactive waste in the UK is classified by radioactivity into Higher Activity Waste (HAW) and Lower Activity Waste (LAW). Disposal of LAW is currently facilitated by surface-level landfill sites or the Low-Level Waste Repository (LLWR) depending on activity levels. The current strategy for disposal of HAW requires the construction of a Geological Disposal Facility (GDF) capable of isolating hazardous radionuclides from the surface environment until they are no longer harmful. As of writing, a consultation process is underway as part of the process for identifying a suitable site for the GDF (NWS, 2022). The specific parameters of the facility are therefore yet to be defined. HAW is divided into two subcategories, High Level Waste (HLW) and Intermediate Level Waste (ILW) based on its ability to produce significant heat via radioactivity (NDA, 2020). Magnox swarf, the principal focus of this work, does not generate a significant amount of heat and is therefore categorised as ILW (Parry, 2017).

Since the UK GDF project is currently in its exploratory phase, it is not possible for waste producers to obtain final regulatory approval for specific waste streams and packages. To provide assurances in the interim period, a process has been set up by which producers can seek guidance and pre-approval from Nuclear Waste Services (formerly Radioactive Waste Management (RWM)/Radioactive Waste Management Directorate (RWMD)) by the Letters of

Compliance (LoC) process (NWS, 2018). LoCs can be issued at several stages of waste stream development, e.g., conceptual, interim, final and periodic review, providing guidance at each stage to aid waste producers and establish the disposability of specific waste forms. A Final Letter of Compliance (FLoC) does not in itself constitute regulatory approval for disposal, which would require input from the Office for Nuclear Regulation (ONR) and Environment Agency (EA), but it is intended to represent the basis of a future safety case that will be required once the GDF is operational (RWM, 2014).

Various streams of Magnox swarf that are encapsulated in cement have previously received FLoCs and additional waste streams from MSSS intended for processing in the now-cancelled Silo Decommissioning Plant (SDP) have received assurances up to the interim stage (NWS, 2018). However, based on publicly available records of issued LoCs (BEIS, 2018; BEIS, 2021), no FLoCs have been issued to underpin the new strategy of expedited retrievals and interim storage of MSSS swarf wastes in 3m³ boxes (Parry, 2017). Based on this information, it must be inferred that these waste forms will therefore require further treatment, by a process such as Cementation, in order to qualify them for final disposal. This course of action would represent a trade-off between the potential future hazards presented by the emplacement of these untreated wastes in secure interim storage, versus the existing (and intolerable (NDA, 2018a)) hazard presented by the facilities in their current state.

3.1.2 Cementation

Encapsulation in cement, known as Cementation, is the preferred method of disposal for non-heat-generating wastes in the UK (Sharp et al., 2003). Hydraulic cements, specifically Portland cements, have been extensively utilised, principally for their ability to form a hard, low permeability product with high water resistance (Ojovan et al., 2019). In addition, cementitious materials are cost-effective with an established supply chain, self-shielding against radiation and can reduce radionuclide solubility by maintaining a high pH environment (Sharp et al., 2003). Cement materials also have the capability to immobilise waste materials at near-ambient temperatures, as opposed to vitrification which requires calcination at high temperatures. That is not to say that the setting and hardening of Portland cements does not produce significant heat via the hydration reaction, which must be controlled to prevent overheating and cracking of the final product (Glasser, 1992). This has led to the development of composite systems including additives of Pulverized Fly-Ash (PFA) and Blast Furnace Slag (BFS) which reduce instantaneous heat by

slowing the setting reaction, or otherwise improve matrix properties such as porosity/permeability (Ojovan et al., 2019).

Alternative cement chemistries have been developed and investigated for use in enabling disposal of radioactive wastes. These include modified calcium-based cements (using aluminium and/or sulphur), geopolymers and hydroceramics. The magnesium-based cements including the oxychloride Sorel cements that are the focus of this work, and also formulations based on silica or phosphates (Ojovan et al., 2019). For a comprehensive review of the history and properties of magnesia cements, the reader is referred to the work of Walling and Provis (Walling and Provis, 2016). For the purposes of developing the Cementisation process, a further exploration of the state of the art in magnesium oxychloride cements is presented in Section 3.4.

The requirements for cements used to encapsulate radioactive wastes in the UK are not set directly by the GDF facility but are instead set internally by each facility and optimised for the specific waste form. The integrity of the GDF and its ability to impede the movement of harmful radionuclides instead relies on the waste containers (such as the 3m³ boxes) and the engineered barriers of the facility itself i.e. its cementitious backfill (Walling, 2016). Nevertheless, encapsulating materials emplaced in a GDF may have to tolerate conditions substantially more demanding than those present during interim storage. For example, in a worst-case scenario the temperature of ILW waste packages could increase up to 80°C (Prentice et al., 2019). This in turn will increase the pressure experienced by the waste materials and significantly alter the nature of chemical interactions e.g., with water. For non-hydraulic cements, such as magnesium oxychlorides, this could be particularly significant as they are highly sensitive to water (Walling and Provis, 2016). For Cementisation to be deployed as a waste conditioning method, it will be essential to demonstrate that its products can withstand the conditions expected during the lifecycle of a GDF.

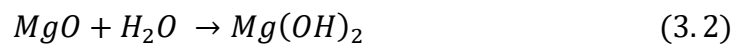
3.2 Magnesium Corrosion

The physical and chemical properties of magnesium have increasingly become the focus of scientific and engineering endeavours, attempting to leverage its position as the lightest structural metal. This has led to the deployment of magnesium and its alloys in a wide range of applications where weight is a primary concern; such as consumer electronics (e.g. laptop computers, cameras), automotive and aerospace environments (Abbott, 2015).

In response to renewed research interest, a comprehensive review of magnesium corrosion was recently published by Esmaily et. al., summarising both the aqueous and atmospheric corrosion behaviour of magnesium and its alloys, as well as documenting the range of experimental techniques that have been applied to their study (Esmaily et al., 2017). The following section, therefore, comprises an outline of the magnesium corrosion reaction and its effects within the context of its application in Cementisation, i.e., facilitating enhanced corrosion of Magnox alloy and supplying the reactants necessary for the formulation of the desired magnesium oxychloride product.

3.2.1 General Behaviour

The standard potential for the reduction of the magnesium cation is extremely electronegative (-2.37V (J. Rumble, 2020a)), such that it is commonly the last (or first, depending on convention) metal listed in compilations of the galvanic series utilised for practical engineering design (Zhang, 2011). This reduction potential drives rapid oxidation of the refined metal, assuming a mechanism for charge transfer is available. In practical terms this leads to the rapid formation of a surface layer of magnesium oxide (MgO) following the exposure of fresh Mg to atmospheric oxygen (Splinter et al., 1993), i.e. as a result of machining, grinding or polishing. The corrosion of Mg in aqueous solution proceeds according to the following reactions:



Despite the resistive properties of this film, when immersed in aqueous solutions the metal continues to exert a significant potential. Such is the magnitude of this driving force, that it enables the direct dissociation and reduction of water, producing hydrogen gas (H₂) and hydroxide (OH⁻) ions. This allows the corrosion of Mg to proceed in the absence of dissolved oxygen, with hydrogen evolution as the sole cathodic reaction (Baril and Pébère, 2001). The hydroxide ions in turn react with both the MgO surface film and with dissolved Mg²⁺ ions to form magnesium hydroxide (Brucite) which precipitates on the metal surface (Vermilyea and Kirk, 1969). The stability of this film and its ability to prevent charge transfer are the primary factors that determines the corrosion potential in different solutions (Zhang, 2011). The precise nature of these layers and their characteristics is still a matter of some debate (Esmaily et al., 2017). Nevertheless, to aid understanding of the aqueous corrosion behaviour of Mg a highly simplified representation of these structures is presented in Figure 3.1.

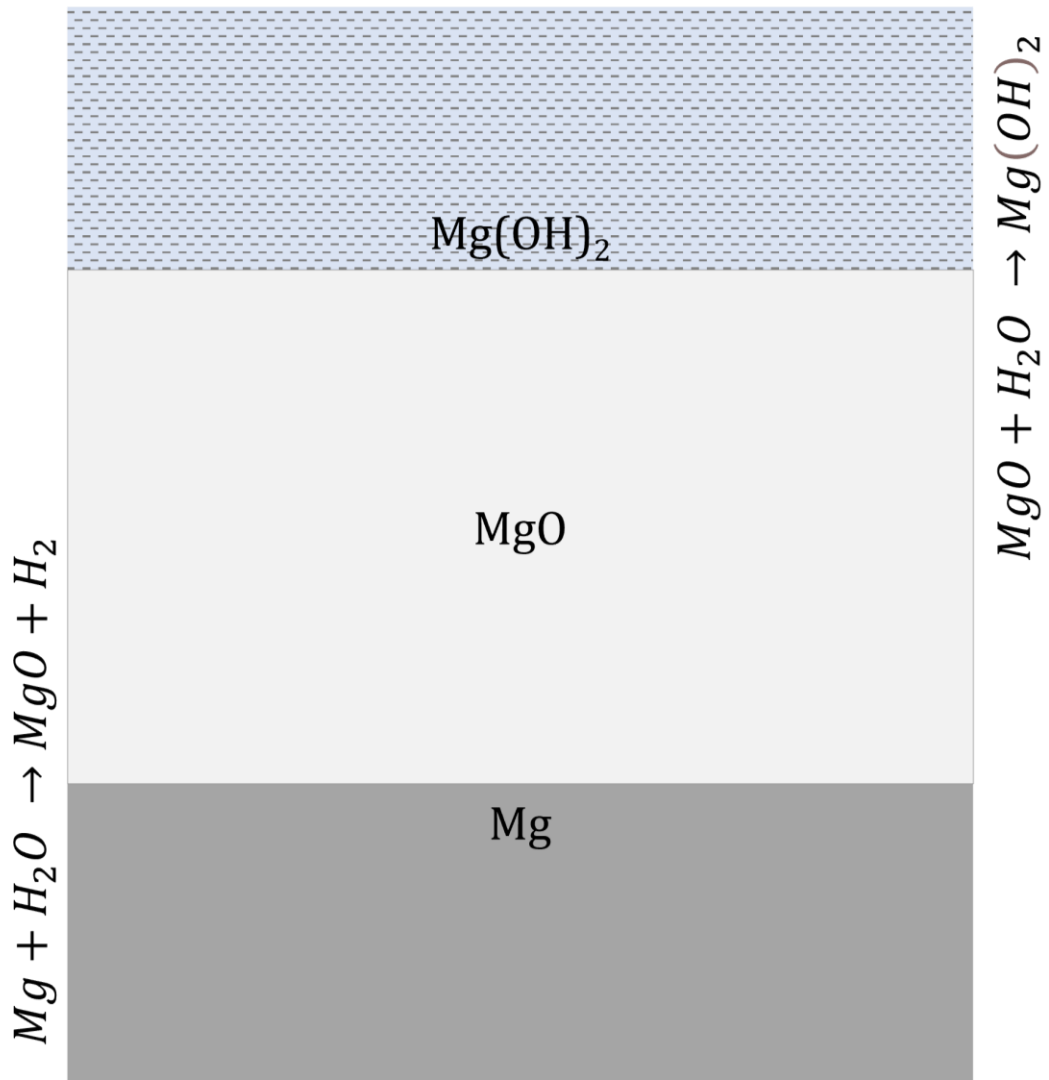


Figure 3.1 Simplified representation of the surface layers formed on magnesium metal surfaces during aqueous corrosion.

In most aqueous environments, the hydroxide film is porous and thus, poorly protective against water ingress (Nordlien et al., 1995). Since water is one of the primary reactants in the corrosion reaction, this leads to continuous and irreversible oxidation of the metal. It is possible to improve the stability of this film by artificially increasing the pH of the solution, for example by addition of NaOH (Taheri and Kish, 2012). By introducing OH^- ions, the precipitation of magnesium hydroxide is encouraged, creating a thicker surface layer that restricts access to the substrate (Vermilyea and Kirk, 1969). Nevertheless, this passive layer is vulnerable to attack, particularly by chloride ions that disrupt film formation by competing with oxygen ions at the metal-oxide interface (Strehblow and Marcus, 2011). In addition, the chloride ion supports acidification induced by the dissolving metal ions, increasing their solubility

and sustaining corrosion currents between local anodic and cathodic sites (Frankel, 1998).

As the dissolution of Mg and precipitation of $\text{Mg}(\text{OH})_2$ reach equilibrium, the aqueous system is buffered to an alkaline pH (Vermilyea and Kirk, 1969). For this reason, studies of Mg corrosion tend to focus on the partially-protective properties of the hydroxide film in alkaline systems (Esmaily et al., 2017). However, as the work of Casey and later Fajardo shows, the formation of the typical surface film can be suppressed in buffered acidic solutions where the hydroxide phase remains soluble (Casey and Bergeron, 1953; Fajardo et al., 2017). In the work of Fajardo, the resistance to pH change was achieved using citric acid buffered with sodium citrate, while the acidic nature of the concentrated MgCl_2 solutions studied by Casey derived purely from the hydrolysing potential of the Mg^{2+} ion (supported by the Cl^- counter ions). In both cases the absence of the typical corrosion film was noted, which in turn promoted uniform dissolution across the sample surface. Casey further investigated this phenomenon by determining the effective activation energy for the reaction, the value of which was found to be 48kJmol^{-1} . With reference to the work of Roller, this was interpreted as a reaction in which there was no single rate controlling step, rather that it was dependent on both mass transport and chemical reaction kinetics in quiescent solution (Roller, 1935). In a follow up publication, Casey postulated a reaction mechanism to explain the shift in corrosion behaviour above and below the threshold MgCl_2 concentration of 1M, with a summary of the key observations for both filmed and filmless regimes (Casey et al., 1962). For the filmless case, defined here for MgCl_2 concentrations in excess of 1M, the key behaviours for the development of Cementisation are as follows:

1. The reaction rate is “abnormally high”
2. The rate is independent of pH
3. The activation energy is $47.7 \pm 4.2 \text{kJmol}^{-1}$
4. The redox reaction is under cathodic control

It was also supposed, from qualitative evaluation of XRD spectra, that the precipitated reaction product in this case was a magnesium hydroxychloride of the form $\text{Mg}(\text{OH})\text{Cl}$. Furthermore, and by extension, it was predicted that the reaction rate would ultimately be determined by the solubility of this product in the concentrated salt solution. In combination, the findings of Casey represent a reaction by which metallic Mg can be corroded at a highly accelerated rate, producing a hydrated oxychloride product that appears to be

consistent with Sorel cement. As such, these works form the basis of the Cementisation process introduced in this thesis.

3.2.2 Experimental Methods

A diverse array of experimental methodologies have been applied to the study of magnesium corrosion, ranging in complexity from simple immersion testing to sophisticated coupling of electrochemical and analytical techniques (Esmaily et al., 2017). Many studies have focussed on localised corrosion in salt solutions, both to assess its performance in typical service environments and because the anomalous hydrogen evolution that defines the dissolution mechanism is most evident at corrosion fronts, i.e. where active dissolution of metal is taking place (Williams et al., 2013). However, for the purpose of enabling Cementisation by maximising the bulk corrosion rate of Mg, the experimental work herein focussed instead on macroscopic measurements of the corrosion rate and electrochemical behaviour.

3.2.2.1 Voltammetry & Tafel Extrapolation

Electrochemical techniques are extensively employed for the study of corrosion systems because they are inherently dependent on charge transfer. Thus, by connecting a sample of corroding metal as an electrode in a potentiostat, for example, the galvanic current and potential can be used to quantify the rate of, and driving force for, corrosion. Furthermore, electrical bias can be applied to the system with the aid of a potentiostat, enabling independent control of the electrochemical potential. This can then be used to examine the coupled reactions that take place at the metal/solution interface, allowing the determination of kinetic parameters as well as inferences to be drawn as to the nature of the reaction mechanism(s) (Bard and Faulkner, 2001).

A complete kinetic analysis of a corrosion system can be acquired by an examination of the Butler-Volmer equation in the low and high overpotential limits:

$$i = i_0 \left\{ \exp \left[\frac{\alpha z F \eta}{RT} \right]_c - \exp \left[\frac{(1 - \alpha) z F \eta}{RT} \right]_a \right\} \quad (3.3)$$

Where the subscripts c and a refer to the cathodic and anodic reactions respectively, i_0 is the exchange current density (proportional to the equilibrium reaction rate), α is a symmetry factor, z is the ion valence, F is the Faraday constant, η is the overpotential in volts, R is the ideal gas constant and T is the temperature in kelvin.

In the high overpotential region (positive and negative), the anodic and cathodic half reactions dominate and can be measured independently. Values of

the current as a function of potential are used to acquire Tafel constants, which are in essence activation energies expressed in electrochemical terms. In the low overpotential region, the small perturbation approximation can be used to measure the polarisation resistance and determine the exchange current density, which is analogous to the exponential pre-factor in the Arrhenius equation (Perez, 2006).

Potentiodynamic polarisation is commonly used for rapid acquisition of Tafel constants, involving the application of a DC bias voltage that is swept between two values, typically an interval of $\geq 500\text{mV}$ centred on the steady state corrosion potential, also known as the Open Circuit Potential (OCP). However, for the case of Mg (and also Al (Curioni and Scenini, 2015)), the measurement of the anodic half reaction is complicated by the appearance of a second reaction causing hydrogen evolution that increases with increasing anodic polarisation (Atrens and Dietzel, 2007). This effect is known variously as the Negative Difference Effect (NDE) or Anomalous/Anodic Hydrogen Evolution (AHE) and will be discussed in greater detail in Section 3.2.3. The presence of an additional anodic half reaction prevents the measurement of a Tafel constant for Mg by purely electrochemical means as the system cannot be simplified to a single exponential term (Curioni et al., 2015). Nevertheless, polarisation measurements remain useful for qualitative analysis, particularly for evaluation of the effect of alloying elements (Esmaily et al., 2017).

3.2.2.2 Electrochemical Impedance Spectroscopy

Electrochemical Impedance Spectroscopy (EIS) is an analysis technique that involves the application of a small alternating bias voltage (typically $\sim 10\text{mV}$) to determine the complex impedance of the metal/solution interface. The frequency of the perturbation signal is typically swept across a wide range (e.g., 100kHz - 10mHz) to examine the response of the interface on different timescales. Surface processes, such as an electrical double layer at the solution boundary, can be modelled as electrical components (i.e., capacitors, resistors, inductors) whose properties can be obtained by nonlinear regression fitting to a circuit model that appropriately represents the interfacial processes. From these observations, inferences can be made concerning the nature of the corrosion reaction, including the formation of surface films, the effect of mass transport and the action of adsorbed intermediates (Orazem and Tribollet, 2008a). In addition, the polarisation resistance of the system can be determined from the impedance value in the low frequency limit as it approaches a real value with zero phase angle (Scully, 2000).

Many studies have been performed utilising EIS to evaluate the corrosion of Mg, employing a variety of different models and interpretations of the impedance response that are more varied still. A summary and review of the development of EIS methods for studying this system was recently published by Feliu (Feliu, 2020). Typically, the impedance of pure Mg at steady state is characterised by processes represented by three time constants – two capacitive and one inductive (Esmaily et al., 2017). Circuit models of this system adopt the generic form outlined by Scully (Scully, 2000) for a reaction involving two adsorbed intermediates, one that adds to the charge transfer resistance (capacitive) and one that enhances the corrosion rate at steady state (inductive). The use of this model to provide non-destructive measurement of the corrosion rate was validated by King et. al. (King et al., 2014) with further development by Bland et al. (King et al., 2014; Bland et al., 2015) for the case of NaCl solutions by comparison to mass loss and hydrogen evolution measurements. In this case, the authors attributed the mid-frequency response to a pseudo-capacitance caused by the potential-dependent formation of an adsorbed layer, with a separate intermediate invoked to explain the inductive response.

An alternative model for the impedance response of corroding Mg was proposed by Baril (Baril et al., 2007). Instead of a circuit analogue, this model directly considered how the chemical reactions involved would affect charge transfer as a function of time/frequency. Essentially, the time dependence of the model is established according to the interplay of a set of reactions with different zeroth order rate constants (expressed in units $\text{cm}^{-2}\text{s}^{-1}$). For this model Baril adopted the univalent Mg theory of dissolution, contending that the two separate adsorbed intermediates described by other researchers are in fact the same species (Mg_{ads}^+), that is reversibly oxidised/reduced at the solution interface. Anodic hydrogen evolution is then attributed to the single electron reduction of water by this intermediate species. For this model, the authors attribute the mid-frequency response to a Warburg-type impedance created by Mg^{2+} diffusion within the corrosion product film.

This model was subsequently included as an example of impedance behaviour moderated by adsorbed species and mass transport by Tribollet in a compilation of physiochemical impedance models (Orazem and Tribollet, 2008b). It was then further developed by Gomes et. al. with the inclusion of an integral term modelling the high frequency capacitance as a constant phase element related to a compact MgO barrier layer with varying resistivity as a function of depth (Gomes et al., 2019). Fitting of this model was achieved using an “in-house made software”, with various parameters, such as solution

resistance, determined graphically and fixed to aid solution of the objective function. Gomes et al. reported excellent fit results were obtained, although the full list of parameter solutions was not published and no supplementary information was provided regarding the software used to perform regression analysis. Furthermore, in the original publication of the model formulation, Baril did not attempt a similar analysis because of overfitting, explicitly stating that:

these three loops are defined by six variables and the kinetics model involved at least eleven parameters, thus only six relations between the kinetics parameters can be obtained by a fitting procedure.

(Baril et al., 2007)

Nevertheless, fitting was used to determine hydroxide layer thickness, corroborating ex situ measurements for a comparable system (Baril and Pébère, 2001; Gomes et al., 2019). This model remains in use for describing the impedance response of Mg dissolution and is cited as a demonstration of the viability of the univalent Mg mechanism (J. Huang et al., 2020).

3.2.2.3 Immersion Testing

While electrochemical methods offer fast and non-destructive means for inferring corrosion rates, immersion testing of a representative sample in a simulated working environment remains the most accurate way to evaluate the behaviour of a given system (Baboian, 2005). Simple measurement of the weight of a specimen before and after immersion is frequently used in corrosion studies, both for determining dissolution of metal (mass loss) and oxide film growth (mass gain). However, for systems where corrosion products remain adhered to the metal surface, a consistent method for removing the mass of the film is required to accurately calculate the degree of oxidation that has occurred. For Mg, the use of chromium trioxide is recommended in combination with salts intended to precipitate chlorides and/or sulphates (ASTM International, 2012).

Alternatively, due to the fact that the corrosion potential is such that the evolved gas is dominated by hydrogen, measurement of the volume of gas produced is regularly used as a method for determining the bulk corrosion rate of Mg and its alloys (Song et al., 2001). In practice, however, objective measurement of gas volumes is difficult to achieve and remains reliant on human observation. In addition, leakage and the sensitivity of the gas volume to environmental factors (temperature, gravimetric pressure, atmospheric pressure, evaporation) increases the complexity of the volumetric method

(Zheng et al., 2008; Kirkland et al., 2012). In light of these factors, Curioni proposed a gravimetric method for measuring hydrogen volumes, utilising an inverted beaker connected to an analytical balance to collect the evolved gas (Curioni, 2014).

Rather than measuring the gas volume directly, it is measured as a function of the weight of water it displaces. As a result, the rate of oxidation of Mg can be measured with much greater precision (due to the high sensitivity of the analytical balance) and objectivity (as modern balance measurements can be exported digitally for analysis). It is for this reason that the method has been developed for use on this project (see Section 4.2)

Following its invention by Curioni, gravimetric hydrogen evolution was further developed by Fajardo who validated it against the volumetric method for Pt and Mg in NaCl solutions. It has since been utilised in a number of works, both for its considerable precision and its ability to resolve corrosion rates in real time (Fajardo et al., 2017). Recently, the method was adapted by Strebl to measure atmospheric corrosion of Mg by retaining a trapped volume of moist air around the sample within the inverted collector (Strebl and Virtanen, 2019). While not directly related to work on aqueous corrosion, the detection of very low corrosion rates necessitated additional development and deconvolution from the effects of temperature and pressure, the results of which should be considered for any hydrogen evolution study, whether by volumetric or gravimetric methods.

3.2.3 Corrosion Mechanism

The exact mechanisms by which atoms of metallic magnesium oxidise and dissolve (requiring charge transfer) are “contentious” and have been the subject of debate for many decades, one which has only intensified in recent years (Esmaily et al., 2017; J. Huang et al., 2020). While the resolution of this conflict was far beyond the scope of this work, some of the observations made are relevant to the ongoing discussion and thus, a brief summary of the most recent developments is included here.

For context, note that if the oxidation number (i.e. valence) of a metal cation is known, then the amount of metal ions that undergo oxidation can be determined by measuring the current generated by the liberated electrons as they pass through an external resistance with reference to Faraday’s Law as described by Equation 3.4 (Bard and Faulkner, 2001).

$$Rate [mols^{-1}cm^{-2}] = \frac{i}{zF\sigma} \quad (3.4)$$

Where i is the current in amps (coulombs per second), F is Faraday's constant (96485 Cmol⁻¹), σ is the surface area in cm² and z is the oxidation number of the charge carrier ion.

If coulometric measurements of this type are combined with direct measurement of the corrosion rate (by mass loss, evolved gas or other methods), then the amount of charge per metal ion can be independently verified. Petty conducted just such an experiment and measured the average valence of the Mg ion to be significantly less than 2, which he attributed to the dissolution of univalent Mg ions whose subsequent oxidation to the 2+ state would not be registered as they were no longer connected to the external circuit (Petty et al., 1954). This theory was extended to explain the anodic hydrogen evolution phenomenon observed during polarisation of Mg, rationalising that the rate of univalent dissolution (and reduction of water by same, producing hydrogen) increases exponentially with anodic bias.

In response, a number of careful measurements of the Mg valence have been performed which have found no deviation from the expected divalent state (Esmaily et al., 2017). Nevertheless, the univalent magnesium interpretation retains support from other researchers, most notably Atrens (Atrens et al., 2015), despite vociferous opposition (Esmaily et al., 2017). In the intervening period, the univalent mechanism has been further developed and many opposing theories have been proposed to prove that the reaction proceeds only by the two-electron transfer reaction (and simultaneously explain how such a mechanism might be misconstrued) (J. Huang et al., 2020). Modern theories for exclusively divalent Mg invoke a change in the fundamental exchange current density, arguing that the surface of Mg samples is activated by anodic polarisation in such a way that the cathodic hydrogen reaction is catalysed (Frankel et al., 2013). This effect has been attributed to various different mechanisms which can be loosely grouped under the label "Enhanced Cathodic Activity" (J. Huang et al., 2020), but none has so far been conclusively proven correct (Esmaily et al., 2017).

To attempt to explain how all these effects could be facilitated by surface activation, Taylor developed a mechanism (based on earlier work by Casey) that attributes the anomalous behaviour to the variable action of adsorbed hydroxyl radicals (Mg*OH) (Taylor, 2016). The viability of the reaction scheme was demonstrated via Density Functional Theory (DFT) modelling. Under cathodic bias, these species are reduced as an intermediate step in the reduction of water, producing hydrogen. Under anodic bias, they are hypothesised to enable the two-electron oxidation of Mg while simultaneously

being reduced to form OH^- , which in turn frees up surface sites that promote additional water splitting, thereby generating hydrogen with increasing anodic bias. This model was further developed and adjusted by Yuwono, with the source of anodic hydrogen evolution shifted to the Mg^*H intermediate (Yuwono, Taylor, et al., 2019). Instead of hydrogen evolving by recombination of adsorbed Mg^*H , it was shown via modelling that a Heyrovsky pathway was kinetically more favourable (Yuwono, Birbilis, et al., 2019), allowing hydrogen evolution to proceed by both oxidation (under anodic bias) and reduction (under cathodic bias) of the Mg^*H intermediate. The proposed Mg^*OH species, conversely, can only be produced and consumed by oxidation and thus only facilitates charge transfer under anodic conditions. Interestingly, proponents of the univalent theory have subsequently argued that the invocation of the adsorbed species Mg^*H and Mg^*OH are actually Mg_{ads}^+ under a different name (J. Huang et al., 2020). For the purposes of discussing the observations made in this work within the context of the enhanced cathodic activity interpretation of Mg dissolution, the reaction scheme proposed by Yuwono is used as it represents the current state of the art. However, it must be remembered that many alternative explanations have been proposed on this theme and thus a single discussion cannot hope to represent each interpretation to its fullest extent (Frankel et al., 2015).

Ultimately, the debate remains open and this work makes no attempt to decisively resolve it. However, for the interpretation of impedance results it is necessary to understand how adsorbed species are thought to participate in the dissolution of Mg. By discussing the observations made herein in the context of these models it is possible to rationalise their origins and suggest how they might fit within the current understanding. Furthermore, it enables the recommendation of further study of the concentrated MgCl_2 system beyond this work for the explicit purpose of determining the nature of the reaction mechanism.

3.3 Differences Between Magnesium and Magnox Corrosion

Since Cementisation is intended as a treatment process specific to Magnox alloys, an understanding of the specific corrosion behaviour of the alloy is necessary to contextualise its behaviour in a MgCl_2 solution. For the purposes of this work, the alloy under consideration is Magnox Al80, since this is the material that was used for cladding the uranium fuel and is therefore the majority component of swarf wastes (Burrows, 2013). Other Magnox alloys have been deployed, such as ZR55, but these were used for ancillary

components such as splitter blades (Hallam et al., 2016), which were removed on site prior to transport of the spent fuel to Sellafield for reprocessing. These materials, known as Fuel Element Debris (FED), are currently being treated by alternative means, such as dissolution and ion exchange and thus are not considered for treatment by Cementisation (NDA, 2018b).

The most recent review of published works concerning the aqueous corrosion behaviour of Magnox Al80 was carried out by Burrows (Burrows, 2013). This work was carried out within the remit of understanding localised corrosion under passivating (i.e., alkaline) conditions, for the purpose of underpinning the continued underwater storage of Magnox-cladded spent fuel. It was concluded from combined electrochemical experiments and DFT modelling that the passivation of Magnox breaks down once a threshold concentration of chloride ions is reached. This effect is attributed to the ability of chloride ions to increase the solubility of the protective $\text{Mg}(\text{OH})_2$ surface layer (Clark et al., 2021), consistent with observations made for pure magnesium (Williams et al., 2013). More generally, it was shown by Burrows that while differences exist, the corrosion mechanism of Magnox is broadly similar to that of pure magnesium (Burrows, 2013). This has since been corroborated by other researchers for the case of atmospheric corrosion (Hallam et al., 2016).

One of the key findings of the work of Burrows was that the behaviour observed during the initiation of pitting corrosion in Magnox alloys is consistent with the formation of a transient salt film, as observed by Beck & Chan under high anodic polarisation (Beck and Chan, 1981). Under substantial bias voltages (+5.0V) the corrosion current density was observed to drop off over time, which was attributed to the formation of a passivating layer of MgCl_2 , formed due to the saturation of Mg^{2+} ions close to the metal surface. This effect was found to be proportional to concentration, with the lowest reaction rate observed for solutions saturated with MgCl_2 . This behaviour also coincided with the elimination of anodic hydrogen evolution. The reaction rate under these conditions was found to be sensitive to fluid velocity and thus the rate limiting step was determined to be the dissolution of the salt film at its interface with the bulk solution. Similar behaviour was catalogued by Beck for aluminium which exhibits similar passive behaviour to magnesium and the characterisation of corrosion beneath salt films has subsequently been extended to stainless steels (Beck, 1984; Rayment et al., 2008; Srinivasan and Kelly, 2016). Burrows linked the formation of salt films to the initiation of pitting corrosion in Magnox alloys immersed in solutions with a threshold chloride concentration. In brief, pitting initiates as the high electric field at

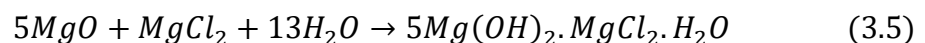
defect sites enables rapid corrosion, followed by repassivation when the local solution in the pit can no longer sustain a stable $MgCl_2$ phase (Burrows, 2013).

Overall, while the corrosion behaviour of Magnox alloy is similar to that of pure magnesium, these observations and the characterisation of salt film effects is highly relevant to Cementisation as the process necessarily involves corrosion of the Magnox alloy in highly concentrated $MgCl_2$ solutions.

3.4 Magnesium Oxychloride Cements

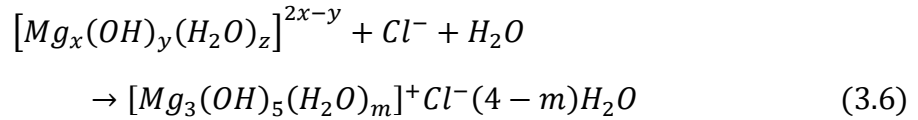
The primary product and end point of the Cementisation process is the production of a magnesium oxychloride cement (MOC) from the magnesium oxide/hydroxides arising from the oxidation of metallic Mg. Hydrated magnesium oxychlorides were first identified as a candidate for use as structural cement by Sorel in the mid-19th century (Walling and Provis, 2016). Sorel cements, as they are alternatively known, are notable for their physical strength and adaptability to diverse filler materials, however their non-hydraulic nature leads to poor water resistance, restricting their application to dry environments, for example as interior walls and flooring (Guo et al., 2018). Nevertheless, a resurgence in scientific and engineering interest in recent years has been driven by decarbonisation efforts in the construction industry (Gartner and Sui, 2018), since unlike Portland cements, the MOC synthesis reaction does not implicitly produce carbon dioxide (CO_2). Research efforts have therefore focussed on optimising the strength and, more importantly, water resistance of MOC phases, particularly in regions such as China where the raw materials (i.e. magnesite deposits) are abundant and thus production is economically favourable (Walling and Provis, 2016). MOC cements have also been investigated as an encapsulating material for use in the geological disposal of radioactive wastes, particularly in regions where the host geology is compatible with high-chloride materials, such as in salt mines (Xiong et al., 2010; Walling and Provis, 2016).

MOC pastes are synthesised by the addition of calcined magnesium oxide (MgO) to concentrated solutions of magnesium chloride, according to molar ratios defined by the particular phase desired (Li and Chau, 2007). The F5 phase (Guo et al., 2018), named for the stoichiometric ratio of $Mg(OH)_2$ to $MgCl_2$ as shown in Equation 3.5, is the most commonly targeted product as it has been associated with increased physical strength and reduced porosity (Ye et al., 2018).



Other phases, such as F2 and F9 (once again named for their stoichiometric $\text{Mg}(\text{OH})_2$ component), stabilise at higher temperatures and the F3 phase is found to be stable at lower temperatures and where there is an excess of MgCl_2 (Liu et al., 2017; Guo et al., 2018). In addition, the F3 phase forms during aging of the F5 phase which is found to be metastable (Mažuranić et al., 1982; Bilinski et al., 1984; Liu et al., 2017).

The oxychloride phases precipitate in preference to the typical magnesium hydroxide species above a threshold concentration of MgCl_2 (Pannach et al., 2017). This threshold, at 1.96M, represents the point at which the mononuclear complex ion $[\text{Mg}(\text{OH})(\text{H}_2\text{O})_5]^+$ becomes sufficiently stable to participate in bridging reactions with other mononuclear complexes, forming polynuclear chains of the form $[\text{Mg}_x(\text{OH})_y(\text{H}_2\text{O})_z]^{2x-y}$. These complexes are most stable at a particular number of units, presumed to correspond to an electrostatic minimum, that coincides with the molar ratios present in the F5 phase. This amorphous gel phase then crystallises with Cl^- ions and residual water, causing the paste to harden and gain strength as shown in Equation 3.6 (Dehua and Chuanmei, 1999), for example.



Where x , y , z and m are indices.

Various analytical techniques have been applied to characterising the MOC system, in line with typical methodologies used in cement science. X-ray Diffraction (XRD) is commonly used to both identify and quantify the phase composition of powdered cement samples, utilising reference spectra obtained by a number of researchers for the different phases (Guo et al., 2018). A set of time series measurements performed by Liu, for example, demonstrated qualitatively the decay of the metastable F5 phase to the stable F3 phase (Liu et al., 2017). In addition, X-ray spectra were used to validate thermophysical calculations predicting the stable phase for different ratios of $\text{MgO}:\text{MgCl}_2$ and $\text{H}_2\text{O}:\text{MgCl}_2$, as well as the effect of temperature on the relative phase proportions. Electron microscopy in both scanning and transmission modes has been used by a number of researchers to study the microstructure of MOC phases, with a view to understanding how their formation affects the mechanical properties of the cement product (Góchez et al., 2017; L. Huang et al., 2020). The pore surface of MOC phases is characterised by needle-like crystals of the F5 and F3 phases (Guo et al., 2018), the interlocking of which is cited as the source of its physical strength (Sglavo et al., 2011). The appearance

of these products, well crystallised, under imaging by SEM or similar techniques is the most widely used indicator of quality in MOC cement systems, alongside the proportion of the F5 phase under XRD analysis (Guo et al., 2018).

Thermal analysis techniques, including Differential Scanning Calorimetry (DSC), Differential Thermal Analysis (DTA) and Thermo-Gravimetric Analysis (TGA) have been frequently used to analyse cement systems (Ramachandran et al., 2002). The dehydration and decomposition of constituent phases can be analysed by one or more of these methods simultaneously to evaluate purity and degree of hydration of cement samples. For the MOC system, thermal analysis techniques have been used to assess the effect of additives on the performance of the cement products. In particular, analysis of bound water has been used to determine the effect of various soluble additives on the water resistance of MOC pastes (Li et al., 2016; Chen et al., 2019; Luo et al., 2020). Furthermore, the characteristic temperature of dehydration can be used to identify individual hydrate phases, for example the F3 and F5 phases. Xia used centrifugation to obtain pure samples of the F3 and F5 phases as individual products which were then characterised by XRD, thermal analysis, IR spectroscopy and electron microscopy. This allowed the individual hydrates to be identified and their thermophysical properties measured, in particular the enthalpy change on dehydration and associated proportional weight.

In addition to destructive thermal testing, calorimetry is often used in cement science to study the progression of the hydration reaction during setting, as the exothermic heat of reaction is measured with reference to a pre-set sample of the material (Ramachandran et al., 2002). This technique was used by Góchez alongside XRD to examine the kinetics of the MOC curing reaction (Góchez et al., 2017). By these methods it was determined that the crystallisation reaction initiates before the dissolution of MgO has been completed, placing an upper limit on the degree of crystallisation. Thus, any means (e.g., the use of acidic additives as previously discussed) by which the dissolution of MgO can be accelerated or maintained during crystallisation is likely to improve the mechanical properties of the final product.

3.5 Summary

The treatment of Magnox wastes by enhanced corrosion (using elevated temperature) has been suggested but not yet attempted in the published literature (Morris, Wickham, et al., 2009). From examination of the existing strategy for the disposal of Magnox swarf wastes, it is evident that there is a need for an in-situ treatment that can be applied to stabilise these wastes and

allow them to transition from interim storage to final disposal in a GDF. The process here described as Cementisation, involving the synthesis of MOC phases from metallic Mg by immersion in concentrated MgCl_2 solutions, is entirely novel and presented here for the first time.

The formation of MOC phases as a product of the corrosion of Mg was postulated by Casey but not confirmed (Casey and Bergeron, 1953; Casey et al., 1962). In the same works, the optimal concentration of MgCl_2 for corroding Mg was identified at $\sim 4\text{M}$. In Section 4, the work of Casey is replicated using the recently developed method of gravimetric hydrogen collection (Curioni, 2014; Fajardo and Frankel, 2015). This work was extended to include measurements on Magnox Al80 as well as measurements in AlCl_3 at the same ionic strength to investigate the underlying mechanisms.

The corrosion mechanism of magnesium in aqueous solution remains a topic of substantial academic interest (Esmaily et al., 2017). In Section 5, the effect of concentrated solutions of MgCl_2 and AlCl_3 on Mg corrosion was investigated in detail by Electrochemical Impedance Spectroscopy (EIS), a technique which was unavailable when this effect was previously studied by Casey. To understand the results of this work, a framework for understanding the impedance behaviour of magnesium was constructed independently from the works of both King and Yuwono (King et al., 2014; Yuwono, Taylor, et al., 2019). This framework was then used to explain variations in the impedance response of Mg and Magnox as a function of salt concentration and its effect on the solubility of corrosion products.

Finally, Section 6 details the proof-of-concept work performed for Cementisation on the lab scale by demonstrating the synthesis of magnesium oxychloride cement phases from metallic Mg powders by simple mixing in MgCl_2 solutions.

4 Corrosion Kinetics of Magnesium and Magnox Alloy in Concentrated Salt Solutions

4.1 Introduction

Typically, corrosion of pure magnesium and magnesium alloys is characterised by the formation of a partially protective surface bilayer of MgO and Mg(OH)₂, promoting quasi-passive corrosion behaviour (Nordlien et al., 1995; Song et al., 1997; Hara et al., 2007; Pardo et al., 2008; Liu et al., 2009; Taheri et al., 2012; Brady et al., 2015; Esmaily et al., 2017; Maltseva et al., 2019). Under this regime corrosion progresses stochastically, concentrated at defect sites and crevices leading to pitting and other forms of non-uniform attack (Hara et al., 2007; Pardo et al., 2008; Brady et al., 2015; Esmaily et al., 2017). The temperature sensitivity of the dissolution reaction is low with activation energies of $\sim < 20 \text{ kJ mol}^{-1}$ (Casey and Bergeron, 1953), where the rate limiting step is attributed to the diffusion of fresh water to reaction sites at the surface. However, under certain conditions this behaviour can be substantially altered. Previous researchers observed that the formation of a surface film is suppressed in buffered acidic solutions where the hydroxide is soluble (Fajardo et al., 2017; Esmaily et al., 2017). Similarly, the corrosion rate of magnesium in highly concentrated magnesium chloride (MgCl₂) solutions has been found to be significantly higher than in comparable solutions of potassium chloride (KCl), accompanied by a lack of surface film formation (Casey and Bergeron, 1953). At peak reaction rate, in 4M MgCl₂, the activation energy of the reaction was measured to be 48 kJ mol^{-1} (Casey and Bergeron, 1953). Under these conditions the rate limiting step can no longer be attributed to the self-diffusion of water and is likely to represent a mixed reaction where diffusion of reactants away from the surface limits access to reaction sites at the surface (Roller, 1935). In solutions where the hydroxide product is soluble, film formation is suppressed, inducing active corrosion similar to that observed for other metals such as iron (Abramson and King, 1939). Therefore, it is hypothesised that uniform, deterministic corrosion of Mg and Magnox can be produced through immersion in concentrated MgCl₂ solutions, enabling a high degree of conversion to oxide phases.

To underpin the first step of the Cementisation process, the corrosion kinetics results of previous researchers for Mg in 4M MgCl₂ were replicated by gravimetric hydrogen collection, validating both the result and the method which remains relatively novel (Casey and Bergeron, 1953; Curioni, 2014; Fajardo and Frankel, 2015). The method was then extended to samples of

Magnox alloy obtained from the fins of a Magnox fuel element to demonstrate whether enhanced corrosion could be achieved in the target material. Furthermore, to investigate cationic effects and pH dependence, the experiment was repeated for solutions of AlCl_3 identical ionic strength (corresponding to 2.67M AlCl_3). Corrosion rates were measured at 10°C intervals over the range 20-60°C to determine the reaction rate (expressed in terms of mmh^{-1}) as well as the temperature dependence, including an effective activation energy for each Alloy/Salt system. These investigations were supported using thermochemical modelling to calculate key parameters and better understand the behaviours observed in highly concentrated non-ambient salt solutions.

4.2 Experimental

4.2.1 Gravimetric Hydrogen Collection

The gravimetric method for measuring hydrogen evolution was selected for use in this study due to its precision and its ability to enable real-time determination of the corrosion rate. (Curioni, 2014). In previous work this method has been combined with electrochemical methods to accelerate reaction rates and investigate specific phenomena such as the anomalous hydrogen evolution observed during anodic polarisation of magnesium (Fajardo and Frankel, 2015). For the case of magnesium and Magnox in concentrated salt solutions, the rate of reaction was found to be so fast that electrochemical assistance was unnecessary. Nevertheless, the electrical connection was maintained to allow for measurement of the Open Circuit Potential (OCP) to determine when the reaction had reached steady state.

The reaction vessel used for gravimetric measurements was a standard 2l wide mouth borosilicate glass beaker with a 250ml tall form glass beaker used for hydrogen collection. An analytical balance (A&D HR250AZ) was mounted on a platform above the vessel with access to the below-balance hook. Weight data were logged once per second via the serial port using the associated software package WinCT. A hotplate stirrer (Scilogex MS-H280 Pro) was used with a PT1000 temperature probe for heating and temperature regulation. The collector vessel was suspended from the balance hook using an adjustable hook that allowed for height adjustment. A simplified representation of the experimental setup is displayed in Figure 4.1.

A bulb pump connected to a rigid length of U-shaped stainless-steel pipe was used to evacuate the collector before each set of experiments. Temperature was monitored and logged using a USB thermometer (TENMA 72-7712) and type K

thermocouple. Atmospheric pressure was measured and logged along with humidity and ambient temperature in the lab (Extech RHT50). OCP was monitored using a potentiostat (Gamry 1010E) in a three-electrode configuration with a custom platinum grid counter electrode (Fiaxcell) and a Ag/AgCl/Cl⁻ (3M) reference electrode (BASi MF-2052).

The use of a counter electrode is superfluous for OCP measurements as no current is being applied to the system. This aspect of the setup was a holdover from previous work where it was expected that external polarisation would be required to measure the corrosion rate, as practised in all other published instances of the gravimetric method (Curioni, 2014; Fajardo and Frankel, 2015; Curioni and Scenini, 2015; Curioni et al., 2017; Strebl and Virtanen, 2019). Also, given the large volume of the vessel and the necessary submersion depth of the sample, there was significant separation between the reference and working electrodes during measurement of OCP. However, since the conductivity of the concentrated salt solution is likely to be very high and no current is flowing during potential measurements, the effects of IR drop can be neglected.

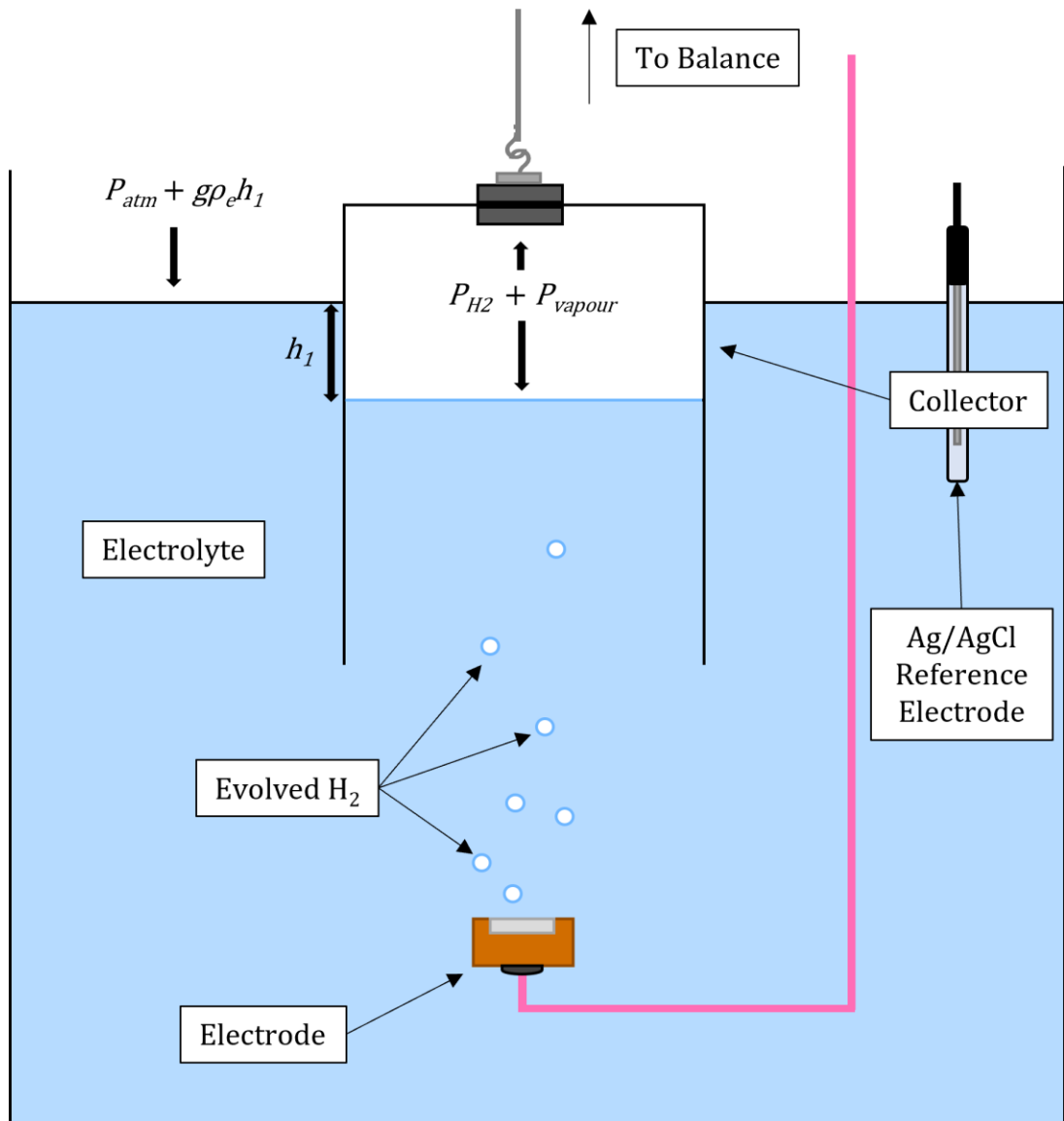


Figure 4.1 Schematic representation of the apparatus used for gravimetric hydrogen collection. As fluid is displaced the net weight of the collector changes, allowing the volume of gas to be determined as a function of time.

4.2.2 Sample Preparation

Samples of magnesium rod (Goodfellow MG007924, 99.9% purity as drawn) and sections of Magnox alloy of ~5mm thickness were mounted in epoxy resin (Struers Epofix) to present a single flat surface with a length of single-core wire (RS PRO 359-043) attached to the rear face of the sample to provide an electrical connection. The overall electrode construction is shown in Figure 4.2. Magnox samples were sectioned from solid fins taken from a dummy fuel rod as shown in Figure 4.3.

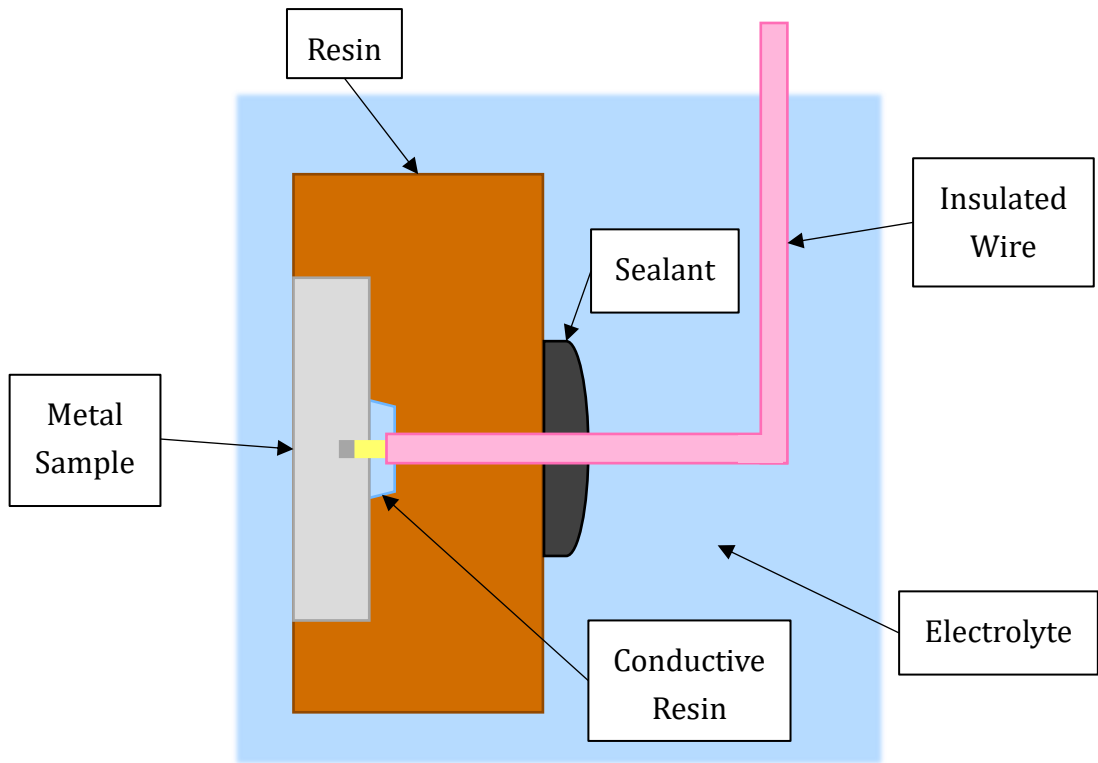


Figure 4.2 Schematic representation of the electrode construction used for dissolution and electrochemical testing.

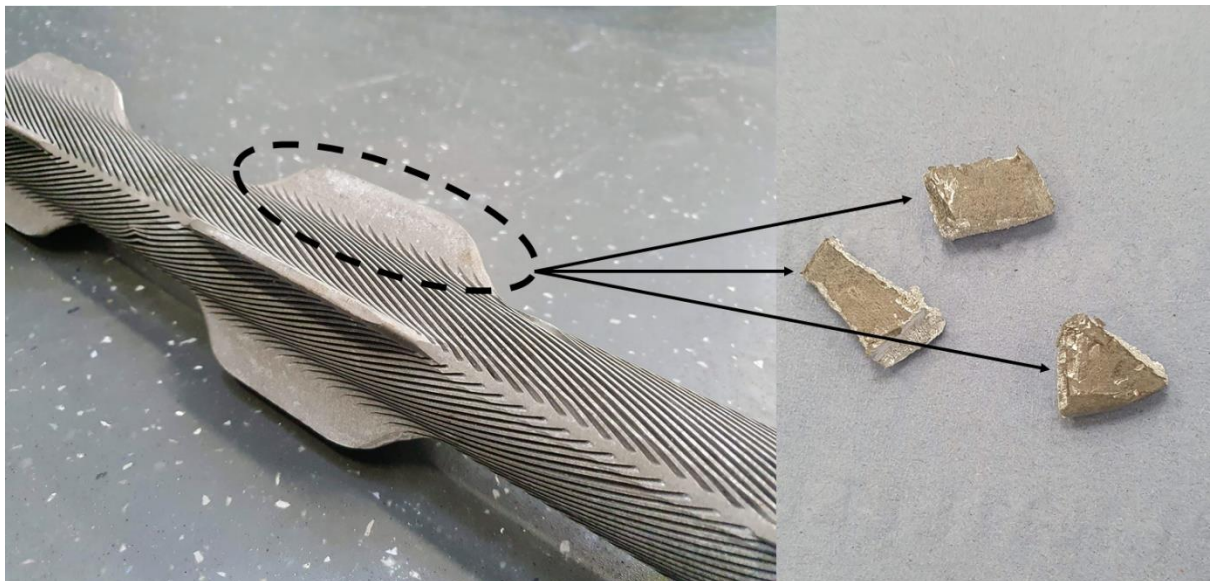


Figure 4.3 Photographs of the dummy Magnox fuel rod (left) and sections of fin that were cut off (right) to produce samples for dissolution testing.

To provide a secure mounting point and ensure good electrical contact, the cable was mounted into 1.7mm diameter holes drilled to a ~2mm depth into the metal; a process adapted from Shi and Atrens (Shi and Atrens, 2011). Conductive silver epoxy (MG Chemicals 8331) was applied immediately prior to mounting to further assure electrical contact. The exposed metal surface was ground by hand to a 2000 grit finish using a sequence of abrasive SiC papers

before immersion. Isopropyl alcohol was used as a dispersant to remove water and surface contaminants.

4.2.3 Experimental Method

Once the OCP of the system stabilised, indicating steady state, data was collected until a balance deflection of >5g was observed, determined to be the threshold beyond which short term fluctuations (turbulence, temperature, pressure) could reasonably be neglected. Figure 4.4 shows a graphical representation of how measurement periods were defined with respect to these criteria.

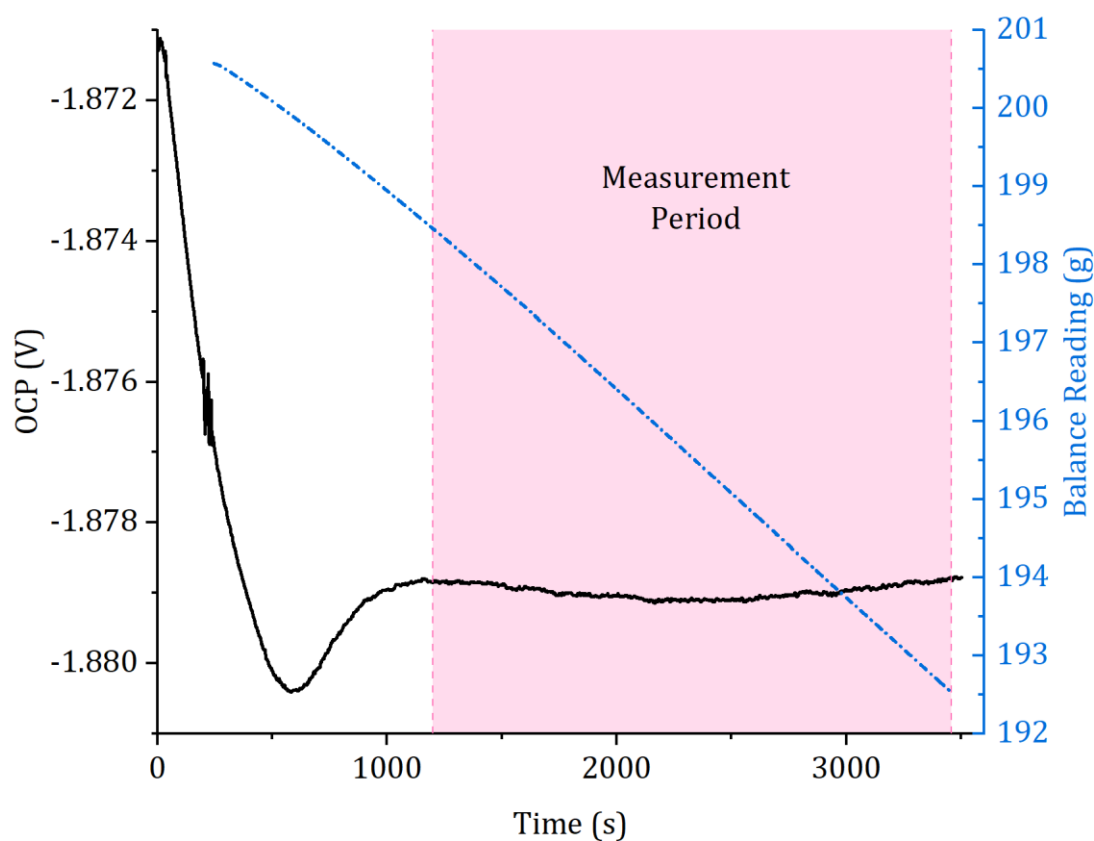


Figure 4.4 Plot showing balance output as a function of time during the collection of hydrogen from Mg corroding in 4M MgCl₂ at ambient conditions (~20°C) with simultaneous OCP monitoring. The highlighted region shows the period from which rate data were extracted corresponding with stable OCP as an indicator of dynamic equilibrium.

The sample was then removed and cleaned with deionised water and isopropyl alcohol. The hotplate was then used to raise the solution temperature to the next measurement point with the assistance of a magnetic stir bar at 200rpm which was removed during measurements. Measurements were performed at ambient conditions (assumed to be 20°C) and then 30, 40, 50 and 60°C in sequential order. Experiments to determine E_a were performed for both magnesium and Magnox samples in concentrated MgCl₂ and AlCl₃. To improve

estimates and demonstrate repeatability 4 replicate measurements were performed for each condition.

Under steady state conditions, the balance of pressures is described by Equation 4.1 as depicted in Figure 4.5:

$$P_{H_2} + P_{vapour} = P_{atm} + g\rho_e h_1 \quad (4.1)$$

where P_{H_2} is the pressure exerted by gas in the collector, g is the standard acceleration due to gravity ($g = 9.81\text{ms}^{-2}$), h_1 is the relative vertical separation between the solution interfaces and P_{vapour} is the vapour pressure of water (Fajardo and Frankel, 2015).

In this work, the collector was not necessarily fully submerged as practised by earlier researchers. Within the theoretical treatment as detailed by Fajardo, this corresponds to a situation where the vertical separation h_1 between the two liquid/gas interfaces is initially allowed to have a negative value, i.e., the bottom of the bubble in the collector is higher than the liquid surface in the reaction vessel. As the collector itself does not move, it does not displace any more or less liquid regardless of the amount of gas collected in it and its contribution to the reaction force registered on the balance remains constant. Only by the evolution of gas is water displaced and thus the only contribution to the reaction force on the balance is from the evolution of gas. The effect of the pressure head defined by h_1 does contribute to the reaction force imposed by the gas bubble, but for low density fluids and/or small submersion depths its contribution represents a negligible systematic error (Fajardo and Frankel, 2015). Nevertheless, by setting up the apparatus in this way, such that the interface separation h_1 is minimised over the course of the experiment, the potential of this error to affect the measurement is minimised.

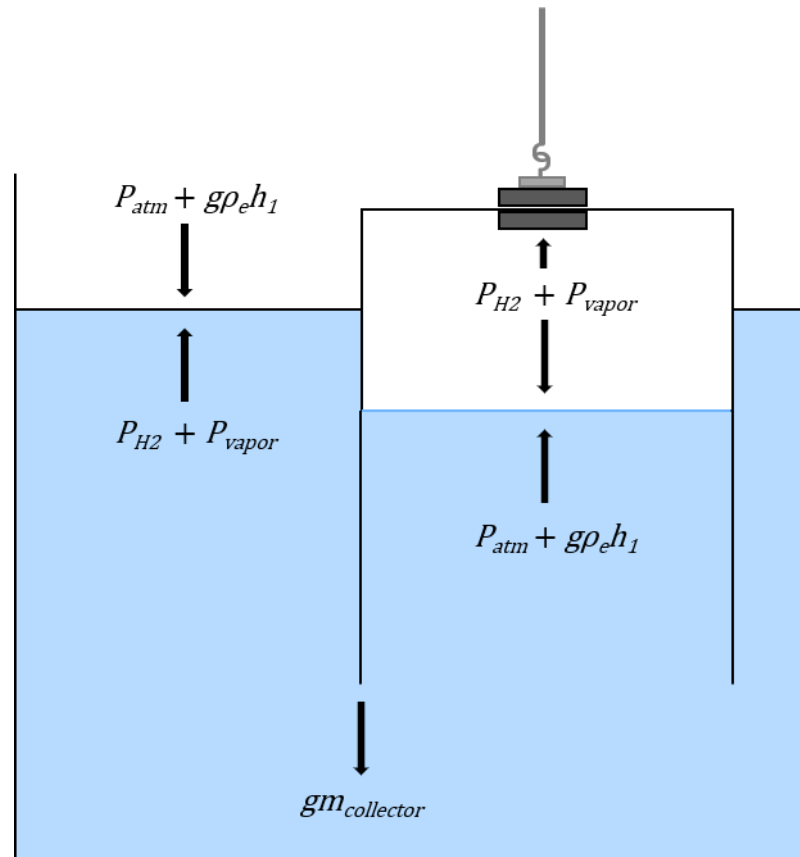


Figure 4.5 Diagram showing the forces acting on the submerged collector at steady state. The mass of the collector is represented as $m_{collector}$.

As a result of the corrosion of a sample of magnesium alloy, molecules of hydrogen gas nucleate and coalesce, creating voids that displace the surrounding fluid. The displacement of fluid in the collector compresses the plenum of collected gas, creating a reaction force that is registered by the balance as a change in the net weight of the collector. Formation of a bubble anywhere in the system will register on the balance, providing instantaneous measurement of the volume of gas present. If the bubble were not collected, the evolved gas will escape into the atmosphere and the system will relax to its former state. The function of the collector, therefore, is simply to prevent evolved gases from leaving the system, allowing cumulative measurements to be made. From the net weight registered on the balance the volume of gas evolved can be calculated from Equation 4.2:

$$V_{H_2}(t) = \frac{-m_{net}(t)}{\rho_e} \quad (4.2)$$

Where V_{H_2} is the volume of evolved gas as a function of time, m_{net} is the net weight of the collector as a function of time (with $m_{net} = 0$ when $t = 0$) and ρ_e is the density of the electrolyte solution (Fajardo and Frankel, 2015).

For each data point the cumulative volume of gas produced is divided by the standard molar volume. This is calculated for each temperature under the assumption that the pressures are equalised and the gas in the collector is in equilibrium with the bulk solution (Equation 4.3):

$$M_{Mg}(t) = \frac{-m_{net}(t) \cdot P_{atm}}{\rho_e \cdot R \cdot T} \quad (4.3)$$

Where M_{Mg} is the cumulative mass reacted in moles as a function of time, P_{atm} is the atmospheric pressure, R is the ideal gas constant ($8.314 \text{ J}\cdot\text{K}^{-1}\text{mol}^{-1}$) and T is the temperature in Kelvin.

The cumulative mass is then divided by the surface area of the sample, which was $1.267 \times 10^{-4} \text{ m}^2$ for Mg samples and determined by photographic analysis (FIJI software package) for Magnox samples. A linear regression analysis is then applied to determine the specific zeroth-order reaction constant k in units of $\text{mols}^{-1}\text{m}^{-2}$. For each set of temperature measurements, the activation energy E_a can be extracted using the Arrhenius equation (Equation 4.4):

$$k = Ae^{\frac{-E_a}{RT}} \quad (4.4)$$

Where k is the rate constant, A is the frequency factor and E_a is the activation energy in kJmol^{-1} .

4.2.4 Error Analysis

With a balance capable of 0.1mg resolution the smallest volume of gas detectable is $\sim 10 \mu\text{l}$ using the gravimetric method. In practice, however, environmental effects such as fluid turbulence, temperature fluctuation and atmospheric pressure changes create significant noise for a given measurement.

Errors due to turbulence are removed by the averaging required to determine the gradient of cumulative gas evolution. The error in atmospheric pressure is calculated as the standard deviation of atmospheric pressure logged over the measurement window. This changes the standard molar volume of gas in the collector but is generally negligible contributing $\sim 0.1\%$ error to each measurement. The relative difference in height between the solution-air interface in the collector and the fluid surface in the reaction vessel causes pressure changes due to gravity according to Equation 4.5 (Fajardo and Frankel, 2015):

$$P_{H_2} = P_{atm} + g\rho_e h_1 - P_{vapour} \quad (4.5)$$

In this study measurements were performed sequentially without evacuating the collector between measurements. This creates a systematic error that

affects earlier measurements more than later ones, but the effect is small with a maximum deflection of order $\sim 0.5\%$ and is therefore neglected. The effect of vapour pressure was calculated and subtracted using steam tables modified by an osmotic coefficient to account for high salt concentrations (J.R. Rumble, 2020). The coefficient used was 2.5 in MgCl_2 (Ge et al., 2007), and 2.8 in AlCl_3 (André et al., 2018) and the values for each test temperature are given in Table 4.1.

Table 4.1 Vapour pressure values calculated from saturation pressure of water modified for osmotic coefficients: $\text{MgCl}_2 = 2.5$, $\text{AlCl}_3 = 2.8$.

Temperature [°C]	P_{vapour} 4M MgCl₂ [Pa]	P_{vapour} 2.67M AlCl₃ [Pa]
20	872.8	779.3
30	1584	1414
40	2755	2460
50	4608	4115
60	7442	6645

Evaporation also affects the measurement by gradually reducing the pressure head in the reaction vessel. The rate of evaporation is proportional to temperature as reflected by the change in vapour pressure. Uncorrected, this will cause overestimates of the reaction rate at higher temperatures leading to a skew that will affect the calculated activation energy. To determine the extent of this effect the rate of evaporation was measured between corrosion measurements and converted into an equivalent reaction rate by linear regression as shown in Figure 4.6. These baselines were then subtracted from the corresponding corrosion rate measurements to correct for evaporative losses.

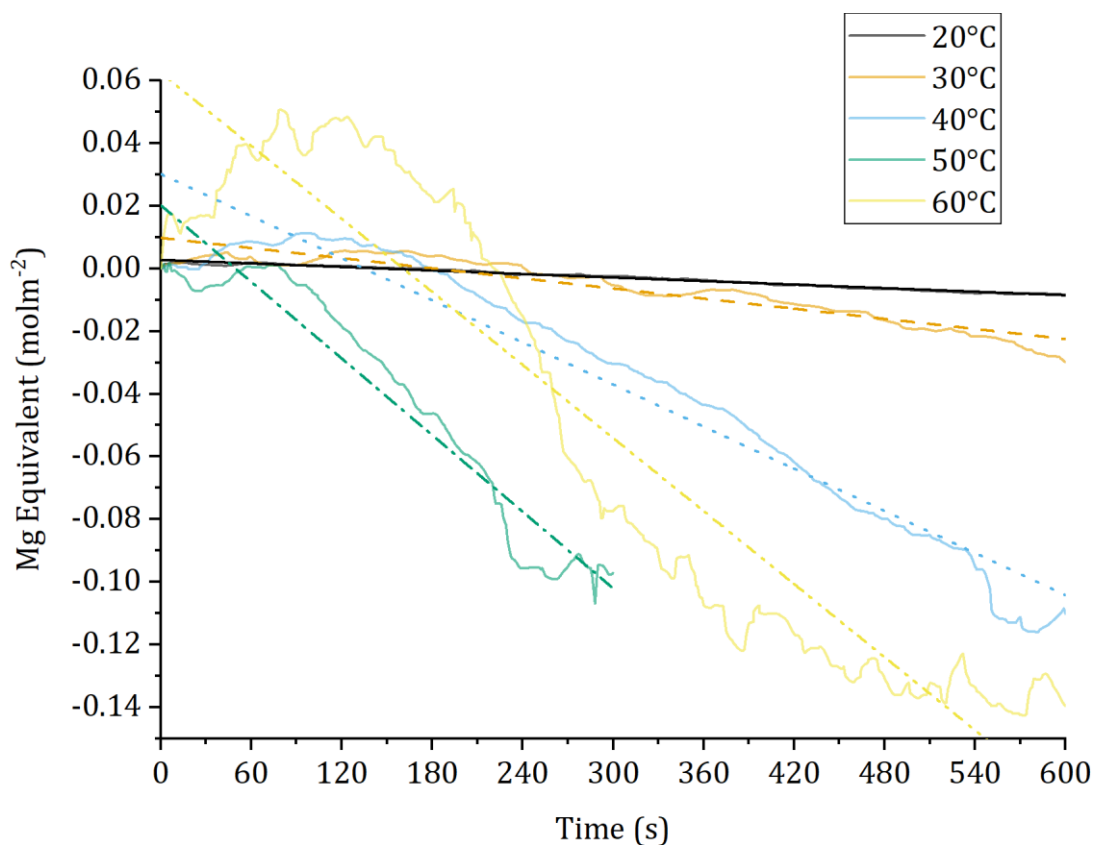


Figure 4.6 Series of plots showing evaporative losses over time measured with no sample present for each temperature in 4M MgCl₂.

Due to time constraints this correction was performed for only one replicate under each electrolyte condition. For these experiments, the corrected value of E_a was found to be 1.6% higher in MgCl₂ and 2.3% higher in AlCl₃ than the uncorrected value. As the results presented in Section 4.3 are uncorrected it may be prudent to assume a systematic error of $\sim +2\%$ for the values and averages displayed. However, given that the effect is comparable to the standard deviation of the results and that the relative error between conditions is small, the effect of evaporation can be judged to not have a substantial impact on the results of this study.

By far the largest source of random error is temperature fluctuations in the bulk electrolyte. With a large fluid volume, it is difficult to maintain a stable temperature with a hotplate in a single-walled beaker. Deflections were usually within $\pm 1^\circ\text{C}$ of the target temperature but instances of 3-4 $^\circ\text{C}$ drops were observed, particularly at higher temperatures. These errors contribute to systematic errors in the value of $1/T$ used to calculate the activation energy. However, given the precise linear relationship assumed by the Arrhenius equation, error in the independent variable $1/T$ will be expressed as error in the gradient calculated by linear regression. Therefore, the target temperature

was used when plotting $1/T$ under the assumption that error in the gradient is dominated by temperature effects for the purpose of calculating E_a .

4.2.5 Thermochemical Calculations

Solution density was calculated using the SPECE8 (Geochemist's Workbench Version 14.0) to perform a charge balance with respect to H^+ ions. In addition, to replicate conditions at steady state additional Mg^{2+} ions were added to the system to find the saturation point beyond which additional dissolution would lead to precipitation of solids out of solution. Magnesium oxide powder (SLS, 98% purity) was used to buffer solutions to this point. The included Yucca Mountain Project database (thermo_ymp.R2.tdat) was used to provide thermodynamic data as it contains entries for aluminium species and utilises the Harvie-Møller-Weare method for calculating activity coefficients at high concentrations (Jove-Colon et al., 2007).

Using SPECE8, equilibrium pH values and activity coefficients for water, Mg^{2+} and Cl^- were calculated for the 4M $MgCl_2$ system from 20-90°C. These values were then used in Act2 to create a set of Pourbaix diagrams for aluminium in 4M $MgCl_2$ based on an Al^{3+} activity of 1×10^{-6} . By comparing the temperature dependence of the Al^{3+} /Boehmite transition to the equilibrium pH of 4M $MgCl_2$ it was possible to predict the corrosion behaviour of Magnox alloy in concentrated $MgCl_2$ as a function of temperature. A TRUEScience pH meter was used to validate the predicted values at ambient temperature (20°C).

4.3 Results & Discussion

4.3.1 Corrosion Rate

Figure 4.7 shows the results of a single experiment where cumulative mass loss of metal over time has been determined from the gravimetric measurement of evolved hydrogen gas.

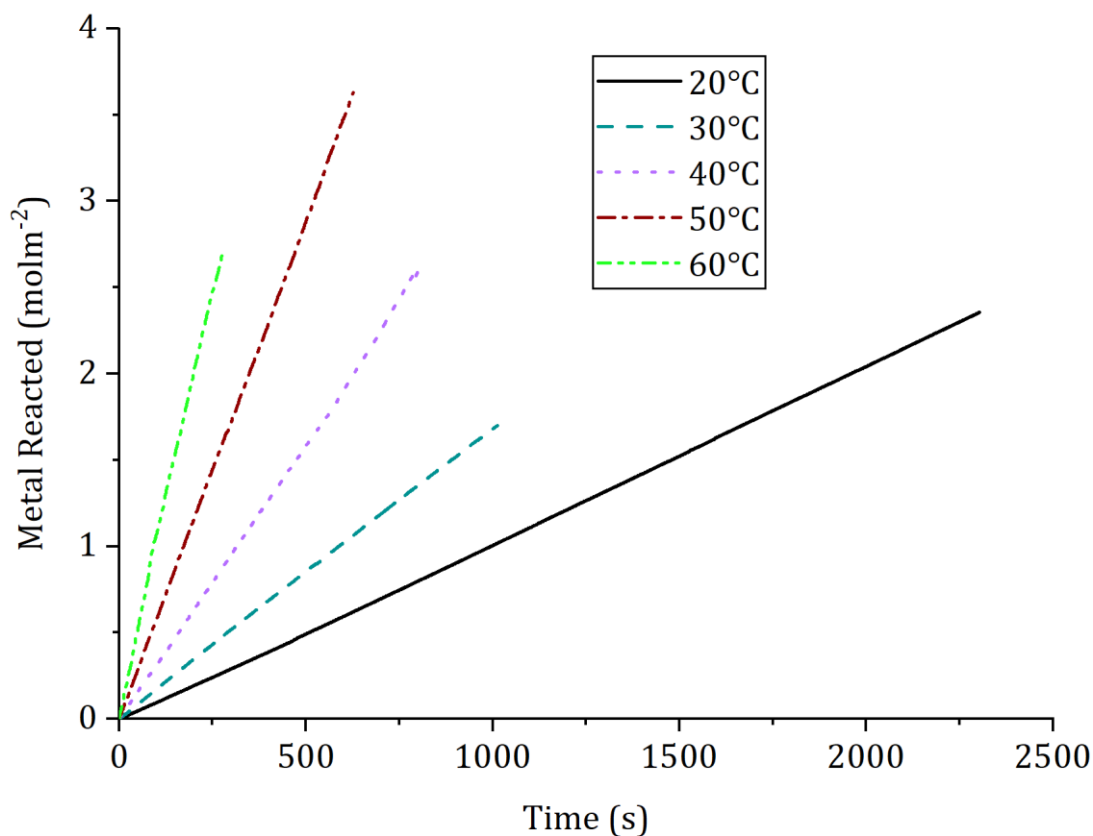


Figure 4.7 Series of plots showing the reaction rate of Mg in 4M MgCl₂ over the temperature range 20-60°C as measured by gravimetric hydrogen collection and expressed in terms of moles per metre squared (molm⁻²).

During periods of stable OCP (see Figure 4.4) the rate of hydrogen evolution is highly consistent, allowing measurements of the corrosion rate to be made with confidence. Gradients were calculated using the LINEST function in Excel with the intercept forced through zero. In all cases the error on the gradient is negligible and is therefore not presented for individual measurements. The mean value and standard deviation of 4 replicates is presented in Table 4.2 and Figure 4.8.

Table 4.2 Table of average corrosion rates in millimetres per hour [mmh^{-1}] \pm standard deviation of 4 replicate measurements.

Alloy/Salt	20°C	30°C	40°C	50°C	60°C
Mg/MgCl₂*	0.052 \pm 0.001	0.088 \pm 0.004	0.155 \pm 0.005	0.282 \pm 0.016	0.467 \pm 0.012 [†]
Mg/AlCl₃	0.054 \pm 0.002	0.128 \pm 0.005	0.222 \pm 0.012	0.410 \pm 0.035	0.637 \pm 0.055
Magnox/ MgCl₂	0.045 \pm 0.004	0.097 \pm 0.015	0.164 \pm 0.014	0.265 \pm 0.045	0.157 \pm 0.063 [‡]
Magnox/ AlCl₃	0.052 \pm 0.006	0.115 \pm 0.009	0.204 \pm 0.015	0.346 \pm 0.023	0.570 \pm 0.068

For Mg in 4M MgCl₂, the corrosion rates measured here are comparable to, yet significantly higher than, those measured previously by Casey and Bergeron (0.031mmh⁻¹ and 0.16mmh⁻¹ at 25°C and 55°C respectively) (Casey and Bergeron, 1953). This discrepancy cannot be decisively resolved, although it may result from the attempts by Casey and Bergeron to measure instantaneous initial mass loss rates at fixed pH values, which, it was noted by the authors, was highly challenging in such a strongly self-buffering acidic salt solution. In this work, it was noted that the corrosion rate typically took ~20 minutes to increase from its initial value to steady state (Figure 4.4). If the measurements made by Casey and Bergeron were made in similar conditions, then the initial rate would be lower than that at steady state as reported here. Despite the discrepancy, the ability to make this distinction demonstrates the value of the time-resolution capabilities of the gravimetric method, as well as the benefit of using OCP as a monitoring tool.

* First experimental replicate performed by Adizatu Alasa, MEng student.

† Distribution of 3 repeat measurements (for this case only).

‡ Steady state condition not satisfied; result is an underestimate of the true reaction rate at steady state.

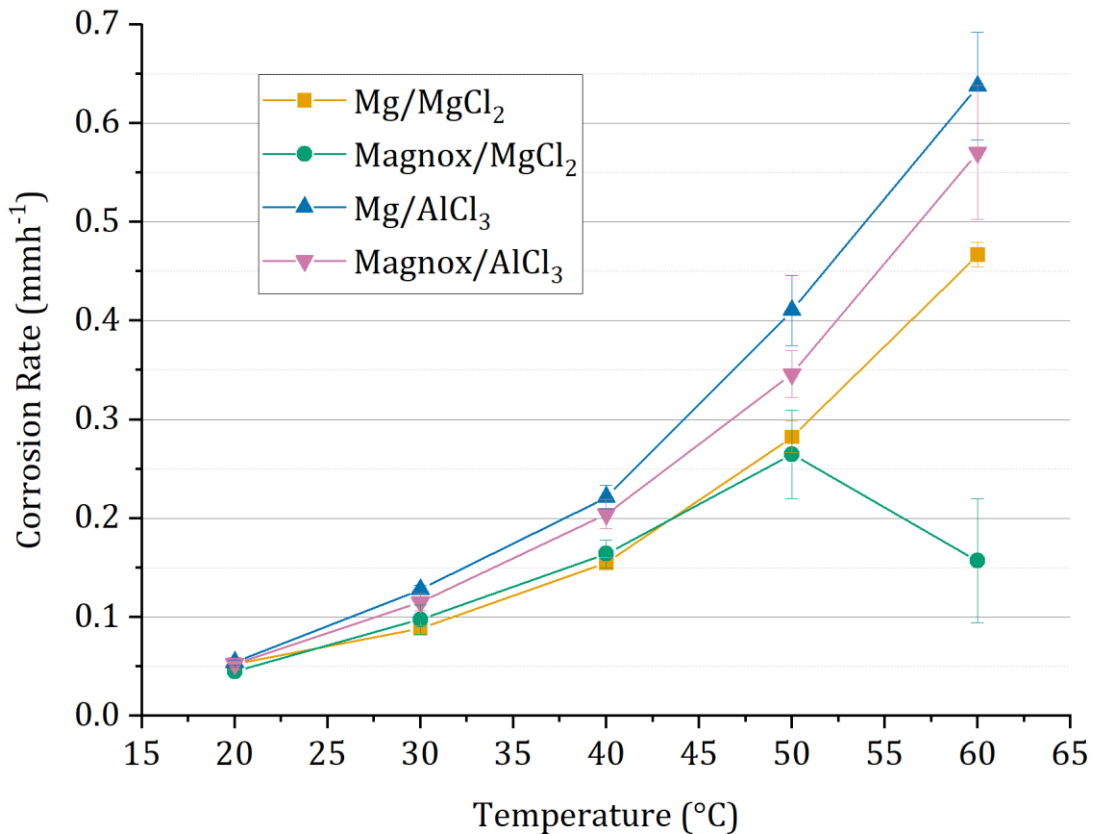


Figure 4.8 Series of plots showing average corrosion rate over the temperature range 20-60°C for all combinations of alloy and salt solution. Error bars are the standard deviation of 4 replicate measurements.

The increase in reaction rate is geometric with temperature, typical of chemical kinetics, with the exception of Magnox in 4M MgCl₂ at 50°C. For the case of Magnox in 4M MgCl₂ at 60°C, the first order differential of the reaction rate of is inconsistent with a zeroth-order reaction as its gradient is definitively negative. A quadratic polynomial fit shows good agreement with the cumulative data in this case, which is consistent with diffusion as the rate controlling step in the shrinking core model for a flat plate (Levenspiel, 1998), indicating the formation of a film that is at least partially protective. Over the same period, the OCP of the system showed constant deflection over time towards a more positive potential ($\sim +7.8\mu\text{Vs}^{-1}$). Both measurements were recorded simultaneously for each replicate as shown in Figure 4.9.

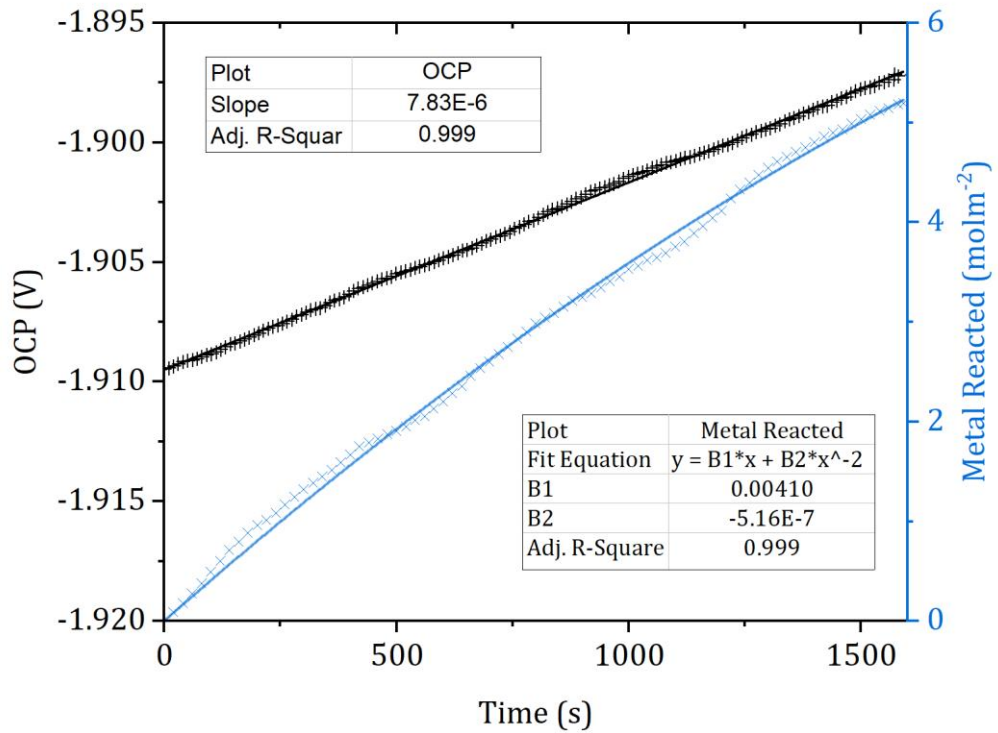


Figure 4.9 Plot showing the cumulative dissolution of a Magnox sample (replicate #4) in 4M MgCl₂ at 60°C as well as the OCP of the system monitored simultaneously.

Finally, visual inspection of samples post-immersion (Figure 4.10) also shows a substantial difference between Magnox/MgCl₂ samples at 60°C and those exposed to comparable conditions, including Magnox/AlCl₃ at 60°C.

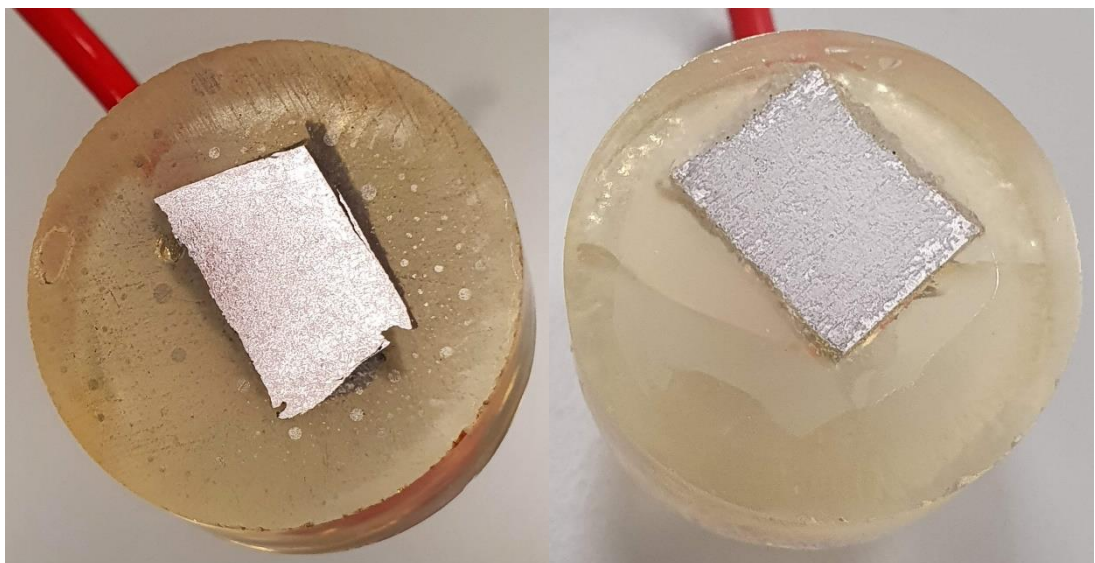


Figure 4.10 Photographs showing Magnox samples post immersion in AlCl₃ (left) and MgCl₂ (right) at 60°C, showing the formation of a surface film.

In combination these observations imply that a surface film becomes stable on Magnox alloys in 4M MgCl₂ at >50°C. This film is at least partially protective as it significantly lowers the corrosion rate relative to both pure Mg at 60°C and Magnox alloy at lower temperatures (Figure 4.8). It is important to note that the measurement for Mg/MgCl₂ at 60°C is an overestimate of the steady state reaction rate as the static OCP condition was not satisfied and thus the system was not at steady state, i.e., the protective film was not fully developed at the point of measurement.

Given that film formation is observed only in the Magnox/MgCl₂ system (and not in Magnox/AlCl₃ or Mg/MgCl₂), it can be asserted by the process of elimination that it is composed of aluminium oxides/hydroxides. Indeed, this behaviour is exactly predicted by prior thermochemical analysis which determines that Boehmite phases are stable in the 8N MgCl₂ system >50°C where aluminium is present.

Precise characterisation of this layer and its properties was beyond the scope of this study. For the purpose of developing the enhanced corrosion treatment process it was considered a priority to determine the linear corrosion rate and its characteristics (via activation energy) in order to evaluate whether it is a viable candidate for the treatment of reactive wastes. At this stage of development, therefore, it was considered sufficient to show that the corrosion rate of Magnox in 4M MgCl₂ is impeded at high temperatures by a partially protective film of aluminium oxide/hydroxides.

From the perspective of process development, the major implication of this result is that the optimum temperature for enhanced corrosion of Magnox alloy in 4M MgCl₂ is ≤50°C. This in turn implies that the rate of enhanced corrosion of Magnox has an upper limit of $0.265 \pm 0.045 \text{ mmh}^{-1}$ in 4M MgCl₂. Changes in concentration may prevent film stabilisation but will also move the system away from stoichiometry with the formation of the F5 magnesium oxychloride product. However, when approached in terms of process stability and safety, the existence of a temperature-dependent protective film could provide a negative feedback effect to the extent that thermal runaway is effectively prevented. For future development, therefore, it may be essential to perform a full characterisation of this layer and its formation, by physical analysis (e.g., microscopy and/or X-ray techniques such as grazing incidence XRD/X-ray Reflectometry (XRR)) to determine its chemical nature and electrochemical techniques to evaluate its growth kinetics with reference to an appropriate model.

4.3.2 Thermochemical Calculations

Following the observation of passivation on Magnox alloy samples in 4M MgCl₂ at 60°C, thermochemical calculations were performed to investigate the stability of oxide phases in this system. Solutions of 4M MgCl₂ were determined to be saturated with the addition of 0.025M Mg ions at which point Brucite (Mg(OH)₂) precipitates. In AlCl₃ the threshold was considerably higher, with saturation at 1.25M of Mg ions precipitating Boehmite (AlO(OH)) and Periclase (MgO). These parameters were used to calculate solution density, pH and viscosity as shown in Table 4.3.

Table 4.3 Parameters used to calculate density, pH and viscosity in solutions of 4M MgCl₂ and 2.67M AlCl₃ using SPECE8.

Temperature [°C]	Mg [molal]	Cl [molal]	Al [molal]	P_{sol} [gcm ⁻³]	Equilibrium pH	Viscosity [poise]
25	4	8	0	1.209	4.746	0.021
20	4.025	8	0	1.211	-	0.023
30	4.025	8	0	1.207	-	0.019
40	4.025	8	0	1.202	-	0.015
50	4.025	8	0	1.197	-	0.013
60	4.025	8	0	1.191	-	0.011
25	0	8	2.67	1.198	0.957	0.021
20	1.25	8	2.67	1.232	-	0.023
30	1.25	8	2.67	1.227	-	0.019
40	1.25	8	2.67	1.222	-	0.015
50	1.25	8	2.67	1.217	-	0.013
60	1.25	8	2.67	1.211	-	0.011

Densities of all solutions were $\sim 1.2\text{gcm}^{-3}$, gradually reducing with temperature as expected for a standard fluid. Both salt solutions were determined to be acidic with 4M MgCl₂ at pH ~ 5 and 2.67M AlCl₃ at pH ~ 1 . Experimental measurements before and after corrosion tests validated the predicted pH values and showed negligible change despite the addition of metal ions from the dissolution of samples. The viscosity of both solutions was determined to be equal at all temperature, decreasing linearly with temperature as expected for

aqueous solutions in such a narrow temperature range. The result of speciation calculations for aluminium in 4M MgCl₂ are presented in Table 4.4 and Figure 4.11 over the range 20-90°C.

Table 4.4 Table of values describing the effect of temperature on 4M MgCl₂ solution calculated via SPECE8 and the consequential effect on aluminium speciation calculated using Act2.

Temperature [°C]	H₂O Activity	Mg²⁺ Activity	Cl⁻ Activity	Eqm. pH	Al³⁺/Boehmite Transition pH
20	0.571	3.427	8.276	4.805	5.148
25	0.576	3.013	7.880	4.746	4.825
30	0.580	2.684	7.532	4.687	4.912
40	0.589	2.095	6.860	4.578	4.689
50	0.598	1.629	6.256	4.480	4.478
60	0.607	1.264	5.712	4.390	4.280
70	0.615	0.978	5.224	4.309	4.092
80	0.624	0.754	4.784	4.236	3.915
90	0.633	0.580	4.388	4.171	3.747

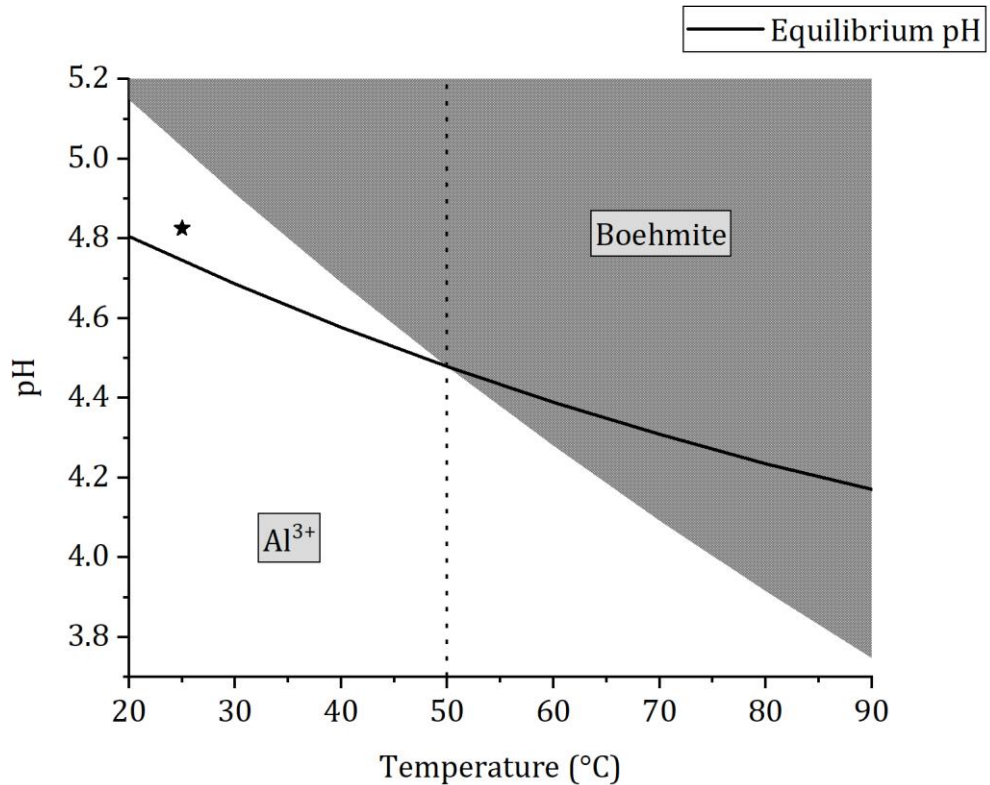


Figure 4.11 Plot showing the result of speciation calculations for aluminium (activity = 1×10^{-6}) in 4M MgCl_2 from 20-90°C. The star icon (★) denotes a special case at 25°C where the transition point is discontinuous and the predicted transition is Al^{3+} to Gibbsite.

For the case of 4M MgCl_2 with trace aluminium present ($>2.237 \mu\text{M}$ equivalent) there exists a transition at 50°C beyond which Boehmite becomes the most stable phase. It is also notable that aluminium is soluble in 4M MgCl_2 solutions at lower temperatures. For Magnox alloy containing 0.8% aluminium by weight, this implies that the alloy will corrode uniformly, but that a surface layer will stabilise at temperatures $>50^\circ\text{C}$.

4.3.3 Corrosion Kinetics

A high degree of correlation with temperature allows the activation energy E_a (Equation 4.4) to be calculated with precision as shown in the example experiment depicted in Figure 4.12, with a value in this case of $E_a = 45.3 \pm 1.2 \text{ kJ mol}^{-1}$.

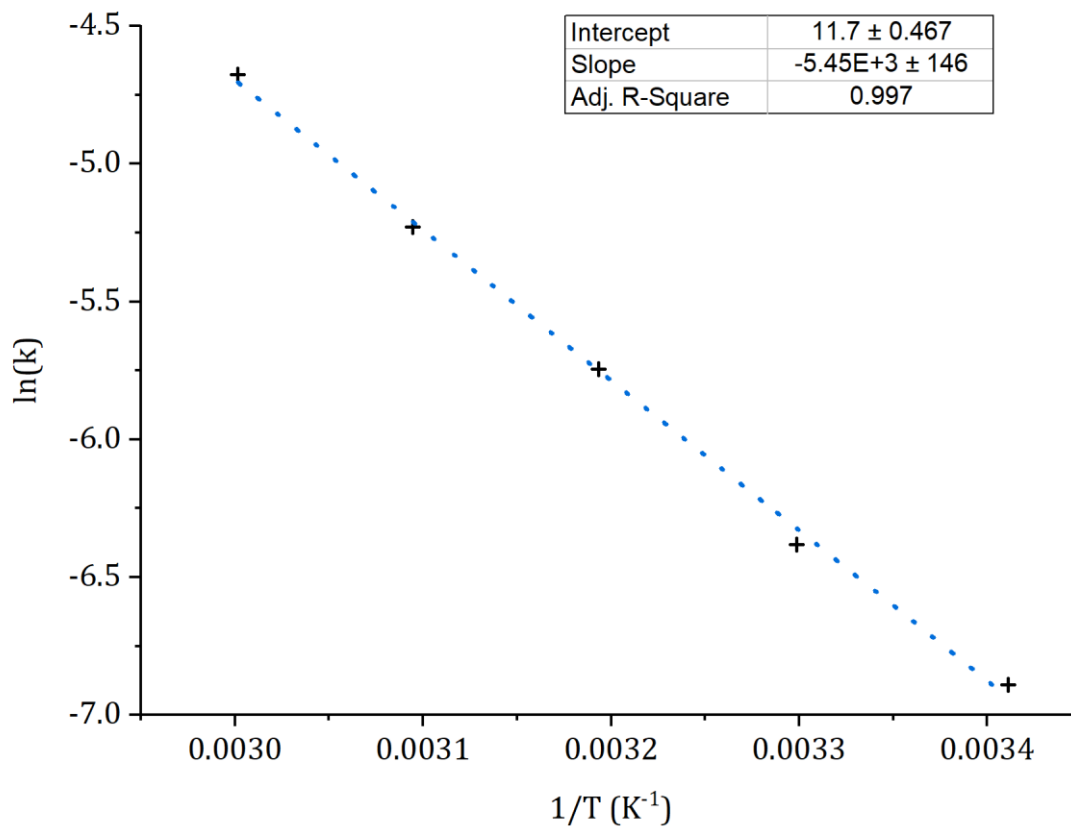


Figure 4.12 Example plot of the natural logarithm of the reaction rate of Mg in 4M MgCl_2 as a function of the inverse of solution temperature ($1/T$).

To determine the average activation energy E_a values were calculated for each replicate experiment from Equation 4.4 and averaged. A box plot displaying the distribution of results alongside the results of individual experiments is shown in Figure 4.13.

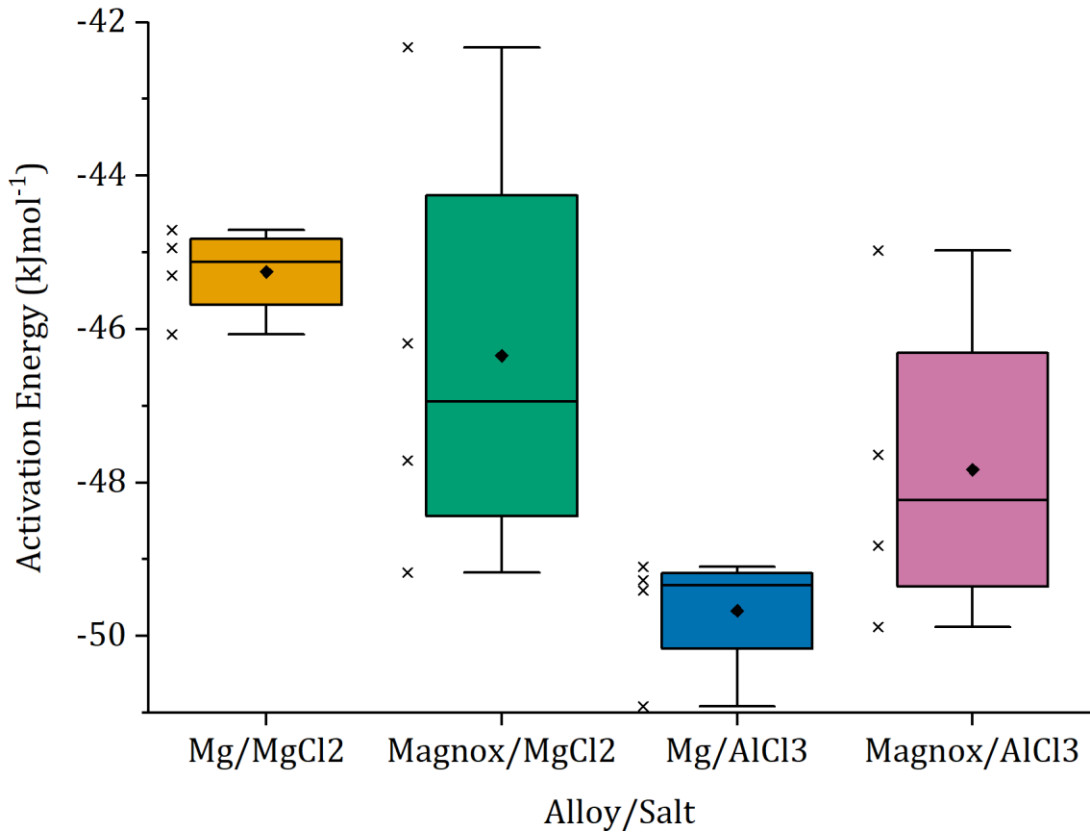


Figure 4.13 Box plot representing the distribution of activation energy measurements for all Alloy/Salt systems. The mean of each distribution (◆) is plotted alongside the results of individual experiments (×).

The data are evenly spread with minimal skew with the notable exception of Mg/AlCl₃ where a single measurement is responsible for a large skew in the distribution. However, the dataset only includes four replicates for each condition and as such no outliers can be identified and removed with confidence.

Measurements using Magnox samples had a higher spread, implying greater variation between samples. This is to be expected as there was much greater physical variation, particularly with respect to cross-sectional surface area compared to the commercial-grade Mg rod. The mean and standard deviation of activation energy measurements across all Alloy/Salt systems tested are displayed in Table 4.5.

Table 4.5 Table of values describing the average measured effective activation energy of Mg and Magnox in 4M MgCl₂ and 2.67M AlCl₃ along with the standard deviation of 4 replicate measurements.

Alloy/Salt	Average E_a [kJmol⁻¹]	Standard Deviation
Mg/MgCl₂	-45.3	0.6
Mg/AlCl₃	-49.7	0.8
Magnox/MgCl₂	-46.3	2.9
Magnox/AlCl₃	-47.8	2.1

Previous researchers have measured the activation energy of Mg dissolution in 4M MgCl₂ to be $48 \pm 4 \text{ kJmol}^{-1}$ (Casey and Bergeron, 1953), which is consistent with the value measured in this study for the Mg/MgCl₂ system. The agreement between this study and previous work demonstrates that the measurements made by gravimetric hydrogen evolution are valid.

Paired t-tests between all conditions show that the only conditions for which a statistically significant difference is observed are between Mg/MgCl₂ (M=-45.3, SD=0.6) and Mg/AlCl₃ (M=-49.7, SD=0.8), $t(3)=6.7$, $p < 0.01$. With better defined values for measurements of Magnox alloy it may be possible to differentiate between the effect of MgCl₂ and AlCl₃, although it is evident from the proximity of these measurements that the corrosion reaction is mechanistically similar in all the conditions tested. All measurements of the activation energy in concentrated MgCl₂ and AlCl₃ lie within the range $42\text{-}51 \text{ kJmol}^{-1}$. To interpret this result and identify the rate-controlling step, it is useful to consider how the rate-controlling step relates to the concentration of reactants at the solid-liquid interface as illustrated in Figure 4.14.

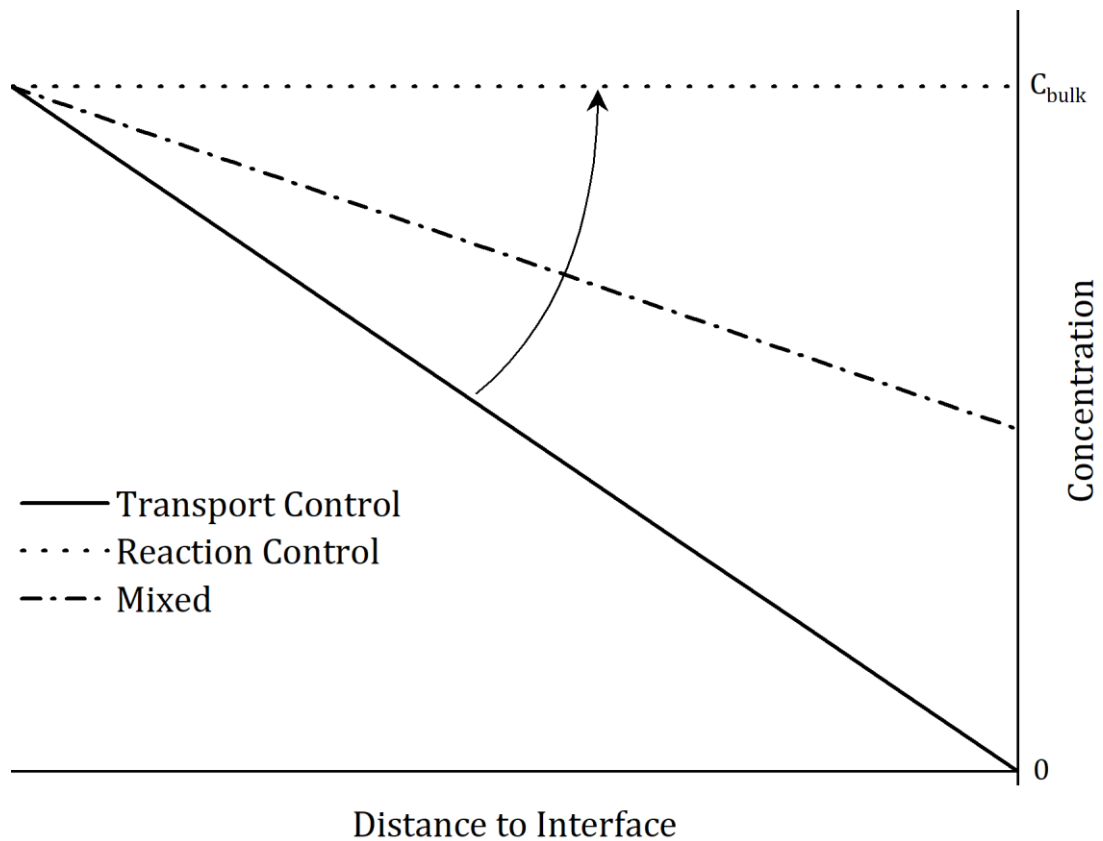


Figure 4.14 Graphical representation of the concentration of reactants approaching the interface under different reaction control schemes. The arrow represents the effect of improving transport in the liquid phase.

Under transport control the concentration of reactants at the interface drops to zero as they are used up faster than they are replaced. Conversely, when the limiting step is purely chemical in nature, the concentration is uniform as the supply of reactants outpaces their consumption (Abramson and King, 1939). In the intermediate case, as observed in this study, there remains a concentration gradient in the liquid boundary layer, however the concentration at the interface is non-zero. Thus, the transport and chemical steps of the reaction must proceed at comparable rates.

The threshold for transport control is generally considered to be $<20\text{kJmol}^{-1}$, comparable to the activation energy of viscosity and/or self-diffusion of water. Conversely, for reactions where $E_a > 60\text{kJmol}^{-1}$ the rate limiting step can be attributed to a purely chemical process (Abramson and King, 1939). From the activation energy values calculated for Mg and Magnox in concentrated MgCl_2 and AlCl_3 in this study, the dissolution reaction can be firmly placed into the intermediate “mixed” control regime where $20 < E_a < 60\text{kJmol}^{-1}$. While this implies that no single step is rate-controlling at quiescent conditions, this result

further supports the conclusion that the enhanced corrosion rate in these systems results from the suppression of surface film formation.

The significant increase in activation energy between solutions of MgCl_2 and AlCl_3 for the Mg system implies that transport is faster in AlCl_3 than in MgCl_2 . Given that no significant difference in viscosity was predicted between the salt solutions (Table 4.3), this effect is unlikely to arise from differences in the transport of reactants (H_2O molecules) to the metal surface. Rather, the increase must result from improved mobility of products (Mg^{2+} ions) away from the surface into the bulk solution.

If the experiments in this study were repeated at a high fluid velocity e.g., with a Rotating Disk Electrode (RDE), then the effect of diffusion could be removed and the “true” activation energy measured. For the purpose of underpinning the corrosion step to be used for Cementisation, however, these measurements definitively show that surface film formation is suppressed in 4M MgCl_2 and that the reaction is moderately sensitive to temperature changes. Furthermore, the measurements performed in AlCl_3 (as well as the anomalous effects in Magnox/ MgCl_2 at high temperature) show that film suppression occurs as a result of pH buffering and the resulting effect on $\text{Mg}(\text{OH})_2$ solubility. It should be noted that this result does not preclude the existence of a MgO barrier layer as identified by previous researchers (Esmaily et al., 2017), but it does indicate that there is direct contact between the solution and the dissolving surface.

Based on the results of thermochemical modelling, visual inspection and activation energy measurements, it can be concluded that corrosion of Mg and Magnox in concentrated solutions of MgCl_2 and AlCl_3 is characterised by the suppression of the typical surface film due to the solubility of magnesium hydroxide in the salt solution. This is in agreement with the general understanding of magnesium corrosion behaviour and the observations of filmless corrosion are consistent with the works of Casey and Fajardo (Casey and Bergeron, 1953; Casey et al., 1962; Fajardo et al., 2017). In this work, observations of this behaviour have been extended to the Magnox alloy and the effect of pH has been examined in greater detail, by use of highly acidic AlCl_3 solutions with validation of oxide stability by thermochemical modelling.

4.3.4 Rate-Controlling Steps in Heterogeneous Reactions

The process examined in this study is characterised by a reaction that progresses from transport control to mixed transport/reaction control as a result of the increasing concentration of salt in solution which induces the solvation of solid precipitates. This behaviour was identified by measuring the

temperature sensitivity of the reaction, expressed as the activation energy E_a as defined by the Arrhenius equation (Equation 4.4). However, an increase in E_a for a given reaction implies that the fraction of molecules with sufficient energy to react is reduced, while the measured reaction rate constant k increased. This can only be reconciled by an increase in the constant of proportionality A , corresponding to the total number of collisions per second. This can be thought of as the number of viable interactions on the molecular level and is also the y-intercept of the Arrhenius equation when plotted on a logarithmic scale against $1/T$ i.e., what the reaction rate would be if every collision resulted in a reaction. It follows intuitively that the number of viable collisions at the reaction site will increase as transport to the surface improves, increasing the overall reaction rate despite a decrease in the proportion of successful collisions.

Typically, for a multi-step reaction the rate-controlling step is identified as the step with largest individual activation energy E_a . Thus, a “fast” chemical step ($E_a \ll 20\text{kJmol}^{-1}$) can be limited by a “slower” transport step ($E_a \sim 20\text{kJmol}^{-1}$). When this framework is applied to the currently studied system, however, a contradiction emerges. Moving from typical behaviour to the enhanced corrosion observed in this study, the slowest step (physical transport through a surface film) is removed and replaced with an even “slower” step, which may be “slowed” even further by agitation or stirring. This runs counter to the observation that the reaction rate is substantially increased and cannot be explained simply by an increase in the number of collisions. Assuming the activation energy of the chemical step remains approximately constant (given that it remains an interaction between Mg/MgO and water), a simplified representation of the process steps can be constructed as shown in Figure 4.15.

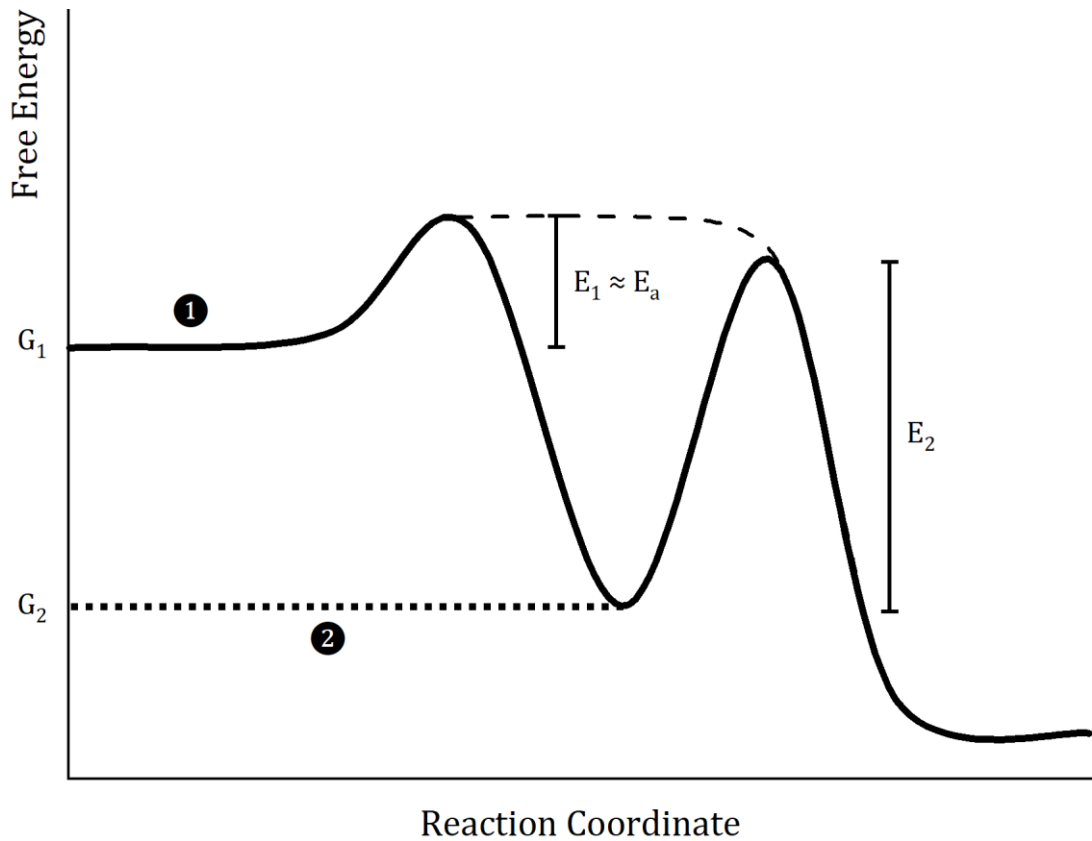


Figure 4.15 Graphical representation of a simplified multi-step process where the rate is controlled by a physical transport process (1), which when removed results in a chemically controlled reaction (2) that proceeds at a faster rate.

It is possible to construct a system of multiple reaction steps where the rate-controlling step does not have the largest individual activation energy. However, this requires that the initial free energy of the reactants plus the activation energy of the limiting step is greater than the sum of the intermediate free energy states and their corresponding activation energies as stated by the inequality described by Equation 4.6:

$$G_1 + E_{a1} \geq G_2 + E_{a2} \quad (4.6)$$

Where G_1 and G_2 are the free energy states of the reactants immediately preceding the reaction steps described by the activation energies E_1 and E_2 .

For this case, if the limiting step is removed (e.g., by removing a surface layer) then the new limiting step will be defined by the activation energy of the remaining step which is larger than that which preceded it. Furthermore, if the removal of the transport limit is continuous and progressive (e.g. for a mixed system where transport is controlled by a stagnant boundary layer) then this scheme can also describe the response of a system with mixed transport and chemical control to agitation, as the increase in transport will correspond to an

increase in the overall activation energy of the reaction, eventually reaching the “true” activation energy as the effect of transport is entirely removed.

For this to be true, however, there must be a corresponding change in the free energy of the reactants as the initial state of the system moves from G_1 to G_2 . Since the temperature, pressure and volume remain the same (no change in enthalpy), the negative change in free energy (Equation 4.7) can only be attributed to a change in entropy, specifically an increase in entropy:

$$\Delta G = \Delta H - T\Delta S \quad (4.7)$$

In physical terms this represents an increase in the availability of states close to the reaction site, corresponding to the absence of a physical barrier between the surface and the bulk fluid. Conversely, the higher initial energy required for the transport step represents the energy required to assemble the reactant molecules at the edge of the boundary layer where they are effectively stationary. From this starting point the molecules must then diffuse or otherwise overcome the energy barrier E_1 required to access the reaction site. Any molecule with the required free energy to cross the E_1 barrier will necessarily have enough energy to complete the reaction, thus the overall activation energy is defined by E_1 making it the rate-controlling step.

It can be concluded, therefore, that the change in activation energy observed for reactions of this type ultimately arises due to changes in the initial free energy of the reactants relative to the individual activation energies for each step, rather than by changes in the activation energies themselves. Given that similar behaviour has previously been observed for other heterogeneous reactions (e.g. dissolution of iron in acids (Abramson and King, 1939)) and even non-chemical processes such as heat transfer in pipe flows (Roller, 1935), it follows that the same principle must hold for all heterogeneous reactions where transport is a significant factor.

4.4 Conclusions

The results of this study provide kinetic data and scientific understanding for the purpose of underpinning enhanced corrosion and proving the concept as a viable treatment method for contaminated Magnox wastes. From the perspective of process development where the system of interest is Magnox/MgCl₂, the following conclusions are key:

1. Corrosion behaviour is radically different from that which is commonly observed in low saline/non-acidic solutions and is characterised by suppression of the partially protective magnesium hydroxide layer. This

allows direct contact to be made between the solution and the dissolving metal surface, promoting sustained, active, uniform corrosion that is not limited by the diffusion of reactants (i.e., water) to the surface.

2. The corrosion rate is $0.045 \pm 0.004 \text{ mmh}^{-1}$ in ambient conditions ($T = 20^\circ\text{C}$). Increasing the bulk solution temperature increases the corrosion rate to a maximum of $0.265 \pm 0.045 \text{ mmh}^{-1}$ at 50°C .
3. When the bulk solution temperature exceeds 50°C a partially protective film of aluminium oxide/hydroxides becomes stable on the surface, drastically reducing the reaction rate. While this places a hard limit on the rate of dissolution, it may also provide a negative feedback mechanism that prevents thermal runaway in large scale reactions.

Measurements of the activation energy were in agreement with previous work, demonstrating validity and increasing confidence in the results produced in comparable systems (Casey and Bergeron, 1953). Cross-comparison with measurements made in the systems Mg/MgCl₂, Mg/AlCl₃ and Magnox/AlCl₃ provided further detail and understanding of pH effects, as well as validation of results with respect to previous work.

Thermochemical modelling predicted that in all systems (with the notable exception of Magnox/MgCl₂ $< 50^\circ\text{C}$ as previously discussed) corrosion products would be soluble in the bulk solution. This was confirmed by visual inspection and by measurement of the activation energy which ruled out diffusion of water through a porous film as the rate-controlling step. This demonstrates that surface films on corroding magnesium form as a result of the precipitation of corrosion products due to pH effects, in agreement with previous researchers but novel for the case of filmless corrosion of Mg in acidic solutions (Fajardo et al., 2017; Esmaily et al., 2017).

The work carried out in this study to determine the kinetic parameters associated with the reaction of Mg and Magnox alloy in concentrated solutions of MgCl₂ and AlCl₃ has demonstrated that enhanced corrosion provides a viable method by which metals can be reliably and deterministically dissolved. Further work is required to acquire a detailed knowledge of the corrosion/dissolution reaction. This is essential as it determines the production of reactants for the curing reaction, which in turn determines the conversion efficiency and overall product quality, as well as the timescale required to complete the process. In addition, more work to determine the coupling between corrosion kinetics and cement curing will be required, along with definition of safety tolerances with respect to thermal runaway before scale-up can begin as a precursor to deployment.

5 Impedance Investigation of Magnesium and Magnox in Concentrated Salt Solutions

5.1 Introduction

By inference, from the activation energy for the dissolution of pure Mg and Magnox in acidic salt solutions (Section 4), it was concluded that the corrosion of these alloys was active, uniform and characterised by the suppression of the typical partially passivating surface film formed from the magnesium hydroxide corrosion product. From a chemical engineering perspective, this conclusion is useful as it provides information on the rate limiting step(s) and defines how the reaction rate responds to changes in temperature and fluid velocity (stirring). However, these indirect measurements lack the level of detail required to develop a fundamental understanding of the corrosion of Mg in acidic solutions. This will be important in the development of Cementisation, as a more detailed understanding of Mg corrosion as the critical step will enable effective optimisation of the process parameters. To directly examine the solid-liquid interface during the filmless corrosion of Mg and Magnox, a series of experiments were performed using Electrochemical Impedance Spectroscopy (EIS).

By fitting impedance data to a circuit model (previously validated for NaCl systems by King), the alteration of features related to charge transfer, surface film formation and the action of adsorbed intermediates can be examined as a function of salt concentration (King et al., 2014). In addition, the effect of solubility as the salt content approaches saturation was evaluated by comparison to AlCl_3 solutions with and without the addition of Mg ions up to the solubility limit. Finally, in 4M MgCl_2 (previously identified as producing optimal dissolution (Casey and Bergeron, 1953)), the impedance response was measured under anodic and cathodic bias to investigate the relationship between the coupled interfacial half reactions. The implications of these results are discussed both in the context of optimising the Cementisation process and with respect to the ongoing debate concerning the fundamental dissolution mechanism of Mg in aqueous systems.

5.2 Theory

5.2.1 Reaction Framework

Despite extensive discussion and debate, there remains no consensus on the exact mechanism by which magnesium oxidises and dissolves during corrosion

(Frankel et al., 2015; Esmaily et al., 2017; J. Huang et al., 2020). In an attempt to address the breadth of current theories, the observations made in this study were examined in the context of works representing the current state of the art within the two major groups of thought, namely the univalent Mg^+ and enhanced cathodic activity theories. The reaction scheme presented by Baril and later developed by Gomes was selected as representative of the univalent interpretation (Baril et al., 2007; Gomes et al., 2019; J. Huang et al., 2020).

An alternative theory concerning the corrosion mechanism of Mg has been presented by Yuwono as a development of an *ab initio* model introduced by Taylor (Taylor, 2016; Yuwono, Taylor, et al., 2019). This interpretation can be considered a state of the art representation of the group of theories that invoke enhanced cathodic activity as the root cause of the anodic hydrogen evolution observed for Mg electrodes (J. Huang et al., 2020). Under this model the dissolution reaction is facilitated by two distinct adsorbed intermediates, Mg^*H and Mg^*OH , that are formed as a result of the water splitting reaction. Mg^*H can be formed by the reduction of H^+ species onto the surface, or alternatively by the two-electron dissolution of Mg from an active site (labelled Mg^*). Mg^*OH , on the other hand, can be formed by the oxidation of OH^- or by a similar dissolution reaction. Once formed, Mg^*H can be desorbed by reduction (i.e., typical cathodic hydrogen evolution) or by oxidation via a Heyrovsky pathway (requiring an additional H^+ ion), leading to the dissolution of Mg ions with concurrent hydrogen evolution. This latter reaction is presented as the source of anodic hydrogen evolution as its rate increases with increasing anodic bias. Conversely, Mg^*OH can only be removed from the surface by oxidation and crucially does not require additional OH^- to do so.

Yuwono used DFT modelling to demonstrate the viability of this reaction scheme and reconstruct many the typical phenomena observed in aqueous corrosion of Mg and contextualise the reaction scheme with respect to the various proposed reaction mechanisms (Yuwono, Birbilis, et al., 2019). One of the key findings of this work was that the Mg^*OH intermediate was only stable under anodic conditions, while Mg^*H was found to be stable on the surface under both anodic and cathodic bias. In a separate study, King used impedance measurements to validate a circuit model description of Mg dissolution (the same model used in this work as shown in Figure 5.2). Models of this type with two capacitive and one inductive loop are common in studies of magnesium corrosion impedance and can thus be considered representative of the current state of the art (Feliu, 2020).

In discussion, King concluded that the dissolution of Mg must be facilitated by two separate intermediates but did not speculate as to their precise nature (King et al., 2014). Furthermore, from impedance spectra measured under anodic and cathodic bias, King concluded that one of the intermediates must be eliminated from the surface under cathodic polarisation, as the inductive component of the impedance was suppressed. Thus, by combining the observations of these two researchers it can be inferred that the inductive response is created by the action of the Mg^*OH intermediate, while the capacitive response arises from the coverage of Mg^*H .

As a result of this inference between the works of King and Yuwono, it is possible to construct a full mechanistic description of magnesium corrosion in terms of its impedance response, as presented in Figure 5.1.

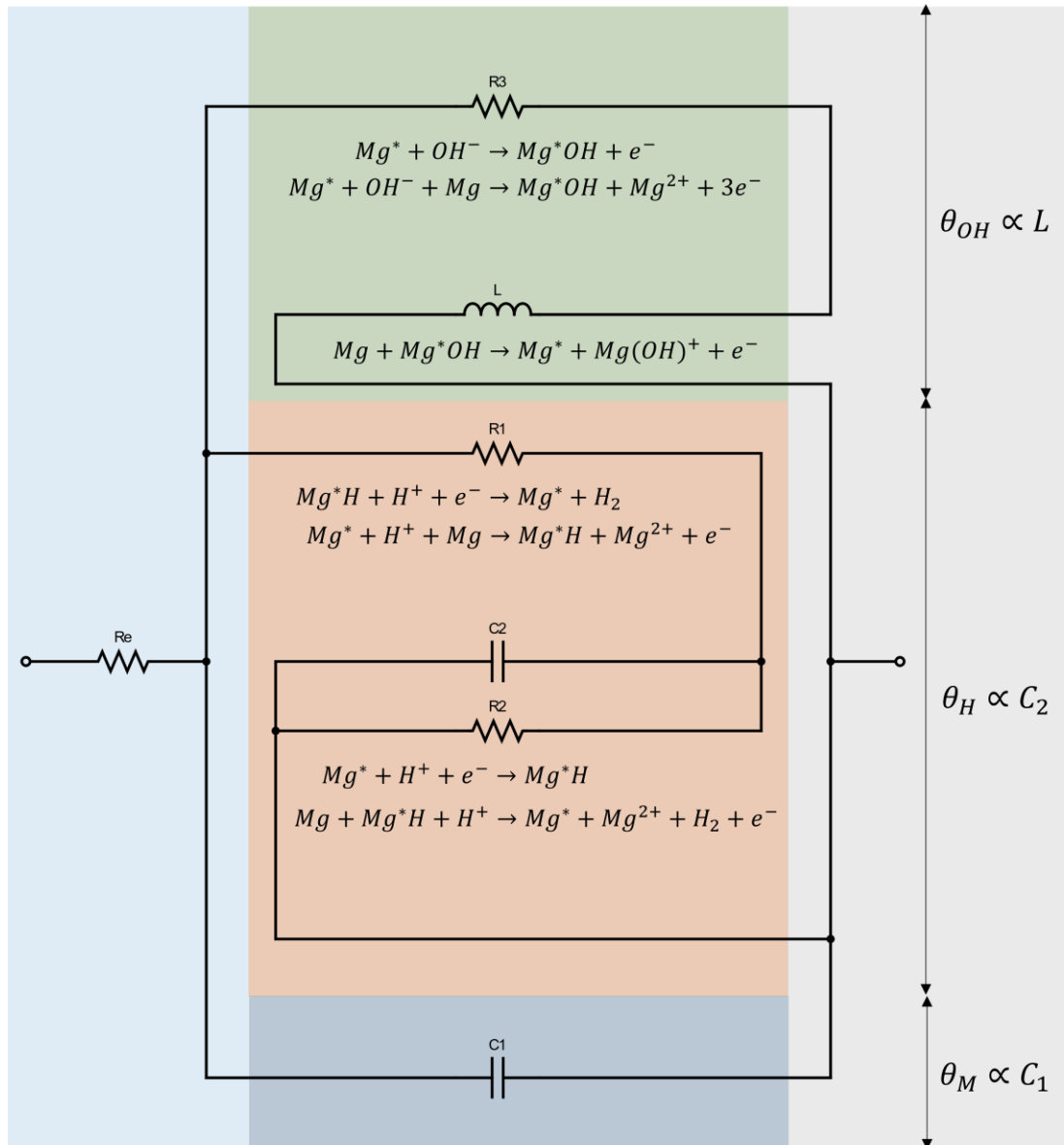


Figure 5.1 Diagrammatic representation of the dissolution of Mg by the action of the adsorbed intermediates Mg*OH (green), Mg*H (orange) in parallel with an electrical double layer (dark blue). The circuit diagram used to model impedance spectra is overlaid with the individual reactions corresponding to each charge transfer step. The surface coverages θ_{OH} , θ_H , θ_M are shown along with their relationship to the circuit parameters L , C_2 and C_1 . The solution resistance is represented by the resistor R_e .

5.3 Impedance Models

To investigate the behaviour of the metal/solution interface, impedance response data were fitted, where possible, to two different models. The first was a circuit model functionally identical to that previously used by a number of researchers for the case of Mg corrosion, labelled in this instance according to the interpretation of King et. al. (King et al., 2014).

As shown in Figure 5.2, the liquid-solid interface between the reference electrode (R.E.) and working electrode (W.E.) is represented by a solution resistance (R_e), an inductive loop (R_3, L), and two capacitive loops at high (R_1, C_2) and intermediate (R_2, C_1) frequency. This is consistent with the generalised impedance models presented by Scully for a corrosion mechanism involving two intermediates, one inhibiting and one enhancing the reaction rate (Scully, 2000).

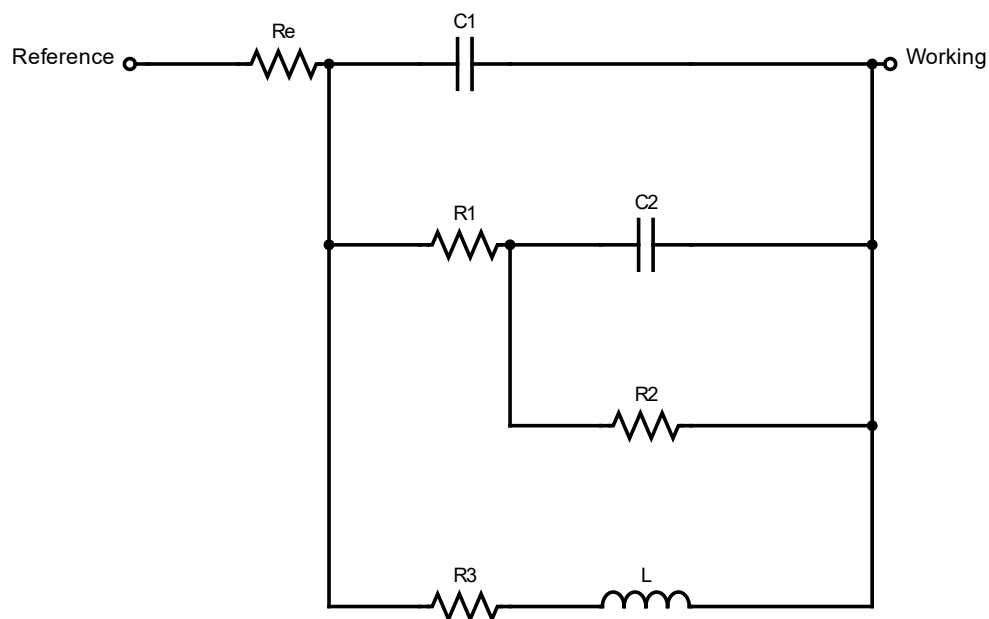


Figure 5.2 Circuit model used to model the impedance response of corroding magnesium alloys, describing a charge-transfer process involving one capacitive (C_2/R_2) and one inductive (R_3/L) intermediate.

Fitting was performed in Echem Analyst using the native simplex algorithm with unit weighting. Impedance values were area-normalised after fitting. To aid the understanding and interpretation of impedance data fitted to this model, a simulated impedance response was generated as shown in Figure 5.3.

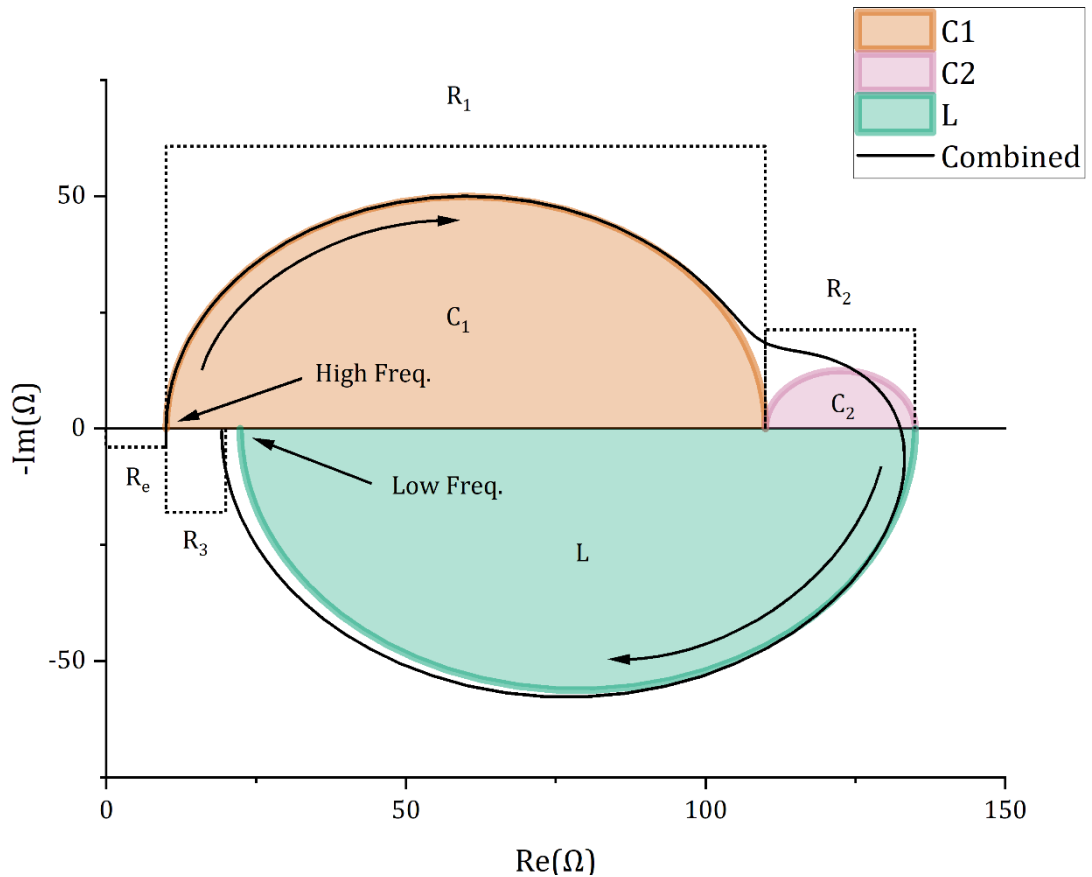


Figure 5.3 Simulated Nyquist plot showing the impedance response of the circuit model used in this work. The impedance was calculated over the frequency range 300kHz-1mHz according to the following parameters: $R_e=10\Omega$, $R_1=100\Omega$, $C_1=10\mu\text{F}$, $R_2=25\Omega$, $C_2=1\text{mF}$, $R_3=10\Omega$, $L=100\text{H}$.

A breakdown of the three process loops generally observed in the impedance response of dissolving Mg is included to show their individual contribution to the combined impedance. The simulated impedance response demonstrates how plots in the Nyquist format respond linearly to changes in the charge transfer resistances R_1 , R_2 and R_3 . The capacitances C_1 and C_2 , along with the inductance L , likewise define the peak phase response for each process loop. For the comparison of different corrosion systems, the Nyquist format is used in this work as the complex impedance can be represented as a single plot, rather than two separate plots as used in the Bode format.

The circuit model used in this study represents a set of reactions with three time constants: two capacitive and one inductive. This model enables key parameters of the system to be determined, including the charge-transfer resistance (R_t) and the polarization resistance (R_p). The latter can be used to estimate the corrosion rate via the Stern-Geary Equation (Equation 5.1) and is derived from the model using Equation 5.2 (King et al., 2014).

$$i_0 = \frac{b_a b_c}{2.3 R_p (b_a + b_c)} \quad (5.1)$$

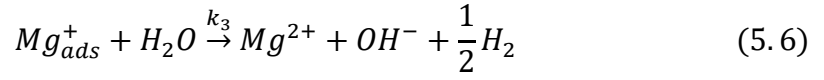
Where i_0 is the corrosion current, b_a is the anodic Tafel coefficient and b_c is the cathodic Tafel coefficient.

$$\frac{1}{R_p} = \frac{1}{R_1 + R_2} + \frac{1}{R_3} \quad (5.2)$$

With reference to the diagram in Figure 5.1, some of the features of the impedance behaviour can be explained in terms of their corresponding reaction steps. For Mg^*H , the adsorption and desorption steps are represented by the resistances R_1 and R_2 , depending on whether the reaction is reducing or oxidising in nature (Murray et al., 1988). Furthermore, the Mg^*H pathway produces a capacitive impedance response as the rate of the desorption reaction is always less than or equal to that of the adsorption reaction (Orazem and Tribollet, 2008b). The formation/adsorption of the Mg^*OH species is represented by the resistance R_3 . As previously noted, the desorption of Mg^*OH does not require interaction with the liquid phase and as such is essentially instantaneous. This can be considered in terms of an additional series resistance R_4 , the value of which is effectively zero and can therefore be neglected. Since the destruction/desorption of Mg^*OH is much faster than its creation/adsorption, the Mg^*OH pathway exhibits an inductive impedance response (Orazem and Tribollet, 2008b). The surface coverage of the Mg^*H and Mg^*OH intermediates are proportional to their respective capacitance and inductance, C_2 and L (Murray et al., 1988; Orazem and Tribollet, 2008b). Similarly, the double layer capacitance C_1 is proportional to the availability of active Mg^* sites (Yuwono, Taylor, et al., 2019). Using this model, it is possible to explain the observations made in this work as well as the general corrosion behaviour of Mg by relating impedance behaviour to the reaction scheme proposed by Yuwono.

The second model used was a kinetic model. This model was developed to evaluate the corrosion behaviour of Mg directly, as a function of frequency relating to a reaction scheme, including the transfer, adsorption, and diffusion of charge carriers (Baril et al., 2007; Orazem and Tribollet, 2008b). This model is built on the incomplete film univalent Mg^+ ion mechanism proposed by Baril et al. and subsequently developed by Gomes et al. (Baril et al., 2007; Orazem and Tribollet, 2008b; Gomes et al., 2019). This mechanism assumes that the oxidation of magnesium proceeds via the following reaction scheme:





Where k_1 , k_2 , k_{22} and k_3 are reaction constants expressed in mols^{-1} . The rate constants for Equations 5.3, 5.4 and 5.5 vary with potential (V) according to Equation 5.7, while the reaction described by Equation 5.6 describes the anodic hydrogen evolution observed for corroding Mg systems. The contribution of this reaction can be removed by setting k_3 to zero (Orazem and Tribollet, 2008b), but this was not found to make a substantial difference to the quality of fitting and thus this reaction was retained for the purpose of this work.

$$K_i = k_i e^{[b_i(V-V^0)]} \quad (5.7)$$

Where i is an index number, b_i is the activation coefficient expressed in V^{-1} and V^0 is a baseline potential. The adsorbed species are assumed to behave according to a Langmuir isotherm and the transport of Mg^{2+} ions is governed by diffusion through a surface layer. For a full derivation the reader is referred to the works of Baril (Baril et al., 2007) and Gomes (Gomes et al., 2019). As the focus of this work is the response at intermediate and low frequencies, the developments of Gomes are neglected in favour of the simple high-frequency capacitance used by Baril. This also ensures that the model is natively compatible with the immfit fitting routine by avoiding the need to repeatedly solve the definite integral term.

The total impedance of the system is described by the faradaic impedance Z_F defined by Equation 5.8 in parallel with the double layer capacitance C_f as shown in Equation 5.9.

$$Z_F = \frac{1}{\sigma F} \left[R_t + R_t K_{22} N(\omega) - \frac{R_t [2r_1 K_{22} N(\omega) + (r_1 - r_2)] (K_2 \beta - K_1)}{(r_1 + r_2) \beta j \omega + K_1 + \beta (K_2 + k_3) + (r_1 - r_2) (K_2 \beta - K_1)} \right] \quad (5.8)$$

$$Z = R_e + \frac{Z_F}{1 + j\omega Z_F C_f} \quad (5.9)$$

Where σ is the sample area in cm^2 , F is the Faraday constant (96485 Cmol^{-1}), R_e is the solution resistance in Ωcm^2 , C_f is the double layer capacitance in Fcm^{-2} , R_t is the charge transfer resistance according to Equation 5.10, $N(\omega)$ is a finite-length Warburg impedance as described by Equation 5.11, ω is the angular frequency, j is the imaginary unit, β is the surface coverage of the adsorbant

expressed in $\text{mol}^{-1}\text{cm}^{-2}$ and r_1 and r_2 correspond to the oxidation of metal and adsorbed intermediates according to Equations 5.12 and 5.13 respectively.

$$R_t = \frac{1}{r_1 + r_2} \quad (5.10)$$

$$N(\omega) = \frac{\tanh\left(\sqrt{\frac{j\omega\delta^2}{D_{Mg^{2+}}}}\right)}{\sqrt{j\omega D_{Mg^{2+}}}} \quad (5.11)$$

Where δ is the thickness of the diffusion layer in cm and $D_{Mg^{2+}}$ is the constant of diffusion for Mg^{2+} ions expressed in cm^2s^{-1} .

$$r_1 = (1 - \theta)K_1b_1 \quad (5.12)$$

$$r_2 = K_2b_2\beta\theta + K_{22}b_{22}C_{Mg^{2+}}^0 \quad (5.13)$$

Where θ is the steady state coverage of the adsorbant according to Equation 5.14 and $C_{Mg^{2+}}$ is the concentration of Mg^{2+} ions at the interface between the adsorbed and diffusion layers as defined by Equation 5.15.

$$\theta = \frac{K_1\left(\frac{D_{Mg^{2+}}}{\delta} + K_{22}\right)}{K_1\left(\frac{D_{Mg^{2+}}}{\delta} + K_{22}\right) + (K_2 + k_3)\frac{D_{Mg^{2+}}}{\delta}\beta} \quad (5.14)$$

$$C_{Mg^{2+}}^0 = \frac{\beta\theta(K_2 + k_3)}{\frac{D_{Mg^{2+}}}{\delta} + K_{22}} \quad (5.15)$$

5.4 Experimental

5.4.1 Sample Preparation

Samples with 5mm thick sections of 12.7mm diameter magnesium rod (Goodfellow MG007924, 99.9% purity as drawn) were mounted in epoxy resin (Stuers Epofix) with single-core copper wire (RS PRO 359-43) mounted into drilled holes (1.7mm diameter, ~2mm depth) in the rear face of the sample, a process adapted from Shi and Atrens (Shi and Atrens, 2011). Conductive epoxy (MG Chemicals 8331) was applied around the mounting point to ensure good electrical contact. Once sealed, electrical continuity was confirmed using a multimeter. Completed electrodes were screened for current leakage by blanking off the sample face with parafilm and attempting to measure the resistance of a conductive solution by the "Get R_u " routine contained in the Gamry Framework. Failure to establish solution resistance was considered proof of electrode integrity. Prior to experiments the sample face was ground to a 2000 grit finish using SiC papers as shown in Figure 5.4. Immediately before

and after immersion the surface was rinsed with isopropyl alcohol to remove contaminants and disperse adhered water.

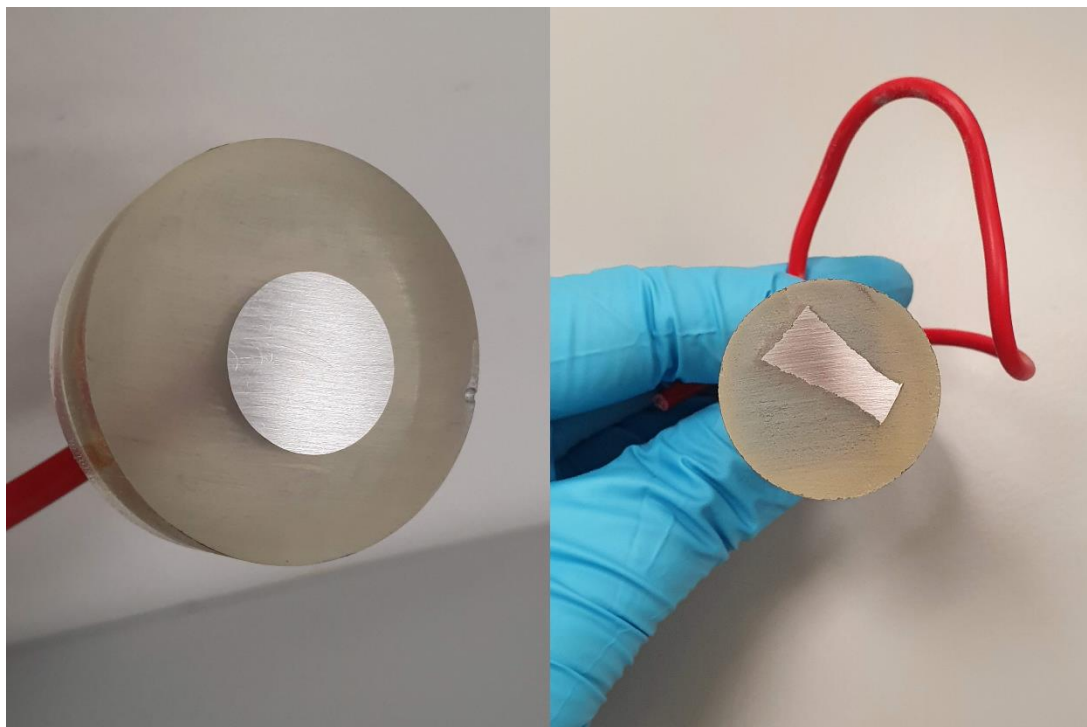


Figure 5.4 Photographs of freshly prepared working electrodes for pure Mg (left) and Magnox alloy (right).

5.4.2 Methods

Electrochemical measurements were performed on static electrodes in quiescent solution at ambient conditions ($T \approx 20^\circ\text{C}$). A platinum grid with large surface area relative to the working electrode was used as the counter electrode and the potential was measured with respect to a $\text{Ag}/\text{AgCl}/\text{Cl}^-$ (3M) reference electrode (BASi MF-2052). Experiments were controlled by a Gamry 1010E potentiostat via the Gamry Framework software, while Echem Analyst was used to analyse and export the acquired data. A diagram of the experimental setup is shown in **Figure 5.5**.

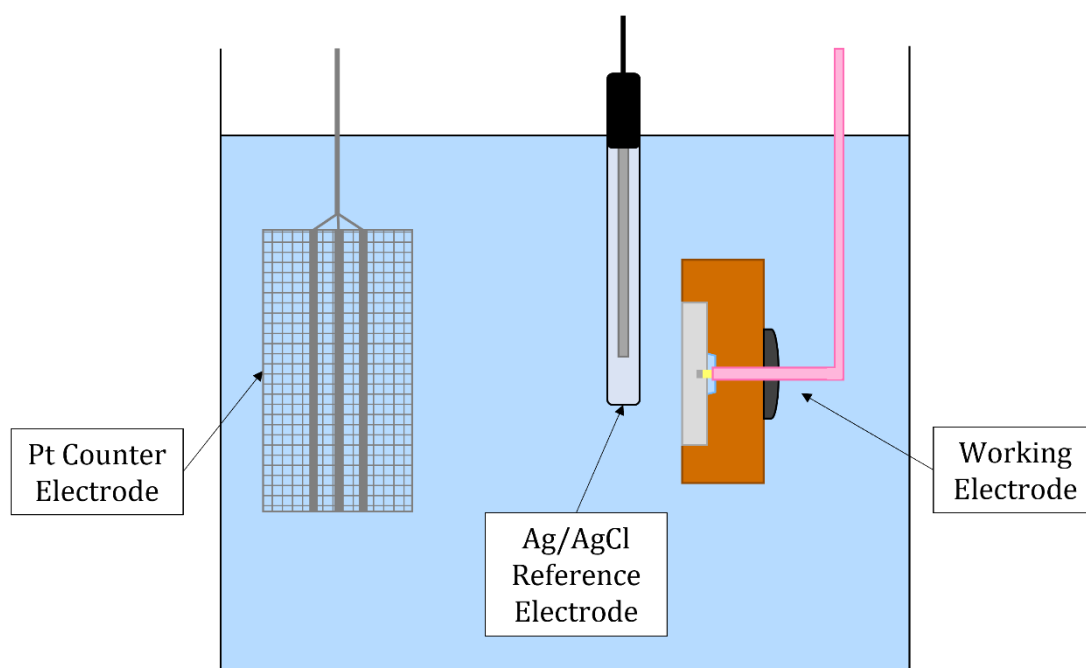


Figure 5.5 Diagram of the three-electrode cell used to perform EIS measurements.

Solutions of NaCl (Fisher Chemical S/3161/65), MgCl₂ (Bioserv BS-382K, Assay 99-101%), CaCl₂ (Bioserv BS-9858K, Assay 99-106%) and AlCl₃ (Acros Organics 217470025, 99%) were made up by weight using Type II deionised water. Solutions saturated with respect to MgCl₂ were made up by dissolving salt into boiled deionised water at a concentration of 6.3M per litre. Following mixing (48h, orbital shaker), the solution was decanted to remove excess salt. To reflect the uncertainty in concentration of these solutions with respect to the expected solubility limit for MgCl₂ (Pannach et al., 2017), their concentration is hereafter quoted as “Saturated” and approximated as ~6M where necessary. Solution properties were calculated using the SPECE8 software package contained in Geochemists Work Bench (GWB). The solubility limit for Mg²⁺ was calculated and magnesium oxide powder (SLS CHE2448, light burned, >98% pure) was added to solutions accordingly to equilibrate ion content in the system.

Electrochemical Impedance Spectroscopy (EIS) measurements were performed in either potentiostatic and galvanostatic modes with perturbation signals of 10mV and 100μA r.m.s. respectively. Linearity was checked by varying the signal amplitude and repeat measurements were performed where practical. The requirements for linearity, stability and causality were checked by monitoring Lissajous diagrams generated during measurements and by performing Kramers-Kronig transforms on the measured spectra.

Linear Sweep Voltammetry (LSV) measurements were performed to obtain Tafel plots in potentiodynamic mode. Scans were performed from negative to positive bias over various potential ranges with scan rates of $1\text{-}5\text{mVs}^{-1}$ and were not corrected for ohmic drop/solution resistance.

Post-immersion Scanning Electron Microscopy (SEM) and Energy Dispersive X-ray (EDX) analyses were performed using a Carl Zeiss EVO MA15 at the Leeds Electron Microscopy and Spectroscopy Centre (LEMAS).

Thermochemical calculation of solution parameters was performed using the SPECE8 program contained in Geochemist's Workbench (GWB). The included Yucca Mountain Project database (thermo_ympr.R2.tdat) was used to provide thermodynamic data as it contains entries for aluminium species and utilises the Harvie-Møller-Weare method for calculating activity coefficients at high concentrations (Jove-Colon et al., 2007).

5.4.3 Data Fitting

Impedance measurements were exported to Maple 2019 for fitting via the immfit procedure (Harrington, 2019). immfit takes impedance measurements and an arbitrary complex function as input. It then generates an objective function in real and imaginary parts. This is then fitted to the data using the native NLPSolve solver in Maple 2019.

Fitting errors in immfit can be calculated by a linear method or, as in this work, by a more intensive Monte Carlo method. This method attempts to calculate the sensitivity of fit parameters by performing multiple fits (500 by default) with random noise added to the datapoints according to a gaussian distribution with standard deviation equal to the that of the residuals for the previous fit. Fitting was performed using the nonlinear simplex algorithm and weighting was calculated according to the magtheory procedure. This weights the objective function in inverse proportion to the magnitude of the fitted function at each frequency.

Tafel parameters were extracted from LSV data using the Tafel Fit method in Echem Analyst, which uses a Marquardt algorithm to perform a nonlinear fit to the Stern-Geary equation (Equation 5.1)(Gamry Instruments, n.d.). For the purposes of Tafel fitting, the data range was restricted to the continuous region around the corrosion potential E_{corr} , i.e., neglecting regions where passive behaviour was induced.

5.5 Results & Discussion

5.5.1 Validation

To validate the equipment and setup used in this study against previous work, the impedance response of commercially pure Mg in 0.6M NaCl was measured over the range 100kHz – 1mHz in galvanostatic mode (10 μ A rms current) following the stabilisation of open circuit potential (\sim 3 hours). To demonstrate satisfaction of the conditions for linearity, causality and stability in impedance experiments, the data was evaluated with respect to the Kramers-Kronig relations via Echem Analyst as shown in Figure 5.6.

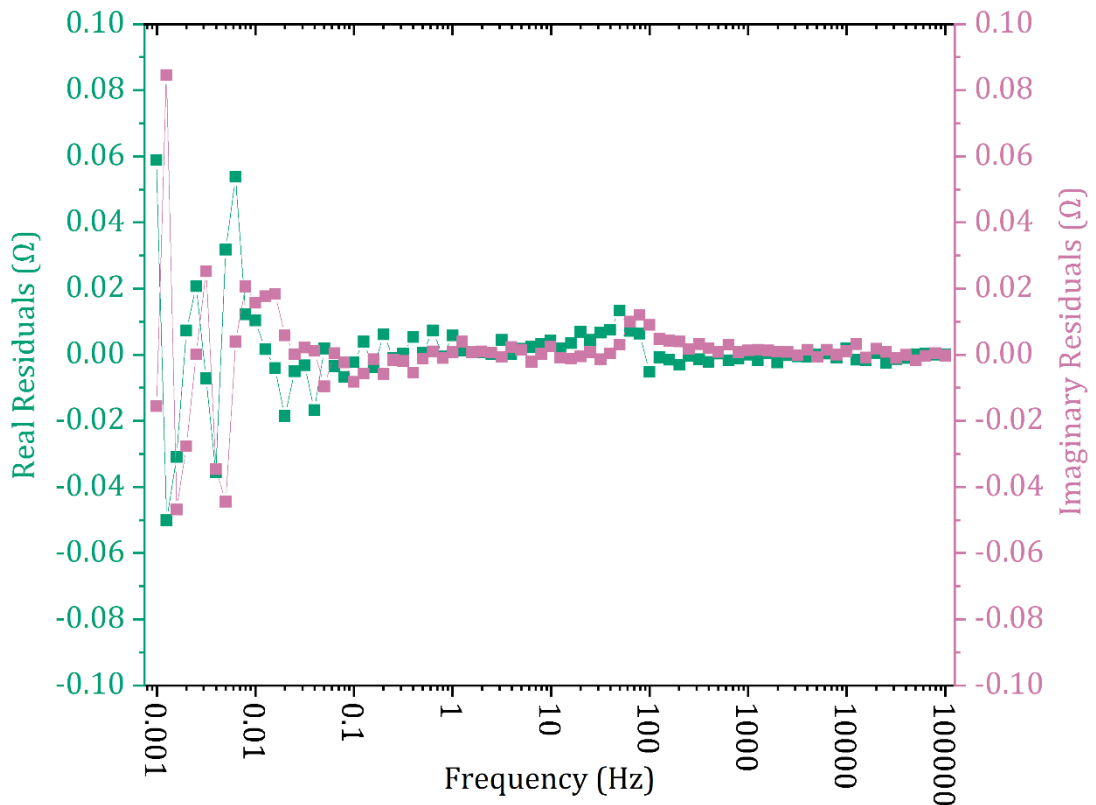


Figure 5.6 Plot of residuals from Kramers-Kronig fitting to impedance data for pure Mg corroding in 0.6M NaCl.

For this experiment, a chi-squared value (X^2) of 3.787×10^{-4} demonstrates that the data is satisfactory, however a significant increase in experimental noise is notable at frequencies < 10 mHz. This is to be expected for systems of this type where localised corrosion effects are dominant, as the OCP of the system will fluctuate significantly during low frequency measurements, violating the requirement for stability. During fitting, both models were found to be sensitive to local minima involving high frequency inductive loops. As this was deemed to be an artifact of the experimental setup, for fitting purposes the bandwidth was typically restricted to the range 1kHz-10mHz. Where fit lines are displayed

the full experimental dataset is shown for consistency. The data were fitted to both the circuit and kinetic models as shown in Figure 5.7.

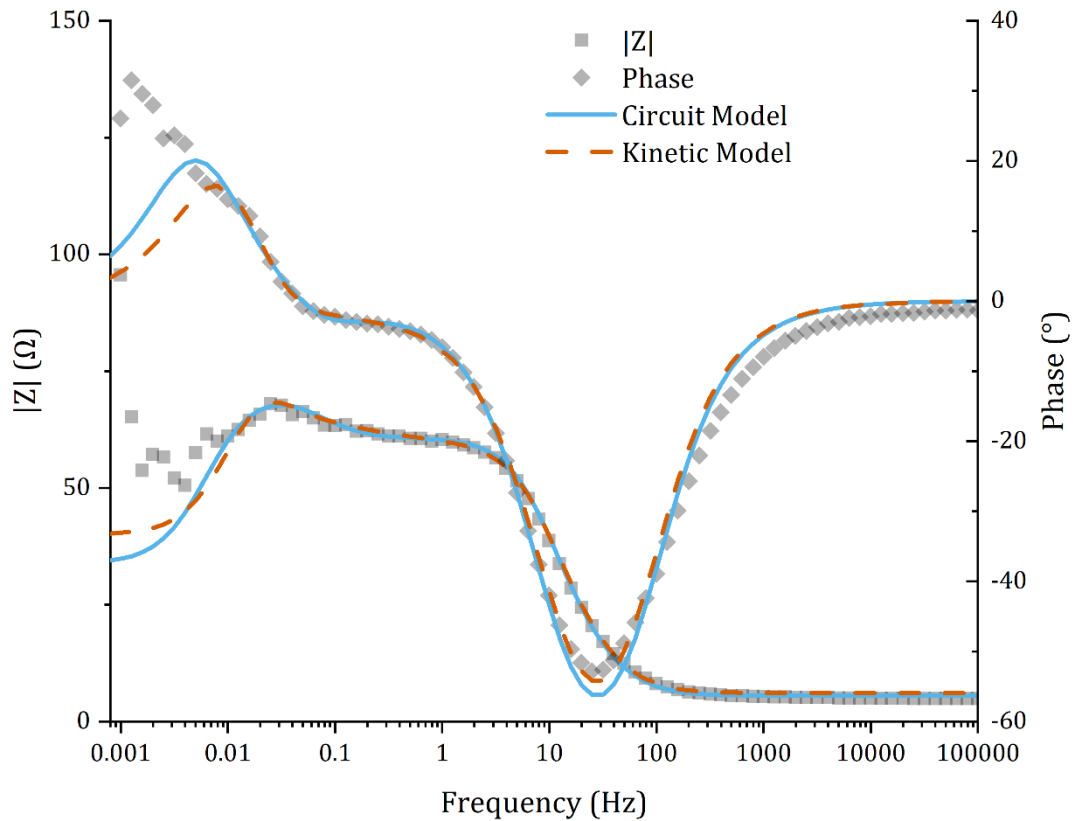


Figure 5.7 Bode plot showing impedance response of corroding pure Mg in 0.6M NaCl solution. The circuit (blue, solid) and kinetic (orange, dashed) models were fitted to the modulus (squares) and phase (diamonds) of the impedance data.

Both models were in good agreement with the data and with each other, showing only minor differences, most notably in the low frequency limit where the kinetic model predicted a slightly higher polarisation resistance and thus a lower corrosion susceptibility. The parameter values for the circuit model are shown in Table 5.1. The values determined by fitting were consistent with those measured by previous researchers for comparable systems (King et al., 2014; Curioni et al., 2015), with small fitting errors granting a high degree of confidence in the experimental setup and the validity of the circuit model. For comparison, the parameter solutions derived for the kinetic model are shown in Table 5.2.

The solution achieved by the kinetic model was generally good, with the Monte Carlo method able to provide reasonable error estimates for all parameters. Where errors exceeded the magnitude of parameters, i.e., for K_2 and k_3 , they remain comparable in size and thus provide a confident order-of-magnitude estimate of the true value. Good agreement was achieved where the models

coincide, i.e., for the high frequency capacitance (C_1/C_f). It must be noted that, without validation against an additional method it is difficult to justify the number of significant figures when quoting values for EIS fit parameters. In this case, the number of significant figures was chosen for comparison to the fitting errors, as a means of evaluating the goodness-of-fit.

Table 5.1 Area-normalised parameter values for the impedance response of pure Mg in 0.6M NaCl fitted to the circuit model.

Parameter	R_e [Ωcm^2]	R_1 [Ωcm^2]	C_1 [F cm^{-2}]	R_2 [Ωcm^2]	C_2 [F cm^{-2}]	R_3 [Ωcm^2]	L [H cm^2]	R_p [Ωcm^2]
Fitted Value	7.02	69.86	4.30×10^{-4}	12.06	0.312	63.74	3120	35.84
Fit Error	0.01	0.01	2.04×10^{-7}	0.04	0.001	0.38	10	0.43

Table 5.2 Table of parameters determined by fitting of the kinetic model to the impedance response of pure Mg in 0.6M NaCl. Where the size of the associated standard error exceeds the value of the parameter the error value is highlighted in orange.

Parameter	C_f [F cm^{-2}]	$D_{\text{Mg}^{2+}}$ [$\text{cm}^{-2}\text{s}^{-1}$]	K_1 [$\text{cm}^{-2}\text{s}^{-1}$]	K_2 [$\text{cm}^{-2}\text{s}^{-1}$]	K_{22} [$\text{cm}^{-2}\text{s}^{-1}$]	R_e [Ωcm^2]	b_1 [V $^{-1}$]	b_2 [V $^{-1}$]	b_{22} [V $^{-1}$]	β [mol cm^{-2}]	δ [cm]	k_3 [$\text{cm}^{-2}\text{s}^{-1}$]
Fitted Value	3.32×10^{-4}	1.99	1.63×10^{-8}	2.58×10^{-2}	1.51×10^{-1}	6.13	11.6	-6.68	8.05	16.3	5.25	1.94×10^{-2}
Fit Error	2.38×10^{-6}	5.32×10^{-1}	2.45×10^{-9}	5.10×10^{-2}	2.48×10^{-2}	6.51×10^{-2}	1.02	3.02	2.47	4.24	1.02	3.42×10^{-2}

However, within the fitted solution (see Table 5.2) there are several parameters that do not agree well with observations and are not physically sensible. Firstly, the values D_{Mg2} and δ are clearly non-physical, as they correspond to a situation where 2 moles ($\sim 50g$) of Mg^{2+} ions are moving through a 5cm thick diffusion layer every second. In addition, the activation coefficient b_2 has resolved with a negative value, implying that it is an anodic rather than a cathodic reaction, which is nonsensical within the model definition. Finally, the value of β corresponds to an adsorbed layer containing 16 moles ($\sim 400g$) of Mg ions, a figure many times greater than the entire content of the system and clearly not representative of any true value.

These effects result from the model having too many parameters to effectively specify the system, an issue highlighted in its formulation (Baril et al., 2007). With several parameters depending on each other (as opposed to being orthogonal), collinearity arises to the extent that making objective causal statements is not possible based on the parameter values in isolation. When solved by a simplex method, which favours parameter values approaching unity, coupled parameters such as D_{Mg2}/δ which have an inverse relationship will tend to adopt values close to 1 as seen in this case. Other parameters need to be scaled in order for their effects to be properly accounted for. β , for example, only has a significant effect on the impedance at very small values (of order 10^{-5} or lower). Thus, with several redundant parameters available, the algorithm will tend to neglect β resulting in a value around unity.

Steps can be taken to address these issues, including scaling as previously mentioned, or fixing parameter values such as R_e and D_{Mg2} to increase the degrees of freedom (Gomes et al., 2019). However, without a robust scaling method or prior knowledge of the parameters that the model is attempting to derive, it is impossible to adjust the model without introducing subjective bias. Nevertheless, useful information may yet be extracted from fit results, either where parameters have minimal dependence on each other (such as K_1 , evidenced by its significant deviation from unity), by relative changes between parameters or by combining parameters, for example D_{Mg2}/δ to estimate a diffusion velocity. For example, the value of K_1 in this study is substantially larger than that observed in the Na_2SO_4 solutions studied by Baril and Gomes, corroborating the observation that the corrosion rate is higher in NaCl.

5.5.2 Potentiodynamic Polarisation

To evaluate the anodic and cathodic processes sustained at high $MgCl_2$ concentrations, the system was examined by potentiodynamic polarisation at saturation with respect to $MgCl_2$ (Figure 5.8).

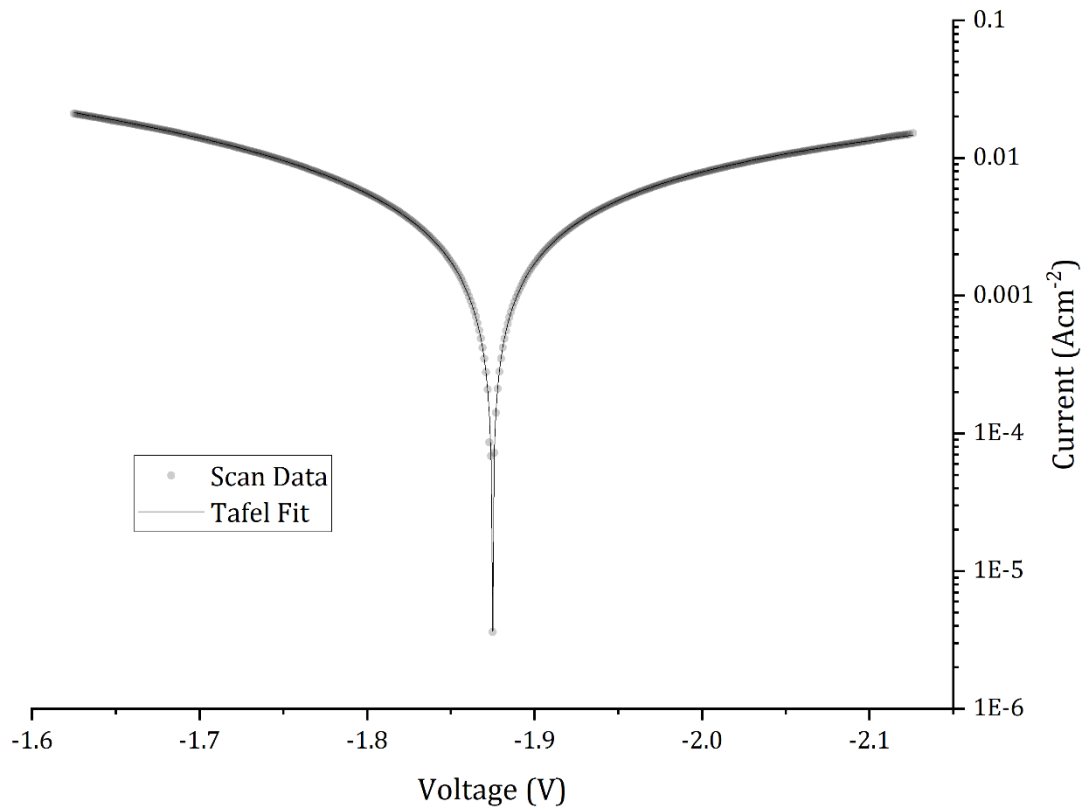


Figure 5.8 Plot showing potentiodynamic polarisation data for pure Mg in saturated MgCl₂ solution (scan rate = 1mVs⁻¹). Fit line corresponds to a Tafel fit where $\beta_a = 1116\text{mV/decade}$ and $\beta_c = 4261\text{mV/decade}$.

In saturated MgCl_2 solutions, magnesium exhibits a much greater degree of cathodic/anodic symmetry than typically observed for other aqueous salt solutions (King et al., 2014; Esmaily et al., 2017). This results from a substantial increase in the cathodic current density which is reminiscent of the enhanced cathodic activity observed by previous researchers following anodic dissolution (Birbilis et al., 2014). The Tafel constants obtained from fitting (see Section 5.4.3) are significantly higher than those measured by previous researchers and when combined with R_p via Equation 5.1 gives an estimated corrosion rate of 0.088mmh^{-1} , significantly lower than direct measurements made by previous researchers (Casey and Bergeron, 1953). Tafel constants are reported in mV/decade by convention as they are typically used to extrapolate the linear response at high overpotential to the corrosion potential to calculate the corrosion current.

These discrepancies may result from ohmic drop as the solution resistance is comparable to the polarisation resistance at these concentrations and thus cannot be neglected. As such, the polarisation measurements presented here cannot confidently be used to determine quantitative information, although qualitative relationships can still be identified. The corrosion rate is sufficiently high that direct measurement by mass loss or hydrogen evolution is straightforward and fast and is thus preferred to electrochemical estimation in this case.

The polarisation resistance R_p can be determined from the gradient of the current response close to the OCP as shown in Figure 5.9.

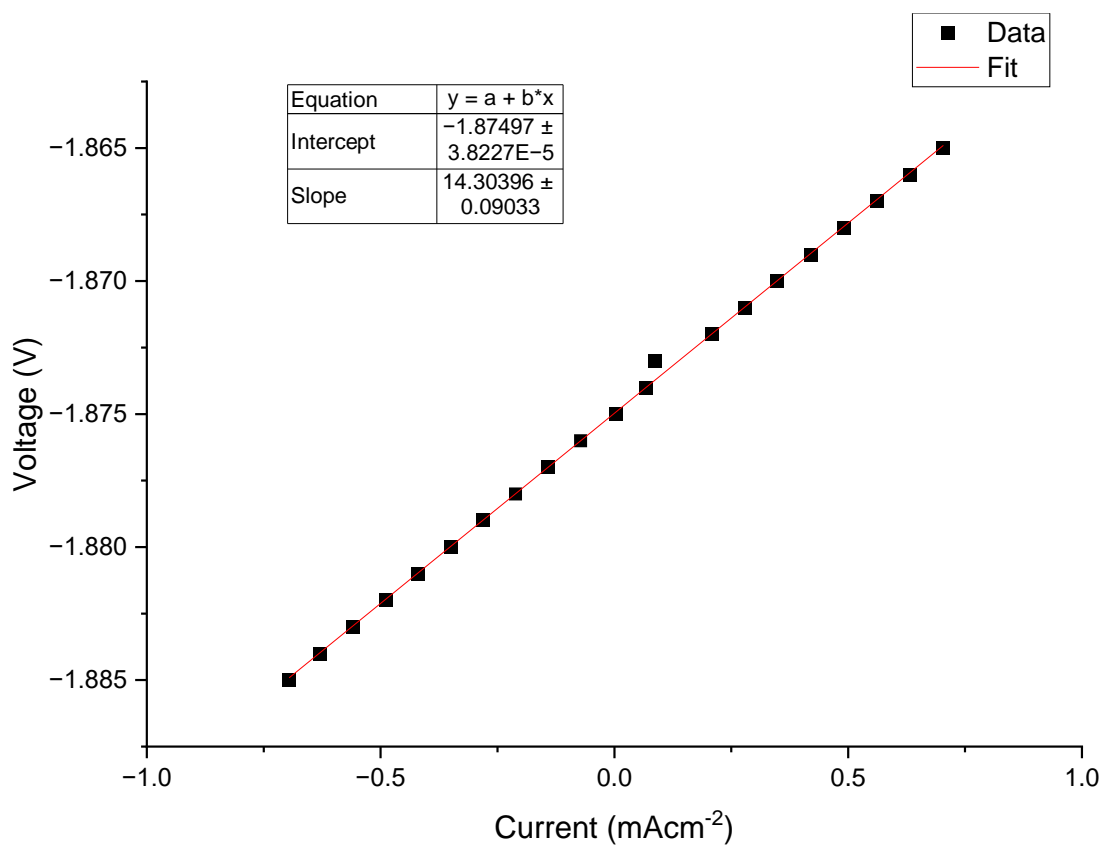


Figure 5.9 Plot of voltage against current close to the OCP (± 10 mV) during potentiodynamic polarisation of Mg in saturated MgCl₂ solution.

The response of pure Mg to potentiodynamic polarisation in 4M MgCl₂ is shown in Figure 5.10.

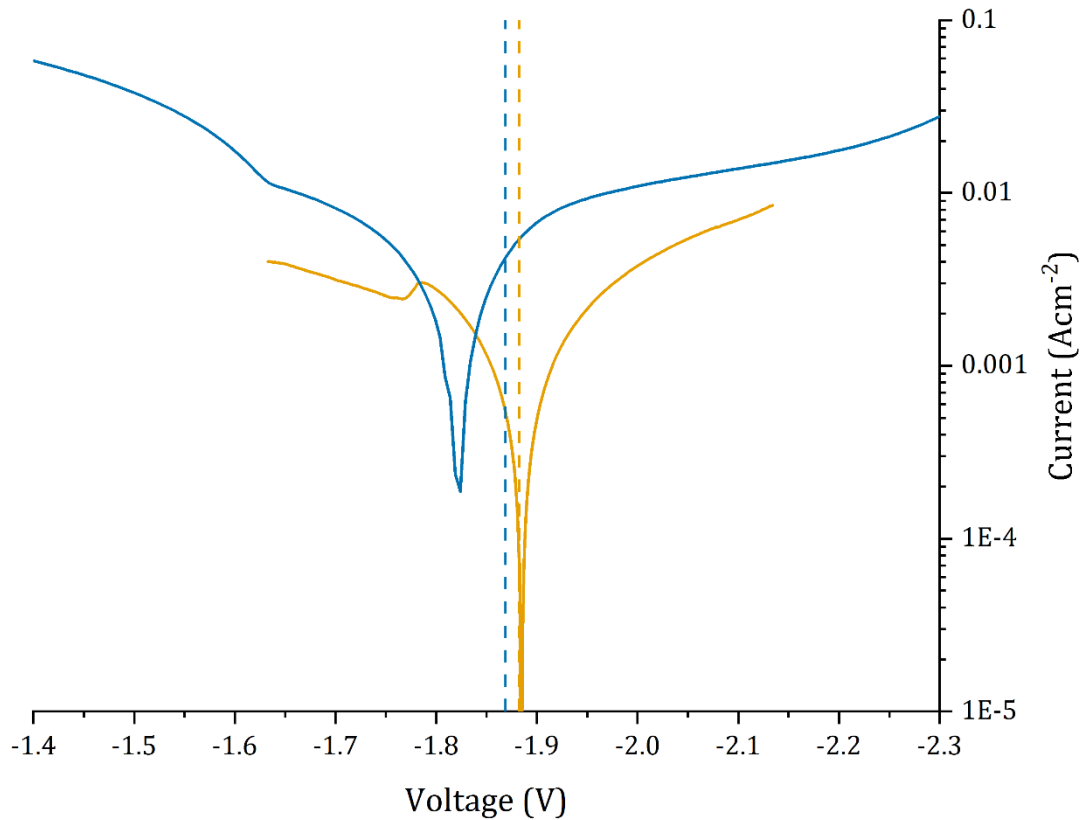


Figure 5.10 Potentiodynamic polarisation plots for pure Mg in 4M MgCl₂ over different voltage ranges (-250/+250mV at 1mVs⁻¹, yellow; -500/+1500mV at 5mVs⁻¹, blue). Dotted lines show the open circuit potential recorded prior to each corresponding voltage sweep.

The change in starting point from -500mV to -250mV is accompanied by a shift in the OCP consistent with a drop in the exchange current density for the magnesium oxidation reaction. This suggests that passivation of the surface is induced at a potential in the range -250/-500mV for the case of 4M MgCl₂, with visual observation confirming a dark grey film similar to the typical hydroxide layer present following polarisation. Similarly, a drop in the anodic current density at ~ -1.8 V implies a pseudo-passivation response can be induced despite the suppression of hydroxide precipitation in these conditions. Interestingly, the drop in anodic current density coincides with the cathodic-anodic transition in the passivated system, suggesting that the same process may be responsible for undermining the surface film and allowing faster oxidation of the metal. These effects do not precisely align between the two traces, although this may result from the difference in scan rate. The subsequent increase in the anodic response at ~ -1.65 V may correspond to the point at which the film induced by cathodic bias is removed, however without more detailed investigation (e.g., an independent anodic sweep starting from OCP) this is merely supposition.

The value of R_p for the $\pm 250\text{mV}$ polarisation was calculated as 30Ω by the same method used previously for voltammetry data (see Figure 5.9).

5.5.3 Post-Immersion Observations

Visual inspection of the samples following immersion in concentrated MgCl_2 shows no evidence of the typical corrosion film as shown in Figure 5.11.

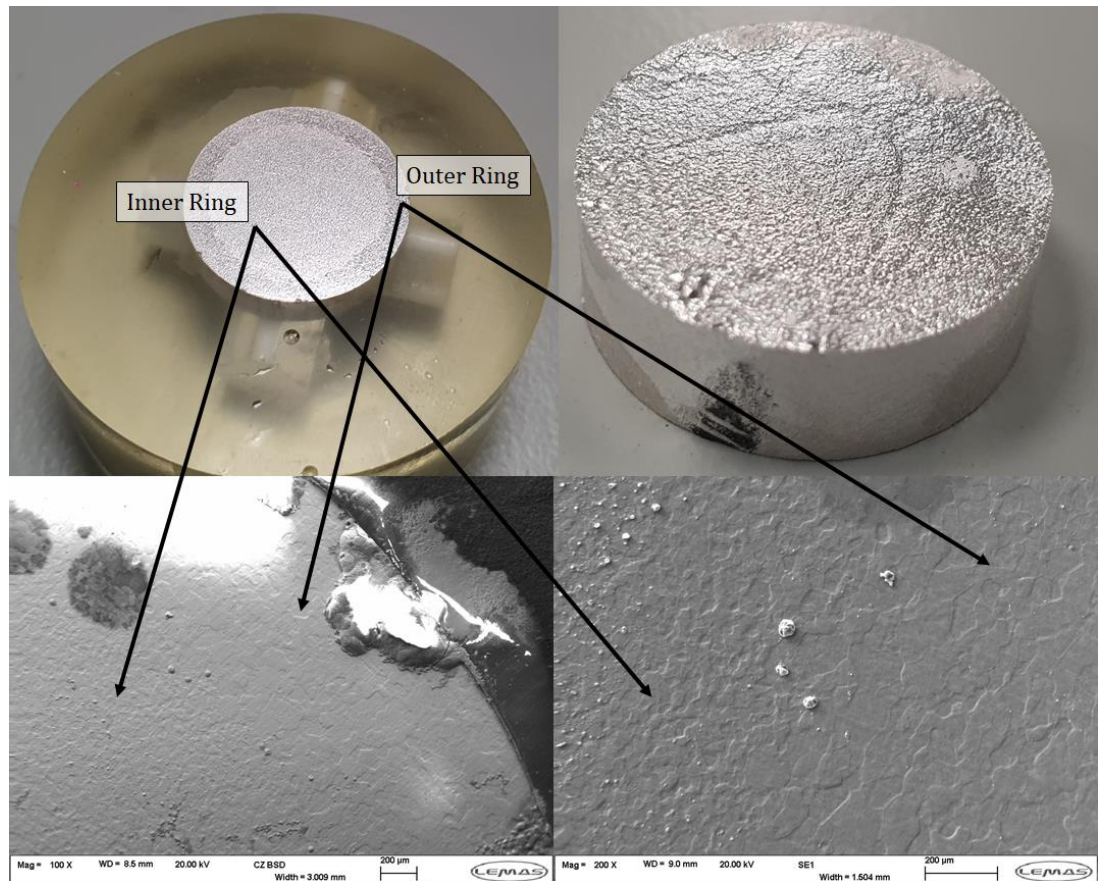


Figure 5.11 Photo/Micrographs of pure Mg samples post immersion in 4M MgCl_2 .

Samples of pure Mg prepared for use as electrodes showed a consistent circular etch pattern following immersion in 4M MgCl_2 . Tests on unmounted samples, meanwhile, did not exhibit the same behaviour, implying that the effect is related to the sample geometry rather than any underlying metallurgical factor.

In general, cathodic and anodic reactions take place at separate sites. However, while these sites are typically distributed on the microscale or otherwise obscured by corrosion products, when restricted to a single face anodic and cathodic sites may be visually distinct even when cleaned and dried. Inspection by SEM techniques shows that there is little to distinguish the two regions on the microscale, other than a relative increase in surface roughness/grain size for the inner region.

This apparent segregation of surface processes observed on two-dimensional Mg surfaces warrants further investigation that is beyond the scope of this work. For example, application of local electrochemical techniques, such as SVET, would be able to resolve whether the observed regions do in fact correspond to regions of cathodic/anodic activity. Furthermore, given that the corrosion mechanism of Mg is generally accepted to depend on the potential-dependent coverage of adsorbed species, a study of the relative size of these areas as a function of potential may be able to substantiate existing interpretations, such as that of Yuwono (Yuwono, Taylor, et al., 2019). An ex-situ cross-sectional investigation of these areas might also, for example, show distinct differences in the relative thickness of an MgO layer (i.e., liquid formed vs. air-formed), which would imply that it is indeed only partially present as assumed under the univalent theory.

5.5.4 Effect of MgCl₂ Concentration

5.5.4.1 Low Concentration

The impedance response of corroding magnesium varied substantially according to the concentration of MgCl₂ in solution. For clarity and comparison, therefore, the results have been plotted separately. The impedance response of magnesium corroding in 0.5 and 1M MgCl₂ is shown in Figure 5.12.

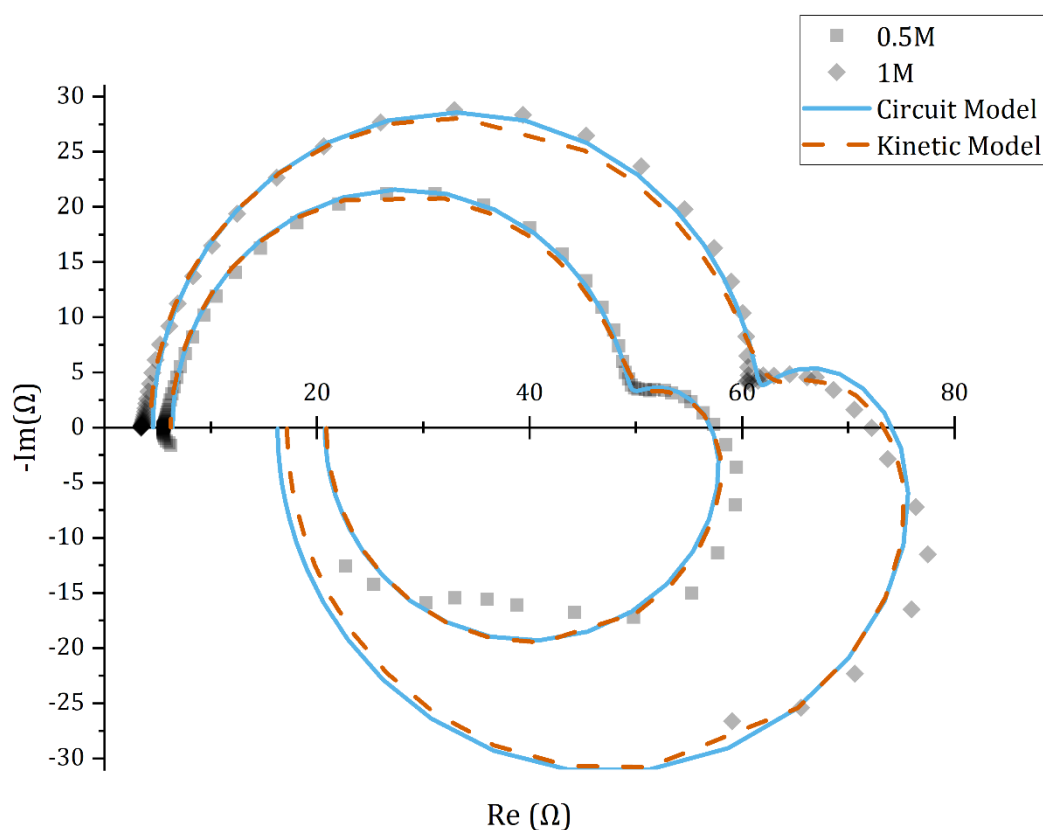


Figure 5.12 Nyquist plot of the impedance response for pure Mg corroding in 0.5 (squares) and 1M (diamonds) MgCl_2 solutions. Fit lines are shown for solutions of the circuit (blue, solid) and kinetic (orange, dashed) models.

At low concentrations of MgCl_2 ($<2\text{M}$), magnesium exhibits similar behaviour to that observed for other salts, e.g., NaCl (see Figure 5.7 for pure Mg in NaCl). Agreement between the circuit and kinetic models was likewise good, with both predicting similar values for the polarisation resistance at the low frequency limit. The charge transfer resistance increased with concentration (see Figure 5.12), implying a thicker surface layer was present, however the larger inductive response and decrease in polarisation resistance shows that the rate of corrosion was higher in 1M solution.

5.5.4.2 Intermediate/Threshold Concentration

The impedance response of magnesium corroding in 2M MgCl_2 is shown in Figure 5.13.

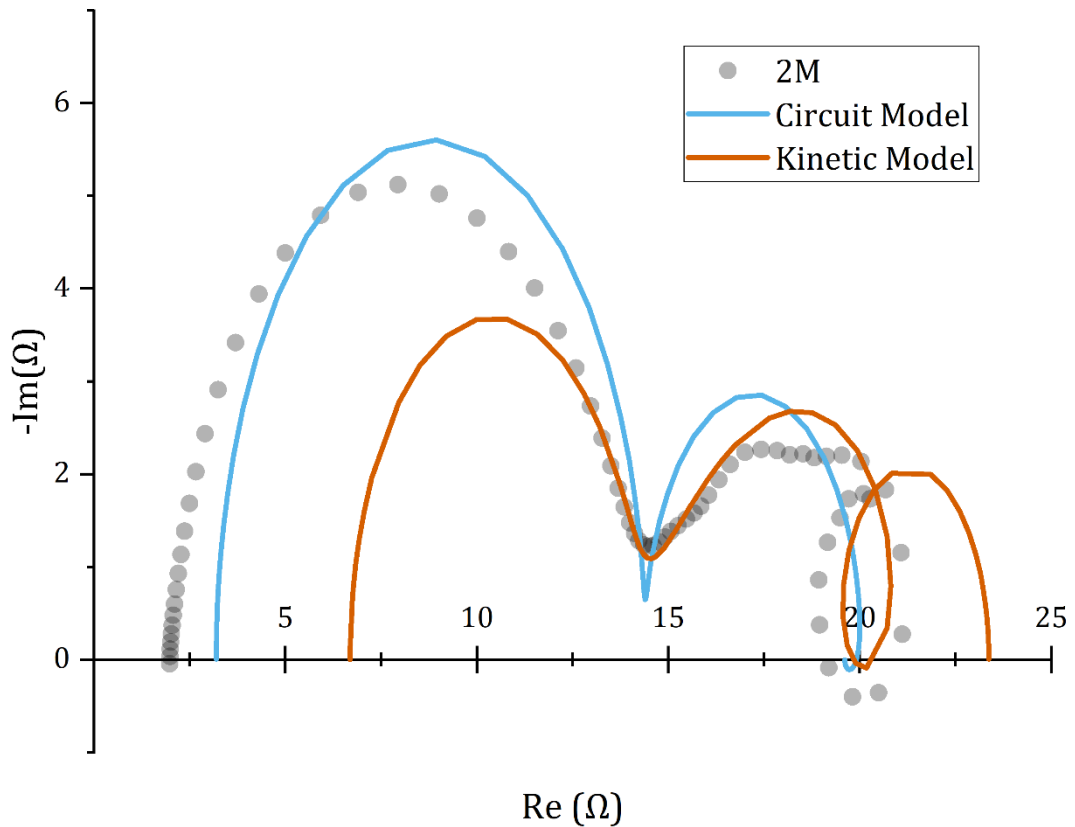


Figure 5.13 Nyquist plot of the impedance response for pure Mg corroding in 2M MgCl₂ solution. Fit lines are shown for solutions of the circuit (blue, solid) and kinetic (orange, solid) models.

At 2M concentration, the overall resistance of the system is considerably reduced indicating accelerated corrosion. At the same time, the mid-low frequency response has become more complex (Figure 5.13), with evidence of overlap between the capacitive and inductive processes in the frequency domain. This may be attributed to the stable corrosion product changing from brucite (Mg(OH)₂) to magnesium oxychloride complexes of the form [Mg_x(OH)_y(H₂O)_z]^{2x-y}, a transition which has been found to occur at 1.96M (Mažuranić et al., 1982; Dehua and Chuanmei, 1999).

Significant divergence was observed between the fits achieved by the circuit and kinetic models. The circuit model achieved a better fit to the high frequency capacitance but was unable to resolve the complex detail in the mid-low frequency range (which was well described by the kinetic model). Thus, it is expected that the polarisation resistance is more accurately predicted by the kinetic model and that the circuit model may therefore under predict the corrosion rate in this system, although no independent verification of this has been performed as part of this work. However, for the reasons previously stated it is unlikely that the kinetic model will be valid for establishing the

physical cause of this behaviour due to its susceptibility to overfitting, therefore any differences in predictions are unlikely to be significant.

5.5.4.3 High Concentration

The impedance response of pure Mg corroding in 4M and Saturated solutions of MgCl_2 is shown in Figure 5.14.

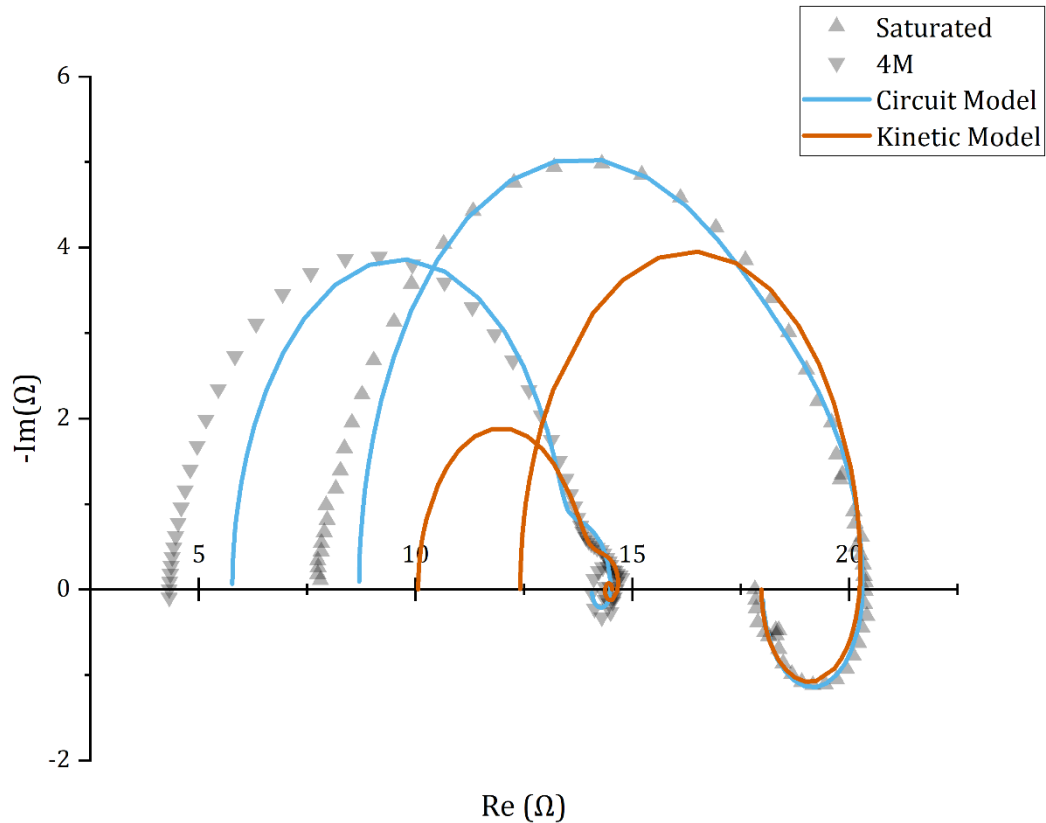


Figure 5.14 Nyquist plot of the impedance response for pure Mg corroding in Saturated (triangles) and 4M (inverted triangles) MgCl_2 solutions. Fit lines are shown for solutions of the circuit (blue, solid) and kinetic (orange, solid) models.

Despite an extremely high rate of corrosion, accompanied by vigorous hydrogen evolution, the impedance response in concentrated MgCl_2 is remarkably stable and reproducible.

At high concentrations, the overall resistance of the system to corrosion is further reduced and the polarisation resistance in the low frequency limit is approximately equal under both 4M and saturated conditions. However, while the previously observed (with 2M MgCl_2) capacitive/inductive overlap is evident in 4M solution, it is notably absent under saturated conditions. Instead, the relative contribution of the inductive component is increased and overlap now appears to exist between the two capacitive processes.

Once again, the two models differ in their solution to the impedance data. The circuit model continues to better reproduce the high frequency capacitance and, for the case of saturated MgCl_2 , results in a better fit to the intermediate and low frequency features as well. Nevertheless, the kinetic model better recreates the looping behaviour observed in the mid-low frequency response in 4M solution. This may be an indicator for higher-order surface processes, requiring the additional variables contained in the kinetic model, or it may simply result from a violation of the stability requirement for EIS (as the system has become highly polarisable), such that the small perturbation assumption may no longer be valid. The parameter values and associated standard errors determined by fitting impedance data to the circuit and kinetic models are listed in Table 5.3 and Table 5.4 respectively.

Table 5.3 Area-normalised parameter values for pure Mg in MgCl₂ solutions determined by fitting to the circuit model with associated standard error.

	R_e [Ωcm ²]	R₁ [Ω cm ²]	C₁ [F cm ⁻²]	R₂ [Ω cm ²]	C₂ [F cm ⁻²]	R₃ [Ω cm ²]	L [H cm ²]
0.5M	8.13 ± 0.15	54.68 ± 0.53	4.82x10 ⁻⁴ ± 7x10 ⁻⁶	13.18 ± 1.19	2.35x10 ⁻¹ ± 3.58x10 ⁻²	24.77 ± 1.47	1864 ± 60
1M	5.79 ± 0.02	72.37 ± 0.02	2.80x10 ⁻⁴ ± 2x10 ⁻⁷	22.72 ± 0.03	1.83x10 ⁻¹ ± 3.17x10 ⁻⁴	17.60 ± 0.18	2415 ± 2
2M	4.05 ± 0.02	14.2 ± 0.02	2.77x10 ⁻⁵ ± 1x10 ⁻⁷	7.20 ± 0.02	3.32x10 ⁻² ± 1.66x10 ⁻⁴	733.09 ± 99.36	3603 ± 364
4M	7.31 ± 0.04	9.79 ± 0.04	3.11x10 ⁻⁵ ± 3x10 ⁻⁷	1.27 ± 0.02	8.49x10 ⁻³ ± 2.90x10 ⁻⁴	211.34 ± 16.74	318 ± 24
Sat.	11.02 ± 0.04	12.7 ± 0.03	2.16x10 ⁻⁵ ± 2x10 ⁻⁷	2.04 ± 0.04	7.48x10 ⁻⁴ ± 2.90x10 ⁻⁵	59.14 ± 0.49	15 ± 0.2

In 4M MgCl₂ under open circuit conditions, the contributions of the Mg*H capacitance and Mg*OH inductance are minimised. The Mg*H dissolution pathway is favoured as the sum of the resistances R₁ and R₂ is less than the inductive resistance R₃. As the typical hydroxide film is not stable in the acidic salt solution, the solution in contact with the surface contains abundant H⁺ that can easily access the reaction interface. Thus, in acidic solutions, the rate of dissolution by Mg*H is high and the OH⁻ assisted dissolution mechanism is not required (Yuwono, Taylor, et al., 2019).

As the concentration of MgCl₂ approaches saturation, the dissolution of Mg via Mg*H remains favoured, but both the adsorption and desorption resistances increase. Interestingly, the quantities C₁, C₂ and L are all reduced at the same time. As the coverages θ_{OH} , θ_H and θ_M must sum to unity (Yuwono, Taylor, et al., 2019), this implies that the active surface area consisting of Mg*, Mg*H and Mg*OH is a subset of the total metal surface. Why certain areas of the exposed surface do not appear to participate in the dissolution reaction is not clear, but is consistent with previous observations (Curioni, 2014). In this case, as the activity of water is substantially decreased by the action of the dissolved salt (Table 5.7), the decrease in active surface area may indicate that the transport of water to the reaction interface is rate-limiting. In addition, the emergence of an inductive loop implies that a surface layer, presumably a salt film, is at least partially stable on the metal surface at open circuit potential in solutions saturated with MgCl₂. This effect likely manifests as a transient film on local anodes at open circuit conditions, the dissolution of which is rate-limiting. Furthermore, this implies that the film free areas represent the local cathodes required to maintain the open circuit. The blocking of these areas by the transient salt film would limit the cathodic current density and thus limit charge transfer. This interpretation explains why the corrosion rate is lower in saturated MgCl₂ vs 4M concentration, with the implication that the latter represents the point at which cathodic and anodic processes can proceed unimpeded by surface film formation.

Table 5.4 Table of parameter values for pure Mg in MgCl₂ solutions determined by fitting to the Kinetic Model with associated standard error. Where error estimates exceed the magnitude of the parameter value the cell is highlighted in orange.

	C_f [F]	D_{Mg2} [cm^2s^{-1}]	K_1 [cm^2s^{-1}]	K_2 [cm^2s^{-1}]	K_{22} [cm^2s^{-1}]	R_e [Ω]	b_1 [V^{-1}]	b_2 [V^{-1}]	b_{22} [V^{-1}]	β [$molcm^{-2}$]	δ [cm]	k_3 [cm^2s^{-1}]
0.5M	$3.74 \times 10^{-4} \pm 2.83 \times 10^{-6}$	0.444 ± 4.328	$3.09 \times 10^{-08} \pm 1.27 \times 10^{-7}$	0.011 ± 1.847	$0.087 \pm 3.87 \times 10^{-6}$	6.25 ± 0.65	12.78 ± 6.92	-9.18 ± 7.99	6.36 ± 16.53	0.027 ± 6.463	1.610 ± 5.731	0.005 ± 0.785
1M	$2.14 \times 10^{-4} \pm 5.72 \times 10^{-6}$	0.412 ± 12.36	$8.10 \times 10^{-09} \pm 8.52 \times 10^{-08}$	0.062 ± 2.349	0.082 ± 0.219	4.33 ± 0.7	12.68 ± 4.51	0.94 ± 17.46	6.09 ± 17.8	0.713 ± 11.752	1.849 ± 18.365	-0.037 ± 2.297
2M	$5.90 \times 10^{-5} \pm 6.73 \times 10^{-2}$	1.901 ± 0.01	$4.03 \times 10^{-08} \pm 7.51 \times 10^{-2}$	1.118 ± 0.082	1.953 ± 0.057	6.69 ± 0.05	12.95 ± 0.18	-5.05 ± 0.05	6.68 ± 0.16	-0.975 ± 0.055	8.138 ± 0.167	0.179 ± 0.014
4M	$1.44 \times 10^{-4} \pm 1.22 \times 10^{-4}$	1.804 ± 0.137	$1.18 \times 10^{-7} \pm 3.32 \times 10^{-7}$	2.000 ± 9.712	1.834 ± 0.462	10.06 ± 2.28	18.98 ± 19.33	-1.86 ± 0.04	1.44 ± 21.34	-145 ± 249	1.689 ± 6.914	1.911 ± 3.47
Sat.	$4.90 \times 10^{-5} \pm 4.99 \times 10^{-5}$	5.181 ± 67.3	$5.95 \times 10^{-08} \pm 6.25 \times 10^{-6}$	0.654 ± 3.633	-0.297 ± 2.836	12.41 ± 1.7	20.62 ± 20.48	-10.48 ± 6.22	11.3 ± 115.89	-14.4 ± 42.9	1.474 ± 11.883	2.059 ± 3.901

Under the univalent interpretation, the gradual elimination of mid-frequency capacitance can be attributed to a progressively thinning hydroxide layer caused by increasing solubility, modelled as a finite-length Warburg impedance where the thickness δ tends to 0 (Galicía et al., 2009). While at high concentrations (e.g., 4M) no hydroxide layer should be stable, diffusion may still occur through a liquid boundary layer as the spectra were obtained in quiescent solutions. The reduction in high frequency capacitance, meanwhile, can be explained by hydroxylation-induced thinning of a MgO sublayer caused by increased access of water to the surface (Gomes et al., 2019).

Nevertheless, despite this plausible interpretation, the kinetic model struggles to obtain solutions with reasonable error estimates. This can be attributed to overfitting as previously discussed, but also to the increased complexity of the system in concentrated MgCl₂. It is clear that at high concentrations of MgCl₂ the surface behaviour has been altered to the extent that the capacitive response at intermediate frequency has become comparably small. For both models this increases the chance that the fitting algorithm will find a local colinear minimum where multiple parameters attempt to describe the same feature. Unfortunately, for the kinetic model these effects are too significant to overcome, even with the use of the computationally intensive Monte Carlo method for estimating errors. Therefore, for the purpose of identifying the cause of depassivation of Mg in concentrated MgCl₂, only the circuit model can be used with any degree of confidence.

The circuit model, by contrast, achieves excellent fit results for all parameters. Standard errors are generally negligible (<1%) although occasionally rising to ~10% (Table 5.3). Making direct inferences from the individual component values is difficult as it is generally agreed that the processes involved occur at different sites with corresponding surface coverages, which are themselves dependent on potential (Baril et al., 2007; King et al., 2014). However, it is evident that the capacitances C_1 and C_2 decrease with increasing concentration, while the associated resistances R_1 and R_2 are high at low concentration and are minimised in 4M MgCl₂. The inductive resistance R_3 is low for the passivated systems and large at higher concentrations, although it appears to correlate inversely with concentration within the two regimes. This effect is examined in further detail in Section 5.5.7. The inductance L rises with concentration to a maximum at 2M beyond which the value collapses by two orders of magnitude as the solution approaches saturation with respect to MgCl₂.

To estimate the effect of MgCl_2 concentration on the corrosion rate, the predicted polarisation resistance was calculated for each model as shown in Figure 5.15. For the circuit model this was determined using Equation 5.2 and for the kinetic model by subtracting the solution resistance R_e from the real value of the impedance in the low frequency limit.

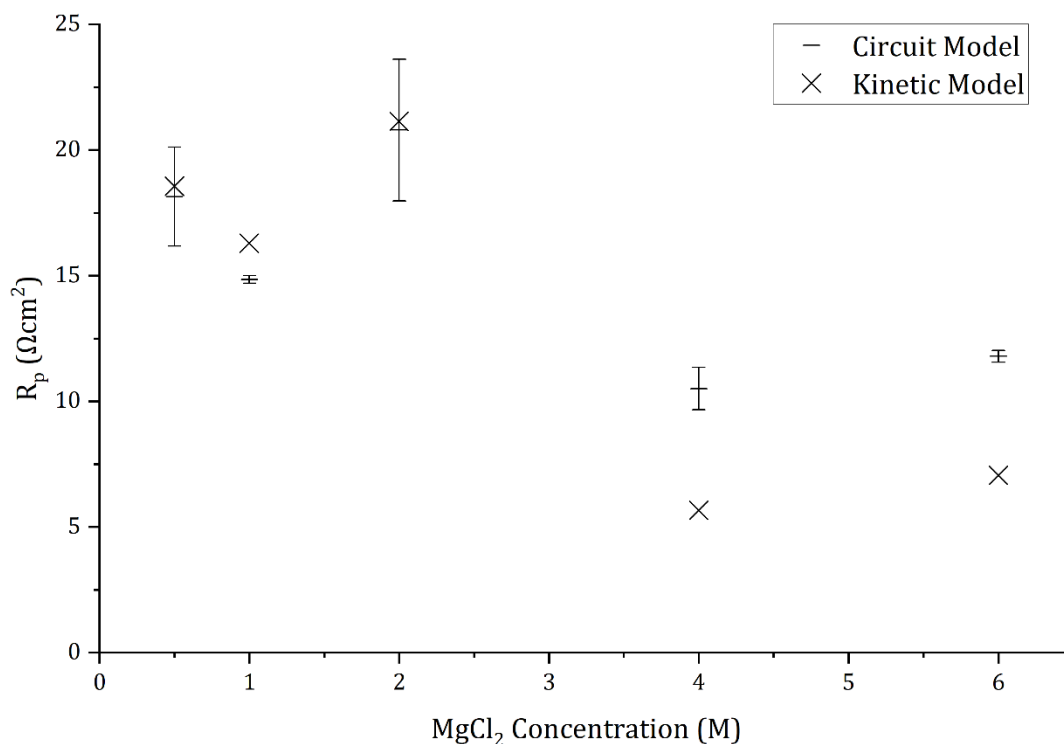


Figure 5.15 Plot of the polarisation resistance as predicted by the circuit (dashes) and kinetic (crosses) models as a function of concentration. Error bars for the circuit model are calculated from the standard error of regression and are not shown for the kinetic model due to poor fitting performance.

While repeated measurements of the polarisation were not performed (hence the lack of error bars), there is generally good agreement between the models, particularly when considering relative changes between concentrations. Also, while not substantial, an increase in R_p was observed as the concentration of MgCl_2 increased from 4M to saturation. This appears to be counterintuitive, as it implies a decrease in the corrosion rate, but is corroborated by previous researchers who attributed the effect to “salting out” of the corroding agent (Casey and Bergeron, 1953). Once again, a detailed treatment of this result is presented in Section 5.5.7 as part of a comprehensive and consistent discussion of all the experiments performed as part of this study.

By comparison to R_p values determined from potentiodynamic polarisation measurements (Figure 5.9 & Figure 5.10), it is evident that, while good agreement is achieved for the saturated salt solution, there is significant

discrepancy at 4M concentration. This shows that despite a very high salt concentration, the effects of IR drop cannot be fully neglected. In turn, this is a demonstration of the power of EIS for accurate determination of R_p , as the effect of solution resistance can be deconvoluted using measurements at high frequency.

5.5.5 Impedance Response under Imposed Potential

To investigate in greater detail the potential-dependent response of the Mg surface in 4M $MgCl_2$, a series of impedance spectra were obtained over a range of bias voltages from -500 to +500mV relative to OCP as shown in Figure 5.16.

The quality of solutions fitted to the circuit model is generally good, particularly for increasing anodic bias where the mid-low frequency response is well reproduced. Under cathodic bias the response is more complex with significant overlap between the domains of the inductive and capacitive response, compromising the effectiveness of the fitting procedure. With increasing bias potential (both anodic and cathodic), the impedance response in the high frequency limit approaches a constant phase angle, giving the appearance of a finite-length Warburg element. When fitted to the circuit model (Figure 5.2), this results in underestimation of the resistance R_1 , which from graphical observation appears to be invariant with increasing bias voltage.

Determination of the capacitance C_1 is less likely to be affected by this behaviour, as the fitted value is representative of the low-frequency limit of the Warburg capacitance.

For bias voltages more negative than -250mV, the impedance response is dominated by a large capacitive feature in the low frequency limit. This likely results from the inception and growth of a hydroxide film as observed during potentiodynamic measurements at cathodic potentials (Figure 5.10), as the bias potential was only imposed at the start of OCP measurements with no preconditioning. While this violates the steady state assumption, the resulting measurements are still useful for understanding the behaviour of dissolving Mg under applied potentials, particularly in the high frequency domain prior to film stabilisation. The solution parameters calculated for the circuit model are listed in Table 5.5.

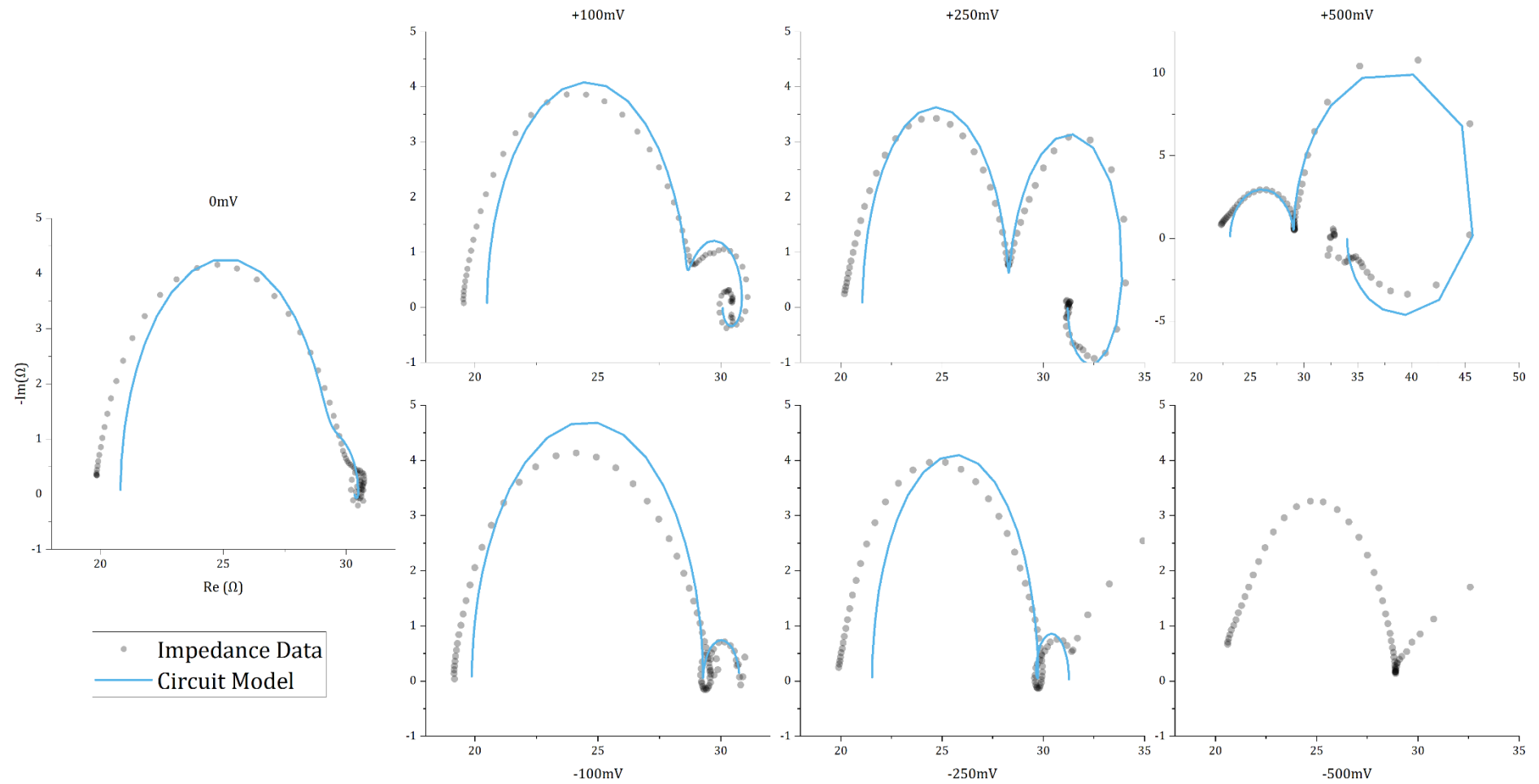


Figure 5.16 Series of plots showing the impedance response of pure Mg in 4M MgCl₂ under different bias voltages with fitted solutions for the circuit model (blue).

Table 5.5 Area-normalised parameter values determined by fitting impedance data to the circuit model for pure Mg in 4M MgCl₂ at bias potentials from -0.25V to +0.5V relative to OCP. Errors are the standard error of the regression for each parameter.

	R_e [Ωcm ²]	R₁ [Ω cm ²]	C₁ [F cm ⁻²]	R₂ [Ω cm ²]	C₂ [F cm ⁻²]	R₃ [Ω cm ²]	L [H cm ²]
+0.5V	29.3 ± 0.03	7.51 ± 0.03	1.49x10 ⁻⁵ ± 1.00x10 ⁻⁷	138 ± 5	7.33x10 ⁻³ ± 1.00x10 ⁻⁵	15.2 ± 0.05	2.87 ± 0.02
+0.25V	26.7 ± 0.02	9.19 ± 0.02	2.20x10 ⁻⁵ ± 1.00x10 ⁻⁷	10.9 ± 0.12	1.08x10 ⁻² ± 4.20x10 ⁻⁵	35.8 ± 0.38	7.32 ± 0.16
+0.1V	26.0 ± 0.02	10.3 ± 0.02	2.54x10 ⁻⁵ ± 1.00x10 ⁻⁷	3.04 ± 0.02	1.45x10 ⁻² ± 1.84x10 ⁻⁴	131 ± 3	50.1 ± 2.4
0V	26.4 ± 0.03	10.8 ± 0.03	2.61x10 ⁻⁵ ± 2.00x10 ⁻⁷	1.43 ± 0.02	4.49x10 ⁻³ ± 1.43x10 ⁻⁴	805 ± 280	1690 ± 419
-0.1V	21.6 ± 0.02	8.20 ± 0.02	2.32x10 ⁻⁵ ± 1.43x10 ⁻⁷	1.97 ± 0.08	3.97x10 ⁻¹ ± 2.82x10 ⁻²	27.2 ± 2.7	222 ± 42.4
-0.25V	23.8 ± 0.07	5.72 ± 0.06	7.25x10 ⁻⁵ ± 1.72x10 ⁻⁶	1.45 ± 0.02	2.86x10 ⁰ ± 7.71x10 ⁻²	19.8 ± 5.11	268 ± 31.6

With increasing positive bias, the impedance response is characterised by an increase in the impedance contribution from the secondary capacitive and inductive processes. Notably, in the low frequency limit the contribution from each process is effectively cancelled out and the polarization resistance remains static or gradually increases. This suggests that the overall rate of corrosion does not increase with anodic polarisation in 4M MgCl₂. Under negative bias, the contribution of the secondary capacitance C_2 increases and the inductive contribution progressively disappears, before ultimately the impedance is dominated by the Warburg-type process. Under high cathodic bias it is expected that the reaction will be dominated by the hydrogen evolution reaction, leading to a large increase in the resistance at low frequency, deliberately omitted in Figure 5.16 to preserve visibility of the high-mid frequency response. Substantial hydrogen evolution would also lead to the Warburg-type response as water at the surface is exhausted, requiring diffusion of water to enable further reduction to take place.

Although the kinetic model described by Baril showed poor fitting performance in this work due to overfitting, the observed impedance behaviour can still be evaluated quantitatively within the context of the accompanying reaction scheme (Equations 5.3-5.15). For example, the decrease in high frequency capacitance with increasing MgCl₂ concentration can be attributed to the progressive hydroxylation of an MgO barrier layer as described by Gomes, as the solubility of the hydroxide film above the 2M threshold substantially improves the availability of water at the interface (Gomes et al., 2019).

Within this model, the inductive behaviour exhibited by corroding Mg is attributed to the adsorbed intermediate Mg_{ads}^+ . In general, adsorbed intermediates that are created faster than they are removed result in a capacitive impedance response (Scully, 2000). Conversely, intermediates that are removed faster than they are created exhibit inductive behaviour (Orazem and Tribollet, 2008b). The elimination of inductive impedance and development of a hydroxide film under cathodic bias in 4M MgCl₂ is consistent with the reversible adsorption of Mg_{ads}^+ onto the metal surface. Under this scheme, cathodic bias kinetically restricts the oxidation of Mg and Mg_{ads}^+ , eliminating the inductive component of the impedance response and saturating the surface with Mg_{ads}^+ . Once a stable surface layer is established, precipitation of a solid hydroxide phase could occur despite being soluble in the bulk solution. Upon removal of the overpotential, oxidation reactions recommence and the surface film is progressively dissolved. Furthermore, the increase in capacitance observed following the addition of Mg²⁺ ions to 2.67M AlCl₃ is

consistent with an increase in the diffusion layer thickness, δ (Equation 5.11) (Taylor and Gileadi, 1995). At the same time, the solubility of Mg^{2+} remains high (Table 5.7), thus the rate of the adsorption reaction described by the constant k_{22} remains low and the overall resistance remains approximately the same. However, as Baril made the assumption that Mg^{2+} diffusion takes place exclusively within a layer of precipitated hydroxide, it is unclear whether the same effect can be invoked in this instance, where a surface film is not stable and diffusion presumably takes place within a liquid boundary layer (Baril et al., 2007). Since these experiments were carried out in quiescent solution, it would be interesting to repeat the measurements with a Rotating Disk Electrode (RDE) to investigate whether the diffusion impedance is affected by an increase in the fluid velocity at the metal surface.

Under anodic bias, the increase in the capacitive impedance attributed to the diffusion of Mg^{2+} could be explained by the stabilisation of a salt film (MgCl_2) which has previously been observed under similar conditions (Beck and Chan, 1981). However, the magnitude of this effect is strongly dependent on the reaction constant k_{22} , which corresponds to the rate of reduction of Mg^{2+} onto the metal surface as Mg_{ads}^+ (Equation 5.5). Under anodic bias, this reaction should be kinetically suppressed and thus the diffusion impedance should be decreased. This behaviour is observed under typical conditions (i.e. with a hydroxide surface film (King et al., 2014)), but the model fails to describe the behaviour observed during dissolution in concentrated MgCl_2 . In addition, the reaction scheme cannot explain the decrease in polarisation resistance/corrosion rate observed as the concentration of MgCl_2 approaches saturation, since the rate of Mg_{ads}^+ (Equation 5.4) should continue to increase with the increasing solubility of Mg^{2+} (Pannach et al., 2017). Thus, the reaction scheme described by Equations 5.3-5.5 cannot fully explain the dissolution behaviour of Mg in concentrated MgCl_2 solutions. It must be noted that these observations do not rule out the existence of univalent Mg^+ , however they do suggest that the mechanism as presented by Baril and Gomes is, at best, incomplete.

The reaction framework described in Section 5.2.1, on the other hand, is capable of explaining the changes in impedance behaviour under imposed bias voltages. Under cathodic bias, the reduction of water and evolution of hydrogen gas is entirely facilitated by the Mg^*H intermediate. Oxidation is suppressed and thus the inductance represented by the Mg^*OH pathway disappears. The origin of the hydroxide surface film observed for the case of cathodic polarisation in 4M MgCl_2 cannot be proved definitively using this model, but a

possible mechanism can nonetheless be suggested. As the Mg^*OH intermediate can only be removed by oxidation, under cathodic bias the desorption of any pre-existing coverage will be kinetically suppressed. These metastable Mg^*OH sites may subsequently provide a nucleation site for the precipitation of $\text{Mg}(\text{OH})_2$ formed from dissolved Mg^{2+} and OH^- species, which continue to be generated by the water splitting reaction required to facilitate reduction via Mg^*H .

Under anodic bias in 4M MgCl_2 (Figure 5.16), the resistance R_3 and inductance L are substantially reduced to the point that the Mg^*OH becomes the preferred pathway. This reflects the increasing stability of Mg^*OH under anodic bias and implies that the anodic Tafel constant for the Mg^*OH reaction is greater than the corresponding anodic Tafel constant for Mg dissolution by Mg^*H . The resistance R_1 , corresponding to water splitting and Mg^*H adsorption, remains approximately constant, while the resistance R_2 , related to the desorption reaction, is increased. While both reactions depend on H^+ (which is abundant in the concentrated salt solution), the desorption reaction also depends on the solubility of the Mg^{2+} ion. Thus, the increase in the resistance implies that the solubility of Mg^{2+} is suppressed, which is consistent with the formation of a salt film under anodic bias in 4M MgCl_2 as previously observed by Beck and Chan (Beck and Chan, 1981). This may also explain the pseudo-passivation and associated discontinuities observed during potentiodynamic polarisations (Figure 5.10).

The corrosion rate under these conditions is controlled by the dissolution of this MgCl_2 layer and thus is limited by the ability of water to access the surface. Underneath the film at the salt/metal interface, the water splitting reaction enables dissolution by the Mg^*OH pathway despite the suppressed stability of OH^- in the bulk of the acidic solution. While the rate of the Mg^*OH desorption reaction is similarly dependent on the solubility of $\text{Mg}(\text{OH})^+$, the large anodic Tafel constant (corresponding to a comparatively small electrochemical activation energy) allows the reaction to proceed at a considerable rate. In effect, this represents a mechanism by which Mg ions can be forced into the aqueous phase in situations where their solubility is suppressed, i.e., beneath a surface film. This effect can be alternatively understood as ligand assisted dissolution by OH^- as described by Taylor (Taylor, 2016).

5.5.6 Impedance in AlCl_3 Solutions

In an attempt to deconvolute the roles of water activity and Mg^{2+} solubility as the MgCl_2 system approaches saturation, the impedance response of corroding pure Mg was measured in 2.67M AlCl_3 in both unsaturated (no added Mg^{2+}) and

saturated (1.25M MgO added) conditions as shown in Figure 5.17, with a fitted solution to the circuit model described by the parameters listed in Table 5.6. Relevant solution properties as determined by thermochemical calculations are listed in Table 5.7.

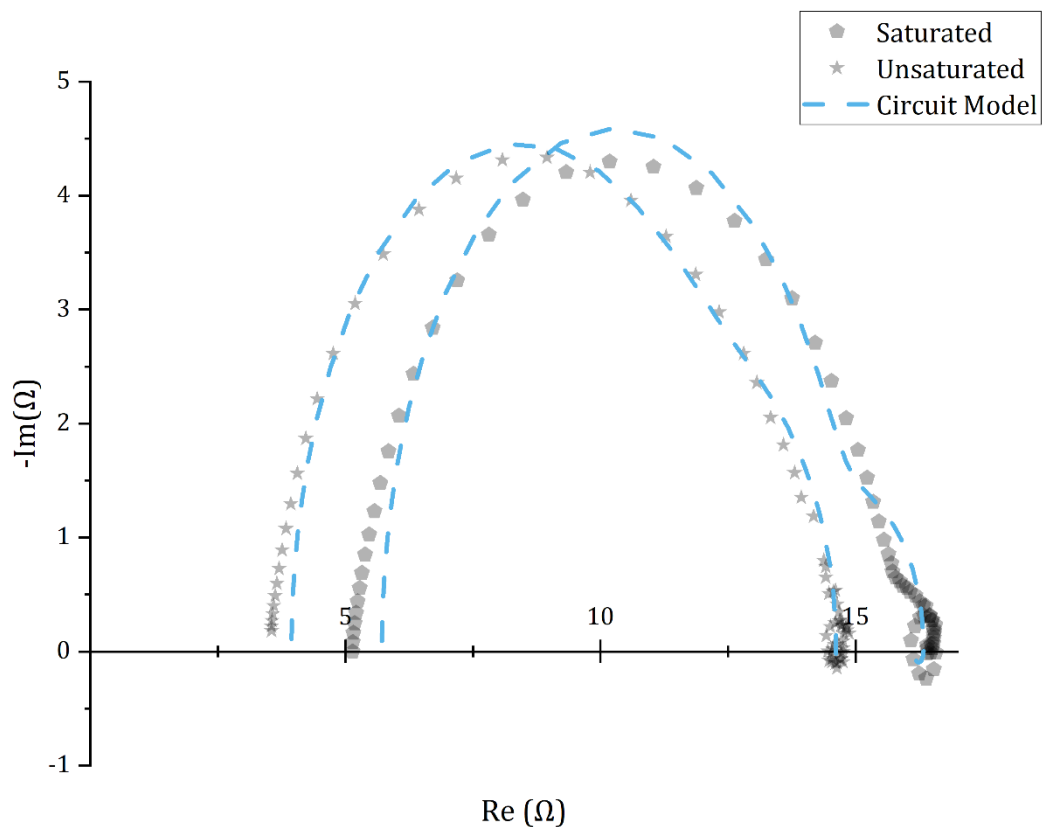


Figure 5.17 Plot of impedance response of pure Mg corroding in 2.67M AlCl_3 both saturated (pentagons) and unsaturated (stars) with respect to Mg^{2+} ions. Fit lines (dashed, blue) correspond to solutions of the circuit model.

Table 5.6 Area-normalised parameter values for solutions of the circuit model fitted to the impedance response of pure Mg in saturated and unsaturated (with respect to Mg²⁺ ions) 2.67M AlCl₃.

	R_e [Ωcm ²]	R₁ [Ω cm ²]	C₁ [F cm ⁻²]	R₂ [Ω cm ²]	C₂ [F cm ⁻²]	R₃ [Ω cm ²]	L [H cm ²]
Saturated	7.24x10 ⁰ ± 1.57x10 ⁻²	1.16x10 ¹ ± 1.94x10 ⁻²	2.21x10 ⁻⁵ ± 8.66x10 ⁻⁸	1.83x10 ⁰ ± 1.76x10 ⁻²	2.76x10 ⁻³ ± 6.87x10 ⁻⁵	7.26x10 ² ± 1.97x10 ²	1.99x10 ³ ± 3.68x10 ²
Unsaturated	5.00x10 ⁰ ± 1.87x10 ⁻²	1.12x10 ¹ ± 2.57x10 ⁻²	1.85x10 ⁻⁵ ± 9.15x10 ⁻⁸	2.28x10 ⁰ ± 2.67x10 ⁻²	6.45x10 ⁻⁴ ± 1.80x10 ⁻⁵	9.14x10 ² ± 3.39x10 ²	2.14x10 ³ ± 4.99x10 ²

Table 5.7 Table of solution properties determined by thermochemical calculations for evaluating dependence of Mg corrosion behaviour on water availability and Mg^{2+} ion concentration.

	[Al ³⁺]	[Mg ²⁺]	[Cl ⁻]	Water Activity	log Mg ²⁺ Activity	Precipitated Minerals
Sat. 4M MgCl₂	0	4.025	8	0.577199	1.0804	Mg ₂ (OH) ₃ Cl:4H ₂ O (F3 Oxychloride), Oxychloride-Mg (F5 Oxychloride), Brucite
Sat. 6M MgCl₂	0	6.025	12	0.301119	2.5106	Mg ₂ (OH) ₃ Cl:4H ₂ O (F3 Oxychloride), Oxychloride-Mg (F5 Oxychloride), Brucite, Bischofite
Sat. 2.67M AlCl₃	2.67	1.25	8	0.764061	0.6622	Gibbsite, Boehmite
Unsat. 2.67M AlCl₃	2.67	1.25	8	0.5642	0	None

The only significant change that addition of Mg^{2+} ions makes to the Mg/AlCl_3 system is to the secondary capacitance, C_2 , which increases by one order of magnitude. The effect on the impedance response is broadly similar to that which is observed between 6M and 4M MgCl_2 , minus the difference in the inductive response. While the addition of ions to the AlCl_3 solution does produce a meaningful Mg^{2+} activity, the primary consequence is that Al^{3+} ions are pushed out of solution and precipitate as oxide/hydroxides. As such, the solubility of Mg^{2+} remains high while the availability of water molecules increases, as the more weakly hydrolysing divalent Mg ions replace the stronger trivalent Al ions.

The behaviour observed in 2.67M AlCl_3 is similar to that of 4M/Sat. MgCl_2 solutions, with the most notable difference being the absence of the inductive loop. Presumably, in the more acidic salt solution, the solubility of Mg^{2+} is sufficient to prevent the formation of a salt film under open circuit conditions. This may in turn explain why the corrosion rate of Mg is higher in 2.67M AlCl_3 relative to 4M MgCl_2 as previously observed (Section 4.3.1). With the addition of Mg^{2+} ions to the AlCl_3 solution, the Mg^*H coverage (proportional to C_2) increases. This can be attributed to an increase in the water activity resulting in an increase in the availability of water molecules at the surface. As such, it effectively increasing the capacity of the system to facilitate dissolution by Mg^*H . The similarities between the concentrated AlCl_3 and MgCl_2 systems offers a rationalisation for why the corrosion rate of Mg is maximised in 4M MgCl_2 . That is, that 4M MgCl_2 represents an inflection point where the controlling factor is no longer the solubility of Mg^{2+} but rather the transport of water molecules to the reaction site in order to facilitate the dissolution reaction.

5.5.7 Mg Corrosion Mechanism in Concentrated Salt Solutions

A combined schematic representation of how the mechanisms presented in Figure 5.1 relate to the experimental observations made in this work is shown in Figure 5.18.

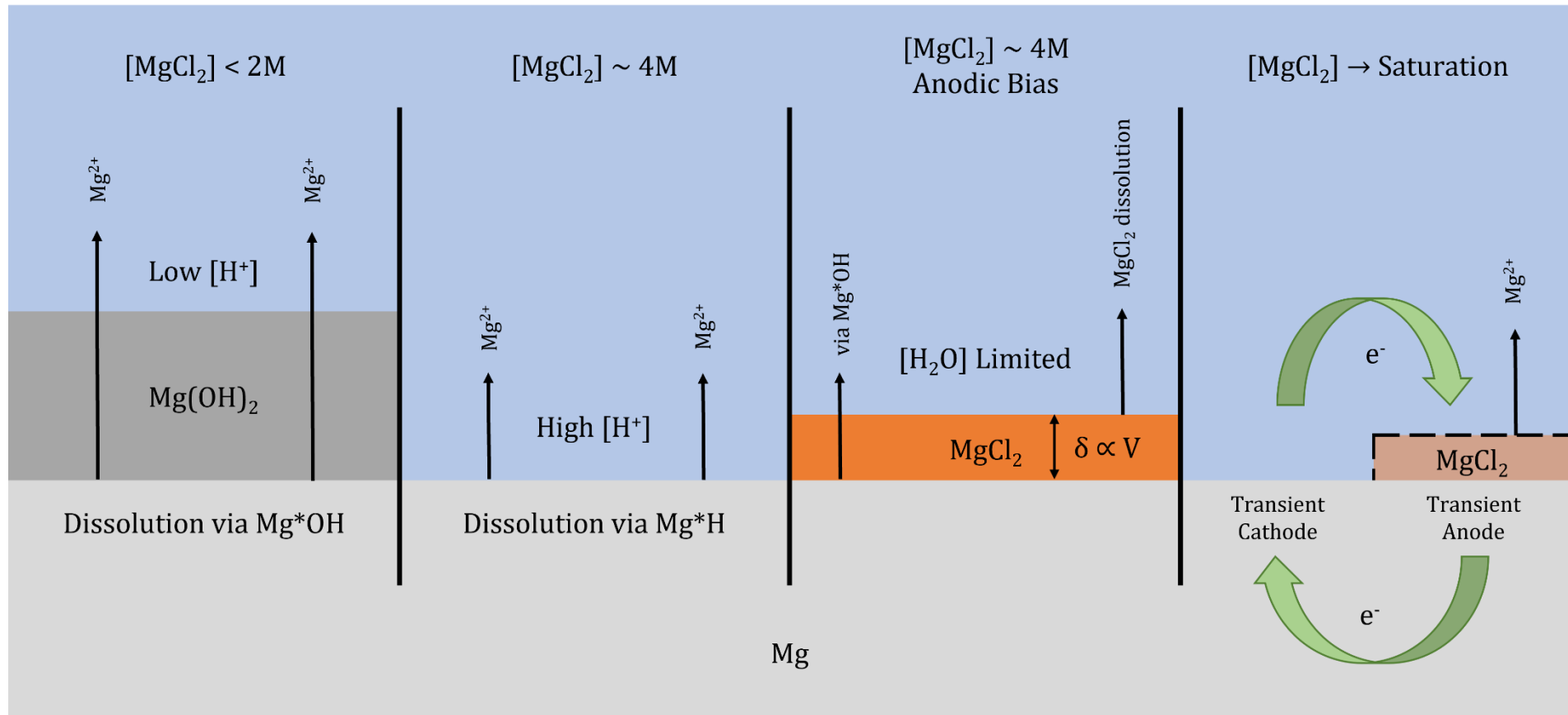


Figure 5.18 Schematic representation of the inferred corrosion behaviour of pure Mg under the various conditions tested in this work. The thickness of the salt film induced by anodic polarisation is represented by the symbol δ .

The combined reaction/circuit model described here can also be used to explain the corrosion behaviour of Mg under more typical conditions, e.g. the corrosion of Mg beneath a precipitated hydroxide film in NaCl solutions as described by King (King et al., 2014). Under cathodic polarisation of -300mV, as previously discussed, the inductive component disappears as the Mg^*OH pathway is suppressed. This coincides with a substantial increase in the resistances R_1 and R_2 , corresponding to the adsorption and desorption of Mg^*H . As Mg^*H is required to facilitate the reduction reactions it must be present beneath the precipitated film. However, the concentration of H^+ at the metal/film interface is suppressed by the presence of the alkaline film with which it will also react, i.e., by local dissolution of $Mg(OH)_2$. Thus, the resistance of the adsorption/desorption reaction is increased.

Under anodic polarisation, the resistances R_1 , R_2 and R_3 are all substantially reduced, leading to a decrease in the polarisation resistance and corresponding increase in the corrosion rate. This implies that an abundance of water is present inside the porous hydroxide, such that the rate of the water splitting reaction (represented by the adsorption resistances R_1 and R_3) is increased. This effect is representative of the enhanced cathodic activity to which anodic hydrogen evolution is attributed (Esmaily et al., 2017). While dissolution by Mg^*H continues at this potential, as evidenced by ongoing hydrogen evolution, the increased contribution of the inductive loop (as $R_3 < R_1 + R_2$) indicates that dissolution via the Mg^*OH pathway is increasingly favoured. This suggests that the solubility of Mg^{2+} remains a limiting factor under anodic polarisation.

At open circuit potential, the impedance response of Mg is dominated by the inductive loop, whereby the capacitive resistance is effectively short-circuited by the inductive resistance R_3 in the low frequency limit. This is evident in the spectra obtained by King for NaCl and is also observed in this study for the case of $MgCl_2$ at concentrations $<2M$ as shown in Figure 5.13 (King et al., 2014). However, while dissolution by Mg^*OH is favoured, the Mg^*H pathway is still required to facilitate the reduction of water. Since the resistance of the combined Mg^*H adsorption/desorption reactions is greater than the resistance of the Mg^*OH pathway, the overall reaction is cathodically controlled, as noted by previous researchers (Curioni, 2014). In effect, the reaction is limited by the transport of water through the hydroxide film to the metal substrate. Following the water splitting reaction, the dissolution of Mg^{2+} ions is facilitated by the ligand assisted Mg^*OH mechanism, forcing the ions into solution at the metal/film interface despite their low solubility.

5.5.8 Magnox Alloy Corrosion in Concentrated Salt Solutions

Following the construction of a framework describing the corrosion mechanism of Mg in concentrated salt solutions, the same suite of techniques was applied to sample of Magnox alloy to examine similarities and differences in its behaviour. This work was performed to better understand the dissolution of Magnox alloy in $\sim 4\text{M MgCl}_2$ to underpin Cementisation and in particular to explain the difference in corrosion rate kinetics as described in Section 4.3.3.

Potentiodynamic polarisation of Magnox samples in 4M MgCl_2 was compared to pure Mg as shown in Figure 5.19.

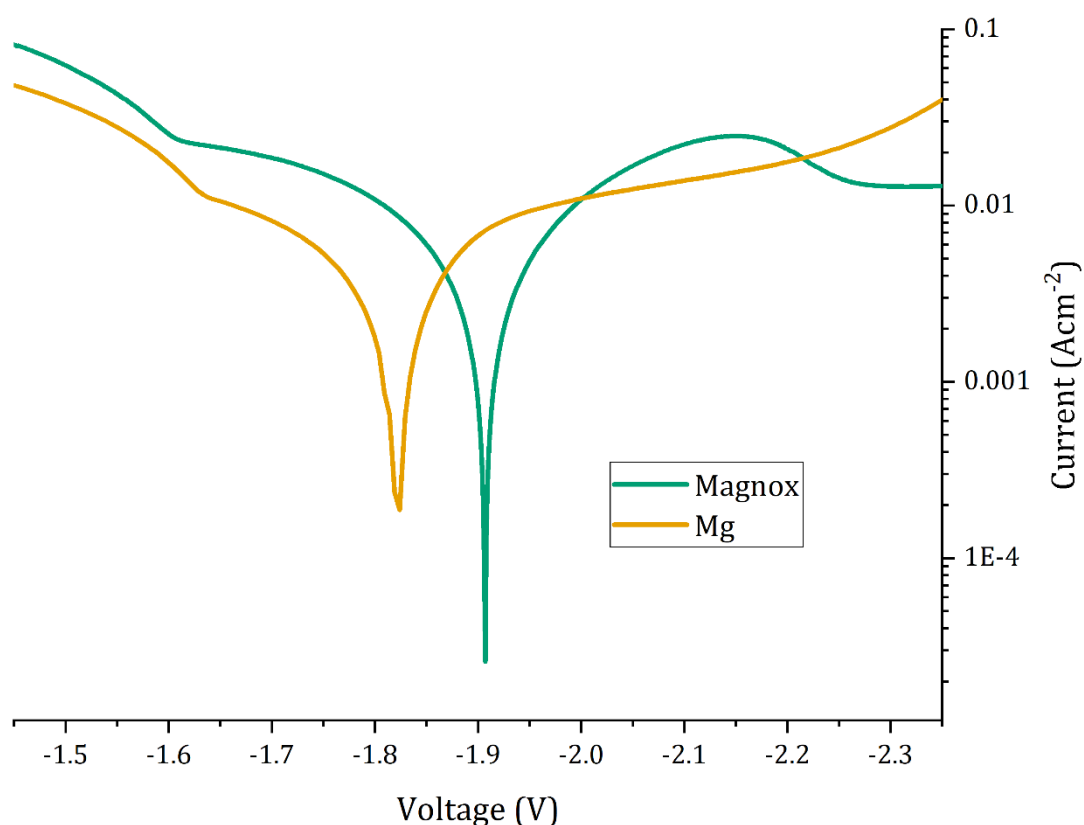


Figure 5.19 Plot of potentiodynamic polarisations for pure Mg (yellow, scan rate = 5mVs^{-1}) and Magnox alloy (green, scan rate = 1mVs^{-1}) in 4M MgCl_2 .

The value of E_{corr} observed for the Magnox alloy was marginally more negative than for pure Mg, consistent with a decrease in the exchange current density for the magnesium half reaction. This is consistent with the improved corrosion resistance generally observed for Magnox alloy relative to pure Mg (Clark et al., 2021). However, the discontinuities (at $\sim -1.6\text{V}$) and inflection points (at $\sim -2.1\text{V}$) observed at cathodic and anodic potentials are consistent with a passive film - suppressing current flow under cathodic bias before being removed under anodic polarisation. However, unlike pure Mg, no shift in the corrosion potential relative to the pre-measurement OCP was observed. This may be a result of the lower scan rate used for the Magnox sample, as the precipitated film would have had more time to dissolve and return to the open circuit equilibrium. Nevertheless, while any induced film may have been removed, the discontinuity observed under positive bias at $\sim -1.6\text{V}$ is indicative of salt film corrosion (Burrows, 2013), which implies that some form of surface film is present on the Magnox alloy corroding at open circuit potential in 4M MgCl_2 .

To investigate how the corrosion behaviour of Magnox varies from that of pure Mg below the 2M MgCl_2 concentration threshold, impedance spectra were obtained for 0.5M and 1M MgCl_2 solutions as shown in Figure 5.20.

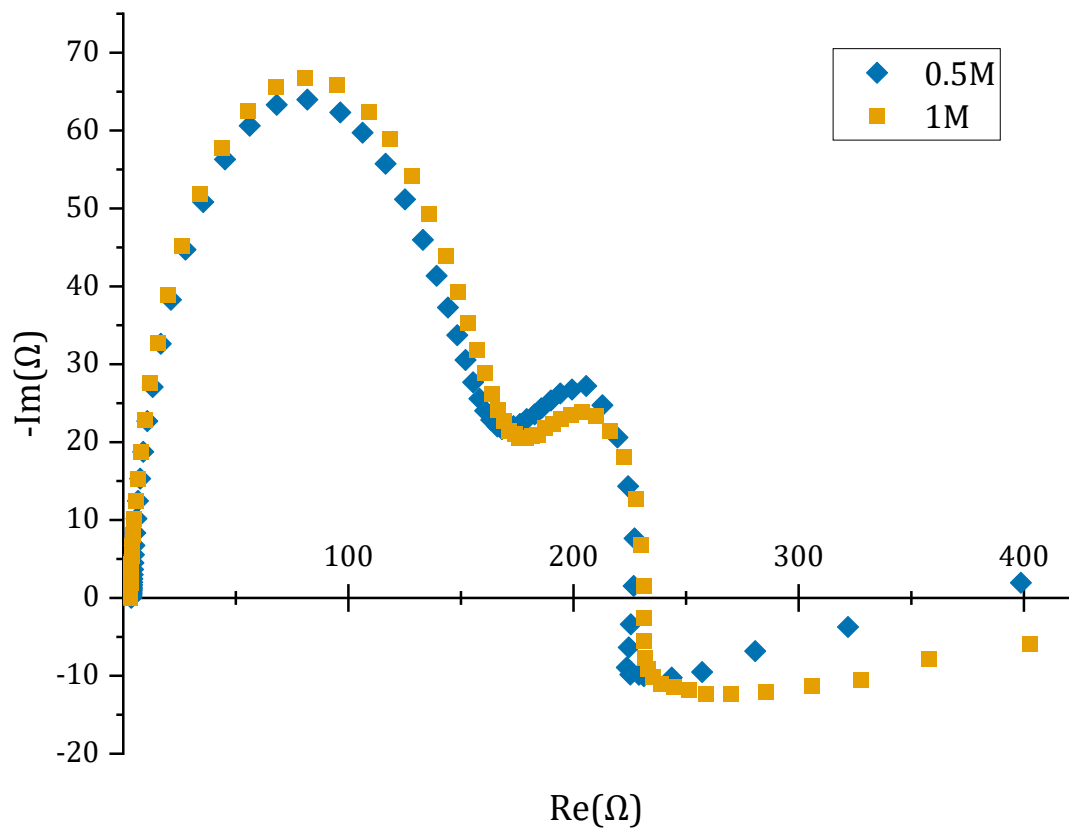


Figure 5.20 Plot of impedance data for Magnox alloy in 0.5M (blue, diamonds) and 1M (yellow, squares) MgCl_2 solution at OCP.

The magnitude of the impedance response for Magnox alloy under these conditions is significantly higher compared to that of pure Mg. Furthermore, while the three characteristic features defined within the circuit model are still observed, a substantial capacitive impedance is observed in the low frequency limit. This is consistent with previous work, which observed the slow formation of a protective surface film in alkaline media (Burrows, 2013). The continued presence of an inductive response shows that dissolution beneath the film is still ongoing (presumably via the Mg^*OH mechanism outlined in Section 5.2.1), yet it is evident that the aluminium component of the Magnox alloy contributes to a substantial increase in the resistance of the surface film. If the film continues to develop and becomes fully protective, the inductive response will disappear. Thus, with sufficient immersion time the inductive response will be removed and replaced with a Warburg-type response as observed by previous researchers (Burrows, 2013). Alternatively, the inductance observed for Magnox may be indicative of ongoing pitting corrosion in localised areas, despite the hydroxide layer being otherwise protective. While interesting, obtaining a full description of the corrosion behaviour in low concentration MgCl_2 would require a series of impedance measurements made over much longer timescales – requiring more time than was available for this work.

For Magnox corroding in 4M MgCl_2 , the impedance response was measured over a range of DC bias voltages as shown in Figure 5.21, with parameter values of solutions to the circuit model listed in Table 5.8.

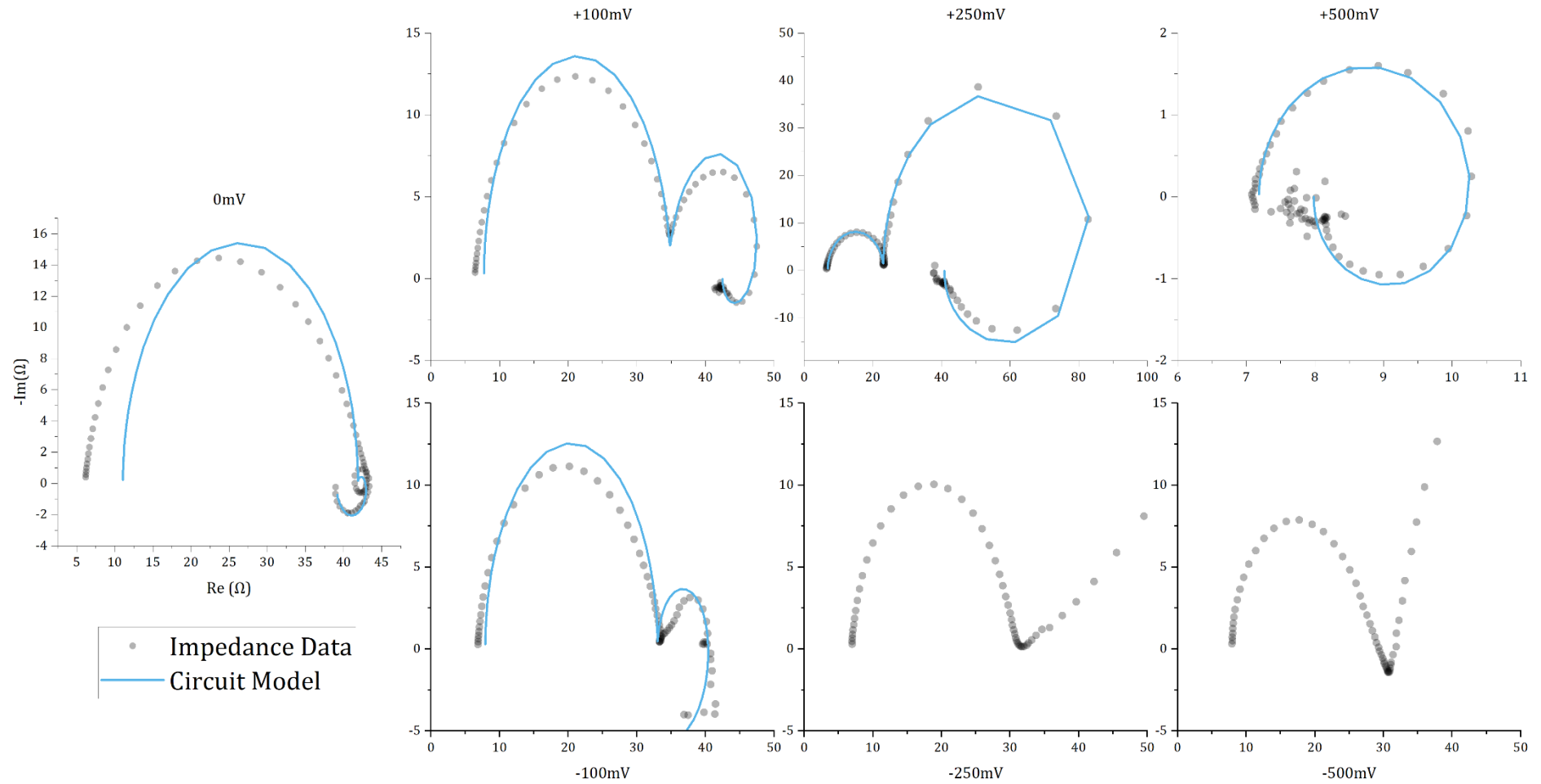


Figure 5.21 Series of plots showing the impedance response of Magnox alloy in 4M MgCl₂ under different bias voltages with fitted solutions for the circuit model (blue).

Table 5.8 Area-normalised parameter values determined by fitting impedance data to the circuit model for Magnox alloy in 4M MgCl₂ at bias potentials from -0.1V to +0.5V relative to OCP. Errors are the standard error of the regression for each parameter. Where standard error estimates exceed the magnitude of the parameter value the cell is highlighted in orange.

	R_e [Ωcm ²]	R₁ [Ω cm ²]	C₁ [F cm ⁻²]	R₂ [Ω cm ²]	C₂ [F cm ⁻²]	R₃ [Ω cm ²]	L [H cm ²]
0.5V	5.25 ± 0.01	2.33 ± 0.01	3.74x10 ⁻⁵ ± 4.01x10 ⁻⁷	9.78 ± 1.52x10 ⁸	1.05x10 ⁻³ ± 3.12x10 ³	0.61 ± 3.86x10 ⁵	2.26x10 ⁻³ ± 1.43x10 ³
0.25V	5.00 ± 0.01	11.9 ± 0.01	2.70x10 ⁻⁶ ± 5.88x10 ⁻⁹	1.11x10 ⁴ ± 4.85x10 ³	1.19x10 ⁻³ ± 4.37x10 ⁻⁷	24.9 ± 0.1	3.79 ± 0.01
0.1V	5.24 ± 0.01	19.9 ± 0.01	3.32x10 ⁻⁶ ± 4.84x10 ⁻⁹	10.94 ± 0.02	1.72x10 ⁻³ ± 3.57x10 ⁻⁶	149 ± 1	45.8 ± 0.00
0V	8.09 ± 0.01	22.5 ± 0.01	4.85x10 ⁻⁶ ± 6.90x10 ⁻⁹	1.19 ± 0.02	4.02x10 ⁻¹ ± 6.81x10 ⁻³	148 ± 1	1200 ± 20
-0.1V	5.78 ± 0.01	18.4 ± 0.01	3.89x10 ⁻⁶ ± 4.75x10 ⁻⁹	5.44 ± 0.01	4.44x10 ⁻² ± 1.60x10 ⁻⁴	46.8 ± 0.6	4450 ± 20

Utilising the framework outlined in Section 5.2.1, the differences in the corrosion behaviour of Magnox and pure Mg in 4M MgCl₂ can be evaluated with respect to the surface reactions that are assumed to take place. At the open circuit potential, it is evident that the polarization resistance of Magnox is substantially greater than that of pure Mg in the concentrated salt solution. This is consistent with previous direct measurements of the corrosion rate which were lower for the Magnox alloy (Section 4.3.1). This can be attributed primarily to an increase in the Mg*H adsorption resistance R_1 . The combined resistance of the Mg*H pathway remains significantly lower than the corresponding resistance for dissolution by Mg*OH, indicating that dissolution still occurs predominantly via the former in the absence of external bias. However, the presence of a small inductive loop suggests that a surface film of some form is at least partially stable on the dissolving metal.

Under cathodic bias, the emergence of a large capacitance in the low frequency limit is similar to that observed for pure Mg and is similarly consistent with the observation of reduced cathodic current density during potentiodynamic tests (Figure 5.19), indicating the stabilisation of a magnesium hydroxide surface layer. Interestingly, at -500mV bias qualitative observation reveals that an inductive component (i.e., a positive value in the imaginary component) re-emerges, suggesting that with increasing cathodic bias the film becomes more vulnerable to pitting or similar undermining via the Mg*OH pathway. This is difficult to reconcile within the existing model unless the nature of the surface film at -500mV is different to that at potentials closer to open-circuit. A possible explanation is that film formation at high negative overpotentials is dominated by the primary magnesium component of the alloy which is porous and thus vulnerable to ligand-assisted dissolution by Mg*OH. Alternatively, this could simply be an artefact of the transition from open-circuit conditions to high cathodic bias, as inductive dissolution of Mg gives way to hydrogen evolution and diffusion (see Section 5.5.5).

Therefore, at open circuit, the corrosion behaviour would be largely determined by the aluminium component of the alloy. While this would explain the observed increase in corrosion resistance, thermochemical calculations have previously shown that aluminium oxides are not stable in 4M MgCl₂ at temperatures below 50°C (Section 4.3.2). Any surface film would therefore have to be transient in nature, i.e., stable enough to fractionally reduce access of water to the interface but not sufficiently to form a contiguous barrier layer. This effect may also explain the significant decrease in the parameter C_1 , which

is assumed to be proportional to the coverage of the double layer next to the active Mg^* metal sites.

With increasing anodic bias, an increase in the Mg^*H desorption resistance is observed, similar to that recorded for pure Mg. For the case of Magnox alloy, however, the resistance increase is much larger for the same imposed voltage. This can be explained under the assumption that partially stable aluminium phases reduce the total active area of the surface (i.e., the availability of Mg^* sites). If the fractional surface area available for Mg dissolution is reduced, the effect of the applied anodic potential is magnified, effectively amplifying the resulting impedance response. The expected result would therefore be a thicker (or denser) salt film on dissolving Magnox anodes relative to pure Mg for the same applied voltage.

At +500mV bias, the measured impedance response is reduced to a single capacitive time constant with an associated inductance, resulting in poor fitting performance in the low frequency domain (Table 5.8). With only one obvious capacitive feature, use of the circuit model (with two capacitive variables) now results in overfitting, as evidenced by the large fitting errors. The polarisation resistance at this point is $\sim 1\Omega$, indicating extremely rapid charge transfer. This may represent a measurement error as this experiment was not repeated, possibly caused by a leakage pathway opened up by aggressive dissolution of the electrode. Alternatively, it is possible that since the standard reduction potential for the aluminium half reaction has been traversed, the metastable aluminium phase no longer restricts access to the interface and dissolution increases substantially. However, this does not explain the absence of the salt film effect noted for the same applied potential in pure Mg, unless the film has become sufficiently thick as to completely suppress dissolution via Mg^*H . This has previously been observed for pure Mg at very high anodic potentials, indicated by cessation of the hydrogen evolution reaction (Beck and Chan, 1981). However, as this observation is not corroborated for the case of Magnox by any supporting evidence within this work, a similar conclusion cannot be made with confidence. If future work requires reliable measurement of the impedance response of Magnox in 4M MgCl_2 at +500mV then this measurement should be repeated.

Finally, to better understand the effect of pH and solubility on the corrosion behaviour of Magnox in concentrated salt solutions, as well as to provide a complementary impedance spectra for each of the corrosion systems previously evaluated by direct measurement (Section 4.3), the impedance

response of Magnox corroding in 2.67M AlCl₃ saturated with Mg²⁺ ions was measured as shown in Figure 5.22.

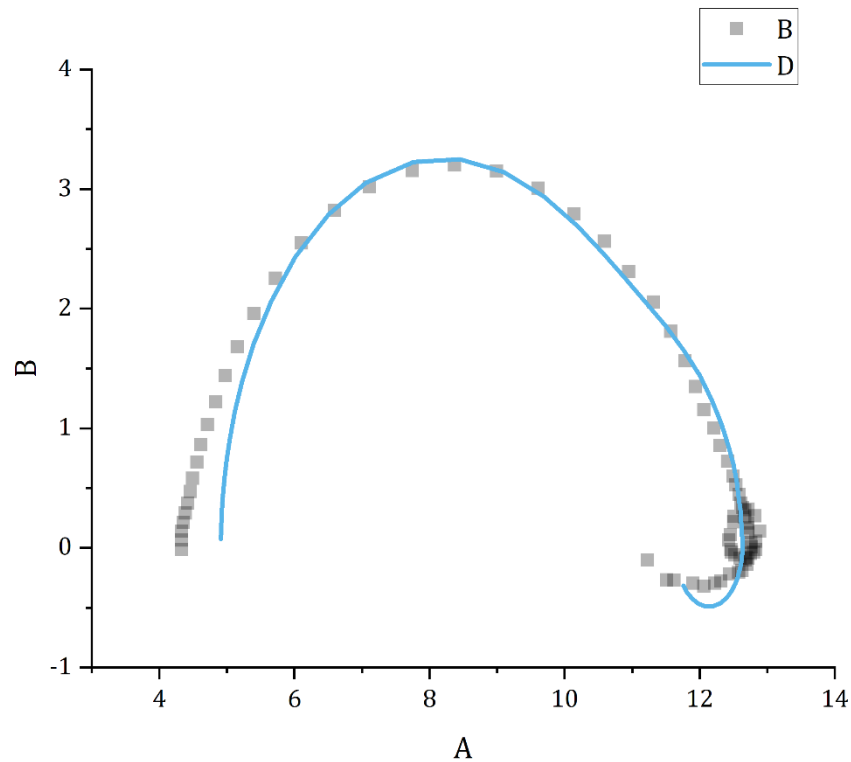


Figure 5.22 Nyquist plot for Magnox corroding in 2.67M AlCl₃ saturated with respect to Mg²⁺ ions (squares). Fit line (blue) corresponds to a fitted solution of the circuit model.

The measured impedance response for Magnox in AlCl₃ solution is similar to that observed for pure Mg in saturated MgCl₂ solution, with the notable addition of an inductive loop at low frequencies. The increased polarisation resistance observed for Magnox in 4M MgCl₂ is not replicated for AlCl₃, instead being more consistent with the values measured for pure Mg in both MgCl₂ and AlCl₃ solutions. Parameter values for the circuit obtained by fitting to the impedance data are listed in Table 5.9.

Table 5.9 Area normalised parameter values determined by fitting impedance data to the circuit model for Magnox alloy in 2.67M AlCl₃.

Parameter	R _e [Ωcm ²]	R ₁ [Ω cm ²]	C ₁ [F cm ⁻²]	R ₂ [Ω cm ²]	C ₂ [F cm ⁻²]	R ₃ [Ω cm ²]	L [H cm ²]
Fitted Value	3.59	4.73	1.57x10 ⁻⁵	0.91	4.93x10 ⁻⁴	38.52	640
Fit Error	0.02	0.02	1.52x10 ⁻⁷	0.02	2.26x10 ⁻⁵	0.91	18

The observation of an inductive loop for Magnox corroding in AlCl_3 solution implies that a surface film of some form is at least partially stable on the dissolving surface. Given the increased acidity of the solution, it is reasonable to assume that the aluminium phase, which was shown to be close to stability in MgCl_2 solutions at ambient temperature (as discussed in Section 4.3.2), is no longer stable. Thus, the charge transfer resistance for Mg^*H adsorption, R_1 , and the capacitance corresponding to Mg^* surface coverage, C_1 , return to values consistent with the dissolution of pure Mg. The inductive behaviour must therefore result from metastable salt film corrosion as depicted in Figure 5.18 for the case of pure Mg corroding in saturated MgCl_2 solution. This effect may similarly be responsible for the inductive loop observed for the impedance response of Magnox alloy in 4M MgCl_2 at open circuit (Figure 5.21). Thus, for the case of Magnox in 4M MgCl_2 , the capacitive response is attributed to a reduction in the active surface due to the effect of the aluminium phase, while the inductive response results from anodic salt film blocking of cathodic sites, resulting in increased dissolution via the Mg^*OH pathway. A schematic representation of the processes is presented in Figure 5.23, representing a means by which the mechanisms outlined in Sections 5.2.1 and 5.5.7 can be related to the specific behaviour of Magnox alloy.

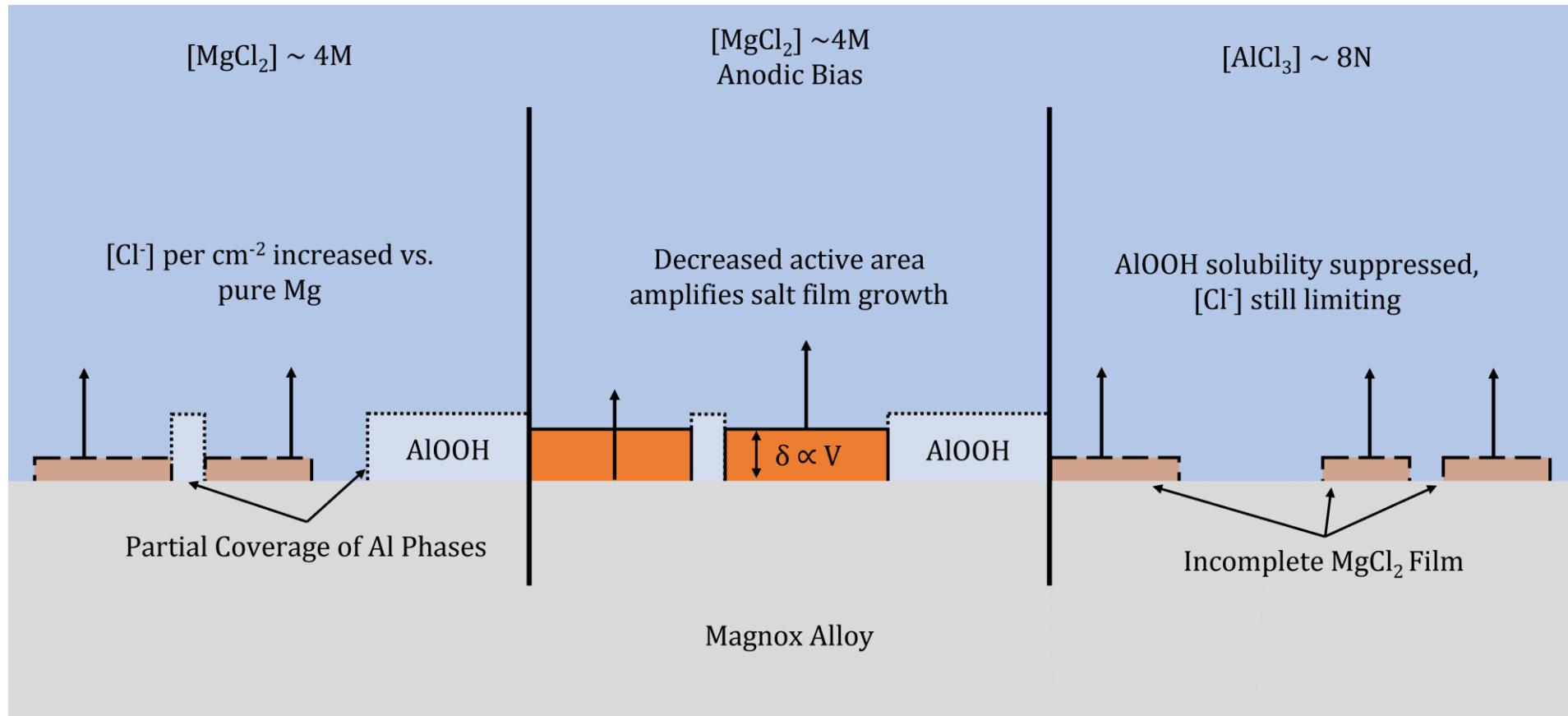


Figure 5.23 Schematic representation of the inferred corrosion behaviour of Magnox alloy under the various conditions tested in this work. The thickness of the salt film induced by anodic polarisation is represented by the symbol δ .

Assuming this interpretation is accurate and representative of the true surface behaviour, it implies that the formation of transient salt films at anodic sites occurs at a much lower salt concentration for the Magnox alloy relative to pure Mg. This in turn suggests, perhaps paradoxically, that the optimum MgCl_2 concentration for the dissolution of Magnox should be lower than that for pure Mg.

While counterintuitive, this conclusion is supported by the corrosion rate measurements previously made for pure Mg and Magnox dissolving in AlCl_3 solutions (Section 4.3.1), which suggested that corrosion was slightly slower for the alloy despite the high solubility of both magnesium and aluminium ions. This is to be expected for Magnox alloy (and indeed magnesium-aluminium alloys in general), which exhibits consistently greater corrosion resistance than pure Mg. In the context of enhancing corrosion for Cementisation, this can be alternatively thought of as pure Mg having a greater capacity for enabling charge transfer in concentrated salt solutions. As such it can sustain higher anodic and cathodic currents than Magnox alloy in the absence of the inhibiting qualities of the latter's aluminium component.

5.6 Conclusions

The aqueous corrosion behaviour of magnesium and its alloys is determined by a complex dynamic interface, the nature of which is intricately linked to the stability of a corrosion product film which itself depends on multiple factors, principally the solubility of the oxidised magnesium ion. Characterisation of this interface by impedance spectroscopy is not straightforward as the redox reaction depends on the coverage of adsorbed intermediates, the precise nature of which can currently only be inferred. In addition, the extent to which impedance models can be validated is limited by a lack of complementary techniques that are capable of resolving the same interfacial processes. However, to the extent that conclusions can be drawn with confidence, the following can be asserted for the case of pure Mg and Magnox alloy corroding in concentrated solutions of MgCl_2 and AlCl_3 :

1. The reaction scheme defined by Yuwono can be combined with the circuit model used by King to produce a framework that is capable of describing the filmless corrosion of Mg in concentrated salt solutions as observed throughout this work. This interpretation of the Mg dissolution mechanism is similarly able to describe the corrosion of Mg under more typical conditions, i.e., corrosion underneath a precipitated

layer of magnesium hydroxide. Where surface films are present, the dissolution of Mg is facilitated by the "ligand-assisted" Mg^*OH pathway.

2. The corrosion rate of pure magnesium metal is maximised in $\sim 4M$ $MgCl_2$. At this point, the formation of a magnesium hydroxide film is suppressed and the abundance of H^+ allows the dissolution reaction to proceed primarily by the oxidative adsorption and oxidative desorption of the Mg^*H intermediate. At higher concentrations of $MgCl_2$, the corrosion rate is limited by the availability of water required for the reduction half reaction. This is attributed to the formation of transient $MgCl_2$ surface films at local anodes.
3. Magnox corrodes at a lower rate in concentrated salt solutions due to the transient stability of aluminium oxide phases on the dissolving surface (presumed to be $AlOOH$). This in turn implies that the optimal chloride concentration for dissolution is lower for Magnox alloy than for pure Mg.

Given the relative simplicity of the $MgCl_2$ system and its ability to suppress the typical surface film on corroding Mg at concentrations $>2M$, further investigation is highly recommended. In summary, pure magnesium and Magnox alloy both undergo active corrosion in concentrated $MgCl_2$ solutions due to the improved solubility of Mg^{2+} , which effectively prevents the stabilisation of a passivating magnesium hydroxide surface layer. Under these conditions, the charge transfer resistance is substantially reduced, leading to rapid dissolution of the metal substrate.

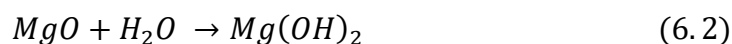
For Cementisation, this detailed investigation of the metal/solution interface during dissolution in concentrated salt solutions offers several opportunities for optimisation of the process. Principally, the observation that salt film effects appear to limit the dissolution rate at high concentration demonstrates that the solution parameters must be finely tuned to maximise the rate of reaction. In addition, and crucially, the concentration required for peak dissolution appears to be different for Magnox relative to pure Mg. Furthermore, the dissolution rate of Magnox in concentrated $MgCl_2$ appears to be limited by the transient formation of aluminium oxide/hydroxide phases. Therefore, the use of additives (e.g., acids) specifically targeted to inhibit the formation of these phases could be used to promote faster dissolution, leading to better conversion efficiency and higher product quality as the corrosion and crystallisation steps are increasingly deconvoluted.

6 Synthesis of Magnesium Oxychloride Cement by the Oxidation of Metallic Magnesium

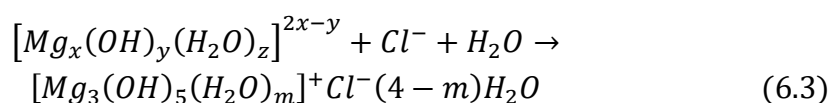
6.1 Introduction

The process of Cementisation enables the transformation of contaminated magnesium metals into Magnesium Oxychloride Cement (MOC) by enhanced corrosion and hydrolysis in concentrated $MgCl_2$ solution. This aims to eliminate the hazards of long-term storage and disposal of reactive metal wastes, i.e., chronic corrosion leading to volume expansion and hydrogen evolution. In this work, the concept of Cementisation was tested at laboratory scale by the simple mixing of metallic powders and raspings in $MgCl_2$ solutions followed by a period of curing. The samples were then processed and analysed using a range of physical analysis techniques to examine the composition of the resulting products.

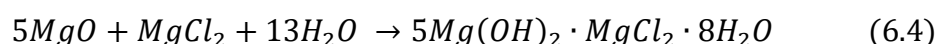
During the typical aqueous corrosion reaction of magnesium, the metal is oxidised and the resulting MgO product reacts with additional water to form $Mg(OH)_2$ as shown in Equations 6.1 and 6.2 (Esmaily et al., 2017):



However, in the presence of sufficient concentrations of Mg^{2+} ions, such as in concentrated $MgCl_2$ solutions, MgO dissolves without forming $Mg(OH)_2$, allowing the formation of complexes of the form $[Mg_x(OH)_y(H_2O)_z]^{2x-y}$ which then crystallise in the presence of Cl^- and H_2O to form hydrolysed magnesium oxychlorides (Dehua and Chuanmei, 1999):



MOC phases are typically made by mixing calcined MgO into $MgCl_2$ solution at the stoichiometric ratio of 5:1:13 as shown in Equation 6.4 (Guo et al., 2018):



It is hypothesised, therefore, that it is possible to synthesise the hydrated cement phase by substituting Equation 6.2 into Equation 6.4 i.e., by corroding magnesium metal in sufficiently concentrated solutions of $MgCl_2$:



Notably, this reaction scheme requires additional water to facilitate the oxidation reaction and generates hydrogen gas.

To investigate the synthesis of MOC from metallic feeds and demonstrate proof of concept for the process of Cementisation, the reaction scheme proposed in Equation 6.4 was tested at laboratory scale by the simple mixing of metallic magnesium fragments in MgCl_2 solutions followed by a period of curing. These samples were then processed before the presence and abundance of MOC phases was analysed via X-ray Diffraction (XRD), Simultaneous Thermal Analysis (STA) and Scanning Electron Microscopy (SEM).

Furthermore, as the process will be required to convert Magnox swarf fragments up to the centimeter-decimeter scale, the effect of particle size was investigated using two different metallic feeds: powder and raspings. This enabled comparison between feed materials on the sub-millimeter and millimeter scales as a preliminary study towards the scale up of Cementisation.

6.2 Materials & Methods

The feed materials used to synthesise cement samples were metallic Mg powder (Alfa Aesar 00869, -20+100 mesh, >99.8% pure metals basis), magnesium oxide (SLS CHE2448, light burned, >98% pure) and raspings of metallic Mg sourced from the National Nuclear Laboratory (NNL) as pictured in Figure 6.1. Calcination was not applied to any of the feed materials and thus an undefined level of water adsorption must be assumed. MgCl_2 solutions were made up using Type II deionised water and magnesium chloride hexahydrate (Bioserv BS-0382K, Assay 99-101%).



Figure 6.1 Photograph showing a representative sample of Mg powder (left) and raspings (right) used to synthesise cement samples.

Raspings were $\sim 0.5\text{mm}$ thick and varied in size, geometry and surface condition, with some showing considerable oxidation and others very little. 5 independent subsamples of raspings were taken using tweezers and image analysis in FIJI (ImageJ) was used to establish a particle size distribution.

Samples were arranged on a flat surface as shown in Figure 6.2 with scale established by the rule included in frame. Individual particles were isolated by colour thresholding for sizing via the “Analyse Particles” method. The particle size distribution was then extracted by excluding extreme values, defined as a threshold at $A \geq 0.25 \text{mm}^2$.

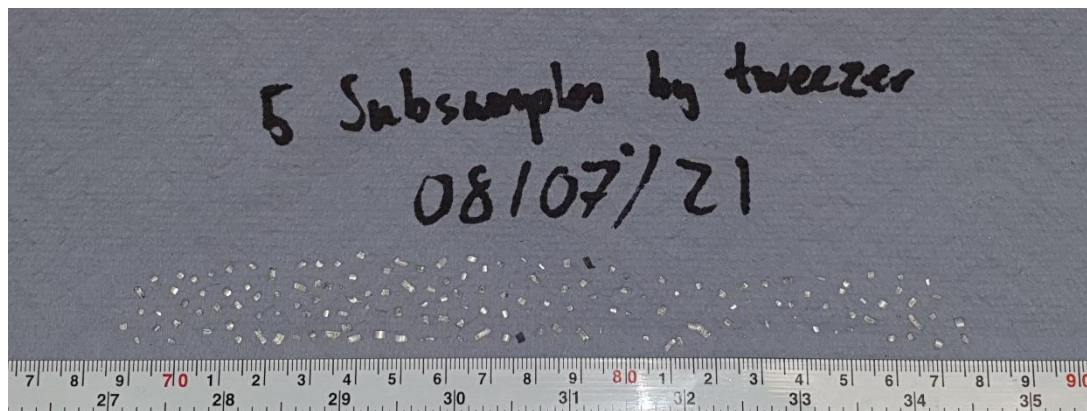


Figure 6.2 Photograph showing aggregated samples of raspings arranged on a flat surface for sizing by image analysis.

As shown in Figure 6.3, the two-dimensional surface area of the raspings ($N=146$) ranged from $\sim 0.2\text{-}6 \text{mm}^2$ with a mean of 1.7mm^2 and a median of 1.5mm^2 . Thus, while there is overlap between the size distributions of the powder and the raspings, the average size of the raspings is substantially larger than the powder particles.

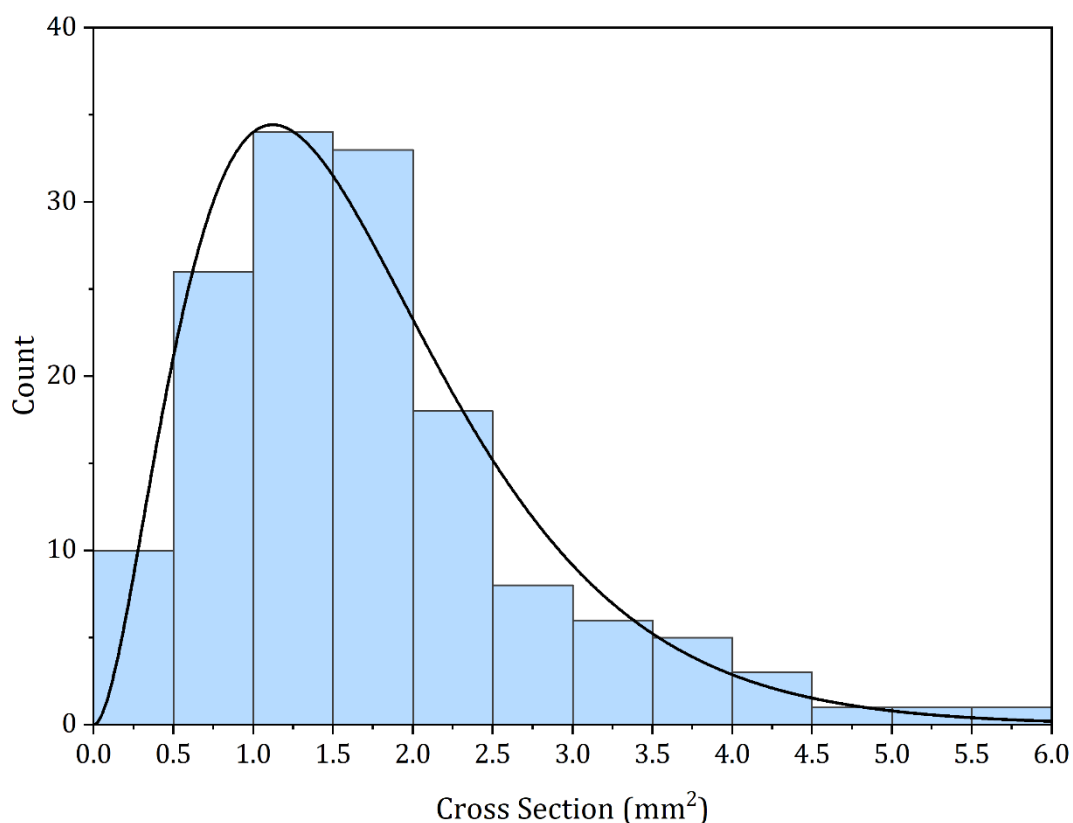


Figure 6.3 Histogram of rasping cross-sectional area determined by image analysis. Fit line corresponds to a two-parameter gamma distribution where $\alpha = 2.92$ and $\theta = 0.58$.

Elemental analysis was carried out to determine the purity of the raspings using X-ray fluorescence (XRF). Six independent 5g samples were pressed into 35mm pellets under 15 tons of pressure for 10 minutes. Pellets were then analysed using a Rigaku ZSX Primus II X-ray fluorescence spectrometer. This work was performed with the assistance of Dr. Jabbar Gardy. The average and standard deviation of significant elements is presented in Table 6.1.

Table 6.1 Elemental distribution of Mg raspings as determined by X-ray fluorescence.

	Al	Ca	Cl	Fe	K	Mg	Mn	Ni	P	S	Si	Zn
Average [wt%]	0.085	0.013	0.034	0.009	0.003	99.672	0.016	0.001	0.003	0.011	0.143	0.005
Standard Deviation	0.058	0.004	0.014	0.009	0.003	0.170	0.002	0.001	0.002	0.005	0.085	0.003

The active surface area of each feed material was determined by adsorption of nitrogen according to the Brunauer–Emmett–Teller (BET) method. This analysis was performed with the assistance of Dr. Ben Douglas. Four independent subsamples of each material were heated at 200°C for four hours to drive off moisture prior to measurement. The results of this analysis are shown in Table 6.2.

Table 6.2 Active surface area of feed materials used to synthesise cement samples. Values shown are the average and standard deviation of 4 independent samples.

Material	Surface Area [m ² g ⁻¹]
Mg Powder	0.0450 ± 0.0015
Mg Raspings	0.1114 ± 0.0069
Mg Oxide	9.3388 ± 0.1433*

The active surface area of the raspings was found to be higher than the Mg powder despite the former being substantially finer (and thus having a higher specific surface area according to geometric arguments). This may be caused by surface roughness introduced during the production of the raspings, or it may indicate a greater degree of surface oxidation, increasing the density of adsorption sites while reducing the proportion of Mg metal. Given that the Mg powders were packaged under nitrogen it is likely that there exists a substantial difference in the degree of oxidation between these materials at the time of sample preparation.

6.3 Experimental

6.3.1 Sample Preparation

For each analysis stream and feed material a set of 4 replicates was produced, each totalling 7g of material mixed and cured in sealed 15ml centrifuge tubes. Samples were prepared by adding feed material to MgCl₂ solution, mixing by inversion for 5 seconds and curing for 7 days with the screw cap tightly sealed. This curing time was selected based on the findings of previous researchers, showing that the F5 phase develops rapidly and does not require extensive

* Average of 3 samples due to error during preconditioning.

curing (Liu et al., 2017; Góchez et al., 2017). Salt solutions were stirred using a magnetic stirrer for 1 minute at 500rpm and then equilibrated for one hour before the addition of feed material. Curing took place in a sealed cabinet in the presence of an open beaker of 3.7M MgCl₂ solution to minimise changes in humidity. Temperature ($19.5 \pm 0.6^{\circ}\text{C}$) and relative humidity ($46 \pm 4\%$) were monitored using an RHT50 data logger (Extech). MgCl₂ solutions were prepared in batches to maintain independence between replicates within the same analysis stream as shown in Table 6.3.

Table 6.3 Matrix of cement samples categorised by MgCl₂ solution batch, analysis stream and fill material.

Sample ID	Analysis Technique	Fill Material	Brine Batch No.	Target Brine Mass [g]	Actual Brine Mass [g]	Target Fill Mass [g]	Actual Fill Mass [g]	Total Sample Mass [g]	Mg : MgCl ₂ Molar Ratio	H ₂ O : MgCl ₂ Molar Ratio
01r	XRD	Mg	1	5.4201	5.4283	1.5770	1.5773	7.0056	5.028	18.030
02r	STA	Mg	1	5.4201	5.4233	1.5755	1.5769	7.0002	5.027	18.030
03r	SEM	Mg	1	5.4201	5.4276	1.5768	1.5656	6.9932	4.991	18.030
04r	XRD	Magnox	1	5.4201	5.4342	1.5910	1.5814	7.0156	5.041	18.030
05r	STA	Magnox	1	5.4201	5.4446	1.5941	1.5830	7.0276	5.046	18.030
06r	SEM	Magnox	1	5.4201	5.4068	1.5830	1.6071	7.0139	5.123	18.030
07r	XRD	Mg	2	5.4378	5.4800	1.5920	1.5892	7.0692	5.066	17.951
08r	STA	Mg	2	5.4378	5.4339	1.5786	1.5669	7.0008	4.995	17.951
09r	SEM	Mg	2	5.4378	5.4054	1.5703	1.5738	6.9792	5.017	17.951
10r	STA	Magnox	2	5.4378	5.4311	1.5901	1.5816	7.0127	5.042	17.951
11r	XRD	Magnox	2	5.4378	5.4870	1.6065	1.6073	7.0943	5.124	17.951
12r	SEM	Magnox	2	5.4378	5.4575	1.5978	1.6035	7.061	5.112	17.951
13r	XRD	Mg	3	5.4250	5.4209	1.5748	1.5621	6.983	4.980	18.007

Sample ID	Analysis Technique	Fill Material	Brine Batch No.	Target Brine Mass [g]	Actual Brine Mass [g]	Target Fill Mass [g]	Actual Fill Mass [g]	Total Sample Mass [g]	Mg : MgCl ₂ Molar Ratio	H ₂ O : MgCl ₂ Molar Ratio
14r	STA	Mg	3	5.4250	5.4331	1.5784	1.5812	7.0143	5.041	18.007
15r	SEM	Mg	3	5.4250	5.4274	1.5767	1.5755	7.0029	5.022	18.007
16r	XRD	Magnox	3	5.4250	5.4401	1.5928	1.5892	7.0293	5.066	18.007
17r	STA	Magnox	3	5.4250	5.4520	1.5962	1.5794	7.0314	5.035	18.007
18r	SEM	Magnox	3	5.4250	5.4297	1.5897	1.6031	7.0328	5.110	18.007
19r	XRD	Mg	4	5.4306	5.4159	1.5734	1.5702	6.9861	5.006	18.004
20r	STA	Mg	4	5.4306	5.4320	1.5780	1.5590	6.991	4.970	18.004
21r	SEM	Mg	4	5.4306	5.3916	1.5663	1.5707	6.9623	5.007	18.004
22r	XRD	Magnox	4	5.4306	5.4198	1.5868	1.5817	7.0015	5.042	18.004
23r	STA	Magnox	4	5.4306	5.4125	1.5847	1.5870	6.9995	5.059	18.004
24r	SEM	Magnox	4	5.4306	5.4167	1.5859	1.5818	6.9985	5.042	18.004
25r	XRD	MgO	5	4.2859	4.2506	2.6870	2.6805	6.9311	5.107	12.985
26r	STA	MgO	5	4.2859	4.3079	2.7232	2.7149	7.0228	5.173	12.985
27r	SEM	MgO	5	4.2859	4.2761	2.7031	2.7231	6.9992	5.189	12.985

Sample ID	Analysis Technique	Fill Material	Brine Batch No.	Target Brine Mass [g]	Actual Brine Mass [g]	Target Fill Mass [g]	Actual Fill Mass [g]	Total Sample Mass [g]	Mg : MgCl ₂ Molar Ratio	H ₂ O : MgCl ₂ Molar Ratio
28r	XRD	MgO	6	4.3148	4.3470	2.7479	2.7462	7.0932	5.193	12.968
29r	STA	MgO	6	4.3148	4.3085	2.7236	2.7083	7.0168	5.121	12.968
30r	SEM	MgO	6	4.3148	4.3469	2.7479	2.7238	7.0707	5.150	12.968
31r	XRD	MgO	7	4.3096	4.2898	2.7118	2.6960	6.9858	5.101	12.956
32r	STA	MgO	7	4.3096	4.2838	2.7080	2.6402	6.924	4.995	12.956
33r	SEM	MgO	7	4.3096	4.3368	2.7415	2.6776	7.0144	5.066	12.956
34r	XRD	MgO	8	4.2992	4.2845	2.7084	2.6681	6.9526	5.071	12.994
35r	STA	MgO	8	4.2992	4.3414	2.7444	2.7051	7.0465	5.141	12.994
36r	SEM	MgO	8	4.2992	4.3313	2.7380	2.6950	7.0263	5.122	12.994

All samples were made up to the stoichiometric ratio corresponding to the F5 phase of magnesium oxychloride ($\text{Mg}(\text{OH})_2:\text{MgCl}_2:\text{H}_2\text{O} = 5:1:8$). For the control samples made using light burned MgO powder, this corresponded to 2.7g of fill material added to 4.3g of 4.3M MgCl_2 solution ($\text{MgCl}_2:\text{H}_2\text{O} = 1:13$). For the samples prepared from Mg metal this required 1.6g of fill material added to 5.4g of 3.1M MgCl_2 solution ($\text{MgCl}_2:\text{H}_2\text{O} = 1:18$).

Weights were determined using an analytical balance (A&D HR250AZ) and recorded at each step to ensure that molecular ratios were not significantly affected by human error. The average Mg: MgCl_2 molar ratio across all samples was 5.067 ± 0.059 , while the average $\text{H}_2\text{O}:\text{MgCl}_2$ molar ratio was 12.976 ± 0.001 for the control samples (MgO) and 17.998 ± 0.0291 for the metallic samples. Thus, the largest error was in the proportion of fill material, with the average sample overfilled by approximately 1% with a random error also of ~1%, which is unlikely to lead to a significant difference between samples.

After the curing period samples were crushed to a fine powder using an agate pestle and mortar to prepare them for analysis. As the control samples were considerably stronger a steel pestle and mortar was used to fracture the monoliths before processing in the agate pestle and mortar.

Trial tests using hydration stopping techniques (heating and solvent rinse using acetone/isopropyl) led to significant degradation (to $\text{Mg}(\text{OH})_2$) and/or alteration of the mineral phases, likely due to the non-hydraulic nature of MOC making them highly sensitive to changes in water content and solubility. As a result, the samples produced for this study were simply crushed and not subjected to any hydration stopping techniques.

6.3.2 Analysis

SEM imaging was performed using a Carl Zeiss EVO MA15 at the Leeds Electron Microscopy and Spectroscopy Centre (LEMAS) with the assistance of Stuart Micklethwaite. Images were captured over a range of magnifications (200X-10KX) with an accelerating voltage of 20kV. This analysis was performed 9 days after post-curing sample processing.

STA was performed using a Mettler Toledo TGA/DSC3+ from 30-600°C at a ramp rate of 10°C per minute with air blown over the sample. These conditions were chosen to match the methods of previous researchers in characterising the thermal response of sorel cement systems (Xia et al., 1991) for the purpose of comparison against products formed from metallic feed material. The thermal analysis work reported here was performed with the assistance of Dr.

Adrian Cunliffe. This analysis was performed 10 days after post-curing sample processing.

XRD analysis was performed using a Bruker D8 diffractometer using Cu K α X-rays with samples mounted in a PMMA powder specimen holder. Scans were performed over the 2θ range 10-70° with a step size of 0.033 at a scan rate of 0.1°s⁻¹. This analysis was performed 56 days after post-curing sample processing.

Efforts were made to perform simultaneous analyses and thus remove aging as a variable. However, due to operational issues and particularly with the XRD analysis, this was not possible. This could have been mitigated using hydration stopping techniques, but due to the non-hydraulic nature of the cement system no such technique exists that does not substantially alter the nature of the samples. As a result, disparate aging cannot be disregarded and must be taken into account during discussion, particularly between XRD and SEM/STA results.

6.4 Results & Discussion

Visual observation of samples immediately after mixing revealed different settling regimes between each feed material in the MgCl₂ solutions. Solid MgO was easily suspended into the characteristic white slurry, while the metallic feed materials settled to the bottom of the vessels. Bubbles of hydrogen gas formed by the rapid corrosion of metal provided a degree of self-agitation, sufficient to keep the powder particles suspended while the raspings remained settled. Heat generated from the corrosion reaction caused vials to become hot to the touch, although this was not quantified. Metal-formed samples were generally found to harden overnight following mixing, although a crackling sound was still audible in close proximity, likely indicating the continued escape of hydrogen gas and presumably ongoing corrosion/hydrolysis.

After curing, while the control samples (MgO) had formed cohesive monoliths the samples generated from metallic feeds showed little cohesion or strength. This likely resulted from hydrogen gas generated during the corrosion reaction creating substantial voids in the cement matrix, preventing the formation of a cohesive network of crystalline phases. In addition, the friability of these samples necessarily prevented the application of a number of common testing techniques, such as setting tests, compressive strength testing and leach testing.

6.4.1 X-ray Diffraction

Obtained diffractograms were compared to reference patterns in the ICDD database PDF-4+ 2021 and an exhaustive search was performed with comparison between alternative characterisations of the expected MOC phases (Sugimoto et al., 2007; Guo et al., 2018). Several expected phases were found to have negligible presence in the measured spectra, including the F2 and F9 phases as well as chlorocarbonate and periclase (representing unreacted/hydroxylated MgO). The contribution of impurities was assumed to be below the limit of detection and was therefore neglected. The reference patterns selected to represent the components in the samples in this study are listed in Table 6.4.

Table 6.4 Reference patterns used for quantitative analysis of diffraction patterns obtained from cement samples. Magnesium (Mg) was only included for samples generated from metallic feeds.

Mineral Phase	Chemical Formula	PDF Card No.
F5	$5\text{MgO}\cdot\text{MgCl}_2\cdot 13\text{H}_2\text{O}$	04-014-8836
F3	$3\text{MgO}\cdot\text{MgCl}_2\cdot 11\text{H}_2\text{O}$	04-011-5211
Brucite	$\text{Mg}(\text{OH})_2$	04-013-9511
Bischofite	$\text{MgCl}_2\cdot 6(\text{H}_2\text{O})$	04-006-8958
Magnesium	Mg	04-015-2580

By comparison to reference patterns, all the major and minor peaks observed in the measured diffraction spectra were assigned to their respective phase as shown in Figure 6.4 for an example spectrum.

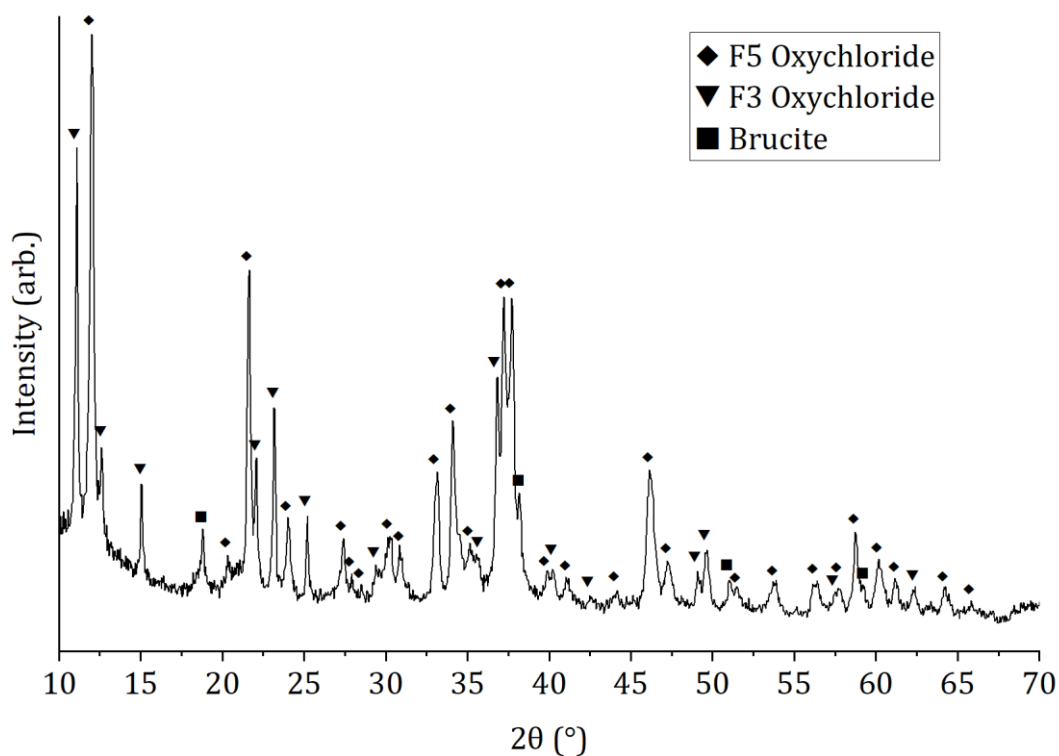


Figure 6.4 Background subtracted scattering data for sample 34r (MgO control), matched to component phases by comparison to reference patterns.

All measured diffraction spectra exhibited excellent agreement with reference patterns, with matching achieved for all components. For the minor components of Bischofite and metallic Mg, direct matching was not possible due to significant overlap between reference patterns (most notably between F3 and metallic Mg at $2\theta = 36.7^\circ$). Thus, there is no difference between the major components in all the produced samples, save for their relative intensities and the absence of metallic Mg in the control (MgO) samples. A comparison between spectra obtained from metallic feeds (powder and raspings) is shown in Figure 6.5.

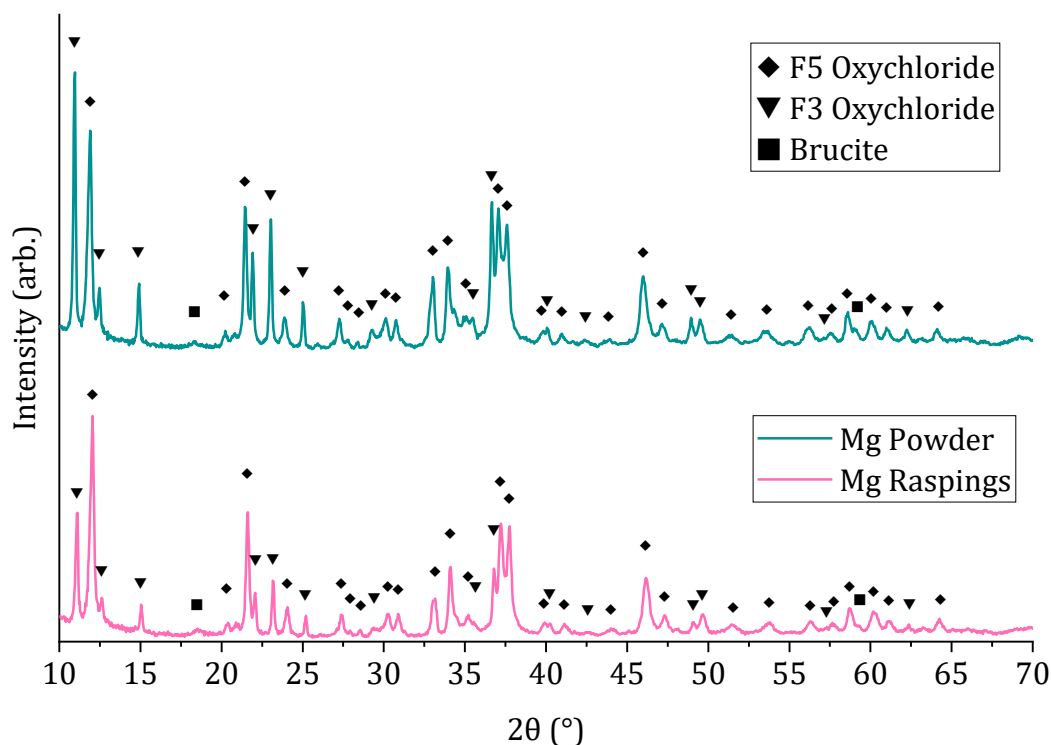


Figure 6.5 Background subtracted scattering data for samples 13r (Mg powder, top, green) and 16r (Mg Raspings, bottom, red), matched to reference patterns.

Notably absent is the major peak at $2\theta \sim 43^\circ$ regularly observed by other researchers (Sugimoto et al., 2007; Liu et al., 2017; Chen et al., 2019), attributed variously to MgO and/or MgCO_3 . The absence of MgO implies that the mixing applied during sample preparation was sufficient to, at minimum, achieve full contact between the liquid and solid phases, promoting total hydrolysis/hydroxylation. Formation of MgCO_3 is commonly attributed to the action of atmospheric carbon dioxide (Walling and Provis, 2016; Guo et al., 2018). It is likely that the absence of MgCO_3 in the samples prepared for this study is a consequence of tighter controls on feed material (small batches at reagent grade or better) and atmospheric isolation i.e. the use of screwcap enclosures vs. samples left open to atmosphere or sealed with polymer films as produced in previous studies (Li et al., 2016; Chen et al., 2019).

A quantitative phase analysis of each sample was performed via the automatic Rietveld refinement protocol contained within the Highscore XRD analysis software suite. No reference material (e.g., alumina) was included in the samples. Therefore, the Degree Of Crystallinity method was used to estimate the proportion of amorphous/gel type oxychloride phase as utilised by previous researchers for the magnesium oxychloride system (Madsen et al., 2011; Liu et al., 2017; Góchez et al., 2017). This method assumes that all the

signal, after background subtraction, that cannot be attributed to crystalline phases belongs to an amorphous phase. This in turn requires the assumption that there is only one amorphous phase. This assumption is considered to be valid in this case, as in the work of other researchers the only amorphous phase that has been identified is the F5 amorphous MOC (Liu et al., 2017; Góchez et al., 2017). The quantity of each phase is listed in Table 6.5 averaged for each feed material.

Table 6.5 Relative phase composition of cement samples as determined by quantitative Rietveld analysis of diffraction spectra. Quantities are expressed as the average weight fraction (wt%) \pm standard deviation.

	Mg Powder	Mg Raspings	MgO
F5 MOC	68.9 \pm 5.5	57.2 \pm 1.7	64.8 \pm 1.5
F3 MOC	17.0 \pm 2.4	24.6 \pm 1.1	22.2 \pm 1.3
Amorphous/Gel MOC	11.9 \pm 7.3	15.4 \pm 0.5	9.6 \pm 1.1
Brucite (Mg(OH)₂)	1.0 \pm 0.2	0.4 \pm 0.0	3.1 \pm 1.3
Bischofite (MgCl₂.6H₂O)	0.1 \pm 0.1	0.7 \pm 0.3	0.3 \pm 0.2
Mg Metal	1.1 \pm 0.2	1.6 \pm 0.2	N/A

From XRD observations, the degree of conversion to the MOC phases (F5, F3 and amorphous) is consistently high, with an average of $97 \pm 1\%$ over all samples, both metal and oxide-formed. In the control samples formed from MgO powders, the amorphous phase content was determined to be $\sim 10\%$ by weight, consistent with measurements made by other researchers for systems matching the stoichiometry of the F5 phase (Góchez et al., 2017). While the F5 phase is dominant, a substantial fraction of F3 was also present. The F5 phase has previously been shown to be metastable and is transformed into the F3 phase over time (Guo et al., 2018). The F3 content of the MgO samples is consistent with samples that have been aged between 28-100 days (Liu et al., 2017). It must be noted that due to the extended period between samples processing (crushing) and XRD analysis, the effect of atmospheric decomposition of F5 to F3 cannot be deconvoluted from that which may have been present at the time of processing. Nevertheless, the control samples formed from MgO powders in this work are representative of MOC samples synthesised by other researchers.

A small fraction of non-MOC phases, namely Brucite and Bischofite, was found in all the control samples (Table 6.5). Hydroxylation of MgO to form the Mg(OH)₂ phase occurs in the MgO-MgCl₂-H₂O system when there are insufficient H⁺ ions to enable the neutralisation reaction (Dehua and Chuanmei, 1999). Furthermore, Mg(OH)₂ formed from the MgO reagent by interaction with moist air prior to mixing would have to be dissolved before it can contribute to the formation of oxychlorides. Thus, the prevalence of non-hydroxylated residues can be attributed either to pre-existing phases that do not dissolve as readily as MgO, or to the post-mixing hydrolysis of MgO in regions of insufficient [H⁺] which form as the neutralisation reaction causes the pH of the system to increase (Bilinski et al., 1984). In either case, the proportion of non-MOC residues is small and does not invalidate comparison between the MgO controls and the metal-formed cements, nor when comparisons are extended to the wider literature concerning Sorel cements.

For samples formed from metallic Mg powders a high degree of conversion to MOC phases was observed, with ~1% residual metallic content. While the target phase (F5) content was maximised for the case of metallic powders, there was substantially greater variance in the F5 content in comparison to samples formed from metal raspings or MgO. This is attributed to a much greater variation in the proportion of the amorphous phase, which implies that the final crystallisation phase of the reaction is being significantly affected by an additional variable. This may be attributable to the “self-mixing” of the powders by the hydrogen bubble formation, growth and detachment that was observed following mixing into the MgCl₂ solution. This agitation represents an additional mode of transport of reactants and products that would typically be dominated by diffusion in a static mixture, particularly as formation of the gel phase reduces the availability of liquid water. In addition, the stirring effect could have a detrimental impact on the crystallisation process, which has been shown to initiate shortly after mixing, ~1-2 hours for standard MgO formulations depending on temperature (Góchez et al., 2017), although from visual observations the level of induced shear is low and crystal growth could feasibly continue unimpeded. Ultimately, the total degree of conversion to MOC phases for these samples remains consistent with the MgO control and thus the base efficiency of the process is unaffected.

However, despite increased variation in the formation of MOC phases, this mechanism presumably increases the rate of dissolution by introducing convection, which may be increasing the supply of water to the unreacted metal surfaces. This may explain the higher average degree of crystallinity observed

for metallic powders relative to the larger raspings (which were observed to form a settled bed unperturbed by hydrogen evolution). In these circumstances, the shrinking core effect would be more pronounced, and the larger average particle size would require faster penetration by the dissolution process before hydrolysis exhausts the availability of water for the corrosion reaction. Given that the Cementisation process is intended for the treatment of metallic fragments on the decimeter scale, it is not clear whether this behaviour will be relevant at larger scales where swarf fragments could be expected to be much less buoyant. Nevertheless, an assessment of self-agitation could be included in further investigations on the effect of stirring, which will itself be highly relevant to the development of this process.

Cement samples generated from metallic raspings demonstrated a high degree of conversion to the MOC phases, although there was a small but significant increase in the amount of unreacted metal relative to the samples formed from metallic powders. In addition, the average degree of crystallinity obtained (~85%) was significantly lower than that of the MgO control (~90%). These results can both be attributed to a lower rate of dissolution, which is to be expected given the larger particle size and thus lower overall contact area between the metallic and aqueous phases. The degree of dissolution is further reduced by the onset of crystallisation as it removes water from the system, leaving unreacted cores of metallic Mg. This can be understood more generally as an example of a shrinking core type reaction, where the “ash” is comprised of the various oxide products (Levenspiel, 1998).

Similarly, as the crystallisation of the amorphous phase into F5/F3 oxychloride requires both water and dissolved chloride (Dehua and Chuanmei, 1999), lower availability of water due to competing corrosion and crystallisation will result in a higher proportion of the amorphous phase in the end product. While the degree of conversion remains very high for the case of metallic raspings as feed, these indicators represent a small but significant decrease in quality relative to the fine powders. Particle size therefore has a significant effect on the ability of the Cementisation process to reduce chemical reactivity and produce a cementitious product.

MgCl₂ content in the metallic powder samples appears to have been all but exhausted, implying that the dissolution and conversion of Mg ions to MOC phases was highly efficient following oxidation. Once the MgCl₂ content dropped below 2M, the remaining ions in solution would be precipitated as Mg(OH)₂ (Dehua and Chuanmei, 1999). It is possible that the substantial heat generated by the oxidation reaction led to a loss of water from the system

despite tight sealing, creating a deficit that prevented total conversion. For larger samples the system would likely be less sensitive to water content and could be counteracted by the progressive addition of supplementary water.

6.4.2 Thermal Analysis

The mass of each subsample used for thermal analysis is listed in Table 6.6.

Table 6.6 Table of data concerning subsamples analysed by STA.

Sample ID	Fill Material	STA Subsample Weight [mg]	TGA Mass Change [mg]	TGA Residue [mg]
02r	Mg	20.223	-10.6419	9.2770
05r	Magnox	19.609	-10.1385	8.6749
08r	Mg	19.856	-10.5962	8.8689
10r	Magnox	19.456	-10.1067	8.4939
14r	Mg	20.603	-10.8408	9.3129
17r	Magnox	19.610	-10.2248	8.4759
20r	Mg	20.930	-11.0177	9.5119
23r	Magnox	19.963	-10.4766	8.6799
26r	MgO	20.738	-10.1730	8.1879
29r	MgO	20.598	-10.2045	8.1699
32r	MgO	20.012	-9.9774	7.9169
35r	MgO	19.877	-9.9511	7.8819

When grouped by feed material, it is notable that there is a significant difference in the discrepancy between the starting mass and the mass lost during thermal analysis (i.e., residual mass minus mass change in Table 6.6). The MgO samples have the largest missing mass (~9%), followed by the samples formed from Mg raspings (~4%) and finally those formed from Mg powder (~2%). This can be attributed to differences in the degree of unbound water, which may have evaporated during the time between processing and analysis, or during sample preparation for TGA (including time spent in the autosampler). The MgO-formed samples, which formed cohesive monoliths, could easily contain the largest amount of unbound water as they were the only samples that could feasibly have formed a significant pore network. Thus, when broken down into powder for processing, proportionally more unbound water would be exposed to the atmosphere and evaporate as a result.

A smaller but nonetheless significant difference exists between samples formed from the two metallic feeds. This could be explained variously by different confounding effects. For example, the larger raspings particles may have acted

as growth sites for local pore networks, containing proportionally more unbound water, which was then exposed by the milling process, or by differences in the initial rate of reaction upon mixing into the MgCl_2 brines.

Alternatively, the powder samples, which are substantially smaller than the raspings and thus expected to present a larger specific surface area for metal-solution interaction (and thus corrosion), would be expected to dissolve (and thus release energy) faster, resulting in a higher peak temperature during dissolution. Despite the use of screwcap enclosures, the resulting gas pressure may have led to a significantly higher loss of unbound water during this initial stage. The resulting powders would therefore have a lower water content at the point of subsampling, and thus lose proportionally less mass during the preparations for STA analysis. This could have been verified by measuring the mass of the samples (including their enclosures) immediately after mixing and then immediately prior to processing, although these measurements were not performed as part of this study.

Finally, a greater proportion of unbound water might remain in the raspings-formed samples due to a lower degree of total conversion to MOC phases. This is consistent with the results of XRD analysis and could plausibly arise due to stalling of the corrosion reaction caused by crystallisation of the MOC phases, which would create a blocking film around the “cores” of unreacted Mg metal. This would result in a higher proportion of unbound water trapped in the sample which would subsequently be able to evaporate following processing.

Differential Scanning Calorimetry (DSC) data obtained from STA measurements is presented in Figure 6.6. Samples 02r and 10r are identified as outliers due to differences in starting temperature and were removed from averaging for both DSC and TGA. The results for each feed material are presented as a confidence interval representing the standard deviation of heat flow measurements.

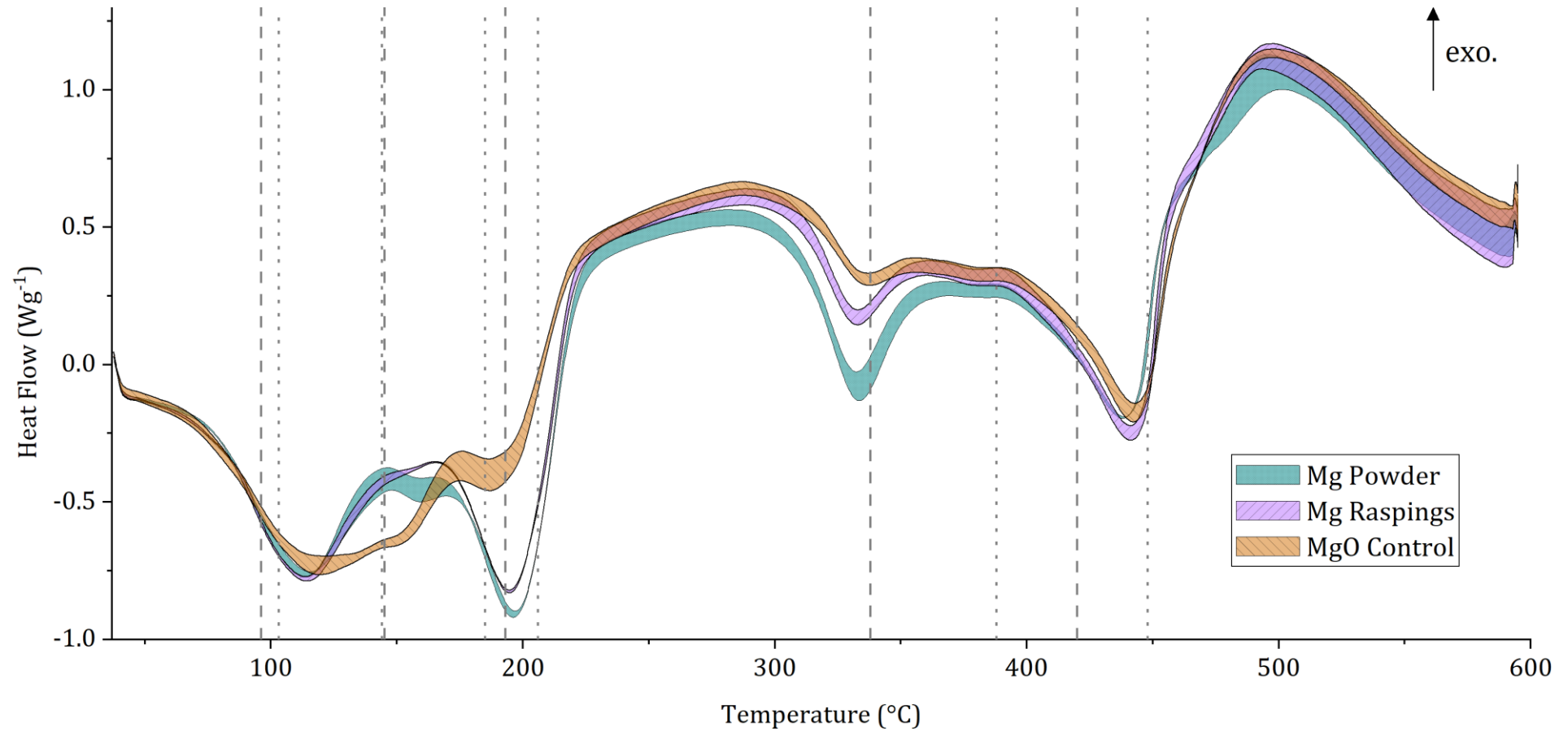


Figure 6.6 Plot of aggregated DSC results obtained during STA. Data for each feed material are presented as a confidence interval representing the standard deviation of heat flow measurements. Reference lines are plotted for transitions corresponding to the F5 (dashed) and F3 (dotted) phases as determined by previous researchers (Xia et al., 1991).

All samples exhibited endothermic behaviour characteristic to MOC phases, with dehydration of the hydrated phases occurring over the range $\sim 100\text{-}200^\circ\text{C}$ followed by decomposition of dehydrated cementitious phases and residues over the range $\sim 300\text{-}500^\circ\text{C}$ (Xia et al., 1991; Li et al., 2016; Chen et al., 2019). This suggests a high degree of conversion to MOC phases was achieved for all samples. Note that the melting point of magnesium (650°C (J Rumble, 2020)) is beyond the upper bound of this test, therefore there is not expected to be any contribution from unreacted metallic phases to heat flow.

While the agreement between observed peaks and reference data is generally good, a substantial overlap between peaks corresponding to the F5 and F3 phases was observed for all samples. This is due to the proximity of the transition points and, from XRD analysis, the comparable proportions of each phase, such that neither could be neglected. The presence of the amorphous MOC phase may also hamper resolution of the F5 and F3 phase, either by introducing additional unique peaks or by in-situ decomposition during the temperature ramp. It was not possible, therefore, to distinguish the enthalpy contributed by each transition and accurately quantify the relative proportion of each phase via DSC for comparison with XRD analysis.

The single exception is the peak observed in all samples at $300\text{-}350^\circ\text{C}$, which is attributed to the decomposition of dehydrated F5 oxychloride (Xia et al., 1991; Dinnebier et al., 2011). The relative intensity of this decomposition peak suggests that the proportion of F5 phase in the raspings samples was higher than in the MgO control. However, in contrast to the XRD data the corresponding dehydration peak at $\sim 200^\circ\text{C}$ would appear to suggest a lower level of F5 content in the control samples. It is possible that the F5 content of the samples generated from raspings experienced a greater degree of conversion to the F3 phase in the interim period between processing, thermal analysis and XRD analysis, but without confident deconvolution of DSC data this cannot be confirmed. Furthermore, it bears restating that comparison between the thermal and XRD data is undermined by the difference the time elapsed after processing and before analysis. For example, it is known that the F5 is metastable and decays to the F3 phase over comparable timescales (Guo et al., 2018).

Thermo-Gravimetric Analysis (TGA) data is presented in Figure 6.7. The results for each feed material are presented as a confidence interval representing the standard deviation of weight measurements.

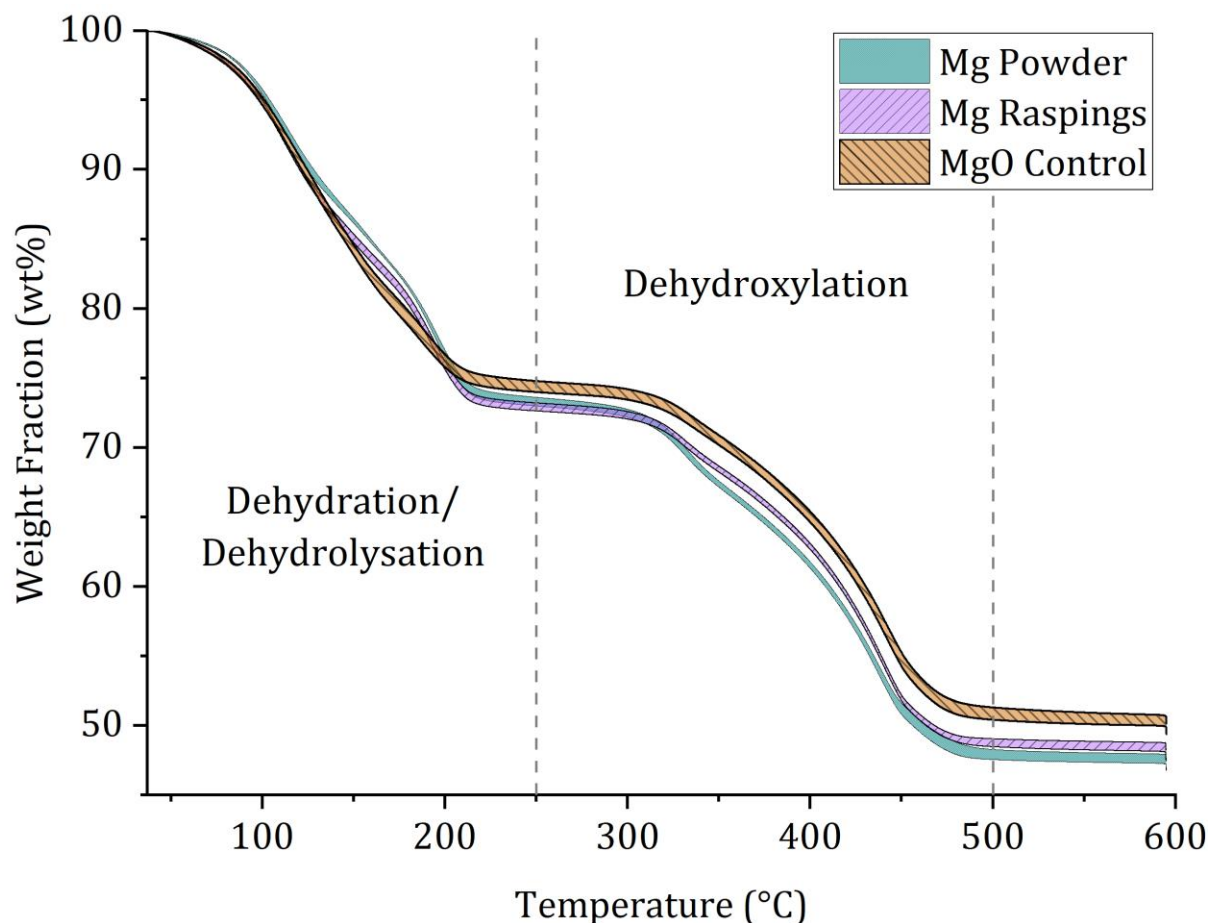


Figure 6.7 Plot of aggregated TGA results obtained during STA. Data for each feed material are presented as a confidence interval representing the standard deviation of weight measurements. After averaging, the data were normalised to originate at 100%.

TGA mass loss measurements were normalised to start at 100% weight fraction before the averaging shown in Figure 6.7. While this had no effect on the average value (versus normalisation post-averaging), it does alter the standard deviation between replicates. The error, forced to zero at the origin by the normalisation, is therefore skewed, although the total variance is not significantly changed and was generally increased by the normalisation process (increased for Mg powder and MgO, slightly decreased for raspings).

The high degree of internal consistency and significant differences in residual masses shows that significant differences exist between the three feed materials. The features previously noted from DSC spectra are visible in the TGA results, particularly the differences in dehydration between the metallic and non-metallic feeds in the range 150-200°C as well as the differences in the decomposition of F5 oxychloride at ~330°C. Again, the proximity of phase transitions makes deconvolution impossible for the purpose of quantifying the relative proportions of MOC phases.

The MgO control samples lose significantly less mass than the metal-formed samples in both the dehydration/dehydrolysis and dehydroxylation phases of the temperature ramp. This implies a lower degree of bound water was present in these samples, implying a lower overall degree of conversion to MOC phases, which is consistent with the results of XRD analysis. As previously discussed, this likely resulted from the conversion of MgO to Mg(OH)₂ due to exposure to atmospheric water prior to the mixing of samples.

In the middle of the dehydration/dehydrolysis phase (approx. 125-200°C), the MgO samples lost mass at the highest rate, followed by the samples formed from raspings and finally those formed from Mg powders. This may be indicative of the differences in F5 & F3 content between the sample groups, however the corresponding DSC peak (Figure 6.6) can be attributed to both phases (Xia et al., 1991). Ultimately, there is no significant difference between the mass lost by the metal-formed samples at the end of the dehydration/dehydrolysis phase, implying that there is no significant difference in the total MOC content, consistent with the XRD results.

Similarly, the divergence in mass loss between the metal-formed samples in the interval 330-450°C may indicate differences in the proportion of the MOC phases. In this instance, the peaks at 330°C and 450°C can be attributed to the F5 and F3 phases respectively (Xia et al., 1991). Which implies that there is a greater proportion of F5 in the Mg powder samples and a greater proportion of F3 in the Mg raspings samples (relative to each other). This is again consistent with the XRD results, but again without confident deconvolution of the DSC data, this conclusion cannot be fully supported.

6.4.3 Microscopy

Micrographs of processed samples (dry powders, see Section 6.3.1) were surveyed for qualitative evidence of crystalline magnesium oxychlorides. The image shown in Figure 6.8 is a micrograph of sample 33r, chosen as representative of the microscale structure of the control samples.

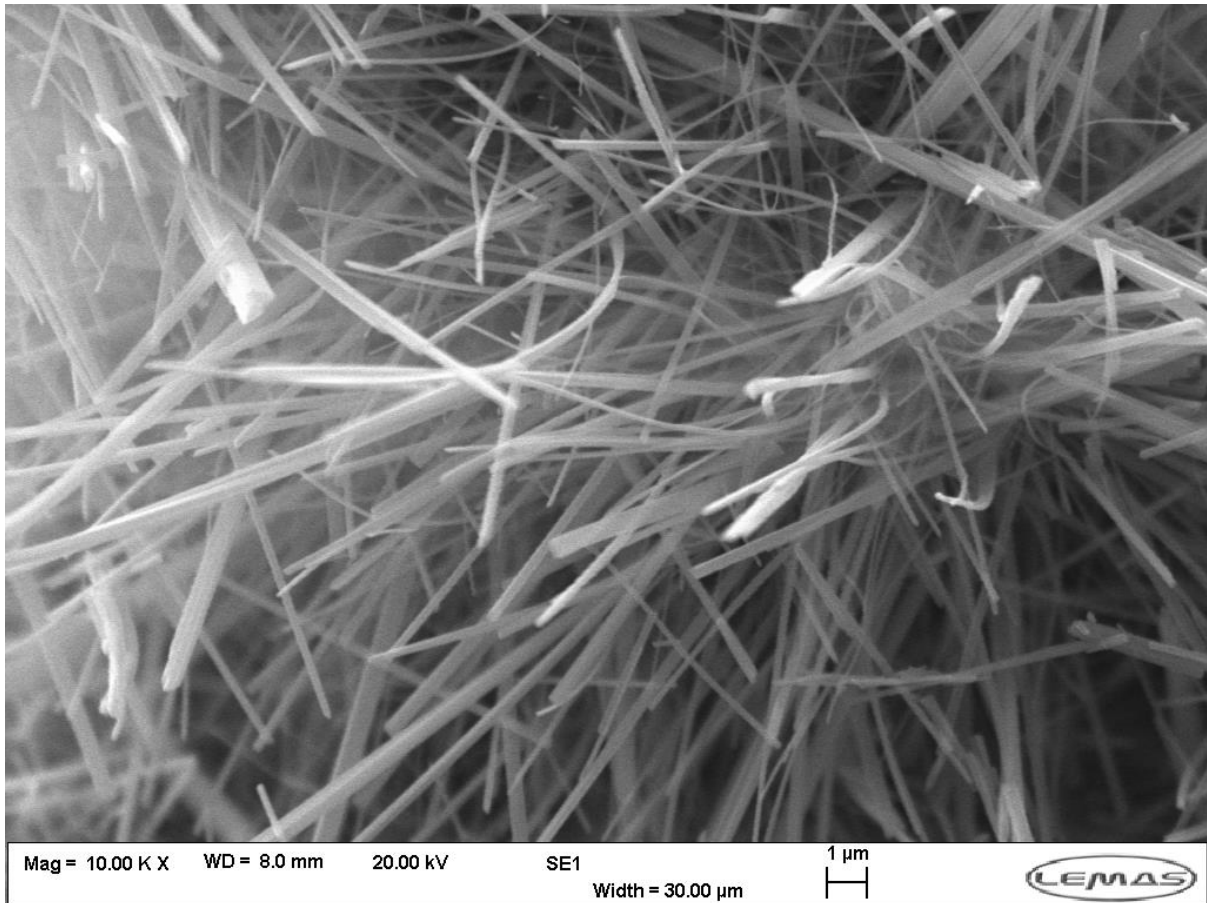


Figure 6.8 Representative micrograph of processed cement powder from sample 33r (MgO control). This image was acquired in Secondary Electron (SE1) mode.

The surface of processed cement samples formed from MgO powders are dominated by crystals of the F5 and F3 phases, described variously as “needle-like” and “scroll-tube whiskers” by previous researchers (Dehua and Chuanmei, 1999; Walling and Provis, 2016; Guo et al., 2018). Crystals are well developed and there is no evidence of substantial brucite platelets or other unreacted residues, consistent with a high degree of conversion to hydrated oxychlorides.

Comparison with micrographs from metal samples (Figure 6.9**Figure 6.10** and Figure 6.10) shows similar prevalence of MOC crystals, with no evidence of substantial residues or unreacted metal. Note that metal particles likely react as shrinking cores with products precipitating on the surface and as such any unreacted metal is unlikely to be visible without sectioning or transmission-based imaging.

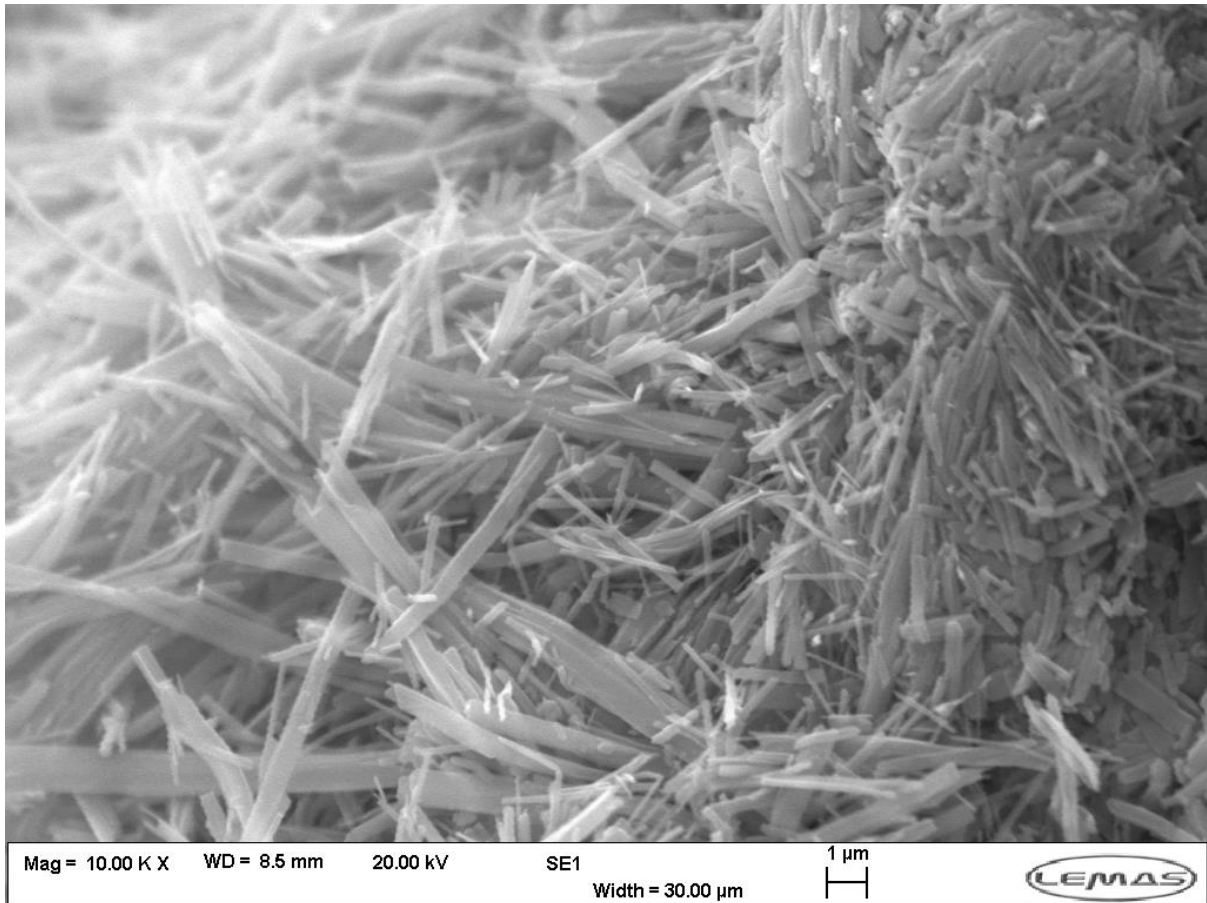


Figure 6.9 Representative micrograph of processed cement powder from sample 21r (Mg powder). This image was acquired in Secondary Electron (SE1) mode.

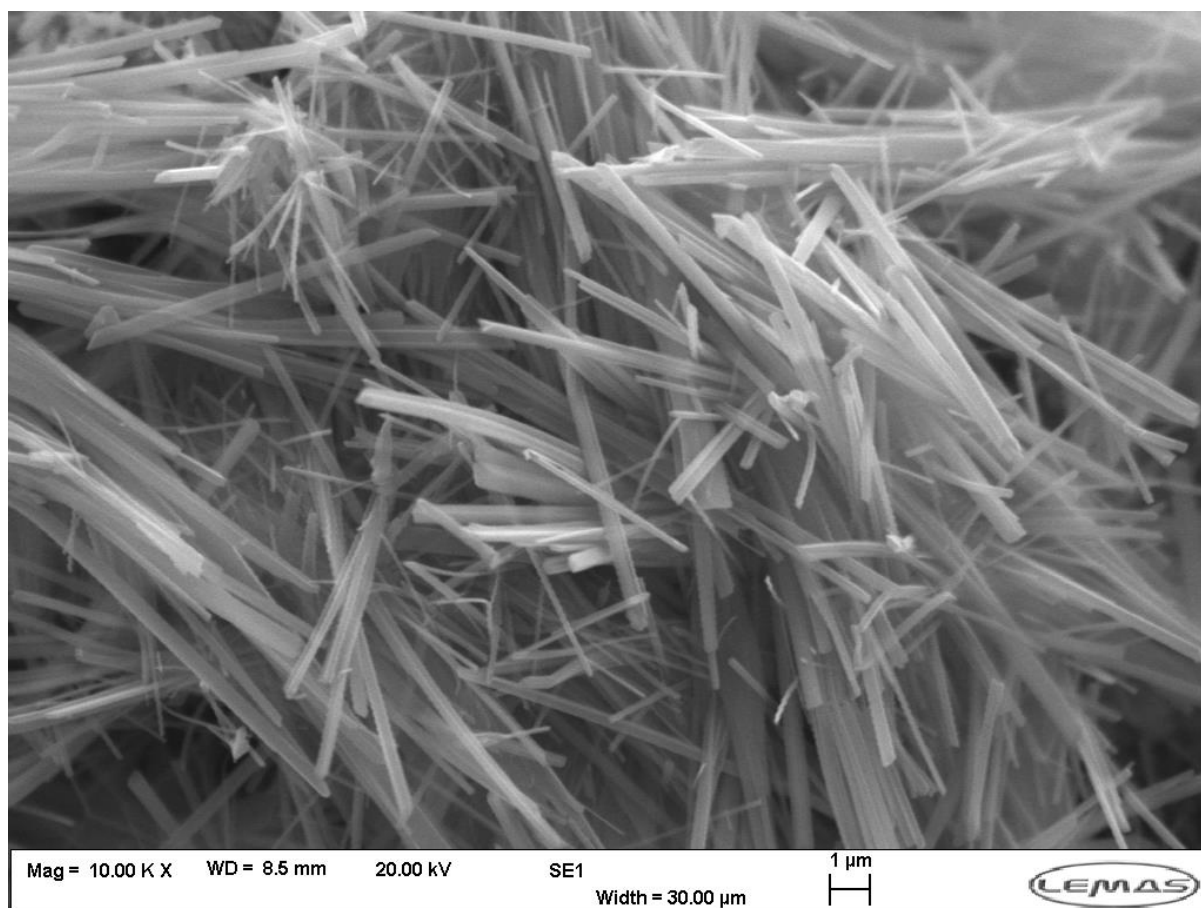


Figure 6.10 Representative micrograph of processed cement powder from sample 24r (Mg raspings). This image was acquired in Secondary Electron (SE1) mode.

Qualitatively speaking there is little to differentiate between the size and quality of crystals formed from Mg powder and those formed from raspings across the full set of micrographs. However, crystals of the MOC phases formed from metallic feeds appear to be shorter and less well developed than in the control samples. The “broken up” appearance is unlikely to be an artifact of sample processing as all samples were treated identically. Instead, the difference likely results from conditions during crystallisation, either by physical occlusion by hydrogen bubble formation or as a result of the time-delayed availability of Mg^{2+} ions introduced by the oxidation and dissolution of Mg metal.

In the control case, rapid neutralisation and dissolution of the MgO feed ensures that the full quantity of Mg^{2+} ions are available almost immediately, satisfying the stoichiometric ratios and allowing the maximum possible time for complexes to form, combine and crystallise. For metallic feeds, the supply of magnesium ions is progressive and dependent on the rate of the corrosion reaction. This then amounts to a race condition whereby the corrosion and crystallisation reactions compete for the same reactants, specifically water. When the water in solution is exhausted the crystallisation stalls and any remaining metal remains unreacted. Nevertheless, imaging of these samples shows

that a high degree of conversion to MOC phases is achievable through simple mixing for feed sizes up to mm-scale.

6.5 Conclusions

The results of XRD, STA and SEM analysis demonstrate that >95% conversion of metallic magnesium to magnesium oxychloride cements can be achieved by simple mixing in $MgCl_2$ with additional water to enable the oxidation reaction. In fact, when considering the total cement content (F5 + F3) by weight, the metallic samples are not significantly distinguishable from the control samples formed by the standard method. However, there remain significant differences between the three product groups that must be examined and addressed as the development of Cementisation moves through scale up towards industrial deployment.

XRD analysis determined that a small fraction of metal remained unreacted for the metallic feeds, implying that the corrosion reaction stalled due to the exhaustion of water and precipitation of solid products. At the same time, SEM micrographs showed that the crystalline phases in these samples were less well developed than in the control samples. This highlights the need to optimise the rate and progression of the corrosion reaction as it is the defining step that determines the quality of the cement products. Suggested improvements to be examined include the use of acids to delay hydroxylation (and potentially increase the rate of corrosion) as studied by previous researchers (Chen et al., 2019). Furthermore, dynamic addition of water could be evaluated, i.e., initiating the corrosion reaction at a higher $MgCl_2$ concentration and adding water continuously during the reaction to satisfy stoichiometry and account for losses from oxidation and evaporation.

Physical inspection of the samples during processing showed that the metal-formed samples were easily friable, presumably because of the ongoing hydrogen evolution from the oxidation reaction preventing the consolidation of a cohesive monolith. STA analysis also showed that variance in the hydrated content between samples was higher for samples formed from metal than for the control samples, implying that the hydroxylation process is less consistent when combined with the oxidation reaction. It is possible that both these issues could be addressed through continuous mixing, which could remove gas holdup and increase the rate of oxidation while also improving the homogeneity of the product. Nevertheless, the high degree of conversion demonstrated for raspings shows that the process is effective even in situations where the feed material forms a settled bed.

7 Conclusions

In this thesis, a new process for stabilising contaminated metallic magnesium wastes was proposed, built on previous proposals for treatment via enhanced corrosion (Morris, Wickham, et al., 2009). This process, termed Cementisation, utilises the coincidence of two observations: that magnesium metal oxidises at an exceptionally high rate in concentrated solutions of magnesium chloride and that magnesium oxide dissolves and reprecipitates as magnesium oxychloride cements under the same conditions (Casey and Bergeron, 1953; Guo et al., 2018). By this method, the chemical reactivity of the metallic species can be effectively removed and stabilised into a cement form suitable for disposal, all in a simple two-step reaction process that can be executed in situ without complex manipulation of contaminated materials.

To demonstrate the viability of Cementisation, this work presents a proof of concept at the laboratory scale, with subsequent development towards a comprehensive understanding of the key reaction step, i.e., the corrosion of Mg and Magnox in concentrated salt solutions. The objectives of this effort were summarised via the following hypotheses:

1. Magnesium oxychloride cement can be produced from the corrosion products generated during dissolution of metallic Mg in MgCl_2 solution
2. MgCl_2 solutions with a concentration greater than 2M promote rapid, active and uniform corrosion of magnesium metal.
3. Hypotheses 1 and 2 remain true for the case of Magnox alloy (Al80)

In this section the conclusions of Sections 4, 5 and 6 will be summarised and the extent to which their findings support these hypotheses will be evaluated. Furthermore, these conclusions will be examined within the context of the development of Cementisation. Opportunities for further work are highlighted in the following section, both with respect to process development and for deepening the understanding of the fundamental science.

7.1 Kinetics of Pure Mg and Magnox Dissolution

The corrosion rate of pure Mg and Magnox alloy was measured in concentrated MgCl_2 and AlCl_3 solutions by the gravimetric hydrogen evolution method. For Cementisation the system of primary interest is that of Magnox/ MgCl_2 , for which the optimum dissolution rate was determined to be $0.265 \pm 0.045 \text{ mmh}^{-1}$ at 50°C . While this is extremely rapid for a corrosion reaction, it may not be sufficient to fully dissolve fragments of Magnox swarf before the crystallisation of MOC begins to compete for H_2O and Cl^- , which has been shown to initiate in less than an hour in MgO systems at this

temperature (Góchez et al., 2017). Trials using full scale fragments up to several mm thick will be required to definitively prove the viability of Cementisation and further optimisation of the solution conditions may be required to underpin the process.

At 60°C the corrosion rate was significantly reduced by the formation of a partially protective surface layer. This observation was corroborated by thermochemical calculations which predicted that a Boehmite (AlOOH) phase stabilises above 50°C in systems where aluminium is present at $>2\mu\text{M}$ concentration. The activation energy of dissolution was calculated to be 48kJmol^{-1} , indicative of a regime where the reaction is controlled by a mixed chemical/transport step (Roller, 1935).

The observation of temperature-induced passive film formation on Magnox in 4M MgCl_2 is of substantial consequence to the development of Cementisation. The rapid oxidation of large quantities of magnesium is expected to release a large amount of heat, which may be sufficient to raise the solution temperature above the 50°C threshold. If passivation is induced then the reaction could stall, such that the corrosion reaction is starved of water by crystallisation of the oxychloride phases. This would ultimately result in a lower degree of conversion to the oxychloride phase with a corresponding increase in the proportion of unreacted metallic residues. On the other hand, this mechanism may represent a useful negative feedback mechanism that prevents thermal runaway by limiting the ability of the reaction to self-heat. Given that one of the aims of Cementisation is to eliminate the flammability hazard presented by the chronic corrosion of Magnox, it may be vital to have such a mechanism in place to ensure that the reaction is self-limiting and does not itself represent a hazard in the event of unexpected variations. Ultimately, experimental proof of concept using Magnox material will be required to establish whether this effect is likely to have a significant effect on the quality of the oxychloride product.

7.2 Corrosion Mechanisms

For the impedance measurements presented in this work, a complete and consistent understanding of the corrosion behaviour of pure Mg and Magnox can be constructed within the reaction scheme presented by Yuwono, coupled to the circuit model used by King and other researchers for fitting to the Mg system (King et al., 2014; Yuwono, Taylor, et al., 2019; Feliu, 2020). The filmless corrosion behaviour observed in concentrated solutions of MgCl_2 and AlCl_3 can be explained within this framework via the action of the Mg^*H adsorbed intermediate. At the optimum concentration (approximately 4M for MgCl_2), the elevated H^+ concentration and absence of the typical hydroxide surface film allows both oxidation and reduction reactions to proceed efficiently via the Mg^*H pathway. At concentrations approaching saturation, the

transport of Mg^{2+} ions away from anodic sites becomes limiting, leading to the formation of a transient salt film. As a result, the dissolution of this layer becomes the rate limiting step (Beck and Chan, 1981).

The polarisation (and by extension, corrosion) resistance of Magnox alloy is significantly higher in $MgCl_2$, which can be attributed to the stabilising effect of its aluminium component. From impedance measurements, this appears to manifest as a reduction in the actively dissolving area as a fraction of the total surface area. It was concluded that an aluminium oxide phase must be partially stable on the surface prior to dissolution in the bulk solution. Furthermore, from impedance spectra obtained in $AlCl_3$ solution, it is apparent that the onset of salt film corrosion occurs at a lower salt concentration for Magnox alloy than for pure Mg. Thus, the optimum $MgCl_2$ concentration for maximising corrosion rate is likely lower for Magnox than pure Mg.

Additionally, it is evident from the work presented herein that the corrosion rate in concentrated salt solutions is dependent on the ability of water to access reaction sites at the solid/liquid interface. This was corroborated by direct measurements of the corrosion rate presented in Section 4, where the activation energy of the reaction implied mixed control by a combination of both physical and chemical steps. Therefore, improving transport of water to the interface will lead to an increase in the reaction rate.

The observation made herein concerning Mg dissolving in concentrated $MgCl_2$ solutions offer a unique perspective on the fundamental reactions that take place. While these solutions are far from representative of typical environmental conditions, conclusions can be drawn that are universally relevant. Most notably, the role of Mg^*OH as a mechanism for undermining surface film is applicable to all Mg corrosion systems and may also be extended to other materials such as aluminium (De Wit and Lenderink, 1996).

7.3 Cement Synthesis

Proof of concept for the Cementisation process was demonstrated on the laboratory scale. The conversion of pure Mg raspings and powders to the oxychloride phases was achieved by simple mixing in concentrated $MgCl_2$ solutions and confirmed by physical analysis techniques. The degree of conversion to the MOC phases was determined to be >97% by quantitative XRD analysis, corroborated qualitatively by STA and SEM micrographs. Particle size was found to have a small but significant effect on the conversion efficiency, resulting in larger proportions of the amorphous and residual metallic phases for the case of raspings relative to metallic powders.

Small amounts of unreacted metal remain in all metallic formed samples due to premature crystallisation/curing of the cement phase, exhausting available water for the dissolution of metal pieces. In comparison to control samples formed from MgO powders, the metal-formed cements have low density, are highly friable and did not form a cohesive monolith. This is thought to result from the evolution of hydrogen generated from dissolving Mg metal, which prevents the formation of a strong cement network. This result is highly consequential for the development of Cementisation, as the prevention of volume expansion is one of the primary aims of the project. Furthermore, physical testing that would qualify the cement product for use in radioactive waste disposal, e.g., strength and leach tests, is predicated on the ability of the process to form coherent monoliths. Therefore, a means by which the quality of the cement can be improved on the lab scale is of primary importance for further development of the Cementisation process.

In essence, the Cementisation process is represented by two simultaneous reactions, the oxidation/dissolution of metallic Mg and the complexing/crystallisation of MOC phases. Both reactions are initiated upon mixing of the metallic feed and salt solution and both reactions are highly dependent on the availability of water in the system. Competition between the two processes for water is detrimental to the quality of the final cement product. The most obvious means by which the overall process can be optimised, therefore, is to deconvolute the two reactions to the greatest extent possible by enhancing the corrosion/dissolution of metal and delaying the hydrolysis/crystallisation of the cement phases.

The lack of cohesion observed for cement samples formed from metallic feeds precludes the application of a number of traditional cement testing techniques, such as strength testing, leach testing and pore network analysis. Given that the average degree of crystallisation determined by XRD for samples formed from metallic powders was consistent with the MgO control, it can be concluded that friability is not the result of poor crystal growth kinetics but rather results from concurrent hydrogen evolution from the oxidation reaction. The nucleation and holdup of bubbles of hydrogen gas could easily disrupt the formation of a cement matrix to the extent that no large-scale cohesion can be established. Ultimately, in its present form the cementitious products formed by enhanced corrosion of magnesium metal in concentrated MgCl_2 do not meet the mechanical and physical requirements for encapsulating material as defined for geological disposal in the UK (RWM, 2015). Therefore, a means by which hydrogen holdup can be reduced with a view to producing cohesive cementitious monoliths will be essential to enable the deployment of Cementisation as a stabilising treatment for contaminated magnesium wastes.

The proof-of-concept work presented in this thesis demonstrates that Cementisation is a viable method for removing chemical reactivity from metallic Mg and producing a hydrated cementitious product on the laboratory scale. However, while powders and raspings of Mg metal are a suitable analogue for Magnox swarf, proof of concept was not demonstrated for the target alloy itself. The corrosion behaviour of Magnox alloy, while similar to pure Mg, has been shown to have clear and relevant differences, most notably the emerging stability of a passivating aluminium phase at $>50^{\circ}\text{C}$ in 4M MgCl_2 . Nevertheless, with considerable scope for further optimisation, the Cementisation process continues to represent a viable means for stabilising reactive contaminated magnesium wastes.

8 Future Work

8.1 Kinetics of Pure Mg and Magnox Dissolution

Measurements of the corrosion rate of Mg and Magnox in concentrated salt solutions were performed with precision and accuracy using the gravimetric hydrogen evolution method, which was validated against the work of previous researchers. Nonetheless, a number of experimental improvements are here suggested for further refinement of these results, as well as further investigations that could be performed towards optimisation of the Cementisation reaction.

More replicates of the experiments as presented here would increase confidence in the calculated values for activation energy. However, when compared with the work of Casey (Casey and Bergeron, 1953), the results presented here were consistent with previous measurements while also achieving greater precision. Optimisation efforts would therefore be more effective if focussed on reducing the effects of experimental error. Uncertainties introduced to measurements of the corrosion rate by the gravimetric method could be improved, principally by better control of the bulk fluid temperature. This would reduce the random error in measurement and also stabilise the rate of evaporation, allowing the largest source of systematic errors to be addressed more reliably. This could be practically achieved by the use of a double-walled beaker fed by a thermostatic bath, using water or another suitable heat transfer fluid.

Further characterisation of the film formed on Magnox in 4M MgCl₂ at >50°C could be performed to better understand its nature and effect on the rate of dissolution. Physical analysis such as SEM and grazing-incidence XRD would likely confirm whether or not the film is composed of Boehmite or an alternative aluminium phase such as Gibbsite (Al(OH)₃). In addition, the kinetics of film formation could be investigated in more detail to determine the full extent to which it is capable of suppressing the dissolution rate of Magnox alloy. Separately, in Section 5 it was inferred from the presence of inductive loops in the impedance response of Magnox corroding in 4M MgCl₂ that salt film effects may be limiting the dissolution rate at this concentration. Thus, it was concluded that the optimum salt concentration for dissolving Magnox may be lower than that observed for pure Mg. Measurements of the corrosion rate via gravimetric hydrogen evolution could be used to perform an optimisation study and identify the optimum concentration for maximal metal dissolution. Once the optimal condition is identified, the thermochemical calculations performed in this work could be repeated to predict the onset point of temperature-dependent passivation.

In this work, thermochemical calculations were performed in response to the observation of film formation on Magnox alloy in 4M MgCl₂ at 60°C. Therefore, while a

pH meter was used to verify the pH of test solutions at ambient temperature, no measurements were performed at elevated temperatures which could be used to validate the results of the thermochemical calculations. If repeated, this additional step could be used to provide additional certainty to the conclusion that film formation in this case was a direct result of the change in pH with temperature. Nevertheless, the acidity of concentrated MgCl_2 and AlCl_3 solutions, as well as the inverse proportionality of pH with temperature are phenomena that are well understood, such that the thermochemical calculations are unlikely to require significant extrapolation from the database values and thus the conclusion can still be supported with high confidence.

If the corrosion rate in the high concentration limit were inhibited by MgCl_2 film formation, it is postulated that the limiting factor is the concentration of the chloride ion $[\text{Cl}^-]$ as it combines with excess Mg^{2+} at rapidly dissolving anodic sites. The minor addition of aluminium chloride might allow for faster dissolution as it has a greater specific hydrolysis potential and thus maximises the solubility of MgCl_2 per chloride ion. Alternatively, non-chloride acids (e.g., nitric, phosphoric or tartaric) may similarly increase the maximum rate of magnesium dissolution by preventing precipitation, however transient, of surface species, thus maximising the ability of water to access the metal surface. However, while additives may enhance the dissolution of Mg^{2+} , it will be important to maintain the stoichiometry of the oxychloride complex reaction in order to preserve the quality of the final cement product.

Finally, and similarly to previous discussion, the dependence of the activation energy on mass transport could be further investigated. This would allow deeper investigation of the "mixed" regime where both transport and chemical effects are rate-limiting, by progressively eliminating the former. While the application of bulk stirring is impractical for the gravimetric method, due to the effects of fluid movement on the suspended collector, fluid velocity could be increased by rotating the sample, with an angled stirrer or a Rotating Disk Electrode (RDE). This would provide an estimate of the efficiency of stirring as a means to improve the performance of Cementisation by removing the requirement for diffusion of water to the metal surface. Furthermore, the effect of stirring on temperature-dependent passivation could be investigated, to determine whether increased convection decreases the onset temperature and thus increases its inhibiting effect on the reaction rate. Investigations utilising bulk stirring are likely to be more effective for investigation of the Cementisation conversion efficiency at larger scales.

8.2 Corrosion Mechanisms

The interface of the corrosion reaction of Mg and Magnox alloy in concentrated solution of MgCl_2 and AlCl_3 was investigated in depth in this work by the application of EIS techniques. Nevertheless, additional refinement of the methods used here, in addition to complementary techniques, could be used to further examine these systems as representative examples of the filmless corrosion of magnesium alloys.

The effect of mass transport can be examined in electrochemical systems using a Rotating Disk Electrode (RDE), or by stirring of the bulk electrolyte. This could be used to determine the change in activation energy as a function of fluid velocity (Roller, 1935), which would in turn predict how the effectiveness of stirring for promoting corrosion in bulk stirred systems. In addition, the impedance response under increasing fluid velocity could be used to further investigate the fundamental dissolution behaviour of Mg^{2+} . For example, the assumption within the Baril model that diffusion of Mg^{2+} ions is responsible for the secondary capacitive impedance in the 4M Mg/MgCl_2 system could be investigated (Baril et al., 2007), to evaluate whether this effect can take place in a liquid boundary layer at quiescent conditions despite the suppression of a precipitated surface film. Similarly, the assertion that the corrosion of Mg in saturated MgCl_2 is dependent on the availability of water, required for the dissolution of transient MgCl_2 surface films and/or the cathodic reduction reaction, could be definitively tested.

The observation that the surface finish of pure Mg post immersion in 4M MgCl_2 is dimorphic warrants further investigation. Given that the effect is only observed for isolated Mg surfaces (i.e., resin-mounted samples), it is evident that this phenomenon is dependent on sample geometry. It is thought that these separate regions correspond to macroscopic anodic and cathodic sites, a conclusion which could be tested by local electrochemical methods such as the Scanning Vibrating Electrode Technique (SVET) (Williams et al., 2013), or by the combination of electrochemical methods with microscopy, such as Electro-Chemical Scanning Tunnelling Microscopy (EC-STM) (Song et al., 1997; Izquierdo et al., 2013). The former utilises a reference microelectrode that is scanned across the surface of a sample to map the current density at different points, with vibration applied to reduce signal noise (Bastos et al., 2017). Both techniques rely on the fine control of electrodes in close proximity to the working electrode, typically 100-200 μm . It is not clear whether these techniques will be effective in the examination of such a rapidly dissolving surface as Mg and Magnox in concentrated salt solutions, but the attempt would nonetheless be valuable in the determination of the phenomena that produced the clearly defined surface features observed herein.

Furthermore, the assumption that these areas correspond to the anodic and cathodic half reactions implies that their relative surface areas will change under applied bias

voltage. In addition, a detailed cross-sectional analysis of the different regions by microscopy techniques (FIB/SEM, TEM or SIMS, for example) may show key differences relating to the corrosion mechanism, such as differences in the thickness of MgO film formation (Gomes et al., 2019), or otherwise evidence of the action of adsorbed intermediates (Yuwono, Taylor, et al., 2019).

Finally, the reaction scheme proposed by Yuwono that was found to be consistent with impedance measurements in this work could in turn be used to further examine the unique corrosion behaviour observed for pure Mg in concentrated salt solutions. For example, by increasing the initial Mg^{2+} concentration used in DFT modelling, the conclusion that dissolution proceeds predominantly via the Mg^*H pathway in 4M $MgCl_2$ could be validated. It may also be possible to substantiate the presence of transient films, such as those thought to exist in saturated $MgCl_2$ systems, as well as Magnox alloy systems in 2.67M $AlCl_3$ with varying degrees of Mg^{2+} concentration.

8.3 Cement Synthesis

The conversion of metallic Mg to MOC phases has been successfully demonstrated on the lab scale. Nevertheless, a number of refinements could be applied to the experimental design, in addition to further investigations towards optimisation of the Cementisation process.

While water loss was effectively prevented during the curing process by the use of screw-cap enclosures, the curing conditions including humidity, temperature and time were simply recorded as it was not possible to adequately control them with the facilities available. Humidity and temperature could be better controlled using a curing cabinet, while better synchronisation of processing and analysis would help to remove time as a confounding variable. Expansion of the dataset to include time series data would also be valuable, particularly within the first day of curing, where the bulk of the combined corrosion/crystallisation appears to take place. Furthermore, the self-heating of samples by the corrosion reaction should be controlled to better understand the dependence of the process effectiveness on temperature at the bulk scale, although maintaining isothermal conditions may be technically difficult, as it would require substantial heat removal. Once adequately controlled, the curing conditions themselves could be investigated as variables, for example to match the conditions expected following emplacement in a GDF (see Section 3.1.2).

Microscopy, while useful for visual identification of features consistent with MOC formations, could have been utilised in more depth to understand the deficiencies of the metal-formed samples when compared to the MgO control. EDX could be used to map the distribution of elements and may be useful for distinguishing different phases but

given that the samples are predominantly composed of four light elements (H, O, Cl and Mg), this may not provide as much detail as molecular or crystallographic techniques. It is assumed that, for samples with residual metallic Mg, these metallic phases are likely to be at the centre of “shrinking-core” formations covered in layers of MOC or other oxide phases. TEM, with the ability to examine below-surface features in fine detail may be able to locate these features and provide understanding of how the reaction stalled. However, if the surface oxides are sufficiently deep, then TEM may not be suitable and an alternative techniques, such as FIB/SEM may be more applicable.

The use of non-chloride acids as additives, previously discussed in Section 7.1, has previously been investigated as a means of delaying the curing of MOC cements, for the purpose of improving the structural properties of the cement by maximising F5 content (Chen et al., 2019). This method enhances the dissolution of MgO by preventing the formation of Mg(OH)₂ phases and increases the water resistance of the product by encouraging formation of the amorphous gel phase. As well as delaying the crystallisation of MOC phases, allowing more time for corrosion/dissolution of metallic feeds, the addition of acids may also allow active filmless corrosion to be sustained for a longer period by delaying the onset of passivation.

Similarly, given that it has been demonstrated that the optimum concentration for Mg dissolution in MgCl₂ solutions is ~4M and the stoichiometric ratio for the production of the F5 phase from metallic feeds is ~3M, the concentration of MgCl₂ could be dynamically adjusted after initiation to maximise the rate of dissolution. This could be practically achieved by initiating the reaction at ~4M concentration with subsequent addition of water to replace that which is lost due to the oxidation reaction. Then, at a point yet to be determined, water would be added at a faster rate to satisfy the ~3M concentration required for optimal MOC phase development. This will require a detailed understanding of the interaction between the corrosion and curing reactions in order to avoid compromising the quality of the cement product. The rate of water addition required could be estimated indirectly by measuring the rate of hydrogen evolution or by measuring the level of heat generated by the oxidation of Mg metal.

Furthermore, from measurements of the corrosion rate in 4M MgCl₂ as a function of temperature, it was shown that an optimum temperature for the dissolution of Magnox alloy exists at ~50°C. Thus, increasing the bulk temperature of the MgCl₂ solution may offer a means to enhance the degree of conversion to MOC phases. The stability of the F5 phase has previously been shown to increase with temperature, with adverse effects on the cement matrix only observed at lower temperatures where precipitation of the F3 phase is preferred (Sglavo et al., 2011; Liu et al., 2017). However, as the rate of hydrolysis would also be expected to increase with temperature, this will be highly

dependent on the relative activation energies for the dissolution of Mg and hydrolysis/crystallisation of the MOC phases. For example, in the event that the activation energy for the formation of MOC phases is greater than for the dissolution of Magnox (i.e., $>46\text{kJmol}^{-1}$ in 4M MgCl_2), optimisation might require the identification of a low temperature point ($\sim 10\text{-}15^\circ\text{C}$) where the rates of the component reactions is maximally separated without compromising the cement product. Fortunately, previous work on the kinetics of MOC formation has shown that the dissolution of MgO is more sensitive to temperature than the crystallisation of the F5 phase (Góchez et al., 2017). Therefore, as both the activation energies for the oxidation of metallic Mg and dissolution of MgO have been shown to be greater than the activation energy for MOC crystallisation, the Cementisation process can confidently be assumed to be most effective at $\sim 50^\circ\text{C}$.

If Cementisation is to be carried out at elevated temperatures for the purpose of maximising the oxidation of metallic feeds, it will be crucial to demonstrate that the reaction cannot achieve thermal runaway. The enthalpy of formation of MgO is -601.6kJmol^{-1} (J. Rumble, 2020b), indicating that the oxidation reaction is capable of generating a substantial amount of heat. Given that the corrosion reaction has been shown to be highly sensitive to temperature (as indicated by its activation energy), the heat generated as a result represents a positive feedback mechanism that could lead to the reaction becoming uncontrolled, with the potential to create an explosive atmosphere due to the evolution of hydrogen gas. For pure Mg, there is no mechanism to prevent positive feedback in this way. However, for Magnox alloy, the observation of passivation by the minor aluminium component may represent a negative feedback mechanism that reduces the rate of oxidation at temperatures greater than 50°C . For continuing development of Cementisation, the potential for thermal runaway could be investigated by adiabatic calorimetry to evaluate the effect of both feedback mechanisms.

Agitation of the mixture by stirring, in addition to promoting faster dissolution of the metal feed, may help to release hydrogen bubbles held up in the crystallising matrix. Continuous stirring during the setting of encapsulating cements has already been achieved for ILW waste packages by the use of sacrificial paddles (RWM, 2016b). On the laboratory scale, both direct (e.g. overhead stirring) and indirect (e.g. vibration, sonication, inversion) mixing methods could be evaluated in terms of their efficacy for the removal of evolving gas. Direct methods, such as overhead stirring, will require monitoring of evaporation to ensure that the stoichiometry of the reaction is not substantially affected by loss of water. At the same time, mixing an open system will allow rapid removal of the headspace gas and is also likely to be more representative of

the process at scale. Alternatively, the nucleation of bubbles could be suppressed by increasing pressure in the gas head, or otherwise agitated by sparging.

If stirring and other optimisations such as bulk heating are successful in producing cohesive MOC monoliths, then the physical and mechanical properties of the product could subsequently be tested to qualify the method as a treatment for contaminated wastes.

8.4 Summary

To examine the impact of the experimental work presented in this thesis, the conclusions made in this section are here re-examined in the context of the hypotheses outlined in Section 2. For each hypothesis, a statement is made as to whether the hypothesis remains valid and to what extent it has been examined:

1. Magnesium oxychloride cement can be produced from the corrosion products generated during dissolution of metallic Mg in MgCl_2 solution.

Yes, by physical analysis techniques it has been proven that the oxidation of metallic Mg can be substituted into the formulation of MOC cements. With simple mixing and curing, >97% conversion to MOC phases was measured on average by XRD. However, while chemically identifiable as MOC phases, samples produced from metallic feeds were extremely friable and did not form a cohesive monolith.

2. MgCl_2 solutions with a concentration greater than 2M promote rapid, active and uniform corrosion of magnesium metal.

Yes, from measurements of the corrosion rate by gravimetric hydrogen evolution the activation energies for dissolution of Mg and Magnox in MgCl_2 and AlCl_3 of identical ionic strength were found to lie in the range 42-51 kJmol⁻¹. Activation energies in this range (~20-60 kJmol⁻¹) are indicative of a process where the rate limiting step is a mixed physical/chemical process, which in turn implies that any diffusion layer on the surface is liquid rather than solid (i.e., a passivating oxide). Visual observation of samples post immersion showed no evidence of the dark-grey surface film typically observed on corroded Mg metal surfaces. Finally, impedance measurements showed a clear difference between the dissolution mechanism in low and high concentrations of MgCl_2 , with a boundary between the two regimes in the region of 1-2M, coincident with the point at which magnesium oxychlorides become the favoured product.

3. Hypotheses 1 and 2 remain true for the case of Magnox alloy (Al80)

Confirmed in part. Magnox alloy was shown to corrode rapidly and uniformly in concentrated salt solutions by both direct measurements and by impedance spectroscopy. However, proof of concept for conversion of Magnox alloy to MOC phases was not demonstrated due to a lack of available powdered material. While Cementisation may be affected by passivation at high temperatures (>50°C), the results presented in this work offer no reason to doubt that the process will remain highly effective when applied to fragments of Magnox alloy.

In this work, the process of Cementisation was introduced as a means to stabilise reactive metallic magnesium wastes and produce a hydrated cementitious product

suitable for ultimate disposal. Proof of concept was achieved on the laboratory scale with a high degree of conversion achieved by simple mixing of metal fragments up to sub-cm scale into concentrated MgCl_2 solutions. The corrosion and dissolution of metallic Mg/Magnox was identified as the most important step for optimisation and the kinetics of the reaction were measured for an isolated surface in concentrated salt solutions. For Magnox in 4M MgCl_2 , passivation was observed for bulk solution temperatures in excess of 50°C. Both pure Mg and Magnox alloy were shown to corrode actively and uniformly in concentrated salt solutions. Impedance measurements showed the breakdown of passive films with increasing salt concentration and were used to examine the fundamental corrosion mechanism of metallic Mg. A unified framework was constructed from the work of previous authors in the field of pure Mg corrosion, which provided a consistent explanation for the corrosion behaviour observed in this work. Overall, therefore, this work has provided new insight into the corrosion behaviour of magnesium and its alloys, as well as demonstrating a viable method by which contaminated metallic wastes could be treated as part of ongoing risk reduction and legacy waste disposal efforts. It is the sincere hope of the author that this work represents a meaningful forward step towards final disposal for one of the most challenging waste streams in the UK Radioactive Waste Inventory.

Publications and Conference Presentations

Vickers, J. A., Hanson, B. C., Mishra, B. 2018. Developing a Pre-Treatment for the Disposal of Magnox and Exotic Wastes [Poster]. In: INEC 2018, October 4-5, 2018, Manchester, UK.

Vickers, J. A., Hanson, B. C., Mishra, B. 2019. Enhanced Corrosion of Magnesium as a Treatment for Legacy SNF - 19369. In: WM2019: Waste Management Symposia, March 3-7, 2019, Phoenix, AZ, USA. WM Symposia. ISBN 978-0-9828171-9-3.

Vickers, J. A., Hanson, B. C., Mishra, B. 2019. Inducing Active Corrosion in Passive Metals [Poster]. In: WM2019: Waste Management Symposia, March 3-7, 2019, Phoenix, AZ, USA. WM Symposia.

Vickers, J. A. 2019. Enhancing Corrosion as a Treatment for Magnox Swarf Wastes. In: TRANSCEND Theme Meetings 2019, November 11-12, 2019, Lancaster, UK. [Online]. Available from: <https://transcendconsortium.org/wp-content/uploads/2019/11/Themes-2019-Theme-4.pdf>, pp.73-83.

Bibliography

- Abbott, T.B. 2015. Magnesium: Industrial and Research Developments Over the Last 15 Years. *Corrosion*. **71**(2), pp.120–127.
- Abramson, M.B. and King, C. V. 1939. The Rate of Dissolution of Iron in Acids. *Journal of the American Chemical Society*. **61**(9), pp.2290–2295.
- André, L., Christov, C., Lassin, A. and Azaroual, M. 2018. Thermodynamic model for solution behavior and solid-liquid equilibrium in Na-Al(III)-Fe(III)-Cr(III)-Cl-H₂O system at 25°C. *Acta Scientifica Naturalis*. **5**(1), pp.6–16.
- ASTM International 2012. ASTM G1-03: Standard Practice for Preparing, Cleaning and Evaluating Corrosion Test Specimens. *Annual Book of ASTM Standards*. **03.02**, pp.1–9.
- Atrens, A. and Dietzel, W. 2007. The negative difference effect and unipositive Mg. *Advanced Engineering Materials*. **9**(4), pp.292–297.
- Atrens, A., Song, G.-L., Liu, M., Shi, Z., Cao, F. and Dargusch, M.S. 2015. Review of Recent Developments in the Field of Magnesium Corrosion. *Advanced Engineering Materials*. **17**(4), pp.400–453.
- Baboian, R. 2005. Immersion Testing *In: Corrosion Tests and Standards: Application and Interpretation (2nd Edition): (MNL 20)*. West Conshohocken: ASTM International, pp.139–146.
- Bard, A.J. and Faulkner, L.J. 2001. *Electrochemical Methods : Fundamentals and Applications* 2nd ed. New York ; Wiley.
- Baril, G. and Pébère, N. 2001. The corrosion of pure magnesium in aerated and deaerated sodium sulphate solutions. *Corrosion Science*. **43**(3), pp.471–484.
- Baril, G.G., Galicia, G., Deslouis, C., Pébère, N., Tribollet, B., Vivier, V., Pébère, N., Tribollet, B. and Vivier, V. 2007. An Impedance Investigation of the Mechanism of Pure Magnesium Corrosion in Sodium Sulfate Solutions. *Journal of The Electrochemical Society*. **154**(2), p.C108.
- Bastos, A.C., Quevedo, M.C., Karavai, O. V. and Ferreira, M.G.S. 2017. On the Application of the Scanning Vibrating Electrode Technique (SVET) to Corrosion Research. *Journal of The Electrochemical Society*. **164**(14), pp.C973–C990.
- Beck, T.R. 1984. Salt film formation during corrosion of aluminum. *Electrochimica Acta*. **29**(4), pp.485–491.
- Beck, T.R. and Chan, S.G. 1981. *Corrosion of Magnesium at High Anodic Potentials*. [Online]. [Accessed 10 November 2021]. Available from: <https://apps.dtic.mil/sti/citations/ADA102339>.
- BEIS 2021. *The United Kingdom's Seventh National Report on Compliance with the Obligations of the Joint Convention on the Safety of Spent Fuel Management and on the Safety of Radioactive Waste Management*. [Online]. Available from: <https://www.gov.uk/government/publications/the-uks-7th-national-report-on-compliance-with-the-obligations-of-the-joint-convention-on-the-safety-of-spent-fuel-and-radioactive-waste-management>.
- BEIS 2018. *The United Kingdom's Sixth National Report on Compliance with the*

- Obligations of the Joint Convention on the Safety of Spent Fuel Management and on the Safety of Radioactive Waste Management.* [Online]. Available from: <https://www.gov.uk/government/publications/the-uks-sixth-national-report-on-compliance-with-the-obligations-of-the-joint-convention-on-the-safety-of-spent-fuel-and-radioactive-waste-management>.
- Bilinski, H., Matković, B., Mažuranić, C. and Žunić, T.B. 1984. The Formation of Magnesium Oxychloride Phases in the Systems MgO-MgCl₂-H₂O and NaOH-MgCl₂-H₂O. *Journal of the American Ceramic Society.* **67**(4), pp.266–269.
- Birbilis, N., King, A.D., Thomas, S., Frankel, G.S. and Scully, J.R. 2014. Evidence for enhanced catalytic activity of magnesium arising from anodic dissolution. *Electrochimica Acta.* **132**, pp.277–283.
- Bland, L.G., King, A.D., Birbilis, N. and Scully, J.R. 2015. Assessing the Corrosion of Commercially Pure Magnesium and Commercial AZ31B by Electrochemical Impedance, Mass-Loss, Hydrogen Collection, and Inductively Coupled Plasma Optical Emission Spectrometry Solution Analysis. *Corrosion.* **71**(2), pp.128–145.
- Brady, M.P., Rother, G., Anovitz, L.M., Littrell, K.C., Unocic, K.A., Elsentriecy, H.H., Song, G.-L., Thomson, J.K., Gallego, N.C. and Davis, B. 2015. Film Breakdown and Nano-Porous Mg(OH)₂ Formation from Corrosion of Magnesium Alloys in Salt Solutions. *Journal of The Electrochemical Society.* **162**(4), pp.C140–C149.
- Burrows, R. 2013. *Passive and Localised Corrosion Behaviour of a High Magnesium alloy (Mgnox AL80).* Manchester: The University of Manchester.
- Casey, E.J. and Bergeron, R.E. 1953. On the Mechanism of the Dissolution of Magnesium in Acidic Salt Solutions: I. Physical Control by Surface Films. *Canadian Journal of Chemistry.* **31**(9), pp.849–867.
- Casey, E.J., Bergeron, R.E. and Nagy, G.D. 1962. On the Mechanism of Dissolution of Magnesium in Aqueous Magnesium Chloride Solutions: Part II. *Canadian Journal of Chemistry.* **40**(3), pp.463–479.
- CEGB and SSEB 1986. *CEGB/SSEB Response to Recommendation 18 in the Environment Committee's Report on Radioactive Waste.*
- Chen, X., Zhang, T., Bi, W. and Cheeseman, C. 2019. Effect of tartaric acid and phosphoric acid on the water resistance of magnesium oxychloride (MOC) cement. *Construction and Building Materials.* **213**, pp.528–536.
- Clark, R.N., Humpage, J., Burrows, R., Godfrey, H., Sagir, M. and Williams, G. 2021. A Study into the Localized Corrosion of Magnesium Alloy Mgnox Al-80. *Corrosion.* **77**(2), pp.168–182.
- Le Clere, S. 2012. Mgnox Swarf Storage Silo Liquor Effluent Management: Sellafield Site, Cumbria, UK In: *Proceedings of the International Conference on Radioactive Waste Management and Environmental Remediation, ICEM.* Reims, France: American Society of Mechanical Engineers Digital Collection, pp.67–75.
- Curioni, M. 2014. The behaviour of magnesium during free corrosion and potentiodynamic polarization investigated by real-time hydrogen measurement and optical imaging. *Electrochimica Acta.* **120**, pp.284–292.
- Curioni, M. and Scenini, F. 2015. The Mechanism of Hydrogen Evolution during Anodic Polarization of Aluminium. *Electrochimica Acta.* **180**, pp.712–721.

- Curioni, M., Scenini, F., Monetta, T. and Bellucci, F. 2015. Correlation between electrochemical impedance measurements and corrosion rate of magnesium investigated by real-time hydrogen measurement and optical imaging. *Electrochimica Acta*. **166**, pp.372–384.
- Curioni, M., Torrescano-Alvarez, J.M., Yang, Y.F. and Scenini, F. 2017. Application of side-view imaging and real-time hydrogen measurement to the investigation of magnesium corrosion. *Corrosion*. **73**(5), pp.463–470.
- Dehua, D. and Chuanmei, Z. 1999. The formation mechanism of the hydrate phases in magnesium oxychloride cement. *Cement and Concrete Research*. **29**(9), pp.1365–1371.
- Dinnebier, R.E., Halasz, I., Freyer, D. and Hanson, J.C. 2011. The crystal structures of two anhydrous magnesium hydroxychloride phases from in situ synchrotron powder diffraction data. *Zeitschrift für Anorganische und Allgemeine Chemie*. **637**(11), pp.1458–1462.
- Esmaily, M., Svensson, J.E., Fajardo, S., Birbilis, N., Frankel, G.S., Virtanen, S., Arrabal, R., Thomas, S. and Johansson, L.G. 2017. Fundamentals and advances in magnesium alloy corrosion. *Progress in Materials Science*. **89**, pp.92–193.
- Fajardo, S. and Frankel, G.S. 2015. Gravimetric Method for Hydrogen Evolution Measurements on Dissolving Magnesium. *Journal of The Electrochemical Society*. **162**(14), pp.C693–C701.
- Fajardo, S., Glover, C.F., Williams, G. and Frankel, G.S. 2017. The Evolution of Anodic Hydrogen on High Purity Magnesium in Acidic Buffer Solution. *CORROSION*. **73**(5), pp.482–493.
- Feliu, S. 2020. Electrochemical Impedance Spectroscopy for the Measurement of the Corrosion Rate of Magnesium Alloys: Brief Review and Challenges. *Metals 2020, Vol. 10, Page 775*. **10**(6), p.775.
- Frankel, G.S. 1998. Pitting Corrosion of Metals: A Review of the Critical Factors. *Journal of The Electrochemical Society*. **145**(6), p.2186.
- Frankel, G.S., Fajardo, S. and Lynch, B.M. 2015. Introductory lecture on corrosion chemistry: a focus on anodic hydrogen evolution on Al and Mg. *Faraday Discussions*. **180**(0), pp.11–33.
- Frankel, G.S., Samaniego, A. and Birbilis, N. 2013. Evolution of hydrogen at dissolving magnesium surfaces. *Corrosion Science*. **70**, pp.104–111.
- Galicia, G., Pébère, N., Tribollet, B. and Vivier, V. 2009. Local and global electrochemical impedances applied to the corrosion behaviour of an AZ91 magnesium alloy. *Corrosion Science*. **51**(8), pp.1789–1794.
- Gamry Instruments n.d. Tafel Fit. [Accessed 27 August 2022]. Available from: https://www.gamry.com/Framework_Help/HTML5_Tripane_Audience_A/Content/DC/Data_Analysis/Experiment-specific_Tools/Tafel_Fit.htm.
- Gartner, E. and Sui, T. 2018. Alternative cement clinkers. *Cement and Concrete Research*. **114**, pp.27–39.
- Ge, X., Wang, X., Zhang, M. and Seetharaman, S. 2007. Correlation and prediction of activity and osmotic coefficients of aqueous electrolytes at 298.15 K by the

- modified TCPC model. *Journal of Chemical and Engineering Data*. **52**(2), pp.538–547.
- Glasser, F.P. 1992. Progress in the immobilization of radioactive wastes in cement. *Cement and Concrete Research*. **22**(2–3), pp.201–216.
- Góchez, R., Wambaugh, J., Rochner, B. and Kitchens, C.L. 2017. Kinetic study of the magnesium oxychloride cement cure reaction. *Journal of Materials Science*. **52**(13), pp.7637–7646.
- Gomes, M.P., Costa, I., Pébère, N., Rossi, J.L., Tribollet, B. and Vivier, V. 2019. On the corrosion mechanism of Mg investigated by electrochemical impedance spectroscopy. *Electrochimica Acta*. **306**, pp.61–70.
- Guo, Y., Zhang, Y., Soe, K. and Pulham, M. 2018. Recent development in magnesium oxychloride cement. *Structural Concrete*. **19**(5), pp.1290–1300.
- Hallam, K.R., Minshall, P.C., Heard, P.J. and Flewitt, P.E.J. 2016. Corrosion of the alloys Magnox AL80, Magnox ZR55 and pure magnesium in air containing water vapour. *Corrosion Science*. **112**, pp.347–363.
- Hanson, B.C. 2014. Nuclear fuel cycle: A UK perspective *In: 247th National Spring Meeting of the American Chemical Society (ACS)* [Online]. Dallas, TX: American Chemical Society (ACS). Available from: <https://eprints.whiterose.ac.uk/97077/>.
- Hara, N., Kobayashi, Y., Kagaya, D. and Akao, N. 2007. Formation and breakdown of surface films on magnesium and its alloys in aqueous solutions. *Corrosion Science*. **49**(1), pp.166–175.
- Harrington, D. 2019. Complex Nonlinear Least Squares Fitting of Immittance Data - Application Center. [Accessed 24 September 2021]. Available from: <https://www.maplesoft.com/applications/view.aspx?SID=154540>.
- Huang, J., Song, G.-L., Atrens, A. and Dargusch, M. 2020. What activates the Mg surface—A comparison of Mg dissolution mechanisms. *Journal of Materials Science & Technology*. **57**, pp.204–220.
- Huang, L., Yang, Z. and Wang, S. 2020. Influence of calcination temperature on the structure and hydration of MgO. *Construction and Building Materials*. **262**, p.120776.
- Izquierdo, J., Nagy, L., Bitter, I., Souto, R.M. and Nagy, G. 2013. Potentiometric scanning electrochemical microscopy for the local characterization of the electrochemical behaviour of magnesium-based materials. *Electrochimica Acta*. **87**, pp.283–293.
- Jensen, S.E. and Nonboel, E. 1999. *Description of the Magnox Type of Gas Cooled Reactor (MAGNOX)*. Roskilde.
- Jones, T. 2014. Development of an Effluent Treatment Process for the Silos Direct Encapsulation Plant *In: IChemE Sustainable Nuclear Energy Conference*. Manchester, pp.0–12.
- Jove-Colon, C., Wolery, T., Rard, J., Wijesinghe, A., Jareck, R. and Helan, K. 2007. *In-drift precipitates / Salts model - Appendix I*. Las Vegas, NV.
- King, A.D., Birbilis, N. and Scully, J.R. 2014. Accurate electrochemical measurement of magnesium corrosion rates; A combined impedance, mass-loss and hydrogen collection study. *Electrochimica Acta*. **121**, pp.394–406.

- Kirkland, N.T., Birbilis, N. and Staiger, M.P. 2012. Assessing the corrosion of biodegradable magnesium implants: A critical review of current methodologies and their limitations. *Acta Biomaterialia*. **8**(3), pp.925–936.
- Levenspiel, O. 1998. *Chemical Reaction Engineering* 3rd ed. New York: Wiley.
- Li, Y., Li, Z., Pei, H. and Yu, H. 2016. The influence of FeSO₄ and KH₂PO₄ on the performance of magnesium oxychloride cement. *Construction and Building Materials*. **102**, pp.233–238.
- Li, Z. and Chau, C.K. 2007. Influence of molar ratios on properties of magnesium oxychloride cement. *Cement and Concrete Research*. **37**(6), pp.866–870.
- Liu, M., Zanna, S., Ardelean, H., Frateur, I., Schmutz, P., Song, G., Atrens, A. and Marcus, P. 2009. A first quantitative XPS study of the surface films formed, by exposure to water, on Mg and on the Mg-Al intermetallics: Al₃Mg₂ and Mg₁₇Al₁₂. *Corrosion Science*. **51**(5), pp.1115–1127.
- Liu, Z., Balonis, M., Huang, J., Sha, A. and Sant, G. 2017. The influence of composition and temperature on hydrated phase assemblages in magnesium oxychloride cements. *Journal of the American Ceramic Society*. **100**(7), pp.3246–3261.
- Luo, X., Fan, W., Li, C., Wang, Y., Yang, H., Liu, X. and Yang, S. 2020. Effect of hydroxyacetic acid on the water resistance of magnesium oxychloride cement. *Construction and Building Materials*. **246**, p.118428.
- Madsen, I.C., Scarlett, N.V.Y. and Kern, A. 2011. Description and survey of methodologies for the determination of amorphous content via X-ray powder diffraction. *Zeitschrift für Kristallographie*. **226**(12), pp.944–955.
- Magnox Ltd. and NDA 2013. *Intermediate level waste (ILW) storage and fuel element debris (FED) treatment optimisation study* [Online]. Available from: <http://www.nda.gov.uk/publication/intermediate-level-waste-ilw-storage-and-fuel-element-debris-fed-treatment-optimisation-study/>.
- Magnox Ltd. and NDA 2017. Magnox Ltd complete FED treatment programme at Bradwell in Essex - GOV.UK. [Accessed 3 January 2022]. Available from: <https://www.gov.uk/government/news/magnox-ltd-complete-fed-treatment-programme-at-bradwell-in-essex>.
- Maltseva, A., Shkirskiy, V., Lefèvre, G. and Volovitch, P. 2019. Effect of pH on Mg(OH)₂ film evolution on corroding Mg by in situ kinetic Raman mapping (KRM). *Corrosion Science*. **153**, pp.272–282.
- Mažuranić, C., Bilinski, H. and Matković, B. 1982. Reaction Products in the System MgCl₂-NaOH-H₂O. *Journal of the American Ceramic Society*. **65**(10), pp.523–526.
- Morgan, S., Barnes, M. and Randall, G. 2019. Progress Towards Treating the Sludges Produced During Spent Fuel Processing - 19546 In: *Proceedings of the Waste Management Conference* [Online]. Phoenix, AZ. Available from: <https://www.osti.gov/biblio/23005405>.
- Morris, J., Richardson, P. and Wickham, S. 2009. *Magnox Spent Fuel Contingency: Review of Options for Drying, Packaging and Storage of Magnox Fuel, Unpublished*.
- Morris, J., Wickham, S., Richardson, P., Rhodes, C. and Newland, M. 2009. Contingency Options for the Drying, Conditioning and Packaging of Magnox Spent Fuel in the UK

- In: ASME 2009 12th International Conference on Environmental Remediation and Radioactive Waste Management, Volume 1.* Liverpool: ASMEDC, pp.817–823.
- Murray, J.N., Moran, P.J. and Gileadi, E. 1988. Utilization of the Specific Pseudocapacitance for Determination of the Area of Corroding Steel Surfaces. *Corrosion*. **44**(8), pp.533–538.
- NAO 2018. *The Nuclear Decommissioning Authority: progress with reducing risk at Sellafield (House of Commons, HC 1126)* [Online]. Available from: <https://www.nao.org.uk/wp-content/uploads/2018/06/The-Nuclear-Decommissioning-Authority-progress-with-reducing-risk-at-Sellafield.pdf>.
- NDA 2019a. *2019 UK Radioactive Waste Detailed Data*.
- NDA 2018a. A step forward for Sellafield's most hazardous building. [Accessed 1 January 2022]. Available from: <https://www.gov.uk/government/news/a-step-forward-for-sellafields-most-hazardous-building>.
- NDA 2018b. *Annual Report & Accounts 2017/2018*.
- NDA 2021a. *Business Plan 2021-2024*.
- NDA 2019b. *Integrated Waste Management Radioactive Waste Strategy*.
- NDA 2014. *Magnox Fuel Strategy Contingency Options*.
- NDA 2019c. Managing nuclear materials and spent fuels - GOV.UK. [Accessed 3 January 2022]. Available from: <https://www.gov.uk/government/collections/managing-nuclear-materials-and-spent-fuels#magnox-fuels>.
- NDA 2013. *Optimising the number and location of FED Treatment (Dissolution) Facilities in Magnox Limited: Credible Options*.
- NDA 2015. *Programmes and Major Projects Report (PILOT 3)* [Online]. Available from: https://www.gov.uk/government/uploads/system/uploads/attachment_data/file/518967/Programmes_and_Major_Projects_Report_-_Pilot_3_Jan_2015_.pdf.
- NDA 2020. Radioactive Waste Strategy September 2019 - GOV.UK. [Accessed 5 August 2022]. Available from: <https://www.gov.uk/government/consultations/nda-radioactive-waste-management-strategy/outcome/radioactive-waste-strategy-september-2019>.
- NDA 2021b. *Strategy: Effective from March 2021*. Nuclear Decommissioning Authority.
- NDA and RWM Ltd. 2011. *Summary of Assessment Report for Magnox Swarf Storage Silo Wastes at the Silos Direct Encapsulation Plant* [Online]. Available from: <https://rwm.nda.gov.uk/publication/summary-of-assessment-report-for-magnox-swarf-storage-silo-wastes-at-the-silos-direct-encapsulation-plant-sdp-interim-stage/>.
- NEA and OECD 2018. *State of the Art Report on the Progress of Nuclear Fuel Cycle Chemistry*.
- Nordlien, J.H., Ono, S., Masuko, N. and Nisancioglu, K. 1995. Morphology and Structure of Oxide Films Formed on Magnesium by Exposure to Air and Water. *Journal of The Electrochemical Society*. **142**(10).
- NWS 2022. *GDF Annual Report 2020-2021* [Online]. Available from: <https://www.gov.uk/government/publications/gdf-annual-report-2020-2021>.

- NWS 2018. Our work with radioactive waste producers - GOV.UK. [Accessed 18 June 2022]. Available from: <https://www.gov.uk/guidance/our-work-with-radioactive-waste-producers#our-letter-of-compliance-process>.
- Ojovan, M.I., Lee, W.E. and Kalmykov, S.N. 2019. Immobilisation of Radioactive Waste in Cement *In: An Introduction to Nuclear Waste Immobilisation* [Online]. Elsevier, pp.271–303. [Accessed 15 January 2022]. Available from: <https://linkinghub.elsevier.com/retrieve/pii/B9780081027028000170>.
- Orazem, M.E. and Tribollet, B. 2008a. Electrochemical Impedance Spectroscopy. *Electrochemical Impedance Spectroscopy.*, pp.1–523.
- Orazem, M.E. and Tribollet, B. 2008b. Kinetic Models. *Electrochemical Impedance Spectroscopy.*, pp.163–181.
- Pannach, M., Bette, S. and Freyer, D. 2017. Solubility Equilibria in the System Mg(OH)₂-MgCl₂-H₂O from 298 to 393 K. *Journal of Chemical and Engineering Data.* **62**(4), pp.1384–1396.
- Pardo, A., Merino, M.C., Coy, A.E., Arrabal, R., Viejo, F. and Matykina, E. 2008. Corrosion behaviour of magnesium/aluminium alloys in 3.5 wt.% NaCl. *Corrosion Science.* **50**(3), pp.823–834.
- Parry, A. 2017. Alternative ILW management approach for Magnox Swarf Storage Silos at Sellafield *In: International Conference on Advancing the Global Implementation of Decommissioning and Environmental Remediation Programmes* [Online]. Madrid, Spain: IAEA. [Accessed 18 June 2022]. Available from: <https://www-pub.iaea.org/books/iaeabooks/11155/Advancing-the-Global-Implementation-of-Decommissioning-and-Environmental-Remediation-Programmes>.
- Perez, N. 2006. Kinetics of Activation Polarization *In: Electrochemistry and Corrosion Science.* Dordrecht: Kluwer Academic Publishers, pp.71–120.
- Petty, R.L., Davidson, A.W. and Kleinberg, J. 1954. The Anodic Oxidation of Magnesium Metal: Evidence for the Existence of Unipositive Magnesium. *Journal of the American Chemical Society.* **76**(2), pp.363–366.
- Prentice, D.P., Walkley, B., Bernal, S.A., Bankhead, M., Hayes, M. and Provis, J.L. 2019. Thermodynamic modelling of BFS-PC cements under temperature conditions relevant to the geological disposal of nuclear wastes. *Cement and Concrete Research.* **119**, pp.21–35.
- Ramachandran, V.S., Paroli, R.M., Beaudoin, J.J. and Delgado, A.H. 2002. 1 - Thermoanalytical Techniques *In: V. S. Ramachandran, R. M. Paroli, J. J. Beaudoin and A. H. Delgado, eds. Handbook of Thermal Analysis of Construction Materials.* Norwich, NY: William Andrew Publishing, pp.1–34.
- Rayment, T., Davenport, A.J., Dent, A.J., Tinnes, J.P., Wiltshire, R.J.K., Martin, C., Clark, G., Quinn, P. and Mosselmans, J.F.W. 2008. Characterisation of salt films on dissolving metal surfaces in artificial corrosion pits via in situ synchrotron X-ray diffraction. *Electrochemistry Communications.* **10**(6), pp.855–858.
- Roller, P.S. 1935. The physical and chemical relations in fluid phase heterogeneous reaction. *Journal of Physical Chemistry.* **39**(1), pp.221–237.
- Rumble, J. (ed.). 2020a. Electrochemical Series *In: CRC Handbook of Chemistry and Physics.* Boca Raton: CRC Press/Taylor & Francis.

- Rumble, J. (ed.). 2020b. Standard Thermodynamic Properties of Chemical Substances *In: CRC Handbook of Chemistry and Physics*. Boca Raton: CRC Press/Taylor & Francis.
- Rumble, J (ed.). 2020. The Elements *In: CRC Handbook of Chemistry and Physics*. Boca Raton: CRC Press/Taylor & Francis.
- Rumble, J.R. (ed.). 2020. Vapor Pressure and Other Saturation Properties of Water *In: CRC Handbook of Chemistry and Physics*. Boca Raton: CRC Press/Taylor & Francis.
- RWM 2015. *Geological Disposal: Guidance on the production of encapsulated wastefoms*.
- RWM 2016a. *NDA RWM Interactions with Waste Packagers on Plans for Packaging of Radioactive Wastes April 2014 to March 2015*.
- RWM 2016b. *Waste Package Evolution*.
- RWM 2014. *WPS/650/03 - Geological Disposal: An overview of the RWM Disposability Assessment Process*.
- Scully, J.R. 2000. Polarization resistance method for determination of instantaneous corrosion rates. *Corrosion*. **56**(2), pp.199–217.
- Sellafield Ltd. 2018. *2017/18 Technology Development and Delivery Summary* [Online]. Available from: https://assets.publishing.service.gov.uk/government/uploads/system/uploads/attachment_data/file/792030/Technology_Development_and_Delivery_Report18_FINAL_LoRes.pdf.
- Sellafield Ltd. 2021. SEP2 moves into position for retrievals - GOV.UK. [Accessed 1 January 2022]. Available from: <https://www.gov.uk/government/news/sep2-moves-into-position-for-retrievals>.
- Sellafield Ltd. 2017a. *The 2016 / 17 Technology Development and Delivery Summary Contents*.
- Sellafield Ltd. 2017b. United Kingdom-Warrington: Containers for waste material 2017/S 210-435691. *Tenders Electronic Daily*., pp.1–4.
- Serco Technical Consulting Services 2010. *Survey of reactive metal corrosion data for use in the SMOGG gas generation model*. Didcot.
- Sglavo, V.M., De Genua, F., Conci, A., Ceccato, R. and Cavallini, R. 2011. Influence of curing temperature on the evolution of magnesium oxychloride cement. *Journal of Materials Science 2011 46:20*. **46**(20), pp.6726–6733.
- Sharp, J.H., Hill, J., Milestone, N.B. and Miller, E.W. 2003. Cementitious systems for encapsulation of intermediate level waste. *Proceedings of the International Conference on Radioactive Waste Management and Environmental Remediation, ICEM*. **3**(January), pp.1425–1433.
- Shi, Z. and Atrens, A. 2011. An innovative specimen configuration for the study of Mg corrosion. *Corrosion Science*. **53**(1), pp.226–246.
- Song, G., Atrens, A. and St John, D. 2001. An hydrogen evolution method for the estimation of the corrosion rate of magnesium alloys *In: TMS Annual Meeting*., pp.255–262.
- Song, G., Atrens, A., Stjohn, D., Nairn, J. and Li, Y. 1997. The electrochemical corrosion of pure magnesium in 1 N NaCl. *Corrosion Science*. **39**(5), pp.855–875.

- Splinter, S.J., McIntyre, N.S., Lennard, W.N., Griffiths, K. and Palumbo, G. 1993. An AES and XPS study of the initial oxidation of polycrystalline magnesium with water vapour at room temperature. *Surface Science*. **292**(1–2), pp.130–144.
- Srinivasan, J. and Kelly, R.G. 2016. One-Dimensional Pit Experiments and Modeling to Determine Critical Factors for Pit Stability and Repassivation. *Journal of The Electrochemical Society*. **163**(13), pp.C759–C767.
- Strebl, M. and Virtanen, S. 2019. Real-Time Monitoring of Atmospheric Magnesium Alloy Corrosion. *Journal of The Electrochemical Society*. **166**(11), pp.C3001–C3009.
- Strehblow, H.H. and Marcus, P. 2011. Mechanisms of Pitting Corrosion *In: Corrosion Mechanisms in Theory and Practice: Third Edition*. CRC Press, pp.349–394.
- Sugimoto, K., Dinnebier, R.E. and Schlecht, T. 2007. Structure determination of $\text{Mg}_3(\text{OH})_5\text{Cl}\cdot 4\text{H}_2\text{O}$ (F5 phase) from laboratory powder diffraction data and its impact on the analysis of problematic magnesia floors. *Acta Crystallographica Section B: Structural Science, Crystal Engineering and Materials*. **63**(6), pp.805–811.
- Taheri, M. and Kish, J.R. 2012. Nature of Surface Film Formed on Mg Exposed to 1 M NaOH. *Journal of The Electrochemical Society*. **160**(1), p.C36.
- Taheri, M., Phillips, R.C., Kish, J.R. and Botton, G.A. 2012. Analysis of the surface film formed on Mg by exposure to water using a FIB cross-section and STEM-EDS. *Corrosion Science*. **59**, pp.222–228.
- Taylor, C.D. 2016. A First-Principles Surface Reaction Kinetic Model for Hydrogen Evolution under Cathodic and Anodic Conditions on Magnesium. *Journal of The Electrochemical Society*. **163**(9), pp.C602–C608.
- Taylor, S.R. and Gileadi, E. 1995. Physical interpretation of the Warburg impedance. *Corrosion*. **51**(9), pp.664–671.
- Trow, A. 2007. *Legacy Pond Solids Interim BPEO Progress Report RP/BEP_B873_PROJ_00025_P3*, Unpublished.
- Vermilyea, D.A. and Kirk, C.F. 1969. Studies of Inhibition of Magnesium Corrosion. *Journal of The Electrochemical Society*. **116**(11), p.1487.
- Walling, S. 2016. *Conversion of magnesium bearing radioactive wastes into cementitious binders*. University of Sheffield.
- Walling, S.A. and Provis, J.L. 2016. Magnesia-Based Cements: A Journey of 150 Years, and Cements for the Future? *Chemical Reviews*. **116**(7), pp.4170–4204.
- Williams, G., Birbilis, N. and McMurray, H.N. 2013. The source of hydrogen evolved from a magnesium anode. *Electrochemistry Communications*. **36**, pp.1–5.
- De Wit, J.H.W. and Lenderink, H.J.W. 1996. Electrochemical impedance spectroscopy as a tool to obtain mechanistic information on the passive behaviour of aluminium. *Electrochimica Acta*. **41**(7–8), pp.1111–1119.
- WNA 2016. Nuclear Development in the United Kingdom |UK Nuclear Energy Development - World Nuclear Association. [Accessed 1 January 2022]. Available from: <https://www.world-nuclear.org/information-library/country-profiles/countries-t-z/appendices/nuclear-development-in-the-united-kingdom.aspx>.

- Xia, S., Xing, P. and Gao, S. 1991. Studies on the basic compounds of magnesia cement: the thermal behaviour of magnesium oxychlorides. *Thermochimica Acta*. **183**(C), pp.349–363.
- Xiong, Y., Deng, H., Nemer, M. and Johnsen, S. 2010. Experimental determination of the solubility constant for magnesium chloride hydroxide hydrate ($\text{Mg}_3\text{Cl}(\text{OH})_5 \cdot 4\text{H}_2\text{O}$, phase 5) at room temperature, and its importance to nuclear waste isolation in geological repositories in salt formations. *Geochimica et Cosmochimica Acta*. **74**(16), pp.4605–4611.
- Ye, Q., Wang, W., Zhang, W., Li, J. and Chen, H. 2018. Tuning the phase structure and mechanical performance of magnesium oxychloride cements by curing temperature and $\text{H}_2\text{O}/\text{MgCl}_2$ ratio. *Construction and Building Materials*. **179**, pp.413–419.
- Yuwono, J.A., Birbilis, N., Taylor, C.D., Williams, K.S., Samin, A.J. and Medhekar, N. V. 2019. Aqueous electrochemistry of the magnesium surface: Thermodynamic and kinetic profiles. *Corrosion Science*. **147**, pp.53–68.
- Yuwono, J.A., Taylor, C.D., Frankel, G.S., Birbilis, N. and Fajardo, S. 2019. Understanding the enhanced rates of hydrogen evolution on dissolving magnesium. *Electrochemistry Communications*. **104**, pp.106–482.
- Zhang, X.G. 2011. Galvanic Corrosion. *Uhlig's Corrosion Handbook: Third Edition*., pp.123–143.
- Zheng, F., Rassat, S.D., Helderandt, D.J., Caldwell, D.D., Aardahl, C.L., Autrey, T., Linehan, J.C. and Rappé, K.G. 2008. Automated gas burette system for evolved hydrogen measurements. *Review of Scientific Instruments*. **79**(8), p.084103.